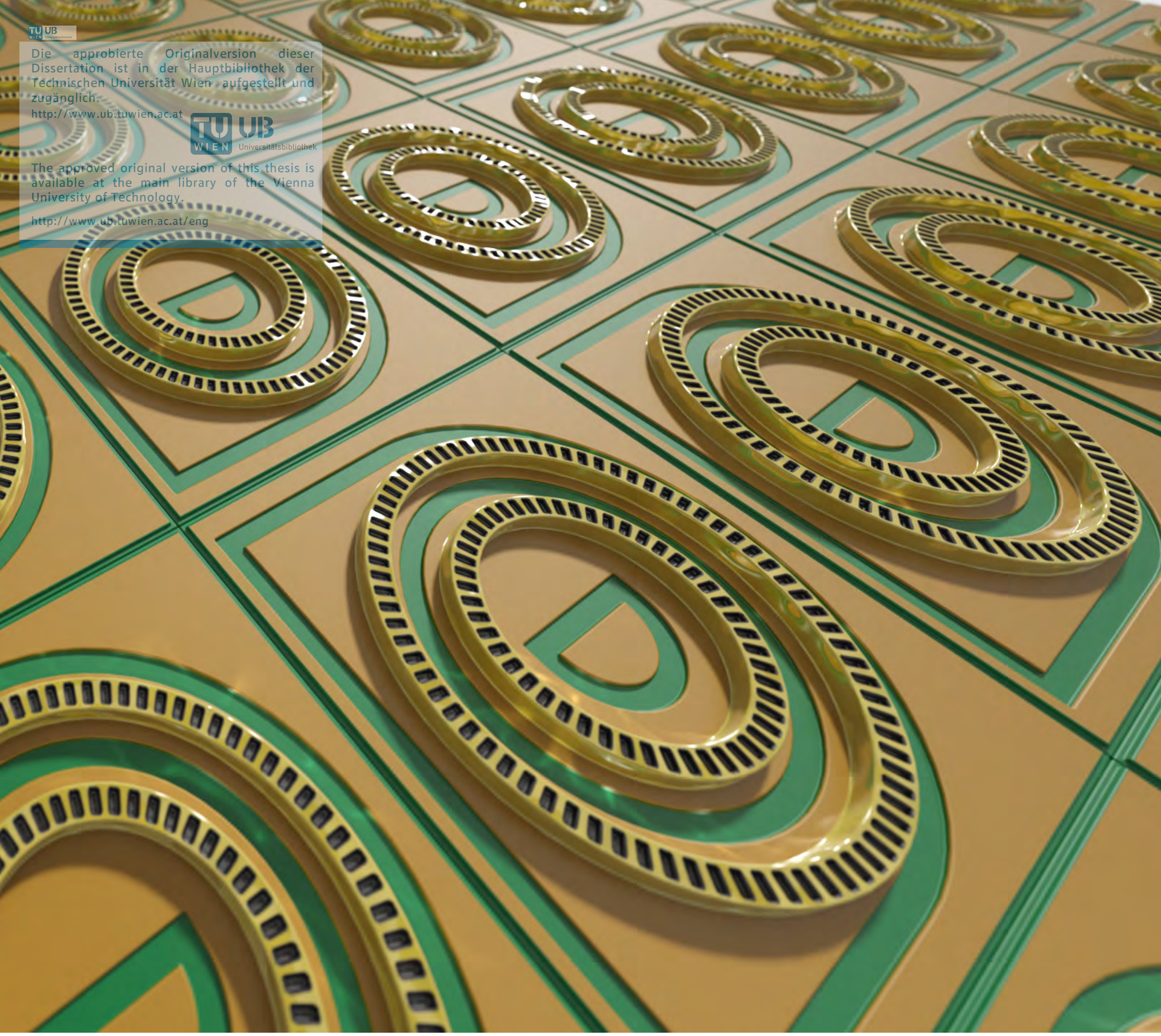

On the Light Emission from Ring Quantum Cascade Lasers and their Application in Spectroscopic Sensing

---

Rolf Szedlak

Dissertation

On the Light Emission from Ring Quantum Cascade Lasers and their Application in Spectroscopic Sensing

ausgeführt zum Zwecke der Erlangung des akademischen Grades eines
Doktors der technischen Wissenschaften

unter der Leitung von

Univ.-Prof. Dr. Gottfried Strasser
Institut für Festkörperelektronik

eingereicht an der

Technischen Universität Wien
Fakultät für Elektrotechnik und Informationstechnik

von

Rolf Szedlak, M.Sc.

Matrikelnummer: 1228454

Wien, Mai 2017

Gutachter: Prof. Dr. Manfred Helm
Director, Helmholtz-Zentrum Dresden-Rossendorf & TU Dresden

Dr. Raffaele Colombelli
CNRS Research Director, Université Paris-Sud

Tag der mündlichen Prüfung: 05. Mai 2017

to Svenja

Source: https://xkcd.com/824/

ABSTRACT

Efficient light sources in the mid-infrared spectral region are desirable for various environmental, industrial and biochemical applications. Quantum cascade lasers (QCLs) facilitate tailorable emission characteristics over a wide wavelength range and provide reliable high-performance operation. Besides the possibility of on-chip testing and two dimensional array integration, surface emitting QCLs offer collimated laser beams induced by their large apertures. A detailed understanding of the formation of the light beam as well as a precise control of the latter is indispensable for most applications. In the first part of this dissertation, beam modifications of vertically emitting ring QCLs are designed and successfully implemented. They provide enhanced beam patterns and make novel applications accessible. Dual distributed feedback gratings with integrated phase shifts create central lobed far field patterns and simultaneously contain detailed information about the location and order of the whispering gallery mode propagating inside the circular resonator. Due to the second order distributed feedback grating, ring QCLs exhibit bi-directional emission in the surface and substrate directions. A microscopic metamaterial is designed and directly fabricated into the semiconductor substrate in order to reshape the substrate beam. Based on this approach dielectric on-chip lenses for light collimation as well as spiral phase structures for orbital angular momentum beams are realized. The second part of this dissertation broaches the topic of ring QCLs for spectroscopic sensing applications. Compatibility of these lasers with substrate integrated hollow waveguides for gas analysis is demonstrated, which represents the first milestone towards compact sensor systems requiring small sample volumes. Heterodyne phase-sensitive detection techniques exhibits not only immunity to power fluctuations but also reveal key insights into the optical and electrical characteristics of ring QCLs. Finally, an innovative sensing concept is introduced which combines laser and detector on a single chip. Utilization of two concentric ring-shaped laser/detector units features mutual commutation and paves the way for ultra-compact sensor systems.

KURZFASSUNG

QUANTENKASKADENLASER sind effiziente Lichtquellen im mittleren Infrarotbereich, die elektronische Übergänge zwischen Subbändern im Leitungsband zur Lichterzeugung nutzen. Diese Subbänder entstehen durch das schichtweise Auftragen von unterschiedlichen Halbleitermaterialien. Die dabei abgestrahlte Wellenlänge des Lichts kann durch die Schichtdicke variabel gestaltet werden, was diese Laser zu vielseitig einsetzbaren Instrumenten in unterschiedlichen Bereichen wie Prozess- und Umweltüberwachung sowie medizinischer und biochemischer Diagnostik macht. Viele dieser Anwendungen profitieren dabei von kompakten und gleichzeitig effizienten Lichtquellen. Ringförmige Quantenkaskadenlaser (Ring QCLs) bestehen aus einem zirkularen Wellenleiter mit einem verteilten Rückkopplungsgitter zweiter Ordnung und gehören somit zu den Oberflächenemittern. Diese Laserstruktur ermöglicht sogenanntes „on-chip testing“ während allen Produktionsschritten und bietet dabei neben der Realisierbarkeit zweidimensionaler Matrixanordnungen auch den Vorteil großer emittierender Flächen, die einen kollimierten Laserstrahl erzeugen. Der erste Teil dieser Dissertation setzt sich zum Ziel diesen Laserstrahl neu zu gestalten um dabei die Leistungsfähigkeit der Laser zu verbessern sowie neue Anwendungsbereiche zu erschließen. Integrierte Phasensprünge im Rückkopplungsgitter sorgen für ein zentrales Intensitätsmaximum im Fernfeld des Lasers. Darüber hinaus ist es möglich mittels dieser Phasensprünge die Lasermode innerhalb des Resonators im Hinblick auf ihren Schwerpunkt sowie ihre Ordnung zu untersuchen. Ein neu entwickeltes duales Rückkopplungsgitter spiegelt dabei diese Charakteristika der Mode im Lichtstrahl des Lasers wider. Ring QCLs emittieren Licht nicht nur vertikal nach oben sondern auch nach unten durch das Substrat. Durch eine mikroskopische Strukturierung der Chip-Unterseite ist es gelungen ein vielseitiges Metamaterial zu entwickeln, das als fokussierende Linse oder als bahndrehimpulserzeugende Spiralstruktur direkt in den Halbleiterchip eingearbeitet werden kann. Im zweiten Teil dieser Dissertation werden potentielle Anwendungen von Ring QCLs in der Spektroskopie aufgezeigt. Durch ihre kompakte Bauweise sind diese Laser ideal zur Integration mit hohlen Lichtwellenleitern, die gleichzeitig als Gasmesszelle verwendet werden können, geeignet. Heterodyn-Spektroskopie in Kombination mit Ringlasern im Dauerstrichbetrieb bietet nicht nur Immunität gegen Intensitätsschwankungen sondern ermöglicht auch Einblicke in die optischen und elektrischen Eigenschaften dieser Laser. Im abschließenden Kapitel dieser Dissertation wird ein neuartiges Sensorprinzip vorgestellt, das Laser und Detektor auf einem einzigen Chip vereint. Darüber hinaus ist es durch Verwendung von zwei konzentrischen Ringstrukturen möglich vertauschbare Emissions- und Detektionseinheiten zu verwirklichen, die den Weg für kompakte Sensorsysteme ebnen.

TABLE OF CONTENTS

CHAPTER 1

INTRODUCTION

THE following chapter provides introductory aspects of light-matter interaction and gives an overview on light sources and detectors. Subsequently, the structure of this dissertation is described.

1.1 Light-matter interaction and infrared spectroscopy

ONE of the greatest endeavors of our time is the identification of matter and analysis of its structure. For this purpose various techniques from different scientific fields have been developed. One of the most powerful technique is optical spectroscopy exploiting the unique interaction between light and matter. According to quantum mechanics light consists of photons possessing the energy

$$E = h\nu = \hbar\omega = \frac{hc}{\lambda} \tag{1.1.1}$$

which is linked with Planck's constant h, the reduced Planck constant $\hbar$, the frequency ν and wavelength λ of the photon, its angular frequency ω and the speed of light c via the Planck-Einstein relation [1]. The nature and strength of any given light-matter interaction strongly depend on the energy of the involved photons. Table 1.1 illustrates how different photon energies induce diverse effects in matter. Photons with energies higher than 10^5 eV are associated with γ-rays and provoke nuclear transitions and even

Electromagnetic wave	Energy (eV)	Wavelength	Light-matter interaction
γ-rays	$> 10^5$	$< 10\,\text{pm}$	Nuclear disintegration
X-rays	10^5 - 10^2	10 pm - 10 nm	Ionization of inner electrons
Ultraviolet	10^2 - 3	10 nm - 400 nm	Ionization of outer electrons
Visible	3 - 1.8	400 nm - 700 nm	Electronic transitions
Infrared	1.8 - 10^{-3}	0.7 μm - 1 mm	Molecular vibrations
Microwave	10^{-3} - 10^{-6}	1 mm - 1 m	Molecular rotations
Radio	$< 10^{-6}$	$> 1\,\text{mm}$	Nuclear spin resonance

Table 1.1: Light-matter interaction classified by means of type of electromagnetic radiation. [2, 3]

disintegration of atomic nuclei. In the energy range between 10^5 and roughly 1.8 eV light interacts mainly with the electrons of atoms. X-ray and ultraviolet photons can ionize atoms by knocking out inner and outer electrons, respectively. Light in the visible part of the electromagnetic spectrum causes electronic transitions without ionization of the atom. For even lower photon energies the significance of electronic transitions declines. In this part of the electromagnetic spectrum, with energies ranging from $1 - 10^{-6}$ eV, infrared and microwave radiation induces molecular vibrations and rotations. The associated frequency of such molecular transitions originates from a discrete dipole alteration and change of the molecule's energy [4]. It is directly connected with the energy of the photon initiating or resulting from this dipole alteration. This is the basic foundation of molecular spectroscopy. Each molecule exhibits inimitable vibrational and rotational resonances resulting in a unique spectral pattern on the basis of which an explicit identification of the molecule is possible. [5, 6]

The simplest model for ro-vibrational transitions is the diatomic molecule which can be approximated by two masses connected via a spring obeying Hook's law. The resulting harmonic oscillation is described by a parabolic potential as given in Fig. 1.1. The quantized energy levels $E_n = h\nu(n + 1/2)$ are equidistant with an energy separation of $\Delta E = h\nu$, where n is the integer vibrational quantum number. This simplification would result in a single spectral line and is valid for small energies only [5]. A more realistic description is given by the Morse potential [7] illustrated in Fig. 1.1. The mathematical expression of the Morse potential $V^M(r)$ and the corresponding quantized energy levels E_n^M are given by

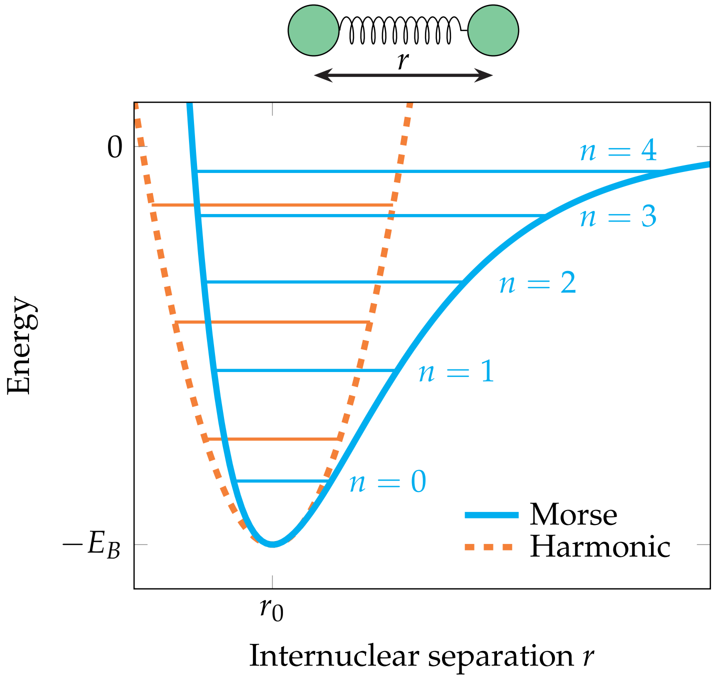

Figure 1.1: Morse potential describing molecular energy levels with dissimilar energy separation in contrast to the harmonic potential with equidistant levels.

$$V^M(r) = E_B e^{-2a(r-r_0)} - 2E_B e^{-a(r-r_0)} \quad (1.1.2)$$

$$E_n^M = h\nu(n + 1/2) - \frac{h^2\nu^2}{4E_B}(n + 1/2)^2 \quad (1.1.3)$$

with the binding energy E_B, the distance r between the atoms, the equilibrium distance r_0 and the constant a influencing the width of the potential. In contrast to the harmonic

potential this approach is capable of describing effects like molecular bond breaking, anharmonic oscillations and unbound states. Furthermore, the strict selection rule of the harmonic oscillator is weakened and non-zero transition dipole moments can be realized for $\Delta\nu \geq 2$ which gives rise to overtone bands. Rotation of molecules does not depend on the atomic mass itself but rather on the mass distribution given by the moment of inertia. Molecules with N atoms in 3 dimensions exhibit $3N - 3$ possible modes associated with non-translational displacements. In the case of linear molecules, 2 modes are rotational and $3N - 5$ are vibrational. Non-linear molecules have 3 rotational and $3N - 6$ vibrational degrees of freedom. Even this simple molecular model features a huge plurality of ro-vibrational resonances resulting in more complex spectra than for electronic transitions. Hence, these molecular spectra contain more information about the molecule and enable a distinct identification and characterization. [6, 8]
Figure 1.2 shows calculated molecular absorption spectra for various substances and illustrates the variety of molecular resonances.

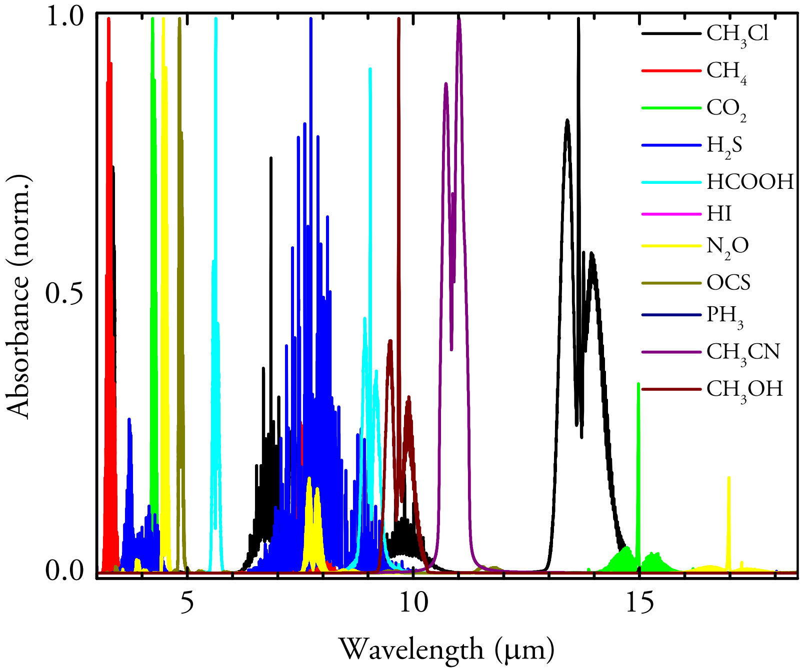

Figure 1.2: Normalized absorption spectra for eleven different chemical substances in the spectral range between 3 µm and 18 µm. Datasets are retrieved from the HITRAN [9] database.

1.2 Infrared light sources and detectors

According to Tab. 1.1 the photon energy required for performing molecular spectroscopy is located in the infrared and microwave region of the electromagnetic spectrum. Two fundamental types of light sources can be defined: (i) Broadband polychromatic emitters usually in the form of a black-body source and (ii) narrowband monochromatic emitters mostly associated with lasers.

1.2.1 Black-body radiators

Planck's radiation law [10] indicates that all matter with a non-zero temperature emits light. Spectral characteristics such as the spectral energy density $u(\nu)$ of such black-body emitters obey

$$u(\nu) = \frac{8\pi h\nu^3}{c^3}\frac{1}{e^{h\nu/k_BT}-1} \mathrel{\hat{=}} u(\lambda) = \frac{8\pi hc}{\lambda^5}\frac{1}{e^{hc/\lambda k_BT}-1} \tag{1.2.1}$$

with the Boltzmann constant k_B, implying an explicit dependence on the black-body temperature T as shown in Fig. 1.3 a). The standard technique for molecular spectroscopy using a broadband light source is Fourier transform infrared (FTIR) spectroscopy [11] based on the Michelson interferometer [12]. Its working principle is given in 1.3 b). The light emitted from the black-body source is divided by a beam splitter and one of the two rays is incident on a fixed mirror while the other ray is reflected by a moveable mirror. Both rays are combined again at the beam splitter and interfere with each other before they impinge on the detector. A change in the position of the moveable mirror directly changes the path length for the second beam. This alters the phase relation at the detector between both rays and influences the type of interference. In the symmetric case both paths are equal and a maximum signal for all wavelengths is measured at the detector due to constructive interference. For a single wavelength, constructive interference is ensured when the path difference $\delta = n\lambda$ is an integer multiple of this wavelength. Sweeping of the moveable mirror induces a continuous shift of δ and results in an oscillatory signal at the detector given by

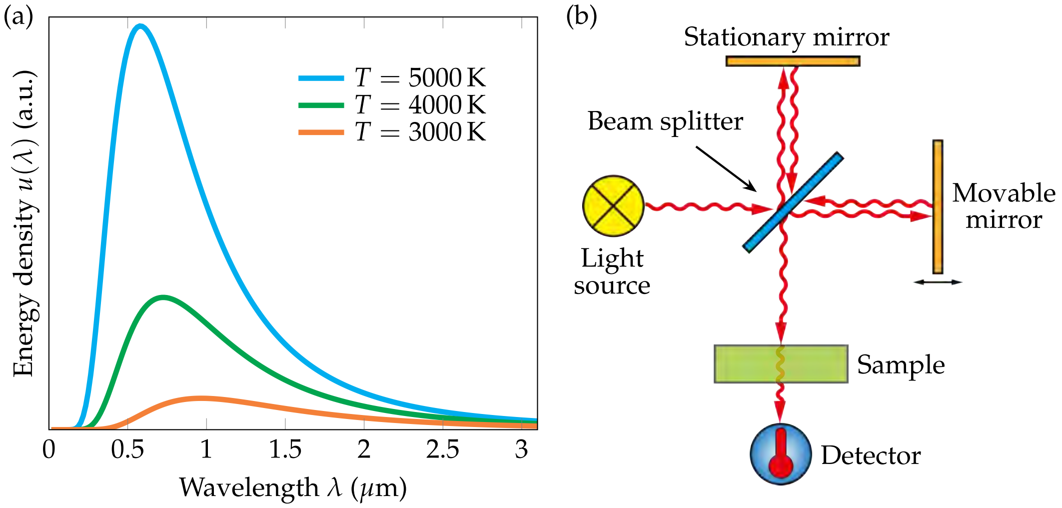

Figure 1.3: (a) Planck's radiation law for three different temperatures. As the temperature decreases the peak value of the energy density is reduced and shifted towards longer wavelengths. (b) Schematic of the working principle of an FTIR spectrometer.

$$I_\lambda(\delta) = \frac{I_0}{2}\left(1+\cos\left(2\pi\tilde{\nu}\delta\right)\right) \tag{1.2.2}$$

with the source intensity I_0 and the spatial frequency $\tilde{\nu} = 1/\lambda$. The interferogram is given by the modulated part in Eq. (1.2.2) without the constant component. For polychromatic light sources the measured detector signal at each δ-value is given by the superposition of all wavelengths resulting in the following integral description

$$S(\delta) = \int_{-\infty}^{\infty} I(\tilde{\nu})B(\tilde{\nu})\cos\left(2\pi\tilde{\nu}\delta\right)d\tilde{\nu} \tag{1.2.3}$$

where $I(\tilde{\nu})$ represents the wavelength-dependent emission characteristics of the source and $B(\tilde{\nu})$ takes into account the efficiencies of the beam splitter, the detector and other involved instruments. Equation (1.2.3) corresponds to the Fourier cosine transform, which for even functions is the same as the complex Fourier transform. Based on this idea the spectrum $I(\tilde{\nu})$ of the light source can be calculated by means of the Fourier transform of the interferogram $S(\delta)$ as follows

$$I(\tilde{\nu}) = B(\tilde{\nu}) \int_{-\infty}^{\infty} S(\delta) e^{i2\pi\tilde{\nu}\delta} d\delta. \tag{1.2.4}$$

FTIR spectrometers are widely used in various fields for structural determination. Their main advantages are the broad spectral coverage and good resolution which is only limited by the spatial dimension of the instrument. [8, 11]

1.2.2 Coherent sources

In contrast to black-body radiation, laser light is coherent and rather monochromatic. The high spectral density, narrow linewidth and excellent beam quality of lasers make them one of the most important light sources ever developed. The acronym “laser” stands for “light amplification by stimulated emission of radiation”. Based on Albert Einstein’s theoretical foundation [13] formulated in 1917 and the theoretical work [14] of Arthur L. Schawlow and Charles H. Towns, the first laser [15] was built by Theodore H. Maiman in 1960. It emitted in the microwave range and was therefore referred to as a “maser”. Since then a multitude of different types of lasers have been developed. While a more detailed description of the physical properties of lasers is given in chapter 2, the emphasis in this section lies in the various possibilities to generate infrared light using different laser types. The main components of a laser are the optical resonator, the pump and the gain medium providing discrete energetic levels. Gain media in all states of aggregation have been realized.

Gas lasers emitting in the infrared include the He-Ne laser at $\lambda = 3.39\,\mu$m [16] and the CO_2 laser at $\lambda = 9.4\,\mu$m and $\lambda = 10.4\,\mu$m [17] commonly used for material processing. Typically, they provide narrow-band emission with a high spectral purity [18] and use electrical discharge as a pump source.

In contrast, **dye lasers** mostly utilize an optically pumped liquid gain medium and operate in the visible and near-infrared (NIR) [19] spectral region. They exhibit a broad and tunable gain spectrum which strongly depends on the used organic molecules. This makes them versatile light sources used in medicine [20] and many other fields.

One of the most prevalent laser types is the **solid-state laser**. Its solid gain medium is usually made of an insulating host crystal containing lattice impurities called dopants which are predominantly rare-earth elements or transition metals. The lasing transition occurs between atomic energy levels of the dopant. Two of the most famous representatives of this laser family are the Ti:Sapphire [21] and the Nd:YAG [22] laser, both capable of emitting in the NIR around $\lambda = 1\,\mu$m. For longer emission wavelengths around $\lambda = 2.5\,\mu$m, various crystal-dopant combinations like Cr^{2+}:ZnSe [23] and Tm^{3+}:YLF [24] have been realized. By using exotic materials such as praseodymium [25] the maximum emission wavelength can be pushed to $\lambda = 7\,\mu$m. One subcategory of solid-state lasers are tunable fiber lasers in which the active medium is a doped fiber instead of a bulk crystal. Typical wavelengths for such lasers are between $\lambda = 400\,\text{nm}$ and $\lambda = 3\,\mu\text{m}$ [26].

Although **semiconductor lasers** are made of solid matter, they are classified as a separate laser type. This insinuates their fundamentally different nature compared with solid-state lasers. Conventional semiconductor lasers, also referred to as laser diodes, are electrically pumped and emit radiation due to an optical transition of an injected electron from the conduction to the valence band. These quantized energy levels are formed due to the crystalline nature of the semiconductor material and critically differ from the atomic energy levels of the dopants in solid-state lasers. At the end of 1962, four different groups demonstrated working diode lasers based on GaAs [27, 28, 29] and GaAsP [30] p-n homojunctions. This kind of semiconductor interface denotes a region where n-doped and p-doped parts of the same semiconductor coincide. Large electron and hole densities are necessary in order to stimulate the electron-hole recombination process and provide lasing [31]. Due to their smooth band alignment such homojunction lasers suffer from a high threshold current preventing continuous-wave (CW) or room-temperature operation. The development of semiconductor heterostructures [32, 33, 34] consisting of dissimilar materials with different band gaps enabled high carrier densities and paved the way to becoming the most widespread laser in the world [35, 36]. Such heterostructure diode lasers exhibit low threshold currents and provide CW operation at room temperature. The direct conversion of electrical current into light enables very high power efficiencies of more than 70% [37] and facilitates a direct current-induced modulation of the emitted light [38]. In addition, their high spectral purity, small size and robustness make them the light source of choice for many applications in various fields from telecommunications and materials processing to medicine and optical storage [36]. The emission wavelength of diode lasers is determined by the energetic distance between the bottom of the conduction and top of the valence bands. This specific material parameter is referred to as the band gap. For GaAs the band gap is around 1.48 eV [39], resulting in an emission wavelength of $\lambda = 840\,\text{nm}$ for the first laser diode. Due to their emission around $\lambda = 1.3\,\mu\text{m}$, InGaAs or InGaAsP diode lasers [40] are widely used for optical telecommunication. Conventional semiconductor diodes are limited to an upper CW room-temperature emission wavelength around $\lambda = 2.6\,\mu\text{m}$ utilizing the InGaAs/Sb material system [41]. This emission wavelength corresponds to a band gap of 0.48 eV. In principle, semiconductor compositions can be fine-tuned in order to create even smaller band gaps down to zero gap materials which would emit arbitrarily long wavelengths. However, a reduction of the band gap energy is accompanied by an increase of non-radiative Auger recombination [42], rendering such lasers impractical. [38, 43, 44]

Nevertheless, there is one class of diode lasers providing emission within a broad wavelength range in the mid-infrared (MIR) from $\lambda = 3\,\mu\text{m}$ to $\lambda = 30\,\mu\text{m}$. These so-called **lead-salt lasers** are IV-VI compounds containing several of the few naturally occurring semiconductors. Due to their non-degenerate band extrema at the L-point, they do not suffer as much from Auger recombination as conventional III-V semiconductors. Since their emission wavelength can be easily tuned, most of their applications are in the field of gas sensing. Despite these promising characteristics, lead salt lasers are still limited to cryogenic operation. This performance shortcoming is not determined by Auger recombination but by some other non-radiative loss mechanism originating from impurities or other material properties [45]. This deficient material reliability prevents not only CW room temperature operation but also greater applications of this laser type. [43, 46]

Still, these light sources dominated the MIR spectral region [47] until the development of the **quantum cascade laser** (QCL) [48] in 1994. Their unique way of producing photons via cascading intersubband transitions within the conduction band facilitates tailorable laser emission from the MIR to the terahertz (THz) spectral region utilizing standard and easily manageable semiconductor materials. A more detailed description of QCLs is provided in section 2.2.

Rather exotic infrared light sources are **non-linear sources** [49], based on effects like frequency-mixing and **free-electron lasers** [50] with an active medium made of fast electrons in a magnetic field.

1.2.3 Detectors

Numerous possibilities for generating infrared light have been specified. Infrared detectors are essential in order to sense the light emitted by coherent sources or black-body radiators. Two different detection mechanisms can be identified: (i) Thermal detectors and (ii) photonic detectors.

The former is sensitive to the absorbed radiation power, which increases the temperature of the isolated detector element. This temperature change can be measured in the form of the thermoelectric effect in **thermopiles** [51], a resistance change in **bolometers** [52, 53] or thermal expansion in **Golay cells** [54].

In contrast, photonic detectors operate upon photon-induced electronic excitations. These electrons are measured via an electronic readout scheme. **Direct band gap detectors** based on materials like mercury-cadmium-telluride (MCT) [55] exploit the fundamental transition from the valence band to the conduction band. In **Schottky barrier detectors** [56] electrons are excited in the metal by incoming photons and have to escape over the barrier where they can be measured. Similarly, in **quantum well infrared photodetectors (QWIPs)** [57, 58] electrons are photo-excited from the lowest energy level in a quantum well to the next level from where they can overcome the barrier and contribute to the photocurrent. Recently, **quantum cascade detectors (QCDs)** [59, 60] have been developed. As in QCLs, the working principle is based on a cascading scheme. Compared with QWIPs, each excited electron is not directly injected into the continuum but rather recycled and guided to the lowest energy level of the next active quantum well. All of the detectors mentioned above can be used for sensing and imaging applications. Figure 1.4 shows an infrared image of a black-body radiator, also referred to as the author of this dissertation, recorded with the FLIR ONE ™ thermal imaging camera. [61, 62]

1.3 Structure of this dissertation

In the present dissertation various aspects of the emission beam of ring QCLs as well as potential sensing applications are outlined. For a successful implementation of these lasers a profound understanding of the formation of the far field is indispensable. By gaining this knowledge, modifications of the laser beam can be put into effect and enable significant performance enhancement. Chapter 2 provides a thorough introduction to elementary principles of optoelectronic devices. In chapter 3 the working principle of light extraction in ring QCLs is discussed. On this basis, beam modifications including

Figure 1.4: Infrared image taken with the FLIR ONE ™ thermal imaging camera.

the generation of central lobed beams, on-chip light collimation and the creation of orbital angular momentum beams are introduced. Implementation of ring QCLs in spectroscopic sensing setups is demonstrated in chapter 4. The latter comprises the first demonstration of a ring QCL integrated with a hollow waveguide as well as utilization of such a laser for heterodyne phase-sensitive detection. The final topic in this chapter is a matter of remote photonic sensing using an innovative on-chip sensor system. Based on bi-functional quantum cascade heterostructures, surface emitting and detecting sensors are demonstrated. Chapter 5 provides a conclusion and specifies concepts for potential future research on ring QCLs.

CHAPTER 2

OPTOELECTRONIC PRINCIPLES

Electrons in a crystalline lattice form electronic bands. Transitions between the latter give rise to lasing processes. In this chapter the theoretical foundation for optoelectronic devices with a focus on intersubband lasers is discussed.

2.1 From crystals to lasers

Free electrons are characterized by energy values according to

$$E = \frac{\hbar^2 \mathbf{k}^2}{2m} \tag{2.1.1}$$

with the reduced Planck constant $\hbar$, the electron mass m_e and the wavevector $\mathbf{k}$. Electrons in solid matter perceive the potential of the atomic nuclei. In the case of a crystal, the atoms are arranged in a regular pattern producing a periodic potential $V(\mathbf{r}+\mathbf{R}) = V(\mathbf{r})$ for all Bravais lattice vectors $\mathbf{R}$. Bloch's theorem dictates that the eigenstates are given by the product of a plane wave with the periodicity $u_{\mathbf{k}}(\mathbf{r}+\mathbf{R}) = u_{\mathbf{k}}(\mathbf{r})$ of the lattice. The wavefunction can then be written as follows

$$\Psi(\mathbf{r}+\mathbf{R}) = e^{i\mathbf{k}\mathbf{R}}\Psi(\mathbf{r}). \tag{2.1.2}$$

Based on this approach there are several simple concepts describing the energetic levels or electronic bands in a solid. The approximation of the “quasi-free” electron or “weak binding” method starts with totally free electrons and adds a weak periodic potential which slightly modifies the electronic energies. This is treated as a small perturbation of the initial system of the free electron. Obviously, this approach describes valence electrons better than core electrons. On the other hand, the “tight binding” method starts from completely separated atomic sites where the electronic energy levels coincide with the atomic levels and no coupling between neighboring atoms is existent. When these atoms are mentally brought closer together, at some point the electron at one atomic site will perceive the potential of the neighboring atom which will slightly modify the electronic energies. In the tight binding approach the energy difference between the raw atomic energy and this modified electronic energy is treated as a small perturbation. The $\mathbf{k}\cdot\mathbf{p}$ method expands the entire band structure on the basis of the $k = 0$ value. In the following, these approaches are explained in more detail.

2.1.1 The quasi-free electron

A general term for the wavefunction is given by a plane wave expansion $\Psi(\mathbf{r}) = \sum_{\mathbf{k}} C_{\mathbf{k}} e^{i\mathbf{kr}}$ with the expansion coefficients $C_{\mathbf{k}}$. This leads to the Schrödinger equation in reciprocal space

$$\left(\frac{\hbar^2 k^2}{2m} - E\right) C_{\mathbf{k}} + \sum_{\mathbf{G}} V_{\mathbf{G}} C_{\mathbf{k}-\mathbf{G}} = 0 \tag{2.1.3}$$

with the reciprocal lattice vector $\mathbf{G}$. Equation (2.1.3) connects only these expansion coefficients whose $\mathbf{k}$-values differ by a reciprocal lattice vector. Since the number of reciprocal lattice vectors is given by the number of unit cells N, Eq. (2.1.3) represents N systems of equations. Each of these equations has a solution given by a superposition of plane waves whose $\mathbf{k}$-values differ only by a reciprocal lattice vector $\mathbf{G}$. The corresponding wavefunction is given by

$$\Psi_{\mathbf{k}}(\mathbf{r}) = \sum_{\mathbf{G}} C_{\mathbf{k}-\mathbf{G}} e^{i(\mathbf{k}-\mathbf{G})\mathbf{r}} \tag{2.1.4}$$

with periodic energy eigenvalues $E(\mathbf{k}) = E(\mathbf{k}+\mathbf{G})$. Therefore, in the one-dimensional case the eigenvalues in the first Brillouin zone at $k = G/2$ are degenerate due to the overlap of two energy parabolas. In the simplest approximation the wavefunctions are described by an overlap of the two corresponding plane waves

$$\Psi_{\pm} \propto e^{iGx/2} \pm e^{-iGx/2}. \tag{2.1.5}$$

The probability density $\Psi_{\pm}^{*}\Psi_{\pm}$ results in a $\sin^2$ function for Ψ_{-} and a $\cos^2$ for Ψ_{+}. Electrons with Ψ_{-} are rather located between atomic sites, which is accompanied by a relative increase of the total energy compared to the traveling plane wave. On the other hand, electrons with Ψ_{+} are more likely found at the atomic sites, which reduces their total energy. In order to quantify the emerging energy gap induced by this band splitting, the reciprocal Schrödinger equation has to be rewritten as follows

$$\left(E - \frac{\hbar^2}{2m}\left|\mathbf{k}-\mathbf{G}\right|^2\right) C_{\mathbf{k}-\mathbf{G}} = \sum_{\mathbf{G}'} V_{\mathbf{G}'-\mathbf{G}} C_{\mathbf{k}-\mathbf{G}'} \tag{2.1.6}$$

where $E^0_{\mathbf{k}-\mathbf{G}} = (\hbar^2/2m)\left|\mathbf{k}-\mathbf{G}\right|^2$ represents the energy of the free electron. The discrepancy between the free and the quasi-free electron are given by the coefficients $C_{\mathbf{k}-\mathbf{G}}$. This means that the strongest deviation is expected for $|\mathbf{k}| \approx |\mathbf{k}-\mathbf{G}|$, that is at the Brillouin zone boundary. In a first approximation only the largest coefficients $C_{\mathbf{k}}$ and $C_{\mathbf{k}-\mathbf{G}}$ play a significant role. Equation (2.1.6) then simplifies to the following equation system

$$\left(E - \frac{\hbar^2}{2m}\left|\mathbf{k}\right|^2\right) C_{\mathbf{k}} = V_{\mathbf{G}} C_{\mathbf{k}-\mathbf{G}} \tag{2.1.7}$$

$$\left(E - \frac{\hbar^2}{2m}\left|\mathbf{k}-\mathbf{G}\right|^2\right) C_{\mathbf{k}-\mathbf{G}} = V_{-\mathbf{G}} C_{\mathbf{k}}. \tag{2.1.8}$$

Its solution is given by

$$E_{\pm} = \frac{1}{2}\left(E^0_{\mathbf{k}-\mathbf{G}} + E^0_{\mathbf{k}}\right) \pm \sqrt{\frac{1}{4}\left(E^0_{\mathbf{k}-\mathbf{G}} - E^0_{\mathbf{k}}\right)^2 + \left|V_{\mathbf{G}}\right|^2}. \tag{2.1.9}$$

Directly at the Brillouin zone boundary $E^0_{\mathbf{k}-\mathbf{G}} = E^0_{\mathbf{k}}$, resulting in the formation of an energy gap given by

$$\Delta E = 2\left|V_{\mathbf{G}}\right| \tag{2.1.10}$$

and schematically illustrated in Fig. 2.1. [63]

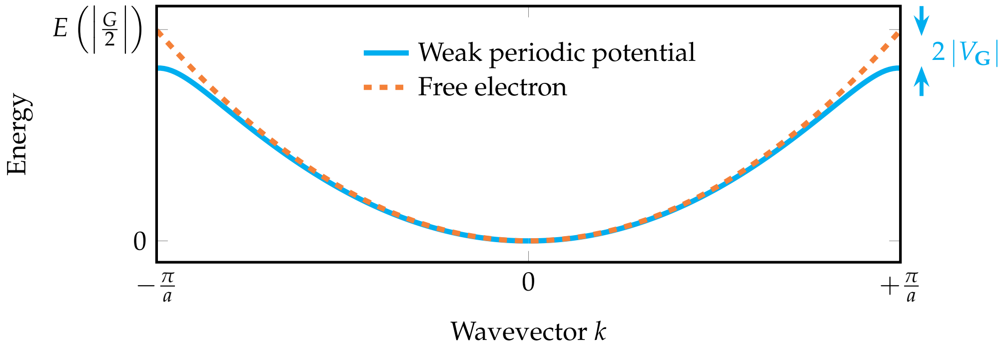

Figure 2.1: Comparison between the energy dispersion of free electrons and electrons in a weak periodic potential. The energy difference at the Brillouin zone boundary introduces forbidden energy bands.

2.1.2 Tight binding

For the tight binding approach the Schrödinger equation and its solution are assumed to be known for the isolated atomic sites. The small perturbation ΔU from the neighboring potentials can be described by an overlap of all atomic potentials V_{at} in the form of $\Delta U(\mathbf{r}) = \sum_m V_{at}(\mathbf{r} - \mathbf{r}_m)$. The modified Hamiltonian is

$$H = \underbrace{-\frac{\hbar^2}{2m}\Delta + V_{at}(\mathbf{r})}_{H_{at}} + \Delta U(\mathbf{r}) \tag{2.1.11}$$

with the known atomic Hamiltonian H_{at}. Due to the periodicity of the system, Bloch waves should solve the corresponding Schrödinger equation. The wavefunction is defined by

$$\Psi(\mathbf{r}) = \sum_{\mathbf{R}} e^{i\mathbf{kR}}\phi(\mathbf{r} - \mathbf{R}) \tag{2.1.12}$$

with the function $\phi(\mathbf{r})$ being close to a stationary atomic wavefunction. This function ϕ, on the other hand, is assumed to be well described by a limited number of neighboring atomic wavefunctions φ_n also referred to as a linear combination of atomic orbitals (LCAO) as in

$$\phi(\mathbf{r}) = \sum_n b_n \varphi_n(\mathbf{r}) \tag{2.1.13}$$

weighed by the coefficients b_n. Using the modified Hamiltonian from Eq. (2.1.11) the Schrödinger equation reads

$$H\Psi(\mathbf{r}) = (H_{at} + \Delta U(\mathbf{r}))\,\Psi(\mathbf{r}) = E(\mathbf{k})\Psi(\mathbf{r}). \tag{2.1.14}$$

Multiplication with the atomic wavefunction φ_m^* and integration over all distances $\mathbf{r}$ yields

$$(E(\mathbf{k}) - E_m)\int_{\mathbf{r}} \varphi_m^*(\mathbf{r})\Psi(\mathbf{r})d\mathbf{r} = \int_{\mathbf{r}} \varphi_m^*(\mathbf{r})\Delta U(\mathbf{r})\Psi(\mathbf{r})d\mathbf{r} \tag{2.1.15}$$

with the atomic eigenvalue E_m. Utilizing Eq. (2.1.12) and (2.1.13) consequently results in

$$E(\mathbf{k}) = E_m + \frac{\sum_n b_n \sum_{\mathbf{R}} \int_{\mathbf{r}} \varphi_m^*(\mathbf{r})\Delta U(\mathbf{r})\varphi_n(\mathbf{r} - \mathbf{R})e^{i\mathbf{kR}}d\mathbf{r}}{\sum_n b_n \sum_{\mathbf{R}} \int_{\mathbf{r}} \varphi_m^*(\mathbf{r})\varphi_n(\mathbf{r} - \mathbf{R})e^{i\mathbf{kR}}d\mathbf{r}}. \tag{2.1.16}$$

Due to the orthonormality of the atomic wavefunctions φ_i, the denominator equals 1 for $n = m$ and $R = 0$. Otherwise, the denominator is zero. Considering the simplest example, the single atomic s-orbital, the $\sum_n$ runs only over a single atomic site and the corresponding band structure is given by

$$E(\mathbf{k}) = E_s + \underbrace{\sum_{\mathbf{R}\neq 0} \int_{\mathbf{r}} \phi^*(\mathbf{r})\phi(\mathbf{r}-\mathbf{R})\Delta U(\mathbf{r}) e^{i\mathbf{k}\mathbf{R}} d\mathbf{r}}_{\alpha e^{i\mathbf{k}\mathbf{R}}} + \underbrace{\int_{\mathbf{r}} |\phi(\mathbf{r})|^2 \Delta U(\mathbf{r}) d\mathbf{r}}_{\beta=\text{const.}} \tag{2.1.17}$$

with the energy E_s of the atomic s-orbital level and the overlap integral α. For a primitive cubic lattice the lattice vectors for the nearest neighbors are $\mathbf{R} = (\pm a, 0, 0)$; $(0, \pm a, 0)$; $(0, 0, \pm a)$. This simplifies the electronic band structure to

$$E(\mathbf{k}) = E_s + 2\alpha \left[\cos(k_x a) + \cos(k_y a) + \cos(k_z a)\right] + \beta \tag{2.1.18}$$

with $\mathbf{k} = (k_x, k_y, k_z)$. The function in Eq. (2.1.18) for the electronic s-band in a cubic lattice is illustrated in Fig. 2.2. The bandwidth of the s-band is determined by the overlap integral and amounts to 4α in the [100] and 12α in the [111] direction. The proportionality between bandwidth and overlap integral demonstrates the fundamental characteristics of the tight binding method. The greater the overlap between the atomic orbitals, the wider the corresponding bands. For a vanishing overlap the electronic bands turn to the discrete energy levels of the scenario with completely isolated atomic sites. Consideration of further atomic orbitals introduces multiple energy bands and a more complex band structure including possible forbidden energies creating band gaps. [63, 64]

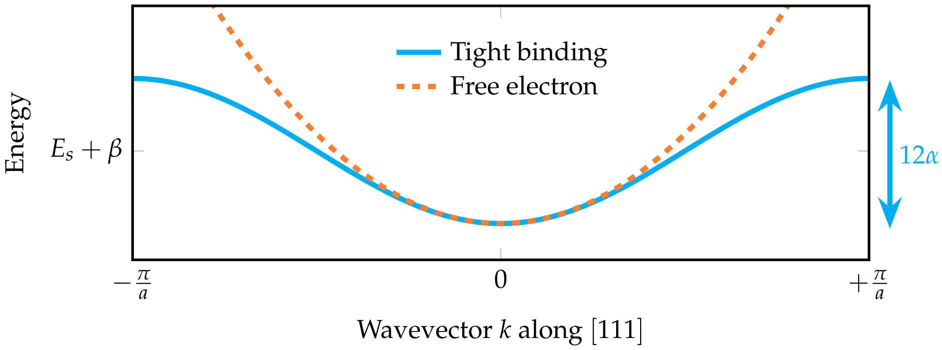

Figure 2.2: Electronic s-band in a cubic lattice calculated with the tight binding approach. In the [111] direction the total bandwidth amounts to 12α.

2.1.3 $\mathbf{k} \cdot \mathbf{p}$ method and envelope function approximation

One of the most widespread techniques for band structure calculations is the $\mathbf{k} \cdot \mathbf{p}$ method. The latter requires the knowledge of the band structure at $k = 0$ and expands the rest of the band structure based on this information. This expansion can be performed by means of perturbation theory which yields the following second order energy correction for the conduction band

$$E_c(\mathbf{k}) = E_c(0) + \frac{\hbar^2 k^2}{2m_0} + \frac{\hbar^2}{m_0} \sum_{m\neq c} \frac{|\langle u_{c,0} |\mathbf{k}\cdot\mathbf{p}| u_{m,0}\rangle|^2}{E_c - E_{m,0}} \tag{2.1.19}$$

neglecting the spin-orbit coupling. Assuming an isotropic interband matrix element $\mathbf{p}_{cv}$ in combination with a non-directional dependence of the energy on $\mathbf{k}$ simplifies this term to

$$E_c(k) = E_g + \frac{\hbar^2 k^2}{2m_0} + \frac{\hbar^2 k^2}{m_0} \frac{|p_{cv}|^2}{E_g} \tag{2.1.20}$$

with the band gap energy E_g. In combination with the envelope function approximation this technique represents a powerful tool for the theoretical analysis of semiconductor nanostructures. The latter consist of at least two different materials (A and B) forming quantum wells or barriers due to differing conduction band edges. The envelope function approximation indicates that the wavefunction

$$\Psi(\mathbf{r}) = \sum_l f_l^{A,B} u_{l,\mathbf{k}_0}^{A,B}(\mathbf{r}). \tag{2.1.21}$$

can be written as a sum of slowly varying envelope functions $f_l^{A,B}$. The latter is modulating the Bloch function and at each point a $\mathbf{k} \cdot \mathbf{p}$ analysis yields the corresponding wavefunction. [65]

2.1.4 Lasers

Depending on the characteristics of the band structure, crystalline materials can be classified into metals, insulators and semiconductors. All available electrons fill the electronic band structure starting from the lowest energy till the Fermi energy E_F at which all electrons are used up. Metals exhibit a Fermi energy level intersecting with an electronic band. Electrons at the Fermi edge can travel along this band which enables easy electron transport. For insulators and semiconductors the Fermi energy is located within an energy gap. In order to achieve electronic transport, an electron at the Fermi edge has to be lifted over the band gap into the next higher band. There the electron can easily travel along these empty bands. The full bands below the Fermi energy are referred to as the valence bands and the empty bands above the Fermi level are the conduction bands. These bands can assume the role of laser levels. Transition rates between these levels can be characterized by

$$R_{ij}^{sp} = A_{ij} N_i \tag{2.1.22}$$

$$R_{ij}^{in} = B_{ij} N_i u(\nu). \tag{2.1.23}$$

with the Einstein coefficients A_{ij} and B_{ij} for spontaneous and stimulated transitions from level i to j. The spontaneous transition process does only depend on the Einstein coefficients and the population density N_i. For stimulated transitions the photon density u from Eq. (1.2.1) with suitable energies plays a role as well. A detailed description of the rate equation of a 3-level systems is given in section 2.2. [31, 38, 66]

In semiconductor laser diodes upper and lower laser level are given by the lower edge of the conduction and upper edge of the valence band, respectively. The pump source are directly injected charge carriers. These electrons and holes recombine at the pn-junction, operated in forward bias, and produce monochromatic light. The pn-junction is an interface between p- and n-doped semiconductor materials. They incorporate impurity atoms providing an additional electron for n-doping or hole for p-doping. These quasi-free charge carriers introduce quasi-Fermi levels E_{qF} near the conduction and valence band edge for electrons and holes, respectively. Stimulated emission takes place when an incoming photon faces a higher probability to induce a stimulated transition from level 2 to 1 than an absorption transition from level 1 to 2. Taking into account the density of states D_i of the initial and final state this results in

$$\begin{aligned} R_{21}^{in} &> R_{12}^{ab} \qquad (2.1.24)\\ \Rightarrow B_{21} f(E_2) D_2 (1 - f(E_1)) D_1 u &> B_{21} f(E_1) D_1 (1 - f(E_2)) D_2 u. \qquad (2.1.25)\end{aligned}$$

with the Fermi function $f(E_i)$. This simplifies to

$$\begin{aligned} f(E_2)(1 - f(E_1)) &> f(E_1)(1 - f(E_2)) \qquad (2.1.26)\\ \Rightarrow f(E_2) &> f(E_1). \qquad (2.1.27)\end{aligned}$$

According to Fermi-Dirac statistics the occupation probability reads

$$f(E) = \frac{1}{1 + e^{(E-\mu)/k_B T}} \qquad (2.1.28)$$

with the chemical potential μ which is given by the quasi-Fermi levels. As a direct consequence this yields

$$E_{qF2} - E_{qF1} > E_2 - E_1 = E_g \qquad (2.1.29)$$

with the band gap energy E_g. Population inversion is reached when the energetic distance between both quasi-Fermi levels is greater than the band gap energy and the quasi-Fermi levels lie inside the corresponding bands. This can be realized via doping and direct injection of carriers. [67, 68]

2.1.5 Quantum confinement

In order to achieve high electron densities in the upper laser level, quantum structures such as quantum wells are beneficial. Quantum wells consist of a semiconductor material encompassed by two different semiconductors with a higher band gap energy. Due to a continuous alignment of the Fermi level both the conduction and valence band form a quantum well providing a two-dimensional confinement with high carrier densities for electrons and holes, respectively. Therefore, the wavevectors in the confinement direction are quantized according to

$$k_z = \frac{n\pi}{w_{qw}} \qquad (2.1.30)$$

with the integer number n and the well width w_{qw}. With the conduction band edge E_c the energy of these quantized states is given by

$$E(k) = E_c + \frac{\hbar^2}{2m^*}\left[\left(\frac{n\pi}{w_{qw}}\right)^2 + k_x^2 + k_y^2\right]. \qquad (2.1.31)$$

For each n-value a separate subband is emerging each with a constant density of states given by $m/(\pi\hbar^2 w_{qw})$. Therefore, less states are available in a given energy range compared with the three-dimensional case. As a result, less injected electrons are necessary to levitate the quasi-Fermi levels into the corresponding bands and a lower threshold current is observed in these lasers. [66, 69]

2.2 Intersubband devices

The most straightforward laser transition in a semiconductor is the one from the conduction band to the valence band. In theory, long emission wavelengths could be achieved by a reduction of the corresponding band gap energy. However, due to a significant rise of non-radiative Auger recombination for decreasing band gap energies, this approach is not feasible, especially for the required high carrier densities. Besides lead salt lasers, which face additional problems as described in section 1.2, this fact demonstrates the necessity for a fundamentally different concept of optical transitions. Instead of using *inter*band transitions between two different bands, a splitting of one band into multiple subbands can be exploited for so-called *intra*band or intersubband transitions between these subbands. Possible approaches for this band splitting include the utilization of magnetic fields [70] and quantum wells [71]. Both are associated with different constraints for the motion of the electron. Magnetic fields initiate a circular electron trajectory, while quantum wells confine the electron in one dimension. The generation and amplification of light originating from intraband transitions in such low dimensional systems was predicted in 1971 by Kazarinov and Suris [72]. It was only much later that this concept could be experimentally realized by Faist et al. in 1993 in the form of a unipolar quantum cascade light emitting diode [73, 74] and finally in 1994 in terms of the first quantum cascade laser (QCL) [48]. These devices were based on the InP/GaInAs/AlInAs material system. Light emitting diodes [75] and QCLs [76] in the GaAs/AlGaAs material system have been realized in the following years.

2.2.1 Interband vs. intersubband transitions

The fundamental difference between an interband and an intraband or intersubband laser is sketched in Fig. 2.3 (a). In contrast to interband lasers, the optical transition in QCLs is not between conduction and valence band but between subbands within the conduction band formed by multiple quantum well structures. Furthermore, replications of these quantum wells yield the cascading scheme of QCLs in which an electron is recycled and travels through multiple quantum well periods. In this way, one electron ideally emits as many photons as there are periods in the structure. For interband lasers the emission wavelength is determined by the band gap energy. In contrast, the emission wavelength of QCLs is not dependent on the band gap but directly determined by the geometrical dimensions of the quantum wells, i.e. the layer thicknesses of the semiconductor materials and the difference between their band gap energies. This allows the use of sophisticated and easy to handle wide gap semiconductor materials with minor Auger recombination. Nevertheless, typical laser thresholds are higher in QCLs than in band gap lasers. This is due to fast ($\propto 1\,\mathrm{ps}$) longitudinal optical (LO) phonon transitions, which require a huge amount of injected electrons in order to compensate for the short lifetime of electrons in the upper laser level. Due to the same curvature of the subbands, QCLs exhibit a sharper joint density of states of the optical transition than interband lasers. This results in sharp gain spectra and high spectral densities. [46]

Besides the main differences between band gap lasers and QCLs, Fig. 2.3 (b) also shows two different types of photon-induced intersubband transitions. The vertical transition scheme exhibits larger transition rates but suffers more from the fast non-radiative transitions. In the diagonal transition scheme the spatial separation between upper and lower laser level located in neighboring quantum wells makes population inversion easier.

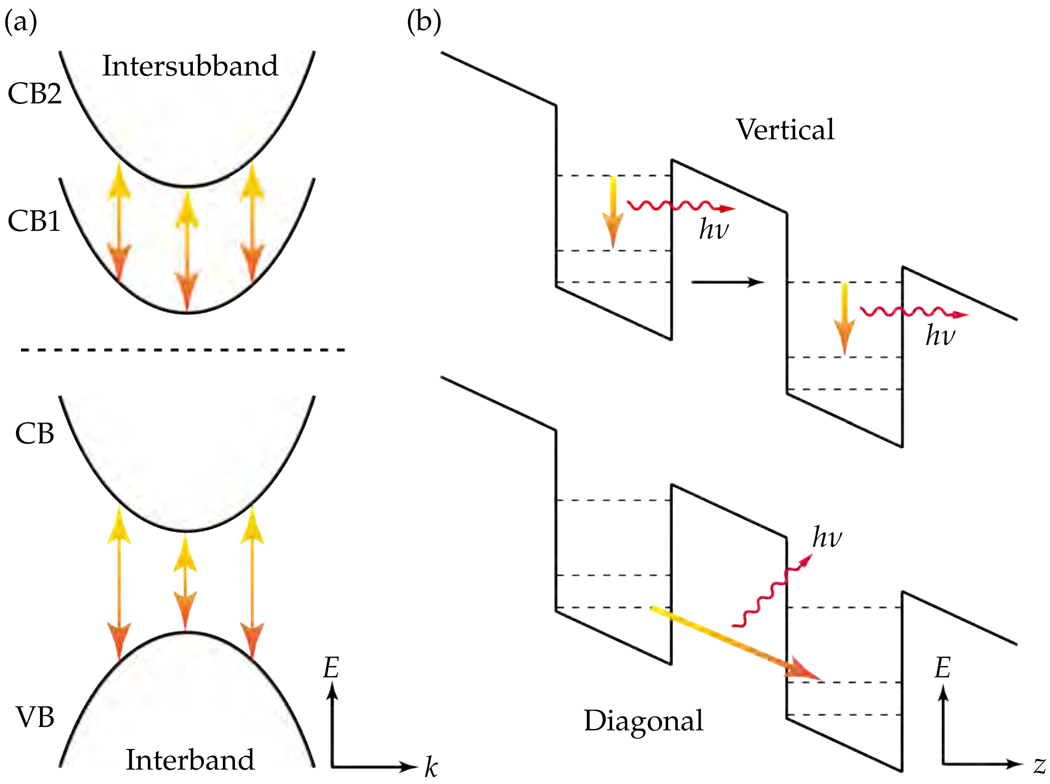

Figure 2.3: (a) Comparison between intersubband (top) and interband (bottom) laser transitions. (b) Schematics of vertical (top) and diagonal (bottom) intersubband transitions.

On the other hand, the reduced wavefunction overlap provides a lower transition rate, resulting in an increased threshold. Both approaches require good electron confinement in the upper laser level and short electron lifetimes in the lower laser level. These criteria can be met by a proper design of the band structure. [77]

2.2.2 Optical transitions

A sketch of the laser levels and the electronic transition channels of a typical 3-level system is illustrated in Fig. 2.4. The upper laser level 3 is supplied with electrons from the injector with which it is energetically aligned. For simplicity, the injector is assumed to consist of only one level with a constant electron population. Electrons are injected at a constant rate R_{inj}. On the basis of Eq. (2.1.22) and (2.1.23), this assumption yields electron rate equations for the upper and lower laser levels as follows

$$\frac{dN_3}{dt} = R_{\text{inj}} - \underbrace{(A_{32} + A_{31} + A_{3c})}_{A_3} N_3 - B_{32}(N_3 - N_2)u \tag{2.2.1}$$

$$\frac{dN_2}{dt} = B_{32}(N_3 - N_2)u + A_{32}N_3 - A_{21}(N_2 - N_1). \tag{2.2.2}$$

An additional scattering channel A_{3c} from level 3 into the continuum is assumed and the injection rate $R_{\text{inj}} = j/e$ is characterized by the injected current density j and the elementary charge e of the electron. Thermal backfilling of electrons into the lower laser state is described by $A_{21}N_1$. In order to connect electron and photon densities, an additional rate equation for the latter has to be established. The photon flux $F_{ph} = c_n N_{ph}$ is given by the product of the photon velocity c_n and the photon density N_{ph}. Consequently, the rate of change of the photon population is calculated according to

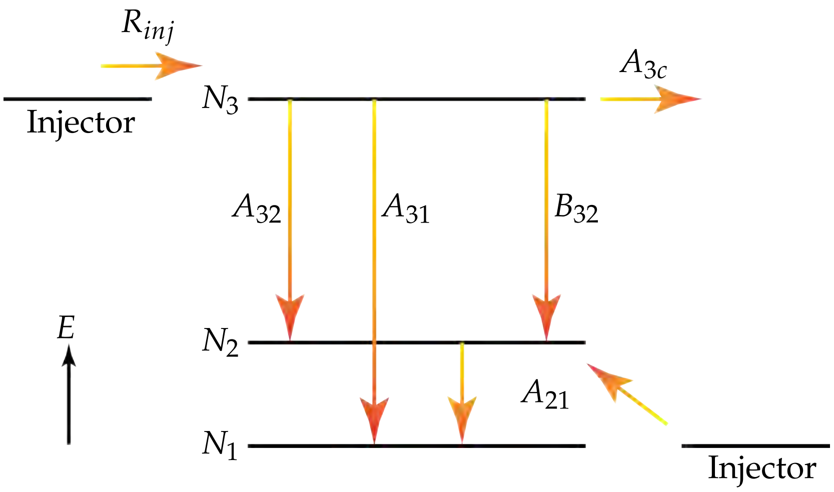

Figure 2.4: Descriptive illustration of the significant electronic transitions in a three level intersubband laser. The levels are labeled N_i and the injection rate is given by R_{inj}. Spontaneous and stimulated transitions between level i and j are indicated by the Einstein coefficients A_{ij} and B_{ij}, respectively.

$R_{ph} = -\alpha c_n N_{ph}$ with the losses α. These losses are a combination of the total losses α_{tot} decreasing the light intensity and the modal gain $g\Delta N = g(N_3 - N_2)$, which provides an increase of the light field. Finally, the photon rate equation reads

$$R_{ph} = \frac{dN_{ph}}{dt} = c_n \left(g\Delta N - \alpha_{\mathrm{tot}}\right) N_{ph}, \tag{2.2.3}$$

neglecting the coupling of spontaneous emission to the laser mode. Since the generation of photons is directly connected to the stimulated electron transitions, the term $B_{32}(N_3 - N_2)u$ in the electronic rate equations (2.2.1) and (2.2.2) can be replaced by $gN_{ph}\Delta N$. The threshold of the laser is reached when the total losses equal the modal gain. For the population inversion this means

$$\Delta N = \alpha_{\mathrm{tot}}/g. \tag{2.2.4}$$

Below threshold all photons are absorbed ($N_{ph} = 0$) and the steady-state solutions of the rate equations read

$$0 = \frac{j}{e} - A_3 N_3 \tag{2.2.5}$$
$$0 = A_{32}N_3 - A_{21}(N_2 - N_1). \tag{2.2.6}$$

From Eq. (2.2.5) it is obvious that

$$N_3 = \frac{j}{A_3 e} \tag{2.2.7}$$

which directly connects the upper state population N_3 to the lifetime $\tau_3 = 1/A_3$ and the pumping current density j. In combination with Eq. (2.2.6) this results in the population inversion

$$\Delta N = \frac{j}{A_3 e}\left(1 - \frac{A_{32}}{A_{21}}\right) - N_1. \tag{2.2.8}$$

A positive population inversion is the key for lasing operation. From Eq. (2.2.8) it is obvious that

$$A_{21} > A_{32} \tag{2.2.9}$$

and

$$j > A_3 e \frac{N_1 + \Delta N}{1 - A_{32}/A_{21}} \tag{2.2.10}$$

in order to achieve lasing. Equation (2.2.9) determines that the relaxation from the lower laser level to the injector, with a relaxation time of $\tau_{21} = 1/A_{21}$, should be faster than the spontaneous relaxation from the upper to the lower laser level. In Eq. (2.2.10) it is shown that the injected current has to exceed a certain value also referred to as the threshold current. At threshold the population inversion can be described as in Eq. (2.2.4) which provides the following threshold current density

$$j_{th} = A_3 e \frac{N_1 + \alpha_{\text{tot}}/g}{1 - A_{32}/A_{21}}. \tag{2.2.11}$$

Above threshold the modal gain is assumed to be constant and equal to the total losses, i.e. $g\Delta N = \alpha_{\text{tot}}$. The steady state solutions of the electron rate equations then include a term associated with the photon densities and read

$$\begin{aligned} 0 &= -gN_{ph}\Delta N + \frac{j}{e} - A_3 N_3 & (2.2.12)\\ 0 &= gN_{ph}\Delta N + A_{32}N_3 - A_{21}(N_2 - N_1). & (2.2.13) \end{aligned}$$

Equation (2.2.12) can be transformed to

$$N_{ph} = \frac{j/e - A_3 N_3}{g\Delta N} \tag{2.2.14}$$

where the photon density is related to the population of the upper laser level. The latter can be expressed by Eq. (2.2.13) as follows

$$N_3 = \frac{\Delta N + N_1}{1 - A_{32}/A_{21}} + \frac{gN_{ph}\Delta N}{A_{21}\left(1 - A_{32}/A_{21}\right)}. \tag{2.2.15}$$

Inserting Eq. (2.2.15) in Eq. (2.2.14) yields

$$N_{ph} = \frac{j - j_{th}}{e\alpha_{\text{tot}}\left(1 + \frac{A_3}{A_{21}(1 - A_{32}/A_{21})}\right)}. \tag{2.2.16}$$

Above threshold the total photon density is directly proportional to the injected current density. Equations (2.2.8) and (2.2.16) describe the laser behavior in terms of population inversion and photon density. These characteristics are illustrated in Fig. 2.5. Below threshold the population inversion increases linearly with the injection current while the photon density is zero due to absorption. At threshold modal gain and losses are equal. All the additional injected carriers above threshold directly contribute to the linearly increasing photon density. [65]

2.2.3 Selection rule and gain derivation

The probability of intersubband transitions due to an incident light field can be calculated by means of Fermi's golden rule. A linearly polarized wave is considered. Its electric field is given by $\mathbf{E} = E_0 \hat{\varepsilon} \cos\left(\mathbf{qr} - \omega t\right)$ with the field amplitude E_0, the polarization $\hat{\varepsilon} = (\hat{\varepsilon}_x, \hat{\varepsilon}_y, \hat{\varepsilon}_z)$, the photon wavevector $\mathbf{q}$ and the angular frequency ω. Introducing the vector potential

$$\mathbf{A} = \frac{iE_0\hat{\varepsilon}}{2\omega}\left(e^{i(\mathbf{qr} - \omega t)} - e^{-i(\mathbf{qr} - \omega t)}\right) \tag{2.2.17}$$

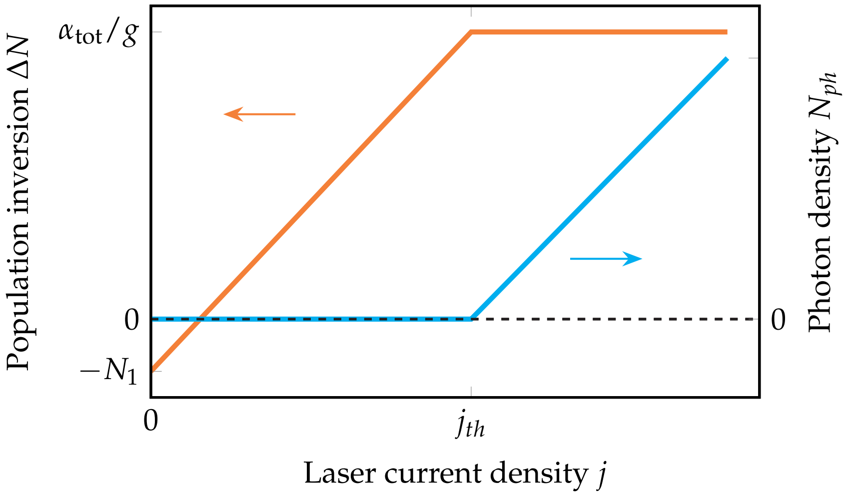

Figure 2.5: Population inversion and photon density as a function of the laser current density. Below threshold the population inversion is building up while no photons are extracted. As soon as the gain exceeds the losses the population inversion is pinned and the excessive energy is used for photon generation.

facilitates a description of the electric field according to $\mathbf{E} = -\partial \mathbf{A}/\partial t$. The light matter interaction of this light wave can be treated as a perturbation of the system and the final Hamiltonian

$$H = \frac{\mathbf{p}'}{2m^*} = H_0 + H_{\text{int}} \tag{2.2.18}$$

is composed of the unperturbed Hamiltonian H_0 of the electronic states in absence of the light field and the interaction Hamiltonian H_{int}. In Eq. (2.2.18) the momentum $\mathbf{p}'$ is modified by the vector potential and reads $\mathbf{p} - e\mathbf{A}$. Assuming a small light induced perturbation the $|\mathbf{A}|^2$ can be neglected and the interaction Hamiltonian is

$$H_{\text{int}} = -\frac{e}{2m^*}\left(\mathbf{A}\cdot\mathbf{p} + \mathbf{p}\cdot\mathbf{A}\right). \tag{2.2.19}$$

Since the wavelength of the light field $\lambda = 2\pi/|\mathbf{q}|$ is in the micrometer range and therefore much larger than the characteristic dimension of the semiconductor heterostructure, i.e. the quantum well width which is on the order of nanometers, the dipole approximation, neglecting the photon wavevector, can be applied. This simplifies the expression for the interaction Hamiltonian to

$$H_{\text{int}} = -\frac{eE_0}{2m^*\omega}\hat{\varepsilon}\mathbf{p}\left(e^{-i\omega t} - e^{i\omega t}\right). \tag{2.2.20}$$

According to Fermi's golden rule, the transition probability for an electron to make a transition from an initial state Ψ_i to a final state Ψ_f reads

$$W_{i\to f} = \frac{2\pi}{\hbar}\left|\langle\Psi_f\left|H_{\text{int}}\right|\Psi_i\rangle\right|^2\delta(E_f - E_i \pm \hbar\omega) \tag{2.2.21}$$

$$= \frac{2\pi}{\hbar}\cdot\frac{e^2E_0^2}{4m^{*2}\omega^2}\left|\langle\Psi_f\left|\left(e^{-i\omega t} - e^{i\omega t}\right)\hat{\varepsilon}\mathbf{p}\right|\Psi_i\rangle\right|^2\delta(E_f - E_i \pm \hbar\omega). \tag{2.2.22}$$

The $-\omega$ and $+\omega$ terms describe the light induced absorption and emission process, respectively. For the case of stimulated emission $E_f = E_i - \hbar\omega$. The corresponding transition probability is given by

$$W_{i\to f} = \frac{2\pi}{\hbar}\cdot\frac{e^2E_0^2}{4m^{*2}\omega^2}\left|\langle\Psi_f\left|\hat{\varepsilon}\mathbf{p}\right|\Psi_i\rangle\right|^2\delta(E_f - E_i + \hbar\omega) \tag{2.2.23}$$

and mainly dominated by the momentum matrix element $\langle \Psi_f \left| \hat{\varepsilon}\mathbf{p} \right| \Psi_i \rangle$. The latter can be described in terms of a one-band model of the envelope function approximation yielding a wavefunction of the form

$$\begin{aligned} \Psi_i(\mathbf{r}) &= u_b(\mathbf{r}) f_s(\mathbf{r}) && (2.2.24) \\ f_s(\mathbf{r}) &= \frac{1}{\sqrt{A}} e^{i\mathbf{k}_\perp \mathbf{r}_\perp} \chi_s(z) && (2.2.25) \end{aligned}$$

with the periodic part of the Bloch function u_b, the wavevector $\mathbf{k}_\perp$ and spatial coordinate $\mathbf{r}_\perp$ in the layer plane, the area of these layers A and the envelope function $\chi_s(z)$. The indices b and s depict the band and subband index, respectively. Using this description of the wavefunction the momentum matrix element can be expressed by

$$\begin{aligned} \langle \Psi_f \left| \hat{\varepsilon}\mathbf{p} \right| \Psi_i \rangle &= \int u_{b'}^*(\mathbf{r}) f_{s'}(\mathbf{r}) \hat{\varepsilon}\mathbf{p} u_b(\mathbf{r}) f_s(\mathbf{r}) d\mathbf{r} && (2.2.26) \\ &= \underbrace{\delta_{s's} \int u_{b'}^*(\mathbf{r}) \hat{\varepsilon}\mathbf{p} u_b(\mathbf{r}) d\mathbf{r}}_{\text{Interband transition}} + \underbrace{\delta_{b'b} \int f_{s'}(\mathbf{r}) \hat{\varepsilon}\mathbf{p} f_s(\mathbf{r}) d\mathbf{r}}_{\text{Intersubband transition}} && (2.2.27) \end{aligned}$$

with b and b' being the indices of the initial and final bands. Equivalently, s and s' are the indices of the initial and final subbands of the transition. As proposed in Eq. (2.2.27), the matrix element is composed of an interband and an intersubband term. The former describes transitions between dissimilar band indices b and b' while for the latter the band indices are the same and transitions between subbands are specified. These intersubband transitions are characterized by the matrix element of the envelope functions which is given by

$$\begin{aligned} \langle f_{s'} \left| \hat{\varepsilon}\mathbf{p} \right| f_s \rangle &= \frac{1}{A} \int e^{-i\mathbf{k}_\perp \mathbf{r}_\perp} \chi_{s'}(z) \left(\hat{\varepsilon_x} p_x + \hat{\varepsilon_y} p_y + \hat{\varepsilon_z} p_z \right) e^{i\mathbf{k}_\perp \mathbf{r}_\perp} \chi_s(z) d\mathbf{r} && (2.2.28) \\ &= \frac{1}{A} \left[\iint \delta_{s's} e^{-i\mathbf{k}_\perp \mathbf{r}_\perp} \left(\hat{\varepsilon_x} p_x + \hat{\varepsilon_y} p_y \right) e^{i\mathbf{k}_\perp \mathbf{r}_\perp} dx dy + \ldots \right. \\ &\qquad \left. \ldots + \int \chi_{s'}(z) \hat{\varepsilon_z} p_z \chi_s(z) dz \right] . && (2.2.29) \end{aligned}$$

The first term is only non-zero if initial and final subband are the same. It corresponds to free carrier absorption and is forbidden in a defect-free heterostructure due to the impossibility of energy and momentum conservation. Consequently, only the second term contributes to the matrix element and therefore to the transition probability which can now be written as

$$W_{i \to f} = \frac{2\pi}{\hbar} \cdot \frac{e^2 E_0^2}{4 m^{*2} \omega^2} \hat{\varepsilon_z}^2 \left| \langle \chi_f \left| p_z \right| \chi_i \rangle \right|^2 \delta(E_f - E_i \pm \hbar\omega). \qquad (2.2.30)$$

Equation (2.2.30) indicates that only the z-component of the electric field couples to the intersubband transitions, resulting in the well-known intersubband selection rule for optical transitions. This selection rule has major impact on intersubband devices since absorption and emission processes can only occur when the polarization of the light field is parallel to the growth direction and the propagation direction of the light lies in the layer plane, i.e. the plane perpendicular to the growth direction. A detailed description of the implications of this selection rule on intersubband devices is provided in section 2.3.2 for emitters and section 4.3.1 for detectors. [65, 71, 78, 79]

2.2.4 Electron injection

Optical transition regions in a QCL, often referred to as active regions, are separated by heterostructure injectors. The latter act as electron reservoirs and deliver electrons from one active region to the next one. The injector is typically designed to provide a broad overlap of the wavefunctions, creating a miniband in which the electrons travel to the lowest injector energy level. From there electrons are commonly injected into the upper laser level via resonant tunneling. In order to provide high injection efficiencies the heterostructure is designed such that the wavefunction of the ground state is localized close to the injection barrier of the next active region. From tight-binding calculations [72, 80] the following expression for the current density can be derived

$$j = eN_{\text{inj}} \frac{2\left|\Omega\right|^2 \tau_\perp}{1 + \Delta^2 \tau_\perp^2 + 4\left|\Omega\right|^2 \tau_3 \tau_\perp} \tag{2.2.31}$$

where N_{inj} is the sheet density of the injector, $2\hbar\left|\Omega\right|$ is the energy difference between the ground state and the upper laser level at the resonance condition, $\tau_3 = 1/A_3$ is the upper state lifetime, $\tau_\perp$ describes the in-plane relaxation of carriers and $\hbar\Delta = E_g - E_3 = ed(F - F_r)$ is the energetic detuning from this resonance. In the latter formula d is the spacing between the average center of electron distributions in the ground state and the upper laser level, F is the mean field over this distance and F_r is the field at resonance. The term $\hbar\Delta$ is zero for the resonance condition $F = F_r$ and therefore the maximum attainable current density is given by

$$j_{\text{max}} = eN_{\text{inj}} \frac{2\left|\Omega\right|^2 \tau_\perp}{1 + 4\left|\Omega\right|^2 \tau_3 \tau_\perp}. \tag{2.2.32}$$

In the weak-coupling regime the relaxation times are much shorter than the inverse splitting, i.e. $4\left|\Omega\right|^2 \tau_\perp \tau_3 \ll 1$ and the resulting maximum of the current density reads $j_{\text{max}}^{\text{weak}} = 2eN_{\text{inj}} \left|\Omega\right|^2 \tau_\perp$. The ground state and upper laser level wavefunctions exhibit a small overlap, which means that the corresponding electron distributions are coupled weakly and transport is dominated by incoherent scattering processes. Obviously, the strong coupling regime with $4\left|\Omega\right|^2 \tau_\perp \tau_3 \gg 1$ is desirable for efficient carrier injection. With $1/\Omega$ being the time required by an electron in the ground state to tunnel into the upper laser level, the strong-coupling regime is characterized by the fact that this tunneling time is much shorter than the time constants of the in-plane relaxation process. The corresponding maximum current density

$$j_{\text{max}}^{\text{strong}} = \frac{eN_{\text{inj}}}{2\tau_3} \tag{2.2.33}$$

only depends on the upper state lifetime and carrier concentration in the injector and not on the tunneling rate Ω. This means that the electron injection in QCLs is optimized when the lifetime of the upper laser levels is the limiting factor for the current flowing through the laser. In this case a quasi-equilibrium between the ground state the upper laser level is established and both states exhibit a common quasi-Fermi level across the injection barrier.

The detailed design of the injector depends on the type of the optical transition, e.g. vertical or diagonal. In order to operate in the strong-coupling regime large values for Ω and τ_3 are beneficial. For the vertical optical transition a large energy splitting $2\hbar\Delta$ can be achieved by a proper design of the ground state wavefunction or a reduction of the barrier thickness between injector ground state and upper laser level. However, a strong injector will induce non-resonant transitions into the lower laser level reducing the population inversion and efficiency of the laser. In QCLs with diagonal optical transitions the relaxation time τ_3 is larger by a factor of $2-3$ compared with vertical transition QCLs. This is due to the reduced spatial overlap between the wavefunctions of the upper and lower laser level which also decreases the non-resonant coupling between injector and lower laser level. The long relaxation time of the upper laser level can cause a depletion of the injector. The resulting undesirable space-charge effects reduce the gain and require greater doping densities in the injector compared with vertical transition QCLs. The latter exhibit the best performance in terms of operation temperature and output power while the diagonal transition QCLs excel with low threshold currents. [81, 82, 83]

2.2.5 Active region

In addition to the efficiency of the electron injection, the performance of a QCL is mainly dominated by the electronic subbands and wavefunctions as well as the corresponding scattering rates. As shown in Fig. 2.4, the laser transition is accompanied by several undesirable parasitic current paths. Several QCL active region designs have been developed in order to reduce the impact of these current paths and provide an optimized laser performance. The most common designs can be divided into (i) laser transitions between discrete energy levels within few quantum wells and (ii) transitions between broad minibands formed by coupling of multiple quantum wells. The simplest design of the former is the **2-well** design providing a fast depletion of the lower laser level through LO-phonon scattering.

Due to a strong coupling between injector ground state and lower laser level, the **3-well** design was developed. The additional well is located between injector and upper laser level and reduces the electron leakage from the injector into the lower laser level having a significant positive effect on the population inversion. Therefore, this design enabled the first room temperature operation of QCLs [84]. Furthermore, it is better suited for short wavelengths since it allows the optical transition to span over a large part of a given conduction band offset compared to other designs. A typical 3-well design is depicted in Fig. 2.6 (a). It can be realized in the form of a **vertical** or **diagonal** laser transition as illustrated in Fig. 2.3 (b). For the former the additional barrier and well between injector and upper laser level are rather thin and the optical transition occurs in the same quantum well providing a large overlap between upper and lower laser level accompanied by a great dipole matrix element. On the other hand, for the diagonal transition upper and lower laser level are located in different quantum wells and are therefore *not* in the same point in real space. This is achieved if the additional quantum well and barrier are rather thick. The laser transition takes place from the ground state of the heterostructure injector miniband to the lower laser level and the emission wavelength can be adjusted by the layer thicknesses of the injector close to the active region. The diagonal transition typically includes an LO phonon emission and has a reduced matrix element but provides longer scattering times and therefore an easier obtainable population inversion compared to the vertical transition scheme. Since the energy difference between two energy levels in neighboring quantum wells is more sensitive to an applied bias than between two levels in the same well, diagonal transition QCLs exhibit a strong emission wavelength dependence on the applied voltage and hence provide a large wavelength tunability. This so-called voltage-induced quantum-confined Stark-effect is also

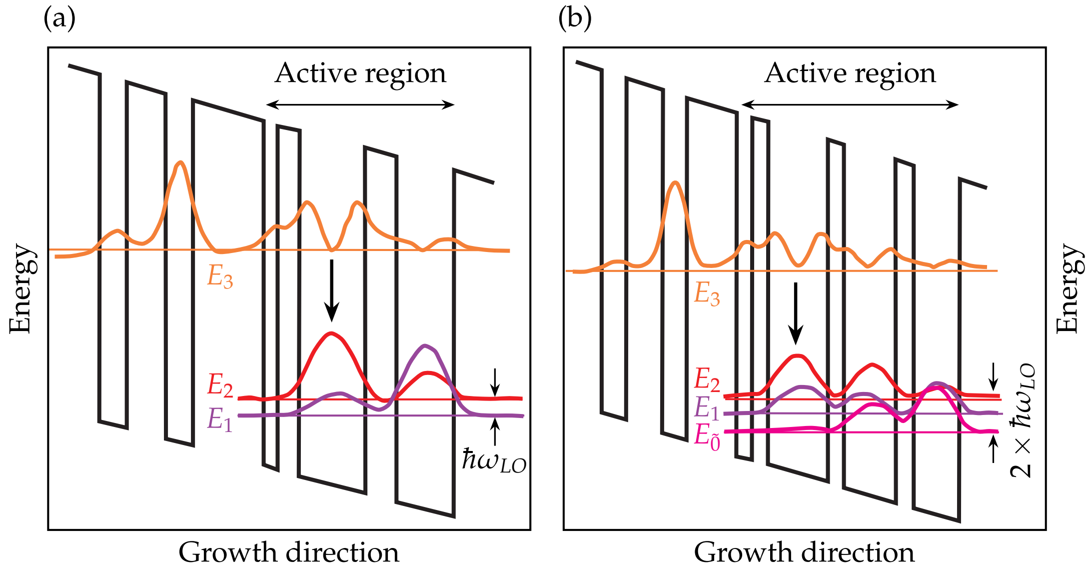

Figure 2.6: (a) Conventional 3-well design of a QCL with a vertical laser transition and depletion of the lower laser level (E_2) via LO phonons. (b) Double phonon design with an additional energy level ($E_{\tilde{0}}$) creating a double phonon ladder for faster depletion of the lower laser level and reduced thermal backfilling.

the reason for the observed blue-shift of the emission wavelength with increasing active region temperature in diagonal transition QCLs. It arises from the higher electric field required due to the increased threshold current at elevated temperatures and is in direct contrast to the observed red-shift with increasing temperature in vertical transition QCLs which results from the temperature dependence of the refractive index.

A main weakness of the 3-well design is the relatively slow extraction of electrons from the active region, i.e. from level $n = 1$ into the subsequent injector. The accumulation of charge carriers in level $n = 1$ gives rise to backscattering from level $n = 1$ to $n = 2$, reducing the population inversion. The solution is a fast electron extraction utilizing 2 consecutive phonon extraction channels as shown in Fig. 2.6 (b). It is realized by an additional quantum well between level $n = 1$ and the injector, creating an additional energy level $n = \tilde{0}$. The corresponding layer thicknesses are designed such that the energy of the $2 \rightarrow 1$ and $1 \rightarrow \tilde{0}$ transition equals the LO phonon energy. This is referred to as the **double-phonon resonance** design and provides a fast electron extraction via the double-phonon ladder.

Superlattices, formed by multiple quantum wells, can be used to create optical transitions between broad minibands as shown in Fig. 2.7. Several periodic nm-thick quantum wells and barriers are forming an artificial crystal, splitting the energy levels into wide minibands. Similar to the 3-well design, electron injection is ensured via the injector ground state near the bottom of the upper miniband. The optical transition occurs from the upper to the lower miniband. This interminiband transition is dominated by LO phonons and usually accompanied by a large momentum transfer providing typical lifetimes on the order of $\sim 10\,\text{ps}$. Phonon wavevectors for scattering processes within the miniband are much smaller and therefore the corresponding lifetimes are typically $< 1\,\text{ps}$. This relationship between inter- and intraminiband scattering rates provides an inherent population inversion in superlattice active region QCLs. Superlattice designs based on InP are typically used for wavelengths $> 7\,\mu\text{m}$ since the broad minibands spare

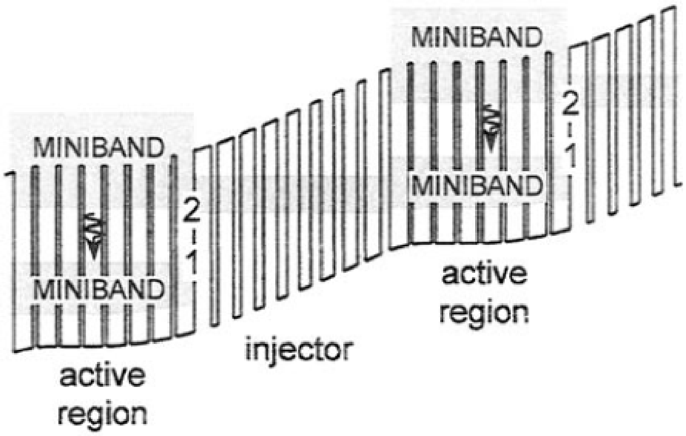

Figure 2.7: Original superlattice QCL heterostructure with a continuum-to-continuum design. Optical transitions occur not between well-defined states but rather between broad minibands which increases the number of possible transition paths and therefore enhances the gain. Reprinted with permission from [85]

less energetic space for the laser transition. The broad minibands enable multiple optical transition paths which results in a broad gain curve, high optical output powers and the ability to support large currents. The required doping levels are relatively high and the dopants have to be equally distributed throughout the heterostructure in order to screen the electric field which would destroy the desirable wavefunction overlap in the superlattice. The concomitant losses reduce the performance of superlattice QCLs in terms of threshold, temperature performance and CW operation. Possible ways for improvement include doping of the injector while ensuring a flat miniband in a way that the applied electric field is compensated by the doping-induced electric field. Another approach uses **chirped superlattices** to compensate for the applied electric field. In the **bound-to-continuum** design the lower laser level is formed by such a chirped superlattice while the upper laser levels is given by a discrete energy state. [65, 85, 86]

2.2.6 Electronic cascading

One key aspect of QCLs is the cascading nature and the accompanying recycling of electrons. Ideally, one electron emits as many photons as active regions are present while passing through the QCL heterostructure. This results in the geometric increase of the gain with increasing number of periods. Such a linear behavior can be assumed when the mode profile is almost constant over the stack of active regions. According to Eq. (2.2.11) an increase of the gain reduces the lasing threshold. This means that the threshold current density is inversely proportional to the number of active region periods N_p as follows

$$j_{th} \sim \frac{1}{N_p}. \tag{2.2.34}$$

This is in direct contrast to band gap laser diodes for which the threshold increases linearly with N_p [87]. Since after the optical transition in diode lasers the electrons are lost and not recycled, an increase of the number of periods in the active region requires more electrons for the optical transition and hence a larger threshold current. [65]

2.3 Laser resonators

BASIC principles of the generation of light in lasers, specifically in intersubband devices, are discussed in section 2.2. In addition, controlling the light is a key factor in order to realize an efficient laser. This control manifests itself in form of optical confinement in all three dimensions as well as optical feedback.

2.3.1 Light in cavities

The refractive index

$$n = n_R + in_I \tag{2.3.1}$$

of a material with n_R as its real and n_I as its imaginary part, strongly influences an electromagnetic wave traveling within this material. The corresponding propagation constant is given by

$$\mathbf{k} = \mathbf{k_0}\sqrt{\epsilon_r} = \mathbf{k_0}n \tag{2.3.2}$$

with the relative permittivity ϵ_r. A sinusoidal electric ($\mathbf{\Psi} = \mathbf{E}$) or magnetic ($\mathbf{\Psi} = \mathbf{H}$) wave propagating in z-direction can be described by

$$\mathbf{\Psi}(\mathbf{r}, t) = \Psi_0(x, y)e^{i(k_z z - \omega t)} \tag{2.3.3}$$

with the amplitude Ψ_0, the z-component of the propagation constant $k_z = k_0 n$, the angular frequency ω and the time t. Exploiting Eq. (2.3.1) and (2.3.3) yields

$$\mathbf{\Psi}(\mathbf{r}, t) = \Psi_0(x, y) \cdot \underbrace{e^{-k_0 n_I z}}_{\text{Absorption}} \cdot \underbrace{e^{ik_0 n_R z}}_{\text{Propagation}} \cdot \underbrace{e^{-i\omega t}}_{\text{Time}}. \tag{2.3.4}$$

The first exponential term in Eq. (2.3.4) describes an exponential decay. Therefore, the imaginary part of the refractive index is responsible for the absorption in a material. The second term represents an oscillation which implies that the real part of the refractive index is associated with light propagation in a medium. The last term describes the time behavior. The field in a material is often described by the propagation constant $\beta = k_0 n_R$ and the attenuation constant $\alpha = 2k_0 n_I$. Neglecting the time dependence results in the following representation of the field

$$\mathbf{\Psi}(\mathbf{r}) = \Psi_0(x, y)e^{-\alpha z/2} \cdot e^{i\beta z}. \tag{2.3.5}$$

In dielectric waveguides and resonators materials with different refractive indices are used to provide a **vertical confinement** of the light. The propagation of light through such a structure is characterized by a “zig-zag”-motion as visualized in Fig. 2.8. The light is guided within the central guiding layer with refractive index n_g, which is surrounded by the cladding and substrate layer with refractive indices n_c and n_s, respectively. Due to basic geometrical conditions the propagation constant is given by

$$\beta = k_z = n_g k_0 \sin(\theta) \tag{2.3.6}$$

with the angle of incidence θ. A successful propagation of an electromagnetic wave inside the guide layer is based on total internal reflection at the cladding and substrate interface. In mathematical terms this means

$$\beta \geq n_g k_0 \sin(\theta_c) = k_0 n_i \quad ; \quad i = c, s \tag{2.3.7}$$

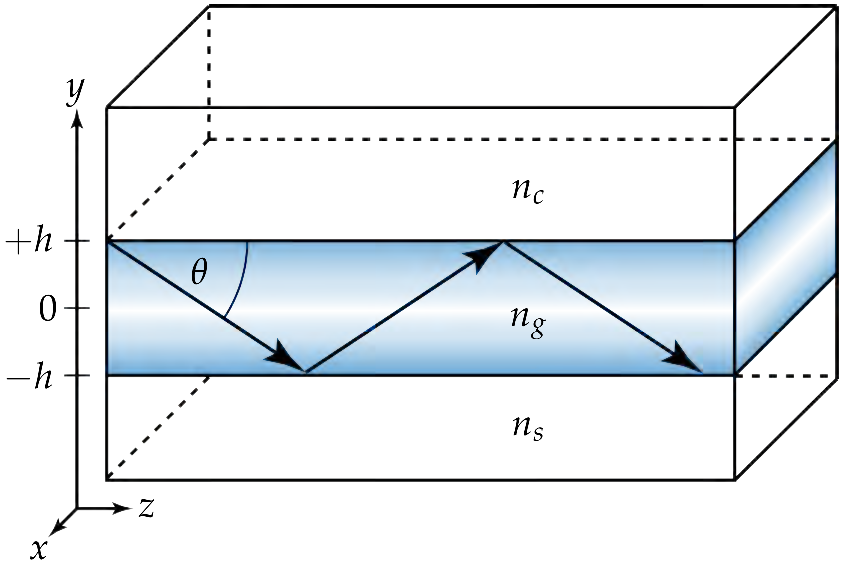

Figure 2.8: Simplified light propagation based on total internal reflection in a dielectric waveguide.

with the critical angle θ_c for total internal reflection.

A detailed analysis of the propagation of an electromagnetic wave traveling inside a dielectric waveguide requires to solve the wave equation

$$\nabla^2 \mathbf{\Psi} = \epsilon\mu \frac{\partial^2 \mathbf{\Psi}}{\partial t^2} = \frac{n^2}{c^2}\frac{\partial^2 \mathbf{\Psi}}{\partial t^2} \tag{2.3.8}$$

also referred to as the Helmholtz equation. A suitable ansatz is given by $\mathbf{\Psi}(\mathbf{r}, t) = \Psi_0(\mathbf{r})e^{i\omega t}$ which yields the following solution

$$\nabla^2 \mathbf{\Psi} + k_0^2 n_i^2 \mathbf{\Psi} = 0 \tag{2.3.9}$$

for all three regions $i = c, g, s$. For a wave propagating in z-direction the field is given by

$$\mathbf{\Psi}(\mathbf{r}, t) = \Psi_0(x, y) \cdot e^{-i\beta z} \cdot e^{i\omega t} \tag{2.3.10}$$

and $\nabla^2 \mathbf{\Psi}$ simplifies to $\frac{\partial^2 \mathbf{\Psi}}{\partial y^2} - \beta^2 \mathbf{\Psi}$. The restriction of light propagation in z-direction only, introduces the following modified wave equation

$$\frac{\partial^2 \mathbf{\Psi}}{\partial y^2} + \left(k_0^2 n_i^2 - \beta^2\right) \mathbf{\Psi} = 0 \quad ; \quad i = c, g, s. \tag{2.3.11}$$

Solutions to this wave equation can be classified into two types.
(i) Oscillation: If

$$k_{yi}^2 = k_0^2 n_i^2 - \beta^2 > 0 \quad ; \quad i = c, g, s \tag{2.3.12}$$

the solution of the wave equation has the form $\Psi_0(x, y)e^{\pm i(k_0^2 n_i^2 - \beta^2)y}$ which represents an oscillating field in y-direction.
(ii) Decay: If

$$k_{yi}^2 = k_0^2 n_i^2 - \beta^2 < 0 \quad ; \quad i = c, g, s \tag{2.3.13}$$

the solution of the wave equation has the form $\Psi_0(x,y)e^{\pm(k_0^2n_i^2-\beta^2)y}$ which represents an exponential decay of the field in y-direction. The intention in a dielectric waveguide is to achieve an oscillating solution in the guiding layer and a decaying solution in the cladding and substrate layers. These requirements can be mathematically summarized as

$$k_0n_g > \beta > k_0n_i \quad ; \quad i = c, s. \tag{2.3.14}$$

Assuming oscillatory behavior in the guide layer and exponential decay in the cladding and substrate layer, the corresponding propagation and decay constants in y-direction are given as follows

$$\begin{aligned} k_{yc} &= \sqrt{\beta^2 - k_0^2n_c^2} && (2.3.15)\\ k_{yg} &= \sqrt{k_0^2n_g^2 - \beta^2} && (2.3.16)\\ k_{ys} &= \sqrt{\beta^2 - k_0^2n_s^2}. && (2.3.17) \end{aligned}$$

The exact solution of the wave equation depends on the orientation of the electromagnetic wave. In intersubband devices only the transverse-magnetic (TM) field components are relevant. Therefore, the solution of the wave equation exhibits the form

$$\mathbf{H}(\mathbf{r},t) = H_x(y)e^{ik_zz}e^{i\omega t}. \tag{2.3.18}$$

Equations (2.3.19) - (2.3.21) show the behavior of the in-plane magnetic field (H_x) along the y-direction in all three layers

$$\begin{aligned} H_{xc}(y) &= H_ce^{-k_{yc}(y-h)} && (2.3.19)\\ H_{xg}(y) &= H_g\cos(k_{yg}y+\Phi) && (2.3.20)\\ H_{xs}(y) &= H_se^{k_{ys}(y+h)} && (2.3.21) \end{aligned}$$

with the phase shift Φ. The boundary conditions at the two interfaces demand the continuity of H_x as well as $n^{-2}\partial H_x/\partial y$ resulting in the following expressions for the boundary conditions between region a and b

$$\begin{aligned} H_{xa} &= H_{xb} && (2.3.22)\\ \frac{1}{n_a^2}\frac{\partial H_{xa}}{\partial z} &= \frac{1}{n_b^2}\frac{\partial H_{xb}}{\partial z}. && (2.3.23) \end{aligned}$$

The continuity of the in-plane field yields

$$\begin{aligned} y = +h \quad &\rightarrow \quad H_c = H_g\cos(k_{yg}h+\Phi) && (2.3.24)\\ y = -h \quad &\rightarrow \quad H_s = H_g\cos(-k_{yg}h+\Phi) && (2.3.25) \end{aligned}$$

and the continuity of the spatial derivative produces the following set of equations

$$\begin{aligned} y = +h \quad &\rightarrow \quad \frac{-k_{yc}}{n_c^2}H_c = \frac{-k_{yg}}{n_g^2}H_g\sin(k_{yg}h+\Phi) && (2.3.26)\\ y = -h \quad &\rightarrow \quad \frac{-k_{ys}}{n_s^2}H_s = \frac{-k_{yg}}{n_g^2}H_g\sin(k_{yg}h+\Phi). && (2.3.27) \end{aligned}$$

Combination of Eq. (2.3.24) - (2.3.27) yields the following two solutions of the eigenvalue equation

$$\tan(k_{yg}h + \Phi) = \left(\frac{n_g}{n_c}\right)^2 \cdot \frac{k_{yc}}{k_{yg}} \tag{2.3.28}$$

$$\tan(k_{yg}h - \Phi) = \left(\frac{n_g}{n_s}\right)^2 \cdot \frac{k_{ys}}{k_{yg}}, \tag{2.3.29}$$

which by applying $\tan^{-1}$ and calculating the sum of both equations results in the final eigenvalue equation

$$2k_{yg}h = \tan^{-1}\left[\left(\frac{n_g}{n_c}\right)^2 \cdot \frac{k_{yc}}{k_{kg}}\right] + \tan^{-1}\left[\left(\frac{n_g}{n_s}\right)^2 \cdot \frac{k_{ys}}{k_{kg}}\right] \tag{2.3.30}$$

relating the propagation constants in all three layers with the corresponding refractive indices and the thickness $2h$ of the guiding layer.

Figure 2.9 shows the refractive index gradient and the corresponding simulated mode profile of a typical QCL heterostructure. This simulation uses on-resonant Floquet-Bloch solutions based on coupled mode theory [89]. As required, the solution of the wave equation indicates an oscillatory behavior in the active region and an exponential decay in the cladding and substrate layers. From this behavior it is clear that only part of the electromagnetic mode is located in the active region of the laser. This portion in relation to the total mode is defined as the confinement factor

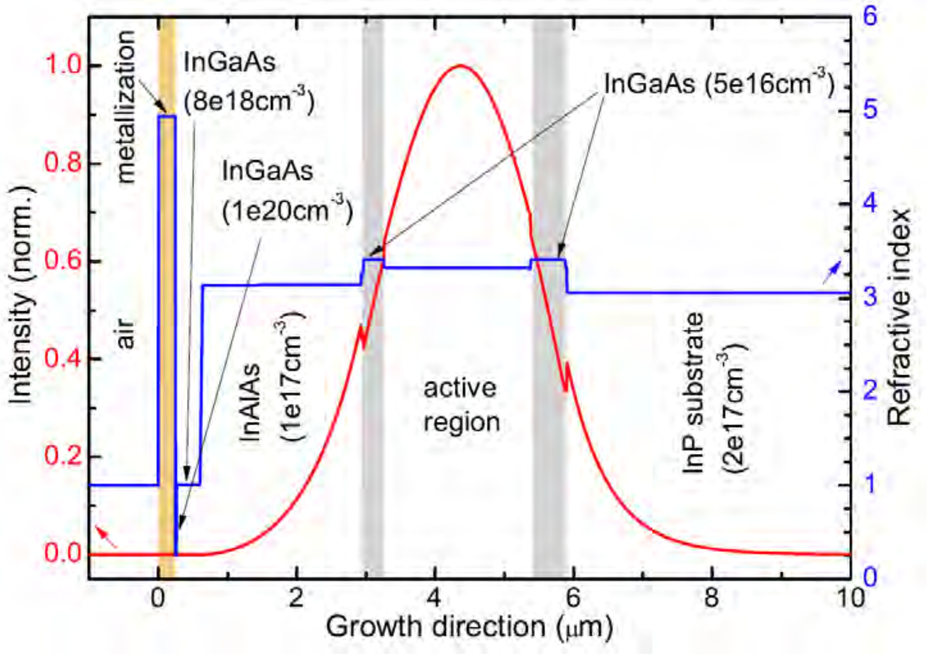

Figure 2.9: Simulated mode distribution in a QCL along the growth direction. Most of the mode is confined within the active region which is encompassed by the InP substrate and the InAlAs cladding layer.
Reprinted with permission from [88]

$$\Gamma = \frac{\iint_{-h}^{+h} \Psi^2(x,y)dxdy}{\iint_{-\infty}^{+\infty} \Psi^2(x,y)dxdy} \tag{2.3.31}$$

and depicts the efficiency of the control and confinement of the mode inside the waveguide. Ideally, this confinement factor is close to unity in order to support high gain and small losses. [65, 90]

In the previous discussion the electromagnetic field was assumed to extend to infinity in the x-direction. A more realistic approach requires additional **lateral confinement** in this direction. Similar as for the y-confinement, the constraints in x-direction can be achieved by a refractive index gradient. In contrast to the y-confinement which is typically realized by material growth using techniques like molecular beam epitaxy (MBE) or metal oxide chemical vapor deposition (MOCVD), the x-confinement is mostly realized in form of material processing including removal and deposition of material. Optical confinement in both x- and y-direction creates a two-dimensional channel waveguide as shown in Fig. 2.10. One possibility to analyze such a waveguide is the effective index approximation. It reduces the two-dimensional to a one-dimensional problem through decomposition of the refractive index environment from Fig. 2.10 into two slab waveguides in x- and y- direction using effective refractive indices $n_{\mathrm{eff},i}$. In QCLs the sidewalls of the waveguide are typically covered with isolating material below a metal layer for current injection. This ensures that the electric field vanishes at the sidewalls and the mode is completely confined inside the active region in horizontal direction. A characteristic mode profile along the lateral dimension is indicated in Fig. 2.11. Again, the oscillatory behavior in the central part of the waveguide is accompanied by exponential decays in the adjacent SiN and metal layers. The intensity profiles for the first three mode numbers indicate that a higher mode number pushes the field closer to the lossy boundary of the waveguide. This implies that the design of the lateral waveguide structure, especially the waveguide width, can strongly influence the mode behavior inside the laser cavity. [90]

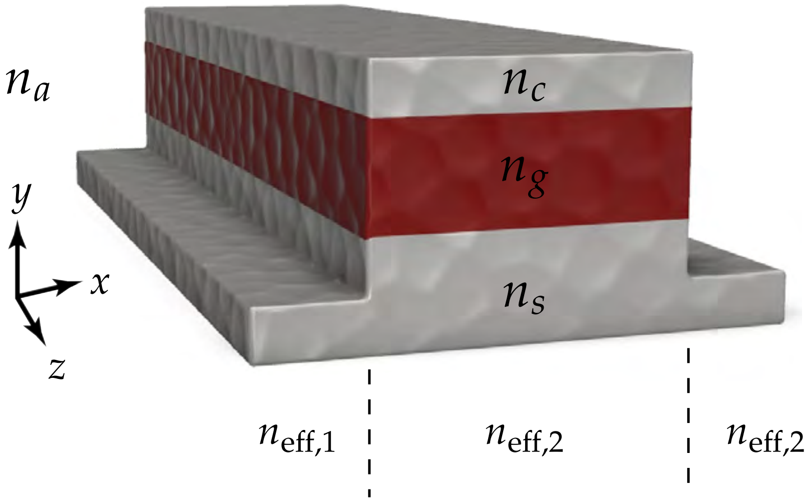

Figure 2.10: Sketch of a dielectric channel waveguide. The effective refractive indices $n_{\mathrm{eff},i}$ are used in the effective index approximation.

As indicated in the previous discussion, the lateral and vertical confinement of light produces a two-dimensional optical waveguide structure. Along these transversal directions no extended light propagation occurs and the light intensity is engineered to oscillate in the active region and show an exponential decay in the surrounding layers. **Longitudinal confinement** in such a laser structure is provided by the end-facets of the waveguide. These facets work as partially reflecting mirrors, which reflect the generated

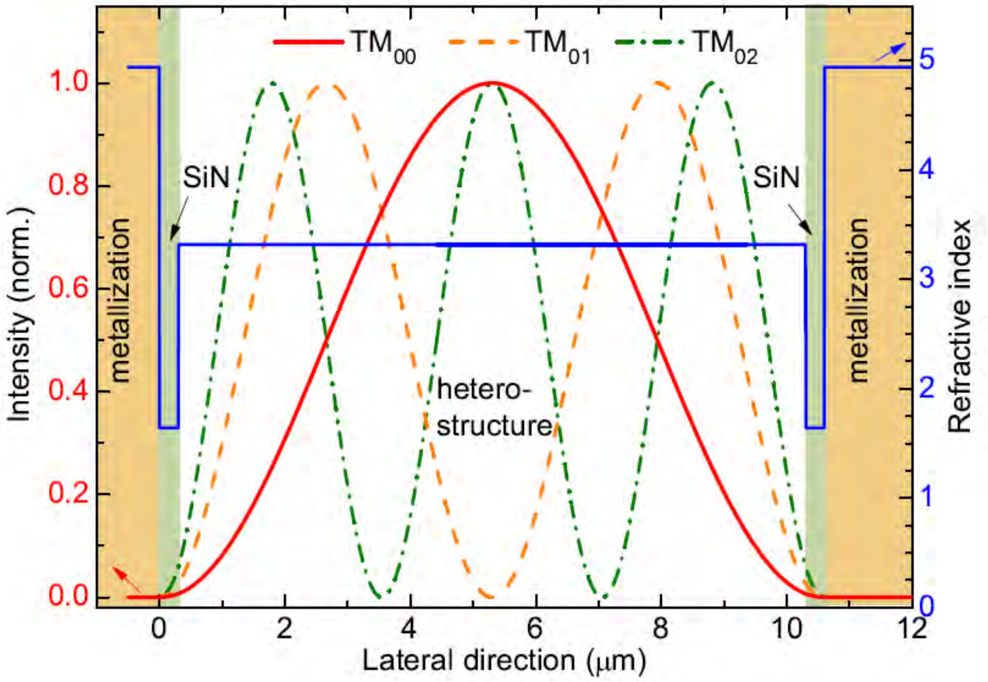

Figure 2.11: Lateral mode distribution in a QCL. The intensity distribution of the first three lateral order modes are depicted.
Reprinted with permission from [88]

light back into the cavity where it is amplified. Mirrors and waveguide together form the laser cavity. If designed properly, standing waves are formed between the two mirror facets. Together with the cavity length L, the standing wave condition reads

$$m\frac{\lambda}{2} = n_{\text{eff}}L \tag{2.3.32}$$

with the mode number m and the effective refractive index n_{eff}. This implies that only specific wavelengths given by

$$\lambda = \frac{2n_{\text{eff}}L}{m} \tag{2.3.33}$$

are supported in the cavity. Considering a specific wavelength with a particular mode number facilitates to express the proximate wavelength as follows

$$\lambda + \Delta\lambda = \frac{2L(n_{\text{eff}} + \Delta n)}{m + \Delta m} \tag{2.3.34}$$

which implicates the dependence of the wavelength on the refractive index and the mode number. Since for neighboring mode numbers $\Delta m = 1$ and the linear approximation $\partial n/\partial\lambda = \Delta n/\Delta\lambda$ is valid, the wavelength spacing between adjacent modes yields

$$\Delta\lambda = \frac{2L\Delta\lambda\,(\partial n/\partial\lambda) - 2n_{\text{eff}}L/m}{m+1}. \tag{2.3.35}$$

Application of Eq. (2.3.32) and solving for $\Delta\lambda$ results in the free spectral range (FSR) of the resonator

$$\text{FSR} = |\Delta\lambda| = \frac{\lambda^2}{2L\underbrace{\left(n_{\text{eff}} - \lambda\frac{\partial n}{\partial\lambda}\right)}_{n_g} + \lambda} \tag{2.3.36}$$

with the group refractive index n_g. For typical laser resonators the length of the resonator is much larger than the wavelength, i.e. $L \gg \lambda$. As a consequence of this relation, the FSR is small compared to the wavelength. Hence, such laser cavities support multi-mode emission for a given gain spectrum as shown in Fig. 2.12 (a). In contrast, a maser (microwave amplification by stimulated emission of radiation) emits at a longer wavelength, which is comparable to the length of typical resonators, i.e. $L \approx \lambda$. In this case the FSR is on the order of the wavelength and typically even larger than the width of the gain spectrum as indicated in Fig. 2.12 (b). Therefore, the longitudinal confinement in a maser operating at long wavelengths is sufficient to produce single-mode emission whereas laser cavities with shorter emission wavelengths naturally support multiple modes.

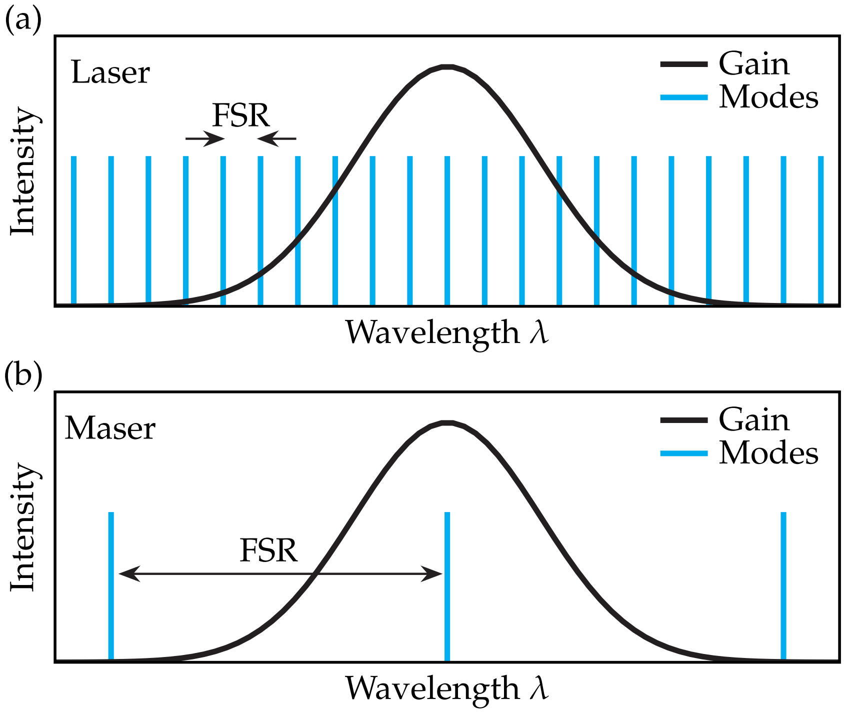

Figure 2.12: Comparison of the optical gain and excited modes in lasers (a) and masers (b). Since the FSR in masers is on the order of the gain bandwidth, they exhibit inherent single mode emission. In contrast, lasers provide shorter emission wavelengths which consequently reduces the FSR relative to the gain. Thus, several modes are situated within the gain curve and can be excited.

These modes travel along the longitudinal direction of the laser and experience three different processes which all have an effect on the light intensity. These processes are sketched in Fig. 2.13 in order to illustrate their fundamental principles. According to Eq. (2.3.4) the intensity $I = |\mathbf{\Psi}|^2$ of a light beam depends only on the absorption component. The generated gain g in a laser is the counterpart of the absorption losses α_w in the waveguide and has to be taken into account. Starting with an initial intensity I_0, the light propagating along the cavity gains a factor of $e^{(g-\alpha_w)L}$. Reflection at the facets adds the corresponding reflectivity factors R_1 and R_2. After one full round-trip the total intensity has to exceed the initial intensity

$$I_0 R_1 R_2 e^{(g-\alpha_w)2L} \geq I_0 \tag{2.3.37}$$

in order to provide an amplification of light. This defines the expression for the threshold

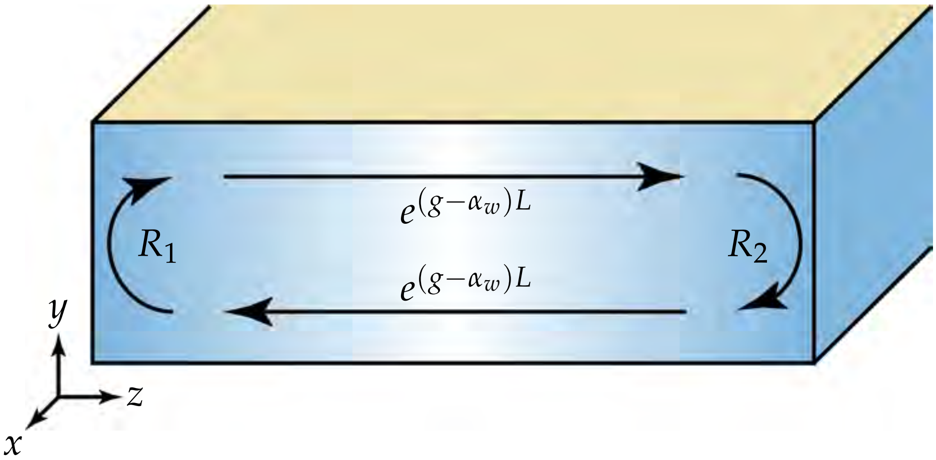

Figure 2.13: Factors affecting the intensity of light propagating in a medium providing gain and losses. At the facets light is partially reflected according to the reflectivities R_i. During propagation through the waveguide the light intensity is modified by the factor $e^{(g-\alpha_w)L}$.

gain

$$g_{th} = \alpha_w + \frac{1}{2L}\ln\left(\frac{1}{R_1R_2}\right) = \alpha_w + \alpha_m \tag{2.3.38}$$

being the required gain to ensure population inversion and light amplification. The right expression can be interpreted as the mirror losses α_m with the reflectivity

$$R = \left(\frac{n_{\text{eff}} - n_a}{n_{\text{eff}} + n_a}\right)^2 \tag{2.3.39}$$

for normal incidence. [31, 44, 65]

These mirror losses determine the optical output power P_{out} emitted from the laser. The internal laser power P_{int} is composed of the product of the photon flux F_{ph} and the photon energy $h\nu$. According to Eq. (2.2.16) the photon flux can be expressed as

$$F_{ph} = \frac{j - j_{th}}{e\alpha_{\text{tot}}}\eta_{\text{iqe}} \tag{2.3.40}$$

with the internal quantum efficiency

$$\eta_{\text{iqe}} = \frac{1}{1 + \frac{A_3}{A_{21}(1-A_{32}/A_{21})}}. \tag{2.3.41}$$

Using these expressions the internal laser power can be written as

$$P_{\text{int}} = h\nu\frac{j - j_{th}}{e\alpha_{\text{tot}}}\eta_{\text{iqe}}. \tag{2.3.42}$$

From this internal power only a portion is coupled out from the laser cavity and represents the output power of the laser. This fraction is specified by the mirror losses as an additional factor which results in the following equation for the laser output power

$$P_{\text{out}} = h\nu\frac{j - j_{th}}{e}\cdot\frac{\alpha_m}{\alpha_{\text{tot}}}\eta_{\text{iqe}}. \tag{2.3.43}$$

By defining the extraction efficiency as

$$\eta_{ee} = \frac{\alpha_m}{\alpha_{\text{tot}}} = \frac{\alpha_m}{\alpha_w + \alpha_m} \tag{2.3.44}$$

the output power yields

$$P_{\text{out}} = h\nu \frac{j - j_{th}}{e} \eta_{ee} \eta_{\text{iqe}}. \tag{2.3.45}$$

The product of extraction efficiency and internal quantum efficiency is often referred to as the external differential quantum efficiency. From the current derivative of Eq. (2.3.45) the slope efficiency can be extracted as

$$\frac{dP_{\text{out}}}{dj} = \frac{h\nu \eta_{ee} \eta_{\text{iqe}}}{e}. \tag{2.3.46}$$

It represents the slope of the photon density curve in Fig. 2.5. [65, 85]

2.3.2 Optical feedback

Longitudinal confinement of light selects discrete wavelengths from the continuous gain spectrum of the laser medium. Due to the round trip condition these wavelengths are separated by the free spectral range and all other wavelengths are attenuated. However, the selection of only *one* specific spectral mode requires additional optical feedback which can be realized in form of distributed feedback (DFB) or an external diffraction grating. For DFB gratings a periodic modulation of the effective refractive index serves as the optical feedback mechanism. [65]

A popular approach for solving such a system is the **transfer matrix method**. It emanates from a simple rectangular modulation of the effective refractive index shown in Fig. 2.14 (a). Furthermore, it relates forward (Ψ^f_{y0}) and reverse (Ψ^r_{y0}) propagating waves. According to Fig. 2.14 (a) and in dependence on Eq. (2.3.10) the magnetic field for TM-polarization in the regions a and b can be written as

$$\begin{aligned} H_{xa}(x,y,z) &= H^f_{x0a}(x,y)e^{-i\beta_a z} + H^r_{x0a}(x,y)e^{+i\beta_a z} && (2.3.47)\\ H_{xb}(x,y,z) &= H^f_{x0b}(x,y)e^{-i\beta_b z} + H^r_{x0b}(x,y)e^{+i\beta_b z}. && (2.3.48)\end{aligned}$$

Utilization of the boundary conditions given in Eq. (2.3.22) and (2.3.23) yields

$$\begin{aligned} H^f_{x0a} + H^r_{x0a} &= H^f_{x0b} + H^r_{x0b} && (2.3.49)\\ \frac{-i\beta_a}{n_a^2}\left(H^f_{x0a} - H^r_{x0a}\right) &= \frac{-i\beta_b}{n_b^2}\left(H^f_{x0b} - H^r_{x0b}\right). && (2.3.50)\end{aligned}$$

Inserting Eq. (2.3.49) in (2.3.50) and vice versa produces the solution of this system of equations which can be depicted in matrix form as follows

$$\begin{pmatrix} H^f_{x0a} \\ H^r_{x0a} \end{pmatrix} = \underbrace{\begin{pmatrix} d^- & d^+ \\ d^+ & d^- \end{pmatrix}}_{D_{ab}} \begin{pmatrix} H^f_{x0b} \\ H^r_{x0b} \end{pmatrix} \tag{2.3.51}$$

with

$$d^{\pm} = \frac{\beta_a n_b^2 \pm \beta_b n_a^2}{2\beta_a n_b^2} \tag{2.3.52}$$

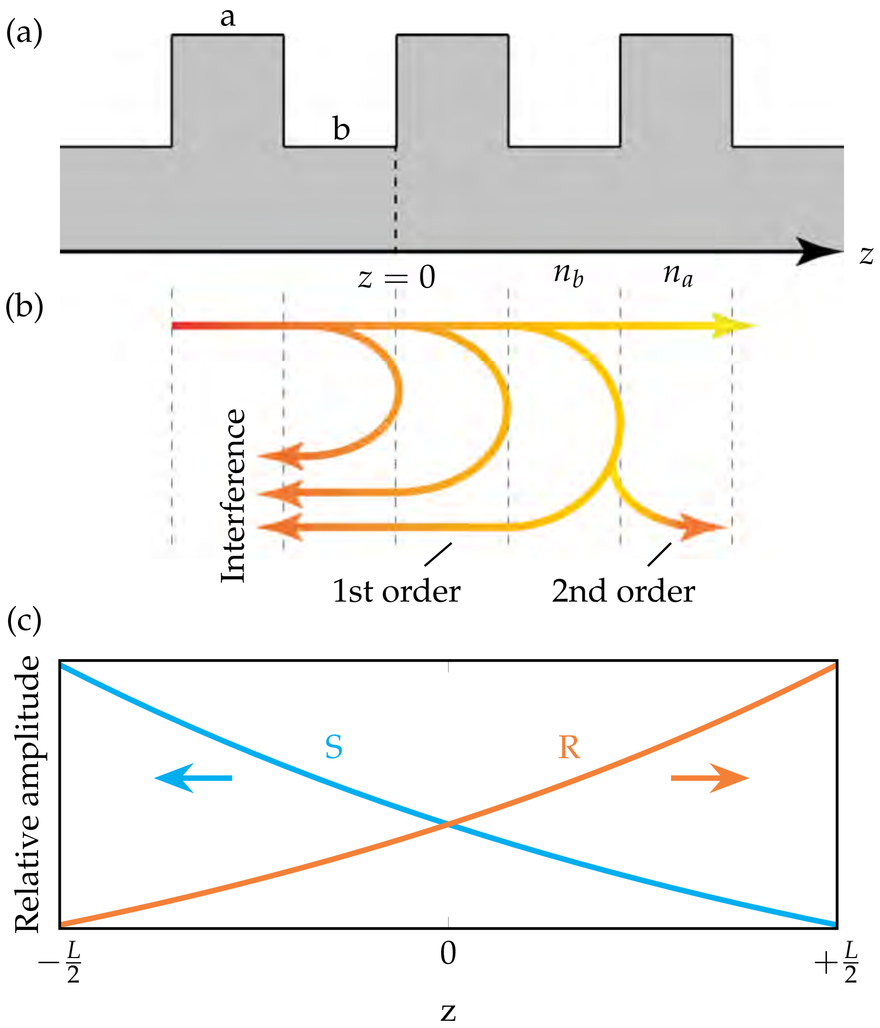

Figure 2.14: (a) Schematic of a refractive index modulation with sharp interfaces between two different materials indicated by a and b. (b) At each interface an incoming electromagnetic wave is partially reflected. For the Bragg wavelength reflected waves interfere constructively with waves reflected from preceding and following interfaces resulting in two counter-propagating waves. (c) Relative amplitude of left and right traveling waves in a conventional ridge waveguide.

where D_{ab} is the transfer matrix describing the field transformations at an a/b interface. In a uniform region in a or b the corresponding transfer matrix assumes the form

$$F_j = \begin{pmatrix} e^{-i\beta_j\Lambda_j} & 0 \\ 0 & e^{+i\beta_j\Lambda_j} \end{pmatrix} \quad ; \quad j = a, b \tag{2.3.53}$$

representing a forward and reverse traveling wave in region a or b without any discontinuities. The grating period $\Lambda = \Lambda_a + \Lambda_b$ is the combined length of region a and b. A simple multiplication of the matrices D and F results in the total transfer matrix

$$T_a = F_a D_{ab} \tag{2.3.54}$$
$$T_b = F_b D_{ba} \tag{2.3.55}$$

for the corresponding region including the upcoming interface. In a periodic structure T_a and T_b are alternating and the transfer matrix per period is given by

$$T_p = T_a T_b. \tag{2.3.56}$$

The transfer matrix of the full structure consisting of m periods is then

$$T_p^m = \begin{pmatrix} T_1 & T_2 \\ T_3 & T_4 \end{pmatrix}^m = \begin{pmatrix} T_1 U_{m-1} - U_{m-2} & T_2 U_{m-1} \\ T_3 U_{m-1} & T_4 U_{m-1} - U_{m-2} \end{pmatrix} \tag{2.3.57}$$

with the Chebyshev polynomial [91]

$$U_m = \frac{\sinh(m+1)\varepsilon\Lambda}{\sinh(\varepsilon\Lambda)} \tag{2.3.58}$$

of the second kind of the order of m and

$$\cosh(\varepsilon\Lambda) = \frac{T_1 + T_4}{2}. \tag{2.3.59}$$

Solving the T_p^m matrix with Chebyshev polynomials is only feasible for shallow grating corrugations implying that $\det(T_p) = 1$. [92, 93]

Although, the transfer matrix method delivers useful results, it lacks the ability to describe the physics of the system. Kogelnik and Shank published their **coupled-wave theory** [94] in 1972, which provides the theoretical groundwork for DFB optical systems and gives insights into the fundamental physics of such devices. As indicated in Fig. 2.14 (b) a wave traveling in a cavity with periodically modulated effective refractive index gets partially reflected at each a/b interface. Waves reflected from consecutive interfaces will constructively interfere if they fulfill the Bragg condition

$$m_{\mathrm{DFB}} \lambda_B = 2\Lambda n_{\mathrm{eff}} \tag{2.3.60}$$

with the Bragg wavelength λ_B and the Bragg order m_{DFB} [95]. This interference condition represents the wavelength-selective mechanism of DFB gratings. According to Eq. (2.3.6) the propagation constant for a wave traveling in z-direction is

$$\beta = k = \frac{\omega}{c_0} n = \omega\sqrt{\mu\varepsilon} \tag{2.3.61}$$

with the permeability $\mu = \mu_0 \mu_r = \mu_0$ and the permittivity $\varepsilon = \varepsilon_0 \varepsilon_r$. In a lossy medium the permittivity is complex and assumes the shape $\varepsilon = \varepsilon'(1 - i\sigma/\omega\varepsilon')$ with the conductivity σ. By using this complex permittivity the propagation constant transforms to

$$\beta^2 = \frac{\omega^2}{c_0^2} \varepsilon_r' - i\omega\mu\sigma. \tag{2.3.62}$$

The modulation of the effective refractive index

$$n = \sqrt{\varepsilon_r'} = n_0 + n_1 \left(\frac{e^{i\mathbf{K}z} +^{-i\mathbf{K}z}}{2} \right) \tag{2.3.63}$$

comes along with a similar modulation of the conductivity

$$\sigma = \sigma_0 + \sigma_1 \left(\frac{e^{i\mathbf{K}z} +^{-i\mathbf{K}z}}{2} \right) \tag{2.3.64}$$

with the grating vector $\mathbf{K}$. Inserting both modulation terms into Eq. (2.3.62) yields

$$\beta^2 = \frac{\omega^2}{c_0^2} n_0^2 - i\omega\mu\sigma_0 + \left[4\frac{\omega^2 n_0 n_1}{c_0^2} - 2i\omega\mu\sigma_1 \right] \cdot \left(\frac{e^{i\mathbf{K}z} +^{-i\mathbf{K}z}}{2} \right). \tag{2.3.65}$$

The average propagation constant can be defined as $\beta_0 = \omega n_0/c_0$, the average losses are denoted by $\alpha = \mu c_0\sigma_0/2n_0$ and the loss amplitude is given by $\alpha_1 = \mu c_0\sigma_1/2n_0$. These substitutions simplify the formula of the propagation constant to

$$\beta^2 = \beta_0^2 - 2i\beta_0\alpha + 2\beta_0 \underbrace{\left[\frac{\pi n_1}{\lambda_0} - \frac{i\alpha_1}{2}\right]}_{\kappa} \cdot \left(\frac{e^{i\mathbf{K}z}+^{-i\mathbf{K}z}}{2}\right) \tag{2.3.66}$$

with the coupling constant κ and the vacuum wavelength $\lambda_0 = 2\pi n_0/\omega$. Figure 2.14 (b) indicates that in general an infinite number of reflections occur in a medium with periodic perturbations. In the coupled-wave theory by Kogelnik and Shank only two waves are taken into account and all others are neglected due to phase asynchronism and a significantly reduced amplitude around the Bragg frequency. These two counter-propagating waves are labeled R and S. The coupling constant κ defines the amount of the backward scattered light and is therefore a measure of the coupling strength and specifies the optical feedback from R to S and vice versa. The field in the cavity with these two counter-propagating waves is described by

$$\Psi(z) = R(z)e^{-i\rho z} + S(z)e^{-i\varrho z} \tag{2.3.67}$$

with the propagation constants ρ and ϱ fulfilling the condition $\varrho = \rho - \mathbf{K}$. Inserting the wave from Eq. (2.3.67) into the corresponding wave equation

$$\frac{\partial^2}{\partial z^2}\Psi + \beta^2\Psi = 0, \tag{2.3.68}$$

neglecting the second derivatives and grouping all terms according to their exponent generates the following equation

$$\begin{aligned}
e^{-i\rho z}\underbrace{\left(-2i\rho R' - \rho^2 R + \beta_0^2 R - 2i\alpha\beta_0 R + 2\kappa\beta_0 S\right)}_{\overset{!}{=}0} &+ \;\ldots \\
\ldots + e^{-i\varrho z}\underbrace{\left(-2i\varrho S' - \varrho^2 S + \beta_0^2 S - 2i\alpha\beta_0 S + 2\kappa\beta_0 R\right)}_{\overset{!}{=}0} &+ \;\ldots \\
\ldots + \underbrace{2\kappa\beta_0 R e^{-i(\rho+\mathbf{K})z}}_{\text{neglect}} + \underbrace{2\kappa\beta_0 S e^{-i(\varrho-\mathbf{K})z}}_{\text{neglect}} &= \;0
\end{aligned} \tag{2.3.69}$$

where R' and S' denote the first derivatives of R and S, respectively. Waves emitted in the directions $\rho+\mathbf{K}$ and $\varrho-\mathbf{K}$ are neglected which consequently requires that the labeled terms are zero. This condition in combination with the approximation $\rho/\beta_0 = -\varrho/\beta_0 \approx 1$, which is valid near the Bragg frequency, generates the coupled-wave equations

$$-R' + (-\alpha - i\delta)R = i\kappa S \tag{2.3.70}$$

$$+S' + (-\alpha - i\delta)S = i\kappa R \tag{2.3.71}$$

with the normalized frequency parameter

$$\delta = \frac{\beta_0^2 - \rho^2}{2\beta_0} = \frac{\beta_0^2 - \varrho^2}{2\beta_0} \approx \beta_0 - \beta_B \tag{2.3.72}$$

and $\beta_B = K/2$. The general Ansatz for the coupled-wave equations is

$$R = r_1e^{\gamma z} + r_2e^{-\gamma z} \tag{2.3.73}$$

$$S = s_1e^{\gamma z} + s_2e^{-\gamma z} \tag{2.3.74}$$

with the amplitude coefficients $r_{1,2}$ and $s_{1,2}$ and the complex propagation constant γ. From the first coupled-wave equation the following two equations

$$\begin{aligned}(-\gamma-\alpha-i\delta)r_1 &= i\kappa s_1 && (2.3.75)\\ (\gamma-\alpha-i\delta)r_2 &= i\kappa s_2 && (2.3.76)\end{aligned}$$

can be extracted by grouping all terms with the same exponent. In the same manner

$$\begin{aligned}(\gamma-\alpha-i\delta)s_1 &= i\kappa r_1 && (2.3.77)\\ (-\gamma-\alpha-i\delta)s_2 &= i\kappa r_2 && (2.3.78)\end{aligned}$$

can be derived from the second coupled-wave equation. Combination of Eq. (2.3.75) and (2.3.77) finally results in the dispersion relation of the coupled-wave system

$$\gamma^2 = \kappa^2 + (\alpha + i\delta)^2. \tag{2.3.79}$$

The definition of the coupling constant in Eq. (2.3.66) indicates two different regimes for the type of coupling. In the **index coupling** regime the coupling constant is real and the structure exhibits a modulation of the refractive index only, i.e. $\alpha_1 = 0$ and $n_1 \neq 0$. In this case $\kappa = \pi n_1/\lambda_0$. In the **gain coupling** regime the situation is reverse. The coupling constant $\kappa = -i\alpha_1/2$ is imaginary and the structure possesses only a modulation of the gain, i.e. $\alpha_1 \neq 0$ and $n_1 = 0$. A schematic visualization of the dispersion relation is given in the dispersion diagram in Fig. 2.15 (a) and (b) for index and gain coupling, respectively. This dispersion diagram shows the normalized imaginary part of the complex propagation constant as a function of the normalized frequency parameter which is a measure for the deviation of the light frequency from the Bragg frequency. Both graphs depict the dispersion relation for different gain-coupling ratios ζ with $\alpha = \zeta|\kappa|$. For a gain-free structure ($\zeta = 0$) the dispersion diagrams show a characteristic behavior. In the index coupling regime a stop band is forming in the

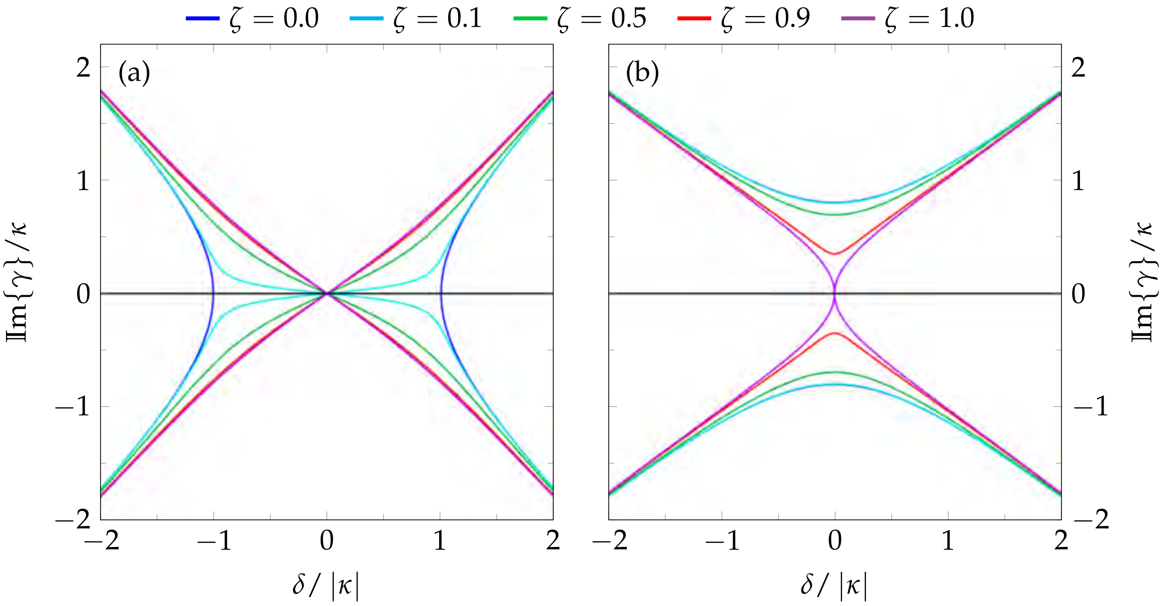

Figure 2.15: Dispersion diagram for index (a) and gain coupling (b) for different gain-coupling ratios $\zeta = \alpha/|\kappa|$ according to coupled wave theory of DFB lasers. Index coupling exhibits a stop band centered at the Bragg wavelength. Gain coupling allows all frequencies but features a gap in the propagation constant.

frequency domain. It is centered at the Bragg frequency $\delta = 0$ and exhibits a width of 2κ. Within the stop band no light propagation is possible and the cavity modes will develop at the edges of the stop band. In contrast, gain coupling creates a gap in the $\mathbb{I}\mathrm{m}\{\gamma\}$-axis. This implies forbidden values for the propagation constant but ensures a continuous dispersion relation in the frequency domain. Therefore, light propagation at the Bragg wavelength is possible. In order to solve the coupled-wave equations certain symmetries and boundary conditions have to be exploited. The symmetry of the device is illustrated in 2.14 (c) and predicts symmetric $\Psi(-z) = \Psi(z)$ and antisymmetric $\Psi(-z) = -\Psi(z)$ solutions. They can be summarized by

$$r_1 = \pm s_2 \tag{2.3.80}$$
$$r_2 = \pm s_1 \tag{2.3.81}$$

where the "+" solution corresponds to the symmetric and the "−" solution to the asymmetric case. In combination with the boundary conditions

$$R\left(-\frac{L}{2}\right) = S\left(\frac{L}{2}\right) = 0 \tag{2.3.82}$$

the asymmetric case yields the following ratios between the amplitude coefficients

$$\frac{r_1}{r_2} = \frac{s_2}{s_1} = -e^{\gamma L} \tag{2.3.83}$$

as well as the following expressions for the complex amplitudes

$$R = r_1\left(e^{\gamma L} - e^{-\gamma(L+z)}\right) \tag{2.3.84}$$
$$S = s_1\left(e^{\gamma L} - e^{\gamma(L-z)}\right). \tag{2.3.85}$$

Considering the ratio between R and S reveals

$$\frac{R}{S} = \frac{r_1}{s_1}\cdot\frac{e^{\gamma z} - e^{-\gamma(L+z)}}{e^{\gamma L} - e^{\gamma(L-z)}}. \tag{2.3.86}$$

By exploiting

$$\frac{r_1}{s_1} = e^{\gamma L} = \frac{e^{\gamma L/2}}{e^{-\gamma L/2}}, \tag{2.3.87}$$

Eq. (2.3.86) can be rewritten as

$$\frac{R}{S} = \frac{\frac{1}{2}\left(e^{\gamma(z+L/2)} - e^{-\gamma(z+L/2)}\right)}{\frac{1}{2}\left(e^{\gamma(z+L/2)} - e^{\gamma(z-L/2)}\right)}. \tag{2.3.88}$$

Applying the definition of the hyperbolic sine results in the final field distribution of the DFB modes

$$R = \sinh\left[\gamma\left(z+\frac{L}{2}\right)\right] \tag{2.3.89}$$
$$S = \pm\sinh\left[\gamma\left(z-\frac{L}{2}\right)\right]. \tag{2.3.90}$$

The minus-sign in Eq. (2.3.90) originates from the symmetric case. Plugging this field solutions into the coupled-wave equations (2.3.70) and (2.3.71) and using the addition theorem for hyperbolic functions provides the following two formulas

$$\begin{aligned}-\gamma\cosh(\gamma z)\cosh(\gamma L/2)-\gamma\sinh(\gamma z)\sinh(\gamma L/2)+\ldots\\ \ldots+(-\alpha-i\delta)\sinh(\gamma z)\cosh(\gamma L/2)+(-\alpha-i\delta)\cosh(\gamma z)\sinh(\gamma L/2)=\ldots\\ \ldots=\pm i\kappa\left(\sinh(\gamma z)\cosh(\gamma L/2)-\cosh(\gamma z)\sinh(\gamma L/2)\right)\end{aligned}\qquad(2.3.91)$$

$$\begin{aligned}\gamma\cosh(\gamma z)\cosh(\gamma L/2)-\gamma\sinh(\gamma z)\sinh(\gamma L/2)+\ldots\\ \ldots+(-\alpha-i\delta)\sinh(\gamma z)\cosh(\gamma L/2)-(-\alpha-i\delta)\cosh(\gamma z)\sinh(\gamma L/2)=\ldots\\ \ldots=\pm i\kappa\left(\sinh(\gamma z)\cosh(\gamma L/2)+\cosh(\gamma z)\sinh(\gamma L/2)\right).\end{aligned}\qquad(2.3.92)$$

Sum and difference of Eq. (2.3.91) and (2.3.92) results in

$$-\gamma\sinh(\gamma L/2)+(-\alpha-i\delta)\cosh(\gamma L/2)\;=\;\pm i\kappa\cosh(\gamma L/2)\qquad(2.3.93)$$

and

$$\gamma\cosh(\gamma L/2)-(-\alpha-i\delta)\sinh(\gamma L/2)\;=\;\pm i\kappa\sinh(\gamma L/2),\qquad(2.3.94)$$

respectively. In a similar manner the sum and difference of Eq. (2.3.93) and (2.3.94) in combination with the Euler identity yield

$$\begin{aligned}(-\alpha-i\delta)-\gamma&=\pm i\kappa e^{-\gamma L}&(2.3.95)\\(-\alpha-i\delta)+\gamma&=\pm i\kappa e^{\gamma L}&(2.3.96)\end{aligned}$$

which is an alternative representation of the dispersion relation in Eq. (2.3.79). Subtraction of these two equations results in the transcendental equation of the coupled-wave formalism

$$\gamma=\pm i\kappa\sinh(\gamma L).\qquad(2.3.97)$$

Inserting this transcendental equation in Eq. (2.3.95) or (2.3.96) yields

$$(\alpha+i\delta)=\gamma\coth(\gamma L).\qquad(2.3.98)$$

The latter equation indicates that for every complex propagation constant γ there is a defined set of parameters composed of a gain constant α and a resonant frequency coefficient δ. Utilizing the substitutions $\Xi=-(\alpha L+i\delta L)$, $\kappa L=\kappa_L$, $\gamma L=\gamma_L=\sqrt{\Xi^2+\kappa_L^2}$ it is possible to rewrite Eq. (2.3.98) in a normalized form as

$$\Xi\sinh(\gamma_L)-\gamma_L\cosh(\gamma_L)=\Upsilon\;=\;0.\qquad(2.3.99)$$

The mode spectra in Fig. 2.16 illustrate the numerical solutions for this problem and show the value of Υ on a logarithmic scale for different sets of α and δ which are represented by Ξ. Values of Υ close to zero indicate a solution of the transcendental equation. In Fig. 2.16 (a) the case for index coupling with a real coupling constant is illustrated. As expected from the previous analysis a stop band is forming around the Bragg frequency and no mode propagation is feasible. The width of this stop band increases with the coupling constant. Just outside the stop band the first resonances are evident. All other resonances farther away from the stop band have an increased threshold gain which suggests that the modes near the stop band will lase first. On the other hand, gain coupling with an imaginary coupling constant is shown in Fig. 2.16 (b). Since no stop

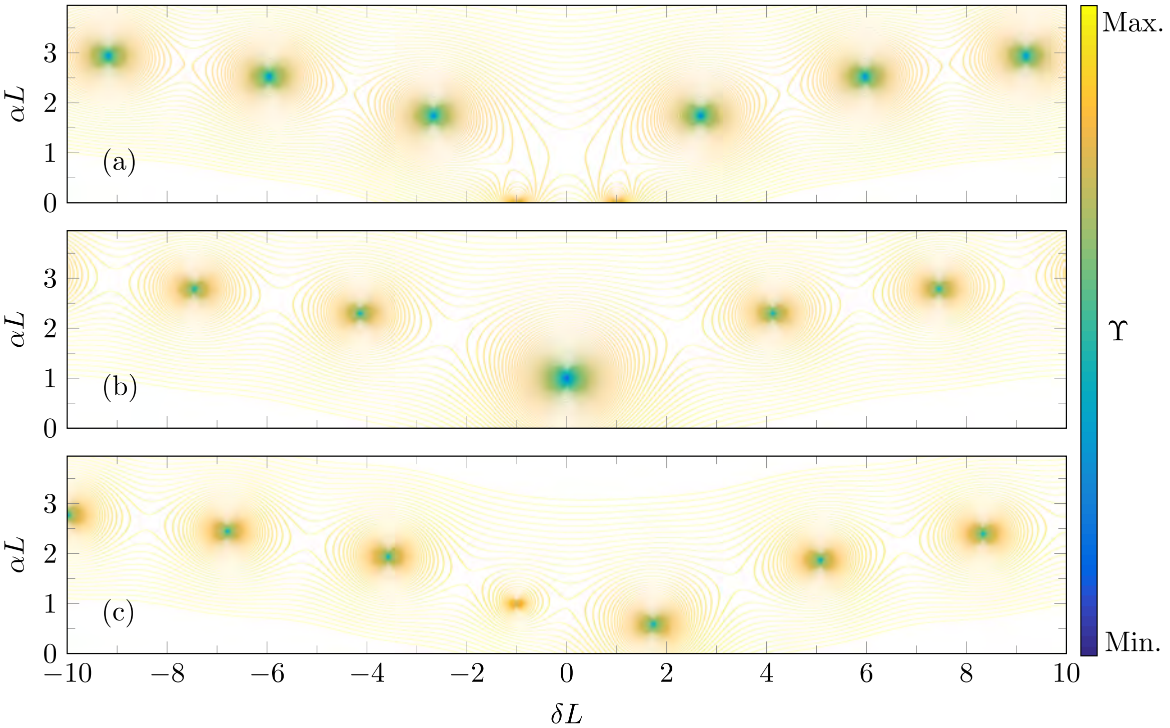

Figure 2.16: Calculated mode spectra for (a) index coupling, (b) gain coupling and (c) complex coupling. The value of Υ is calculated for several normalized threshold gain values αL and frequency detuning parameters δL and plotted on a logarithmic scale. Small values are indicated according to the color bar and represent solutions for Eq. (2.3.99). For index coupling the coupling constant $\kappa_L = 5L$ is real and a clear stop band is forming. In contrast, a Bragg mode is appearing in the gain coupling case with an imaginary coupling constant $\kappa_L = i5L$. The complex coupling situation is calculated with $\kappa_L = 5L + i5L$. The length of the device is set to $L = 0.2\,\mathrm{cm}$.

band is existent a resonance can be found exactly at the Bragg frequency. This mode exhibits the lowest threshold gain compared to the outer modes. In real devices typically a mixture between index and gain coupling occurs. The latter is also referred to as complex coupling. In such a case the coupling constant γ is a complex number and the mode spectra are not symmetric as shown in Fig. 2.16 (c). The degree of the asymmetry as well as the deviation of the central mode from the Bragg frequency is determined by the specific values of the real and imaginary part of the coupling constant. [89, 94, 96]

The first DFB QCL [97] was demonstrated by Faist et al. in 1997. Two laser structures showed room-temperature operation and provided tunable single-mode emission around $5.36\,\mu$m and $7.8\,\mu$m.

CHAPTER 3

BEAM SHAPING

LIGHT emission in QCLs can be realized in a variety of different ways. The very first QCLs were based on the simple Fabry-Pérot resonator geometry. As discussed in section 2.3.1 the light is confined in growth direction and in the lateral dimension by the heterostructure and refractive index gradient. In addition, cleaving this structure creates mirror-like facets providing longitudinal confinement. This cuboid-like configuration is often referred to as a laser ridge. Typically, the reflectivities of the facets are suitable to provide sufficient reflection back into the laser cavity and at the same time ensure significant light outcoupling. Modifications of this conventional laser geometry can lead to a tremendous performance improvement of the device. A DFB grating [97] is capable of selecting and amplifying one specific lasing mode and at the same time attenuate all the other modes in the gain spectrum. In a master oscillator power amplifier configuration [98, 99, 100] the wavelength selection process occurs in the master oscillator section and the amplification process takes place in the power amplifier section of a two-section QCL device. In this way higher order modes can be suppressed and watt-level output powers are feasible while maintaining the single-mode character of a DFB laser. Such a suppression of higher order waveguide modes can also be accomplished by tilting the emitting facet [101] of the QCL ridge which results in higher output powers and improved emission beams [102]. Collimation of the far field profile of QCLs has been demonstrated using plasmonic antennas [103, 104] directly fabricated on the edge of the semiconductor chip near the emitting facet. A rather unconventional laser geometry is the QCL microdisk [105] with a circular resonator. The absence of facets facilitates low lasing thresholds due to the lack of mirror losses.

A fundamentally different approach for light emission in QCLs is represented by **vertically emitting lasers**. In contrast to the in-plane emission of previously discussed edge emitting QCLs, such devices exhibit light emission perpendicular to the surface plane of the semiconductor chip. These kind of lasers offer several advantages like the possibility for on-chip testing and two-dimensional array integration. Furthermore, the relatively large output aperture produces an emission beam with a rather small divergence angle. Due to the intersubband selection rule, discussed in section 2.2.3, a vertical cavity surface emitting design is not feasible for QCLs [106, 107]. Hence, different techniques for surface emission in QCLs have to be applied. The first vertically emitting QCL [108] was demonstrated by Hofstetter et al. in 1999 utilizing a second order DFB grating. The latter provides optical feedback in the in-plane dimension and at the same time vertical light outcoupling due to Bragg diffraction [109]. By applying spatially separated first and second order DFB gratings [110], a deterministic mode selection can be achieved and the latter serves solely as a light extractor. Photonic crystal QCLs [111, 112, 113] utilize artificial periodic structures in order to achieve optical feedback as well as surface emission. Recently, it was shown that controlled vertical emission is possible without any periodicity. Such random medium QCLs [114, 115] exhibit a fortuitous mode formation and can produce collimated beam profiles. Circular metal DFB grating structures [116] and graded photonic heterostructures [117] enable efficient wave engineering in QCLs. Figure 3.1 depicts an overview of several edge emitting and surface emitting QCL concepts.

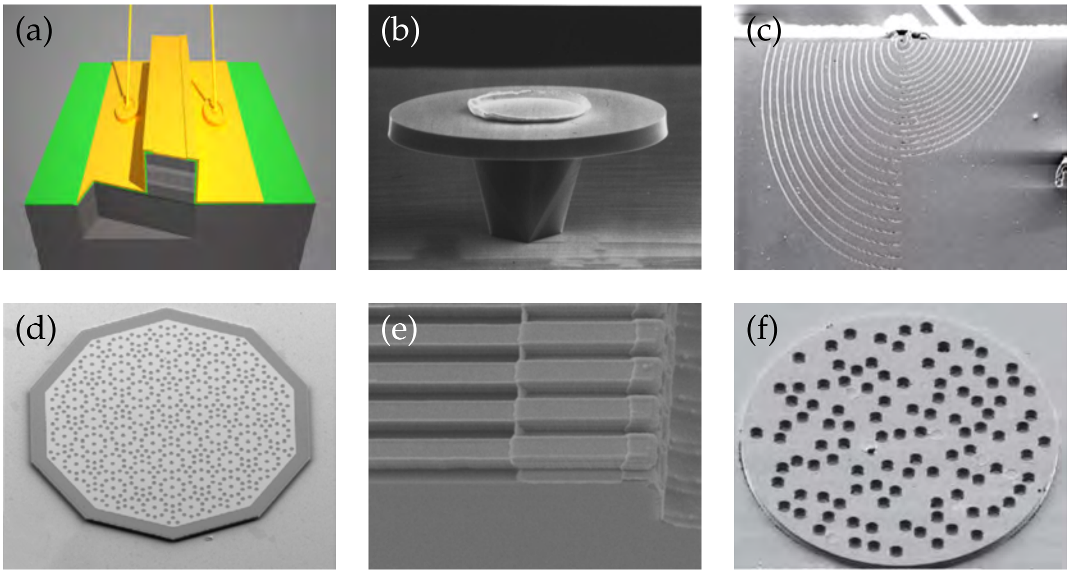

Figure 3.1: Overview of different QCL cavities applying various light extraction techniques for in-plane (top row) and surface emission (bottom row). (a) Tilted front facet. (b) Microdisk laser. (c) Plasmonic antennas. (d) Photonic quasi-crystal. (e) Second order DFB grating. (f) Random laser.
Reprinted with permission from [102, 105, 106, 113, 115, 118]

Ring QCLs are composed of a circular resonator with a second order DFB grating on top. A scanning electron microscope (SEM) image as well as a sketch of these lasers is provided in Fig. 3.2 (a) and (b), respectively. Ring QCLs were demonstrated in 2008

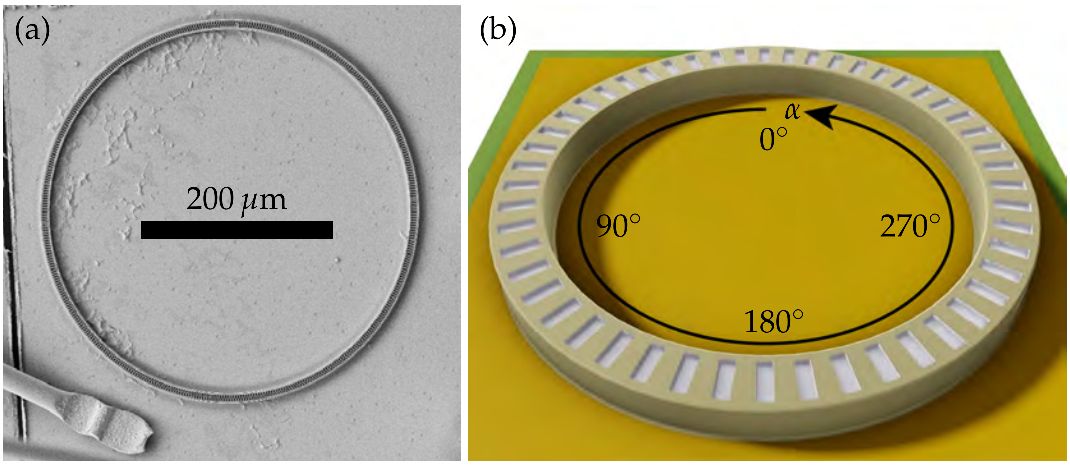

Figure 3.2: SEM image (a) and sketch (b) of a ring QCL featuring a circular waveguide with a second order DFB grating for vertical light emission.

by Mujagić et al. [119, 120] showing surface emission and single-mode operation with a collimated beam profile. These desirable characteristics initiated intensive research activities in the field. Shortly after the demonstration of the first ring QCL in the wavelength region around 4 μm, the first THz ring QCLs [121, 122] and microdisks [123] around 94 μm were realized. Within the next two years operation at elevated temperatures [124] as well as high optical output powers [125] utilizing buried heterostructures were accomplished. Mutual coherent coupling of ring QCLs [126] indicated a phase-locking mechanism in these devices for the first time. The demonstration of a 4x4 array [127] consisting of 16 ring QCLs with different emission wavelengths exemplified the feasibility of two-dimensional integration and paved the way for the utilization of such ring lasers in spectroscopic sensing applications.

3.1 Light extraction

In the following a detailed description of the second order DFB grating utilized in ring QCLs is given. This discussion will lead to the matter of fact that these ring lasers exhibit vertical emission from the surface in upward direction and simultaneously from the substrate in downward direction. Several implications are evident and explored in the subsequent sections. The topics and findings discussed from section 3.2 to 3.7 deal mainly with surface emission but can in general also be transferred or adapted for substrate emission. In contrast, sections 3.8 to 3.10 are explicitly devoted to substrate emission and potential beam modifications of the latter.

3.1.1 Second order distributed feedback grating

Light outcoupling in ring QCLs is ensured by a second order DFB grating. It provides wavelength selective optical feedback in the horizontal plane of the cavity and refracts the light, traveling inside this cavity, by 90° in vertical direction. This characteristic behavior of DFB gratings is depicted in the Bragg condition

$$\lambda_B = \frac{2\Lambda n_{\text{eff}}}{m_{\text{DFB}}} \tag{3.1.1}$$

with the Bragg wavelength λ_B, the grating period Λ, the effective refractive index n_{eff} and the order number of the DFB grating m_{DFB}. The grating equation for two different media with refractive indices n_i and n_o is

$$\Lambda \left[n_i \sin(\alpha_i) + n_o \sin(\alpha_o)\right] = m_{\text{diff}} \lambda_B \tag{3.1.2}$$

with the angles α_i and α_o to the grating normal of the incoming and outgoing waves, respectively. The diffraction order is given by m_{diff}. In a DFB laser the incoming wave is perpendicular to the grating normal with $\alpha_i = 90°$. Furthermore, the corresponding refractive index equals the effective refractive index of the laser medium. In the case of surface emission, the outgoing light is propagating in air and $n_o = 1$ while for substrate emission $n_o = n_{\text{eff}}$. Combination of Eq. (3.1.1) and (3.1.2) provides an explicit expression for the emission angle

$$\alpha_o = \arcsin\left[\frac{n_{\text{eff}}}{n_o}\left(\frac{2m_{\text{diff}}}{m_{\text{DFB}}} - 1\right)\right] \tag{3.1.3}$$

of the outgoing wave. For a first order DFB grating $m_{\mathrm{DFB}} = 1$ and Eq. (3.1.3) shows that the only solution is $\alpha_o = \pm 90°$ with $m_{\mathrm{diff}} = 1$ and $n_o = n_{\mathrm{eff}}$. On the other hand a second order DFB grating allows more than one diffraction order. Since $m_{\mathrm{DFB}} = 2$, Eq. (3.1.3) can have solutions in the first and second diffraction order. The former provides the trivial solution $\alpha_0 = \arcsin(0) = 0° \pm 180°$. Due to the fact that this result is independent of n_o, surface and substrate emission occur exactly in the vertical direction. In the second diffraction order the only solution is $\alpha_o = \pm 90°$. Hence, the first diffraction order in a second order DFB grating copes with the task of vertical light emission while the second diffraction order is responsible for the optical feedback. Figures 3.3 (a) - (d) show grating vector plots for several DFB grating orders. Higher order DFB gratings and especially detuned gratings can exhibit oblique emission directions in combination with a suppression of the surface emission.

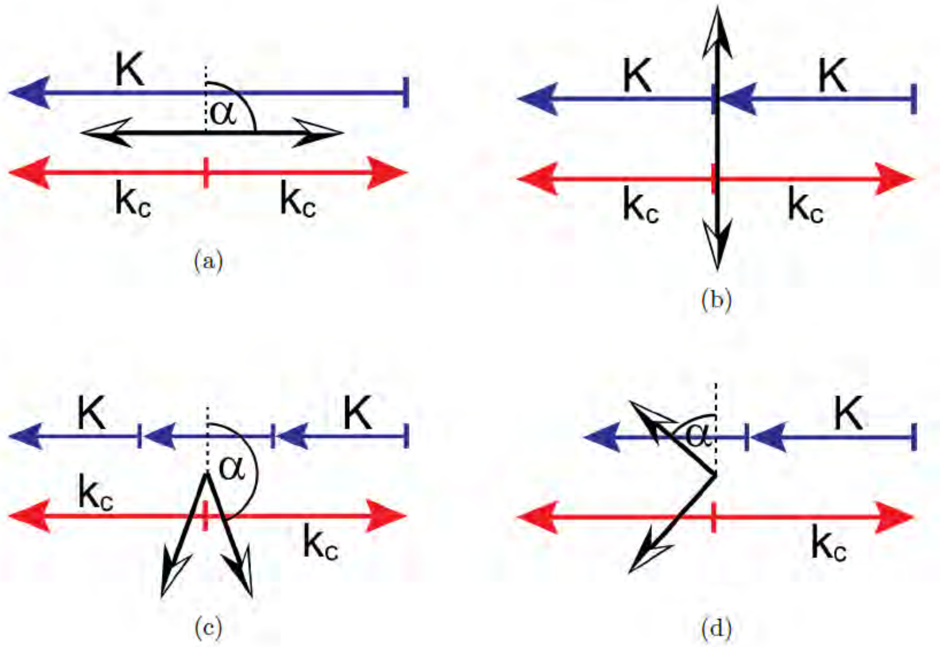

Figure 3.3: Grating vector plots for a (a) first order, (b) second order, (c) third order and (d) detuned grating. K denotes the grating vector and k_c indicates the light's wavevector. Reprinted with permission from [128]

3.1.2 Mode characteristics

It is obvious that in a second order DFB laser two complementary modes can be generated [129, 130]. For TM-polarization the electric and magnetic field distributions for the symmetric (a) and antisymmetric (b) mode are illustrated in Fig. 3.4. In the symmetric case the magnetic field lobes of the H_x component are at the locations of the grating tooths and slits. Consequently, the electric field E_y exhibits negative and positive maxima of the field strength at the edges of the grating slits. This arrangement creates a dipole moment within the slit and facilitates light emission in the vertical direction. The latter is indicated by the electric field lobe of the E_z component in the slit center. On the other hand the antisymmetric mode shows precisely the inverse behavior. The magnetic field is located at the slit edges while the electric field features a maximum intensity at the slit and tooth positions. In contrast to the symmetric mode alignment the generated dipole moments in each slit are of opposite sign and cancel each other out. Hence, the antisymmetric mode is non-radiating in vertical direction. Theoretical investigations

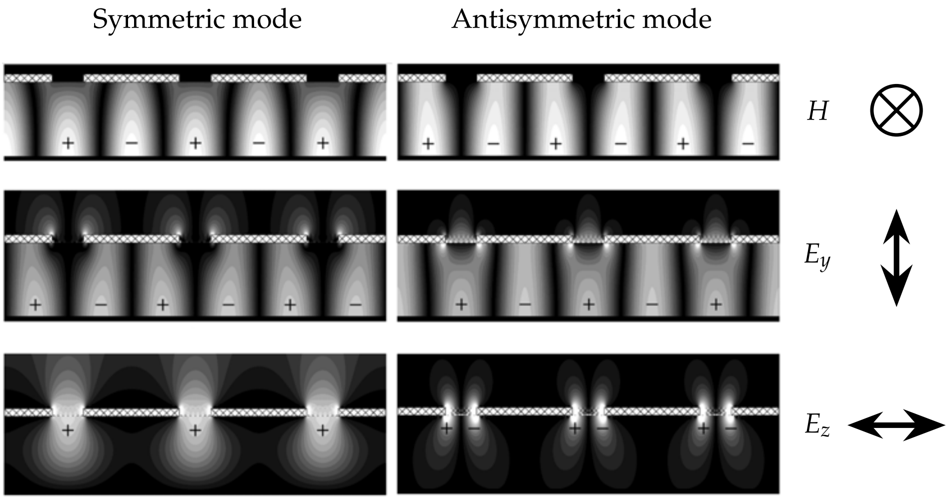

Figure 3.4: Field distribution of the symmetric and antisymmetric DFB mode. The shaded areas indicate the grating teeth. In a straight DFB laser only the symmetric mode provides vertical light emission which consequently is accompanied by additional surface losses. Reprinted with permission from [131]

[129] reveal that the antisymmetric mode in an infinite length laser exhibits the lowest losses and is therefore the first mode to lase. Considering a metallic grating the losses of the antisymmetric mode are given by $\alpha^a_{\mathrm{metal}}$. For the symmetric mode the total losses $\alpha^s_{\mathrm{metal}} + \alpha^s_{\mathrm{surf}}$ include the surface losses representing vertical emission of light. As a consequence, the infinite second order DFB laser provides no surface emission. However, in lasers with a finite length the reflecting facets break the grating symmetry and induce a superposition of antisymmetric and symmetric mode [131] with slowly varying envelope functions. Especially for high reflectivity facets the antisymmetric mode can be forced to zero at the facets. This implies that the symmetric mode is more prominent at the edges of the device and results in surface emission from the outer parts of a straight second order DFB laser. Due to the different sign of the polarization in the left and right part of the device, the far field of such a laser exhibits two lobes with a central intensity minimum [131, 132]. It is possible to compensate for this minimum by using a central grating π phase shift [133, 134, 135]. The latter flips the polarization of the left part of the device with reference to the right part and provides a single lobe emission beam. Such desirable far fields are achievable with quite different techniques as well. Graded photonic heterostructures [117] and DFB double slit configurations [136] represent valid approaches for achieving single lobe emission patterns. Introducing significant losses for the antisymmetric mode facilitates to suppress the latter and favor the symmetric mode [137, 138, 139, 140]. In this approach the losses of the antisymmetric mode $\alpha^a_{\mathrm{metal}} > \alpha^s_{\mathrm{metal}} + \alpha^s_{\mathrm{surf}}$ are higher than the losses of its symmetric counterpart.

Circular laser structures like rings and disks do not feature any facets. Therefore, the symmetry of the DFB grating is unbroken and no superposition of antisymmetric and symmetric mode occurs. Nevertheless, surface emission in these structures has been experimentally demonstrated [119]. Different mechanisms can be identified in order to explain this behavior. Assuming the antisymmetric mode exhibits the lowest losses and is the lasing mode, the field vectors at one grating slit are sketched in Fig. 3.5. The curvature of the waveguide introduces an angle between neighboring vectors of the magnetic field [123] resulting in a non-zero magnetic field component H_t in tangential direction within the waveguide. This implies a radially polarized emission beam. However, as

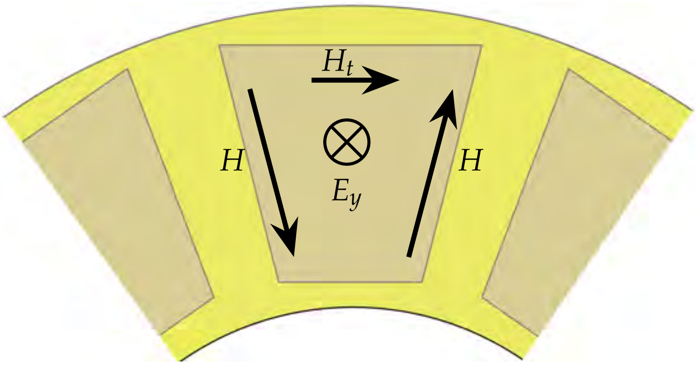

Figure 3.5: Field vectors of the antisymmetric mode in a circular cavity. Due to the bending of the waveguide, vector addition of the magnetic field vectors at the slit/tooth interfaces results in a finite tangential component of the magnetic field. Thus, surface emission is feasible. However, this vector configuration implies radial polarization of the emitted beam which is *not* the case for ring QCLs.

shown in Fig. 3.6, near field investigations of ring QCLs clearly demonstrate tangential polarization for these devices. These experiments suggest a symmetric lasing mode. Assuming the symmetric mode is responsible for the surface emission in ring QCLs, the

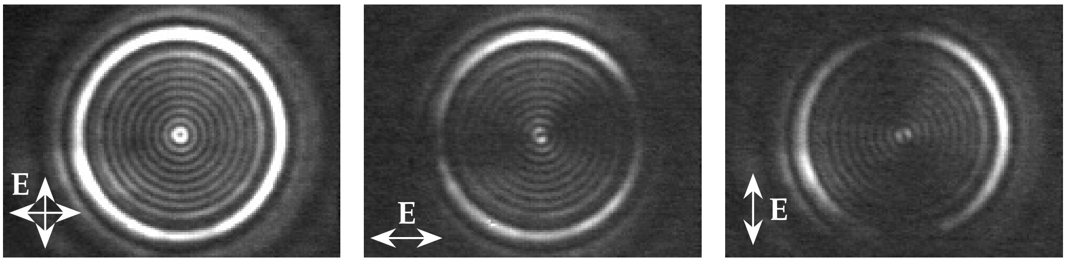

Figure 3.6: Near field images of a ring QCL obtained in a setup with a lens collimating the laser light onto a bolometer camera. Furthermore, a wire grid polarizer is placed between lens and bolometer in order to investigate the origin of both polarization components. The arrows denote the transmitted component of the *electric* field. From this study the tangential polarization of ring QCLs is evident.

dipole moment created by the electric field components E_y facilitates light emission in vertical direction and results in an overall tangential polarization of the emission beam. A rigorous analysis determining the type of the lasing mode in ring QCLs is subject of current investigations.

3.1.3 Surface and substrate emission

Facet emitting QCLs typically emit from both cleaved facets in two opposite directions. In a similar manner vertically emitting ring QCLs provide light outcoupling in the upward and downward direction, i.e. surface and substrate emission, respectively. A promising advantage of substrate emitting QCLs [141] is the potential performance improvement in conjunction with enhanced thermal dissipation. Substrate emitting ring QCLs provide continuous-wave (CW) operation in higher order modes [142] and exhibit a varying ratio between the output power of the surface and substrate emission depending on the grating duty-cycle [143]. Figure 3.7 (a) shows SEM images of six different DFB gratings on ring QCLs with different grating duty-cycles ranging from 14% to 83%. These devices were investigated in terms of spectral performance and optical output power. It was found that all ring QCLs provided single-mode operation at the

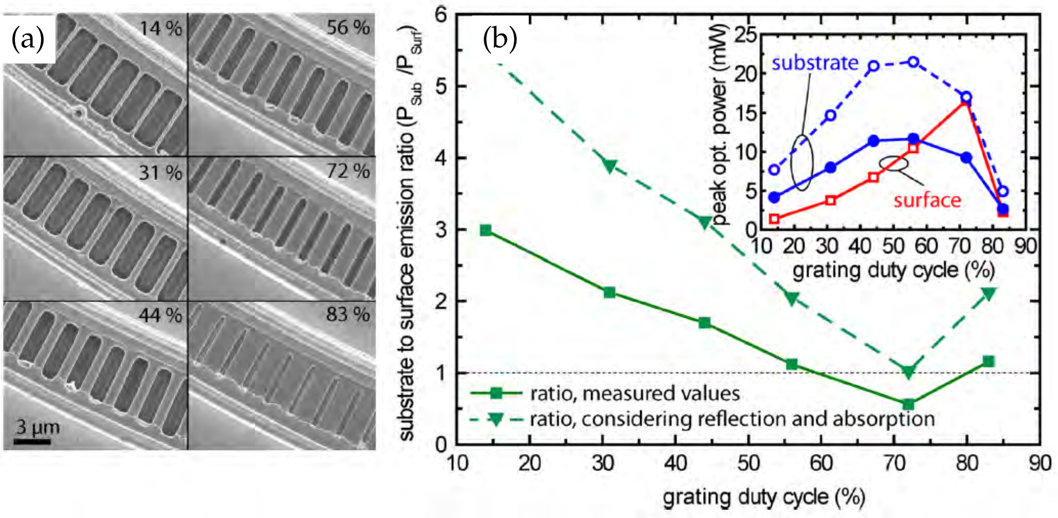

Figure 3.7: Emitted output power for the surface and substrate emission for different grating duty-cycles. (a) SEM images of the realized grating duty-cycles ranging from 14% to 83%. (b) Ratio between surface and substrate emission. The inset indicates the absolute power measured for both emission directions. The dashed curves account for the absorption within the substrate and reflections at the substrate-air interface.
Reprinted with permission from [143]

same wavelength. The analysis of the output power for surface and substrate emission is depicted in Fig. 3.7 (b). It shows the substrate-to-surface emission ratio as a function of the grating duty-cycle. It is striking that up to 60% duty-cycle the substrate emission exhibits a higher output power. Considering absorption within the 200 μm thick substrate as well as reflection at the semiconductor-air interface, the substrate emission is actually stronger for all tested duty-cycles. These findings suggest that the preferred emission direction of second order DFB gratings in ring QCLs is through the substrate. A maximum in optical output power for the surface emission if found at 72% and for the substrate emission at 56% which is in good agreement with simulations of a infinitely long DFB waveguide [143].

The insight that the DFB grating of ring QCLs can be tailored to promote substrate emission as well as the fact that the latter facilitates a manifold of opportunities for beam shaping by means of micro-manipulation of the bottom side of the chip makes substrate emission one of the most interesting features of ring QCLs. A detailed discussion of such modifications of the emission beam is provided in the sections 3.8 to 3.10. Prior to that, fundamental principles and beam shaping approaches for the surface emission are reviewed in the following sections.

3.2 Far field pattern

COMBINATION of a circular resonator with a vertically emitting DFB grating facilitates an extraordinary laser beam based on unique interference mechanisms. They can be best described in terms of principles adapted from Fourier optics. A Fourier transform [144] is the expansion of a function into complex harmonics. In optics this describes the segmentation of light into plane waves with different propagation directions. The independent generation and manipulation of these plane waves as well as their superposition is the key aspect of Fourier optics. An extended two-dimensional object in the object plane is composed of a multitude of points each weighed by an object function $o(x', y')$. Each of these points is a source for a plane wave. Every single point in the observation plane is composed by the phase-sensitive integration of all components from the object plane. All points in the observation plane establish the corresponding field distribution

$$f(x, y) = \iint_{-\infty}^{+\infty} o(x', y')\delta(x - x', y - y')dx'dy' \tag{3.2.1}$$

with the delta function $\delta(x)$. Considering that all points are sources for plane waves, the delta function can be replaced by spherical waves in

$$f(x, y) = \iint_{-\infty}^{+\infty} o(x', y')\frac{1}{r}e^{in\mathbf{kr}}dx'dy'. \tag{3.2.2}$$

In the far field approximation $1/r \approx 1/z$ assuming propagation in z-direction. Therefore, the spatial coordinate r can be written as $r = \sqrt{z^2 + (x' - x)^2 + (y' - y)^2}$. Since the far field approximation also specifies $\sqrt{1 + x} \approx 1 + x/2$, the field distribution in the observation plane yields

$$f(x, y) = \underbrace{\frac{1}{z}e^{ink\left(z + \left(x^2+y^2\right)/2z\right)}}_{A} \iint_{-\infty}^{+\infty} o(x', y') \underbrace{e^{ink\left(x'^2+y'^2\right)/2z}}_{\approx 1} e^{-ink(y'y+x'x)/z}dx'dy'. \tag{3.2.3}$$

The first exponential term in the integral equals 1 in the far field approximation. Utilization of $k = 2\pi/\lambda$ and the spatial frequencies $\nu_x = x/z\lambda$ and $\nu_y = y/z\lambda$ provides the final expression of the field distribution in the observation plane

$$f(\nu_x, \nu_y) = A \iint_{-\infty}^{+\infty} o(x', y')e^{-i2\pi n(x'\nu_x + y'\nu_y)}dx'dy' \tag{3.2.4}$$

$$\hat{=} \ \mathfrak{F}\left(o(x', y')\right) \tag{3.2.5}$$

which corresponds to the Fourier transform of the object function. [67, 145, 146]

In the same manner the field distribution in the observation plane, i.e. the far field, of a ring QCL can be calculated. Typical geometric parameters of these lasers are an outer diameter of 400 μm and a waveguide width of 10 μm. Light emission is provided by the DFB grating with a width in the range between 6 μm and 8 μm. In Fig. 3.8 (a) the object functions of such a ring QCL are shown. Vertical and horizontal polarization components are calculated separately in order to ensure phase-dependent relationships between different parts of the ring. The angular near field amplitudes of both components are given by

$$A_{NF}^{V} = \sin(\theta) \tag{3.2.6}$$

$$A_{NF}^{H} = \cos(\theta). \tag{3.2.7}$$

It is evident that the emitting area is defined by the DFB grating on top of the waveguide and that the light intensity is uniformly distributed over the ring. According to Eq. (3.2.5) the far field of this laser can be calculated by a simple two-dimensional Fourier transform. Therefore, the intensity distribution of the emitted beam amounts to

$$I_{FF} = I_{FF}^{V} + I_{FF}^{H} = \left|\mathfrak{F}_{2D}\left(A_{NF}^{V}\right)\right|^2 + \left|\mathfrak{F}_{2D}\left(A_{NF}^{H}\right)\right|^2. \tag{3.2.8}$$

Each polarization component is displayed in Fig. 3.8 (b). The far field pattern exhibits concentric intensity rings originating from interference effects and a central intensity

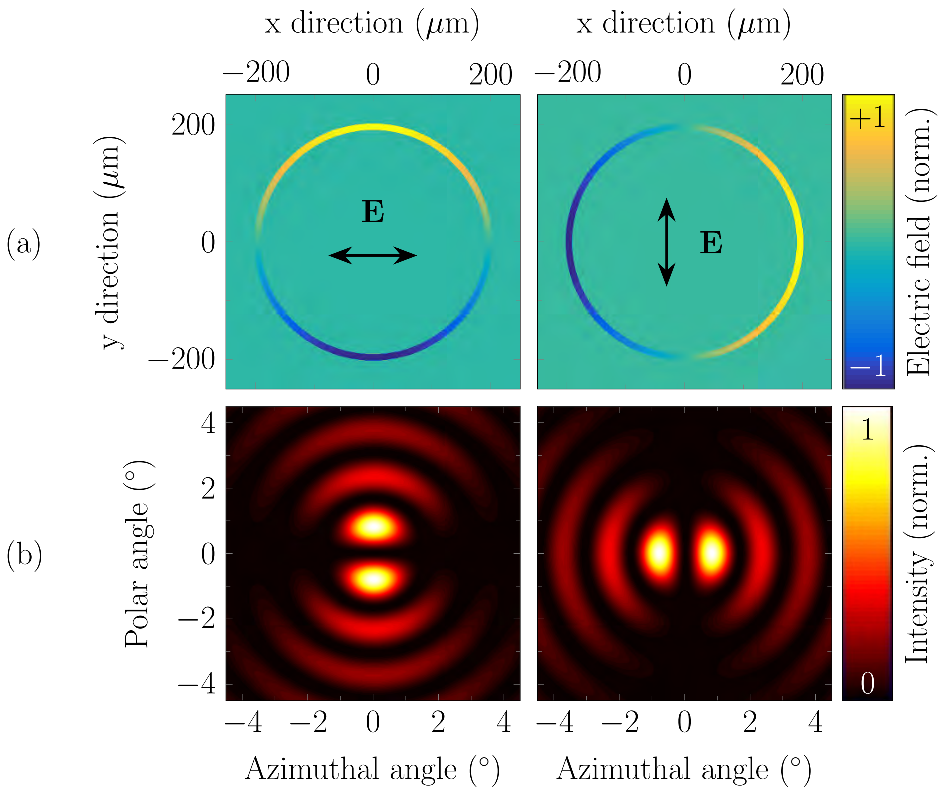

Figure 3.8: Near field object functions for both polarization components and corresponding simulated far fields. Due to the circular nature of ring QCLs the emitted electric field vectors from opposing sides of the ring exhibit an antiparallel orientation. This results in the inversely phased object functions and induces a central intensity minimum in the far fields. The latter represent the 2D Fourier transform of the corresponding object functions.

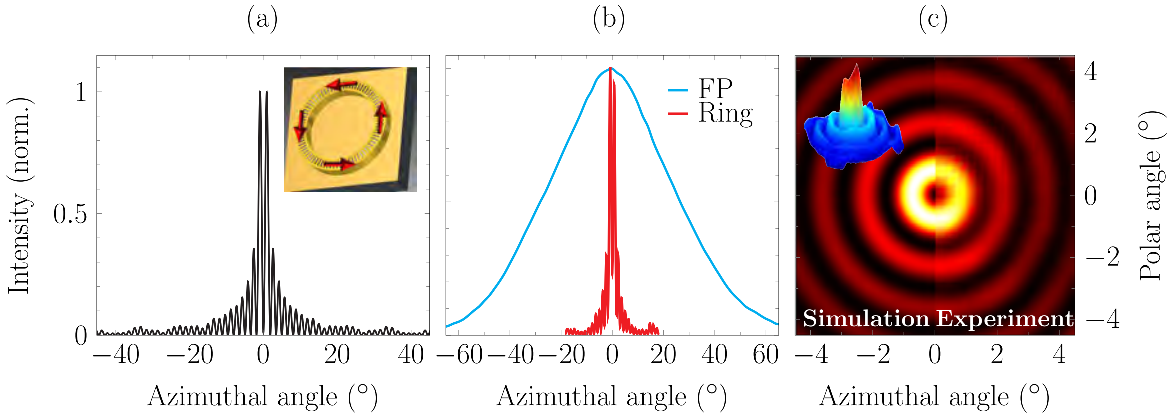

Figure 3.9: (a) Cross section of the far field simulation based on a 2D Fourier transform of the near field object function. The inset illustrates the orientation of the emitted electric field vectors along the ring. Opposing sides exhibit an antiparallel orientation creating the central intensity minimum. (b) Comparison between experimentally obtained normalized far fields from a facet emitting Fabry-Pérot and a surface emitting ring QCL with similar geometrical dimensions. The latter provides a collimated laser beam. (c) The comparison of simulated and measured two dimensional far field patterns shows a very good agreement between theory and experiment. The inset illustrates a three dimensional representation of a measured beam emitted from a ring QCL.

minimum. Investigation of the far field's cross section, as indicated in Fig. 3.9 (a), enables a more profound understanding of the formation of the far field. Similar to the double-slit experiment the emission beam of ring QCLs consists of distinct interference fringes. However, the latter displays an inherent intensity minimum in the center of the beam which is in contrast to the traditional double-slit experiment. The reason for this phenomenon can be found in the circular cavity structure of ring QCLs. The central intensity peak in the double-slit experiment originates from constructive interference between two rays with identical phase. In ring QCLs the phase of light emitted from opposing sides of the ring possesses indeed the same phase but the emitted electric field vector is rotated by 180° as sketched in the inset of Fig. 3.9 (a). This bears comparison with a phase shift of exactly π and induces the central intensity minimum. The fringe separation for a given wavelength is determined by the diameter of the ring and the envelop function is influenced by the width of the emitting ring structure, i.e. the width of the DFB grating. It is worthwhile noticing that the cross section of the far field pattern for a two-dimensional ring emitter is different compared to the diffraction pattern of a one-dimensional double-slit. In the two-dimensional case the field distribution is composed by the integral over all contributions from the object plane. This includes by far more plane wave contributions as in the one-dimensional case which in turn strongly influences the far field pattern. As a consequence of the large emitting area of ring QCLs their light beam exhibits a smaller divergence as in edge emitting Fabry-Pérot lasers. Figure 3.9 (b) shows a comparison between the far field of a surface emitting ring QCL with a FWHM of $\sim 3°$ and an edge emitting Fabry-Pérot laser with a FWHM of $\sim 60°$.

The previous theoretical discussion of the emission beam of ring QCLs certainly needs experimental validation. Figure 3.9 (c) depicts the good agreement between calculated and an experimental far field patterns. The inset provides a three-dimensional representation of the measured far field. The latter was recorded with a liquid-nitrogen cooled mercury-cadmium-telluride (MCT) photodetector with a detector element size of $1\,\mathrm{mm}^2$ on an x-y translational stage. The laser was operated in pulsed mode with a pulse length of 100 ns and a repetition rate of 5 kHz. If not otherwise indicated all far field measurements in this dissertation were conducted with these parameters.

3.3 Polarization control

Optical feedback for single-mode surface emission in ring QCLs is provided by the second order DFB grating. In the course of light outcoupling the DFB grating influences the polarization of the light. The inset of Fig. 3.9 (a) illustrates the tangential orientation of the emitted electric field vector. This feature of ring QCLs is verified by the polarization dependent near field measurements in Fig. 3.6. Even ring QCLs operating on higher order modes show a clear tangential polarization [125] in the near field. Control of the polarization of the emitted light is a key factor for potential performance improvements and beam optimizations. In a first step the inherent tangential polarization feature of ring QCLs is modified. Therefore, the radially aligned grating slits are tilted by a specific angle α_t as shown in the SEM image and the sketch in Fig. 3.10 (a) and (b), respectively. Without loss of generality the orientation of the grating slit tilt is in the counter clockwise direction with reference to the center of each grating slit. Since a change of the grating duty-cycle has a significant effect on the optical output power, as shown in section 3.1.3, comparable results for different values of α_t require an adaptation of the slit width according to $s_t = s \cdot \cos(\alpha_t)$ in order to ensure a constant effective slit width s_{eff}. In the present study four different tilt angles from $\alpha_t = 0°$ to $\alpha_t = 30°$ were realized. Due to the still existing rotational symmetry, all

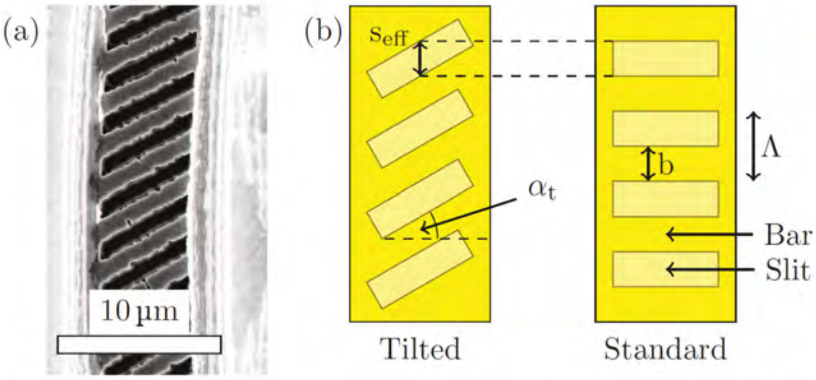

Figure 3.10: SEM image (a) and sketch (b) of a DFB grating with tilted grating slits. In order to provide a constant grating duty-cycle for different tilt angles α_t the absolute width of the slits has to be adapted.
Reprinted with permission from [147]

lasers exhibit the conventional far field pattern presented in Fig. 3.9 (c). Although these emission beams resemble non-modified light beams, they carry exceptional characteristics in the polarization domain. In Fig. 3.11 (a) these features are revealed by means of polarization dependent measurements. An external wire grid polarizer with a vertical orientation of the wires was placed between the laser and the MCT detector. Thus, only horizontally polarized light reaches the detector. In conventional ring QCLs this light is generated at the top and bottom of the ring as shown in Fig. 3.6, i.e. at 0° and 180° according to Fig. 3.2 (b). The experimental far fields in Fig. 3.11 (a) show modifications of the conventional polarization characteristics for tilt angles $\alpha_t > 0°$. The regions of horizontal light emission are shifted in clockwise direction. The larger the tilt angle the greater the shift. In order to quantify this rotation of the far field pattern the vertical symmetry axis of the conventional far field ($\alpha_t = 0°$) is indicated by the green

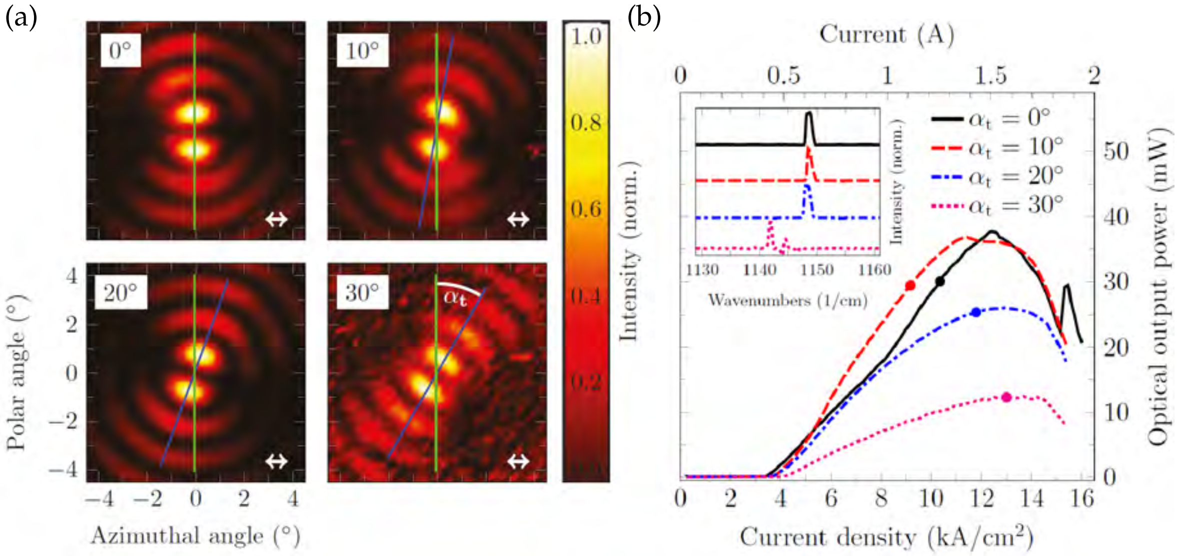

Figure 3.11: (a) Horizontal polarization component of far fields emitted from ring QCLs with different grating tilt angles ranging from 0° to 30°. The rotation of the far field pattern indicates a shift of the origin of horizontally polarized light. Hence, the emitted light carries a finite radial polarization component. (b) Light-current (LI) curves measured for all four tilt angles in (a). An increase of α_t is accompanied by a reduced output power. The inset shows the corresponding spectra.
Reprinted with permission from [147]

line. With reference to the center of the far field the blue line represents a rotation of α_t. Comparison of the blue axis with the corresponding underlying far field shows a good agreement and suggests that the far field rotation is given by the tilt angle α_t of the grating slits. As a consequence the emitted polarization in ring QCLs is always perpendicular to the grating slits. For non-metallic gratings is was shown that this is not a compulsory condition. In a system with several DFB ridge lasers and a perpendicularly oriented collector waveguide this enabled coupling of light with the polarization vector parallel to the grating slits and consequential TE-polarized emission from the facet [148] of the collector waveguide. In ring QCLs with a metallic DFB grating any reorientation of the slits entails a corresponding alteration of the emitted polarization of the emitted electromagnetic field. For the presented laser devices this implies that their emission beams are not purely tangentially polarized but exhibit a specific degree of $\sin(\alpha_t)$ of radial polarization. The ring laser with $\alpha_t = 30°$ exhibits a rather noisy far field which can be seen as a result of the lower output power indicated in the light-current (LI) curves in Fig. 3.11 (b). In contrast, the devices with the two smallest tilt angles exhibit rather high and comparable output powers. The inset in Fig. 3.11 (b) contains the measured spectra of all four lasers. While the lasers with $\alpha_t = 0°$, 10° and 20° emit at exactly the same wavelength, the $\alpha_t = 30°$ laser emits at a neighboring mode. The correlation between increasing tilt angle and decreasing output power can be attributed to a perturbation of the lasing mode and concurrent suboptimal coupling of the DFB grating resulting in a reduction of the emitted output power. [147]

3.4 Integrated phase shifts

Far field patterns emitted by ring QCLs feature characteristic concentric intensity rings and exhibit a distinct inherent intensity minimum in the center of the beam. As discussed in section 3.2 and illustrated in Fig. 3.9 this minimum originates from the curvature of the circular resonator and the accompanying rotation of the emitted electric field vector. The latter corresponds to a phase shift providing an anti-parallel orientation of electric field vectors from opposing sides of the ring. In the far field this results in destructive interference and a central intensity minimum. It is comparable to the double-lobe emission beams from straight second order DFB QCLs [89, 106, 107]. Many applications, however, require as much intensity as possible in the center of the laser beam. For straight surface emitting QCLs a central grating phase shift [131, 132] can be exploited to alter the polarization in the left part of the device with reference to the right part. For QCLs with a DFB phase shift of π, single-lobe far field patterns are obtained in a similar manner as in band gap lasers [133, 134, 135].

A similar approach can be utilized for ring QCLs in order to generate a central intensity maximum in the laser beam. Figure 3.12 (a) contains a SEM image of a ring QCL with two π phase shifts in the DFB grating. In contrast to straight DFB QCLs with only one phase shift, ring QCLs require the implementation of *two* grating phase shifts which is due to their circular geometry. These phase shifts are realized in the form of two adjacent grating teeth as shown in the inset of Fig. 3.12. They are located at the top and bottom of the ring with an angular distance of 180°. The functional principle of the π phase shifts is demonstrated in Fig. 3.12 (b). On the left side the DFB grating on top of the fundamental mode of the electric field E_y of a conventional ring QCL is depicted. The arrows indicate the momentary orientation of the emitted electric field

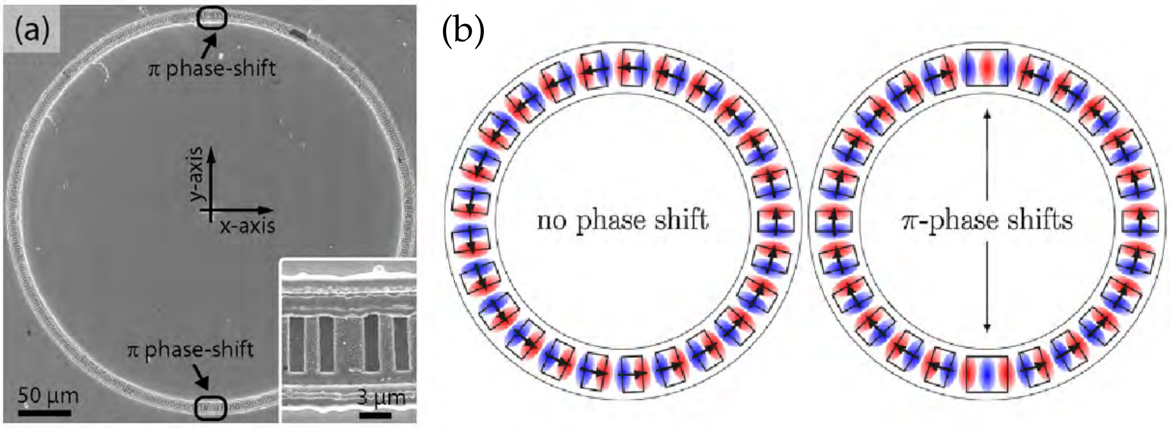

Figure 3.12: (a) SEM image of a ring QCL with two integrated π phase shifts in the grating. The inset shows a magnified image of the phase shifts. (b) Sketch of the location of the out-of-plane electric field mode relative to the DFB grating for a conventional and a π phase shift ring QCL. The arrows denote the emitted polarization vectors. The phase shifts induce a rotation of the field vectors on one side of the ring which results in a parallel orientation of the vectors emitted from the left and right side of the ring.
Reprinted with permission from [149, 150]

vector. The resulting anti-parallel orientation of the polarization produces destructive interference. On the right side the DFB grating and mode profile of a π phase shift ring QCLs are shown. In contrast to the SEM image in (a) the phase shift is achieved by means of two adjacent grating slits. In any case, it is found that the type of π shift does not influence the performance of the ring QCL. Since the DFB grating provides the same feedback mechanism as in a conventional ring QCL, the mode pattern stays unchanged. However, due to the phase shift of the grating, opposing sides of the ring exhibit a parallel orientation of the emitted polarization vector. In the far field this leads to constructive interference in the beam center. For the simulation of the corresponding far field the near field amplitudes of the vertical and horizontal polarization are given by

$$A_{NF}^{V} = \left|\sin(\theta)\right|, \tag{3.4.1}$$

$$\tag{3.4.2}$$

and

$$A_{NF}^{H} = \begin{cases} \cos(\theta), & \text{if } 0^\circ < \theta < 180^\circ \\ \cos(\theta - 180^\circ), & \text{if } 180^\circ < \theta < 360^\circ \end{cases} \tag{3.4.3}$$

respectively. Figure 3.13 provides the two dimensional near field object functions (a), the near field amplitudes as a function of the angular position on the ring (b) as well as a false color plot (c) of experimentally determined near fields for vertical and horizontal polarization. All parts of Fig. 3.13 clearly display the π phase shifts at $\theta = 0^\circ$ and $\theta = 180^\circ$. In the experimental near field of the horizontal polarization a sharp intensity drop at the location of the phase shifts is evident. This can be attributed to local destructive interference of light. Based on the near field object functions in Fig. 3.13 (a) far field simulations were conducted. These theoretical results are shown together with the experimental data in Fig. 3.14. Each graph consists of a left and right part, representing the simulated and measured far field patterns, respectively. The entire emission beam is provided in Fig. 3.14 (a) and exhibits a clear central intensity maximum

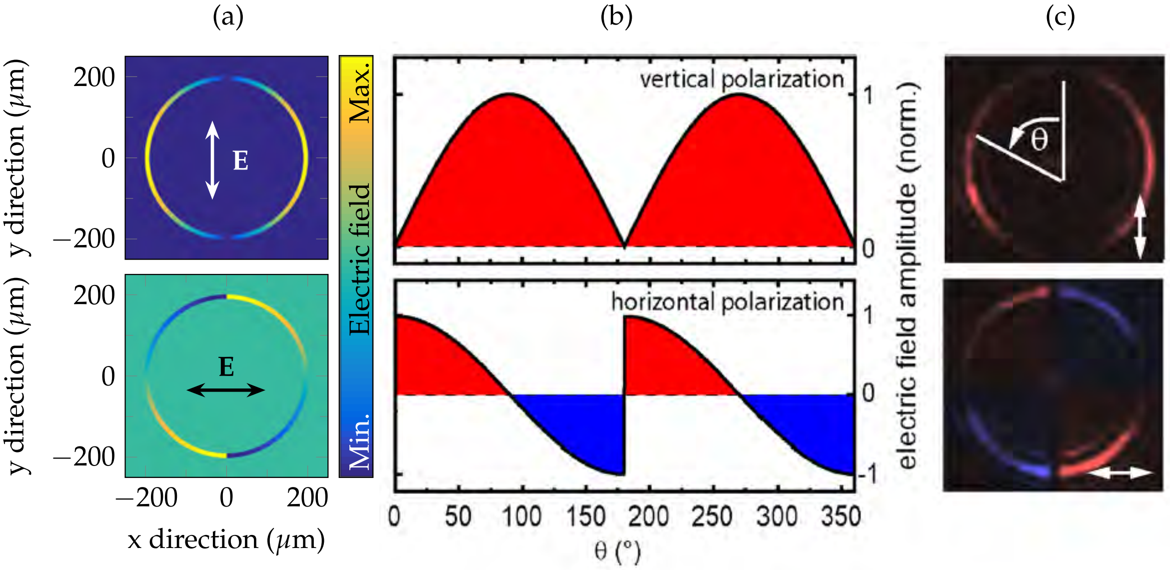

Figure 3.13: (a) Two dimensional near field object functions for a π phase shift ring QCL. Due to two phase shifts at the top and bottom of the ring, opposing sides exhibit the same phase. (b) Electric field amplitude as a function of the spatial coordinate θ along the ring. The phase shifts are located at $\theta = 0°$ and $\theta = 180°$. (c) Experimentally obtained false color near field images showing a good agreement with the object functions in (a). The near field clearly shows dark spots at the locations of the phase shifts.
Reprinted with permission from [149]

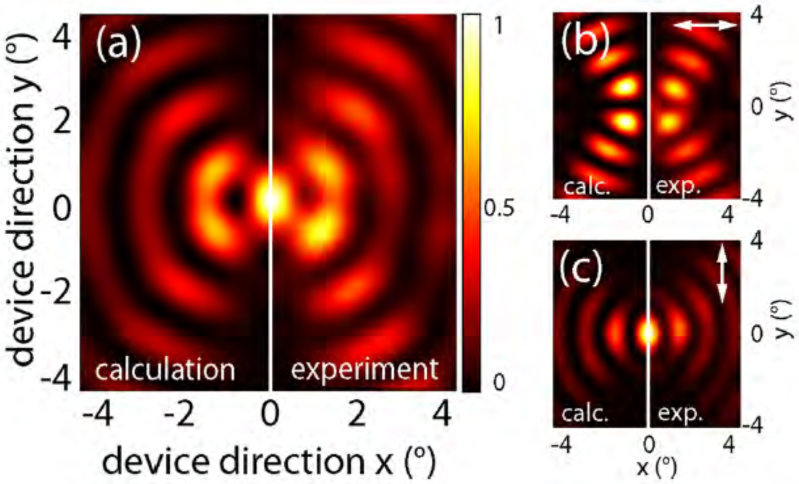

Figure 3.14: (a) Comparison between simulated and measured far field of a π phase shift ring QCL. The phase shifts generate a central intensity maximum. Along the axis going through both phase shifts the far field exhibits negligible intensity except for the central lobe. (b) and (c) indicate the far field's horizontal and vertical polarization component, respectively. This analysis shows that the central lobe of the far field is exclusively formed by vertical polarization.
Reprinted with permission from [149]

as expected from previous theoretical considerations. The outer intensity lobes exhibit a circular shape except for the top and bottom of the far field corresponding to the locations of the π phase shifts. Overall an excellent agreement between theory and experiment is observed. This statement also holds for the horizontally and vertically polarized parts in 3.14 (b) and (c), respectively. While the latter possesses a central maximum as well, the horizontal polarization yields an X-shaped far field with almost no intensity in the center. Therefore, the central intensity lobe with a full-width-at-half-maximum (FWHM) of 1° along the y-axis and 0.8° along the x-axis is exclusively produced by vertically polarized light. According to Eq. (3.2.8) the entire emission beam is composed of the superposition of the horizontally and vertically polarized far fields. Further insight into the principles of grating phase shifts can be obtained by an analysis of intensity cross sections. Intensity profiles along the x- and y-axis are shown in Fig. 3.15 (a) and (b), respectively. They demonstrate the quantitative agreement between experiment and theory. Along the x-axis the π phase shift laser exhibits intensity maxima where conventional ring QCLs possess minima and vice versa. Hence, π phase shifts provide an intensity-flip-mechanism not only for the central part but almost for the entire beam. Along the y-axis the phase shifts induce a lack of light intensity and produce a nearly single-lobe far field pattern exhibiting a strong suppression of the interference fringes. This investigation of π phase shifts in ring QCLs not only provides enhanced output beams but also confirms the theoretical approach to understand the light emission mechanism in these lasers. [149]

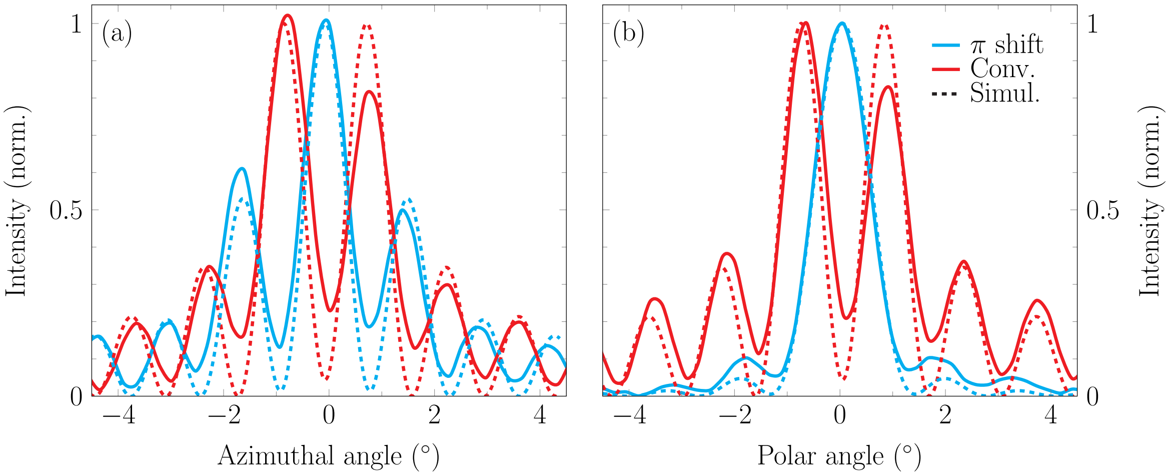

Figure 3.15: Comparison between far field cross sections along the azimuthal (a) and polar (b) far field coordinate. Blue curves indicate far fields emitted by π phase shift ring QCLs while red curves represent conventional far fields. The dashed curves show the simulated far field cross sections. This comparison demonstrates that the application of π shifts in the grating exchanges the locations of intensity minima and maxima between conventional and π shift lasers.

3.5 Alignment of waveguide and grating

INTEGRATED phase shifts in a DFB grating are capable of breaking the symmetry of the DFB grating and providing central lobe emission beams due to constructive interference. Similar features of the far field have been theoretically observed for DFB gratings with a spatially separated center point with reference to the waveguide [122]. In Fig. 3.16 a linear shift of $\Lambda/4$ of the grating is illustrated. The latter breaks the symmetry of the grating and induces a superposition of symmetric and antisymmetric mode. In addition it constitutes a chirped grating [130, 151] with a varying effective grating period along the perimeter of the ring, assuming the relocation of the grating does not influence the propagation path of the mode. This produces a spatially dependent relative phase shift between grating and mode as depicted in Fig. 3.17 (a). It varies continuously between $+\pi/2$ and $-\pi/2$ which is equivalent to the $\Lambda/4$ offset of the grating. The corresponding

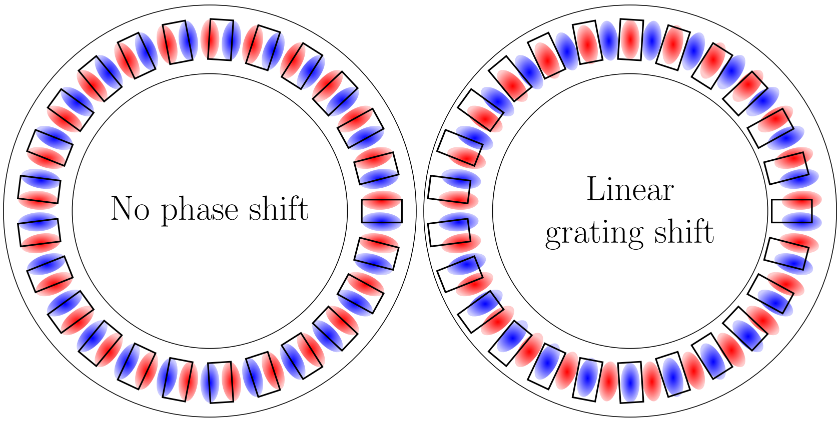

Figure 3.16: The location of the out-of-plane electric field mode relative to the grating in a conventional ring QCLs is compared to the situation in which the DFB grating exhibits a linear shift in a specific direction. For a shift to the left the situation along the horizontal axis does not change significantly whereas a phase shift of π is evident between the top and bottom of the ring.

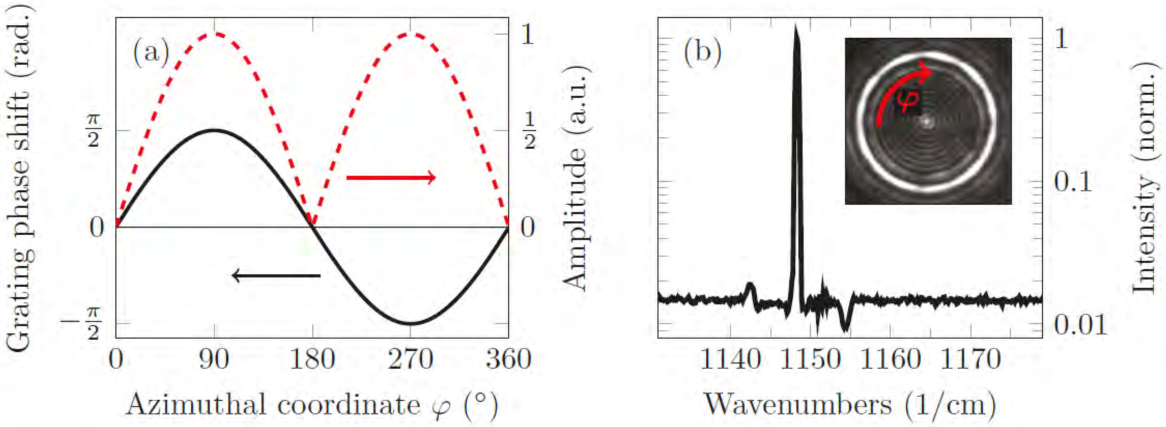

Figure 3.17: (a) Theoretical near field amplitude and continuously varying grating phase shift with respect to the mode of a linearly shifted DFB grating ring QCL along the azimuthal coordinate. (b) Spectrum of the laser showing single mode emission. The inset shows a near field image of a laser with a linear grating shift. Contrary to the varying near field amplitude in (a) the ring exhibits steady light emission along the perimeter of the ring. Reprinted with permission from [147]

near field amplitude, generated by this phase shift, exhibits maxima at $\varphi = 90°$ and $\varphi = 270°$ and null values for $\varphi = 0°$ and $\varphi = 180°$. The latter imply a reduced light outcoupling. Figure 3.17 (b) provides the recorded spectrum of this laser. The single mode behavior eliminates the possibility of an overlap effect by two lasing modes. Hence, the near field intensity pattern shown in the inset can be attributed to a single mode. A constant intensity distribution along φ is evident. At first glance this observation is inconsistent with the near field amplitude given in Fig. 3.17 (a) which would possess darker areas and a significantly varying near field intensity distribution.

In order to clarify these results the experimentally determined far field is investigated in Fig. 3.18. It exhibits a central intensity maximum as a consequence of constructive interference. Furthermore, the far field pattern consists of concentric interference rings and displays a distinct circular symmetry with a constant intensity distribution along the azimuthal direction φ as observed for the near field. This is in contrast to far field simulations using a double slit configuration which showed an asymmetric intensity

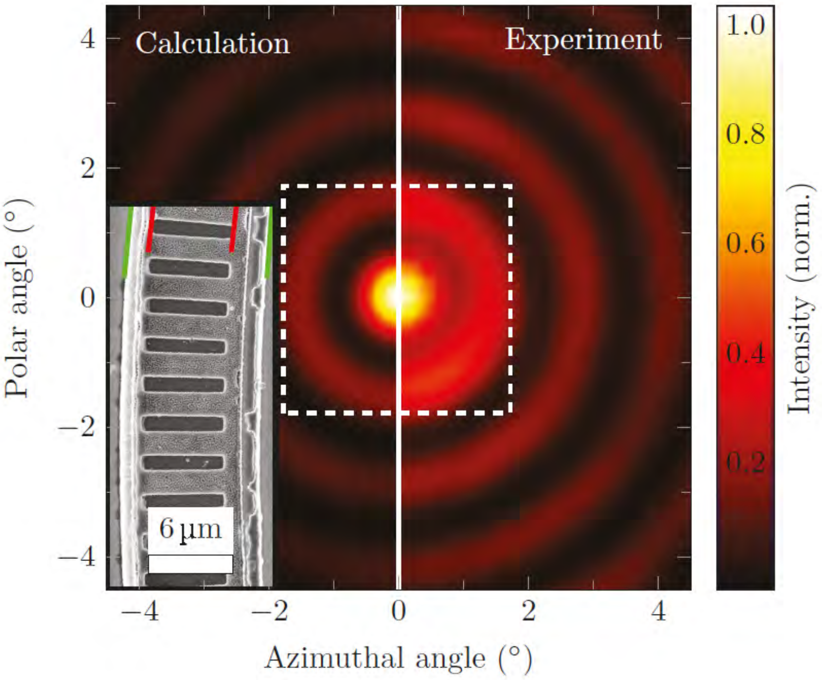

Figure 3.18: Comparison between calculated and experimentally obtained far field patterns for a ring QCL featuring a linear shift of the grating. The far field is rotationally symmetric and exhibits a central intensity maximum. For the calculation of the far field a stepwise rotation of the near field amplitude in Fig. 3.17 (a) along φ was assumed. Such a rotation provides rotational symmetry while the inherent phase shift introduces the central intensity maximum.
Reprinted with permission from [147]

distribution of the beam [122]. The inset in Fig. 3.18 shows a SEM image of a DFB grating section with an off-centered grating with respect to the waveguide. The red lines mark the location of the grating which is shifted to the left compared to the waveguide indicated by the green lines. A precise adjustment between grating and waveguide is ensured by a simultaneous exposure using electron beam lithography. By comparing π phase shift gratings with off-centered gratings in ring QCLs, the central intensity maximum can be identified as the most striking similarity. However, this maximum possesses different polarization characteristics in both cases. While the π shift laser produces a linearly polarized central lobe, Fig. 3.19 demonstrates that the central intensity maximum of an off-centered DFB ring QCL is composed of *all* polarization components. Six far fields are shown which correspond to the dashed square in Fig. 3.18. Every far field is measured with a different orientation of an external wire grid polarizer placed between laser and MCT detector. The orientation of the transmitted electric field is indicated by the white arrow in each subgraph. Here again, the characteristic tangential polarization behavior of ring QCLs is demonstrated. In addition, every polarization component features a distinct central lobe. Hence, the central intensity maximum is formed by all polarization components originating from the entire ring. It is worth noticing that for different polarization components the central intensity lobe is rotating round the center of the beam indicated by the black cross-hair. Polarization vectors are always tangential in a ring QCL and constructive interference implies a parallel orientation of these vectors for opposing sides of the ring. These conditions can only be realized with a grating phase shift somewhere on the ring. In turn, a phase shift would appear as an area with a reduced light intensity. However, experimental data shows that the ring exhibits a continuous light distribution in the near and far field as shown in Fig. 3.17 (b) and 3.18,

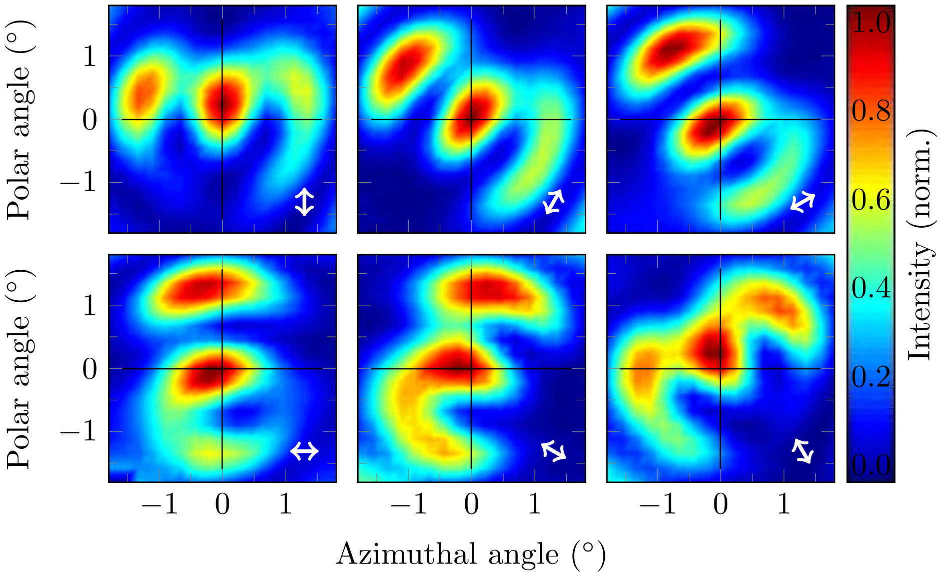

Figure 3.19: Central far field recorded with different orientations of a wire grid polarizer placed between the laser and the MCT detector. The white arrows denote the orientation of the transmitted polarization. The central maximum is existent for every polarization direction which suggests a parallel orientation of opposing field vectors for the *entire* ring. This configuration suggests a non-static case with a time-dependent behavior of the mode. Reprinted with permission from [147]

respectively.

These matters of fact suggest a time-dependent behavior of the mode inside the waveguide. More precisely, the demonstrated characteristics of a ring QCL with an off-centered grating can be explained by a mode motion in azimuthal, i.e. tangential direction. In this way, the location of the chirp-induced continuous phase shift varies along φ. Time integrating near and far field measurements like in Fig. 3.17 (b) and 3.18 are not capable of detecting such a behavior and the resulting summation over all possible orientations of the mode provides the experimentally measured rotationally symmetric beam profile. The calculation of such a far field is based on a continuous shift of the near field amplitude from Fig. 3.17 in φ-direction. For each shift value the far field is calculated according to the technique introduced in section 3.2. Finally, all calculated far fields are superimposed in order to create the effective far field distribution. The left side of Fig. 3.18 depicts this calculated beam profile for six different shift values evenly distributed between 0° and 180°. Even this rather low number of simulated far field components results in a quite good agreement with the experimental data.

3.6 Matryoshka ring lasers

Spectroscopic investigations of chemical substances often require the utilization of multiple distinct wavelengths. This is crucial especially in order to distinguish between analytes with similar absorption characteristics or even facilitate spectroscopy of several substances at once [152]. Widely tunable emission from QCLs is enabled by broadband active regions [153, 154] in combination with external cavity configurations [155, 156]. However, due to the incorporation of moving mechanical parts, these devices can be unstable, suffer from vibrations and thus provide only a limited applicability for spectroscopic sensing. A different approach to realize multi-wavelength sensing experiments is based on single-mode laser arrays [157]. Typically, several facet emitting DFB QCLs are placed side by side on a single chip. Collimation of the individual laser beams with a single lens leads to a different emission angle for each beam. For most applications with a rather long light propagation path this is not feasible given that the use of only a single small detector is desirable. At this point, beam combining optics become essential. The latter comprises optical components featuring a wavelength dependent deflection of the beam such as diffraction gratings [158, 159], prisms, dichroic mirrors and Dammann gratings [160]. The goal is to combine several laser beams with different frequencies into a single output beam while preserving the beam quality. However, the additional optical elements can limit the performance and increase the size of the entire setup. Therefore, on-chip beam combining is favorable. It has been demonstrated for facet emitting QCLs by consecutively merging neighboring waveguides [161]. This approach provides superposition of light from eight different DFB QCLs and subsequent emission from a single facet. The vertically emitted light from second order DFB ridge QCLs can be collected with a collector waveguide which facilitates emission of multiple wavelengths from a single facet [148].

Arrays of surface emitting ring QCLs [127] in the mid-infrared (MIR) and photonic crystal QCLs [162] in the terahertz (THz), each featuring sixteen individual lasers possessing different optical axes, have already been demonstrated. In order to produce a single output beam with different wavelengths sharing the same optical axis, a concentric arrangement of ring QCLs is proposed and investigated. Such a concentric ring laser array is depicted in Fig. 3.20. It is referred to as *Matryoshka ring QCL array* in dependence on the similarity to the traditional Russian nesting doll. This array consists of six ring QCLs which can be equipped with different DFB grating periods featuring emission at six independent wavelengths. In order to facilitate autonomous operation, each of the lasers possesses its own extended electrical contact. Silicon nitride below the contact stripes prevents shortcuts between different rings. The realization of this concept with equal waveguide widths results in different resistances for the lasers depending on their surface area. In order to provide identical lasing thresholds for all lasers, the waveguide width has to be adapted accordingly. Far field simulations based on the method in section 3.2 were carried out to investigate the beam performance. Figure 3.21 summarizes

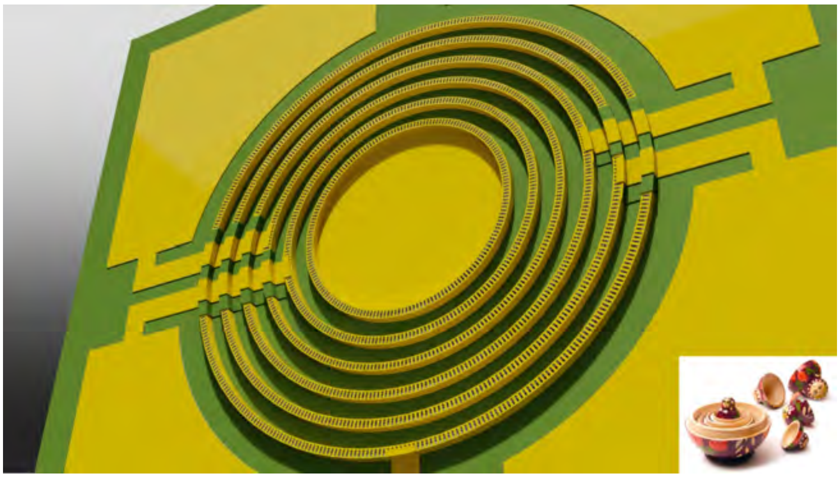

Figure 3.20: Sketch of the Matryoshka ring QCL array consisting of six concentrically aligned ring QCLs. This concept provides six different emission wavelengths confined to the same optical axis which makes beam combining optics obsolete.

the results. The outer diameters of the six rings are equally distributed between 250 μm

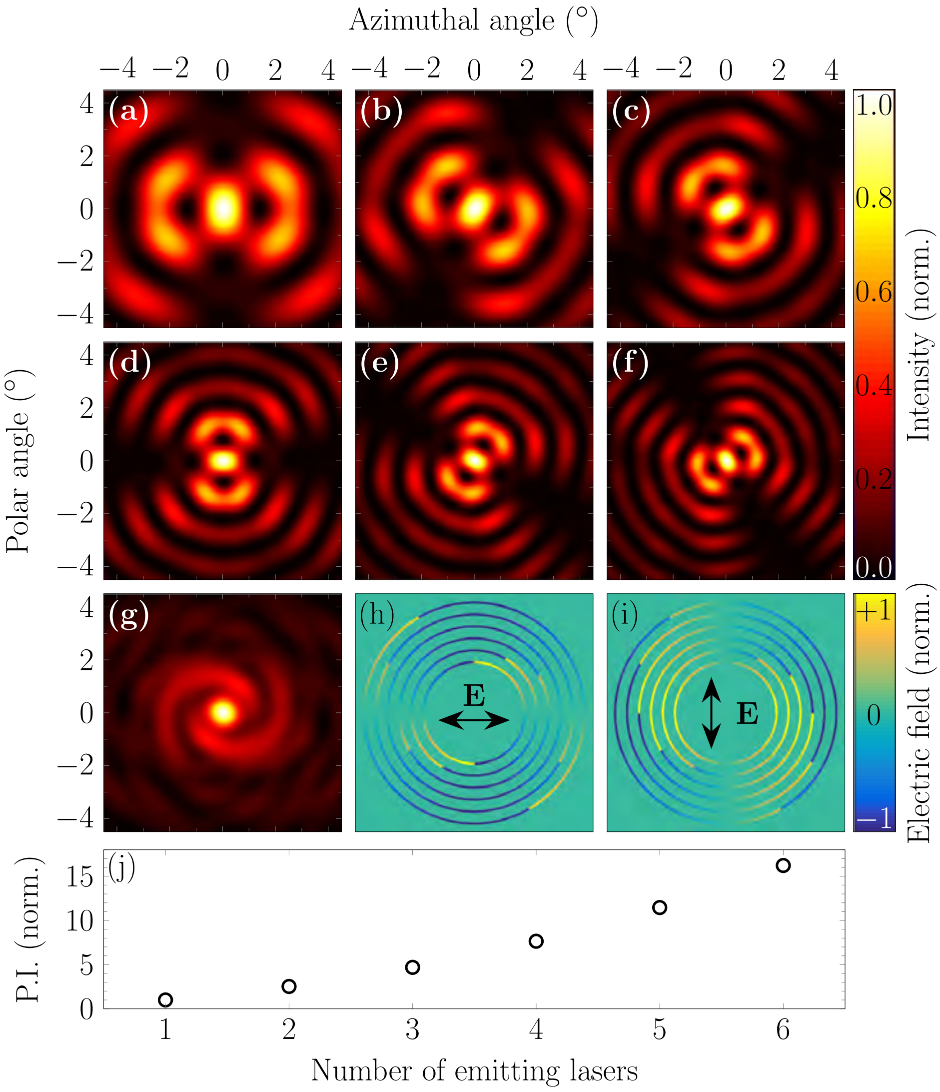

Figure 3.21: Simulated far fields of the Matryoshka ring QCL array from the innermost (a) to the outermost (f) ring. Depending on the ring diameter the far fields exhibit a different fringe separation but share the same optical axis. Furthermore, each ring is equipped with two π phase shifts for the generation of a central intensity maximum. The location of the phase shifts is varying from ring to ring. Incoherent combination of all far fields generates the far field shown in (g). Near field objection functions of the entire array for the horizontal and vertical polarization are provided in (h) and (i), respectively. (j) Power scaling of the central peak intensity (P.I.) as a function of the number of emitting lasers starting with the innermost laser.

and 550 μm. The corresponding far fields, starting with the smallest ring, are provided in Fig. 3.21 (a) - (f). Operating all rings at once provides an incoherent superposition of all emission beams and creates the far field in Fig. 3.21 (g) . π shift ring QCLs as described in section 3.4 were utilized in order to create central intensity maxima. The location of the grating phase shift is different for each ring and illustrated in the near field object functions given in Fig. 3.21 (h) and (i) for the horizontal and vertical polarization component, respectively. Considering the linear polarization of the central far field region, as described in section 3.4, each ring emits a beam with a differently polarized central intensity lobe. The interference fringe separation of the beams depends on the diameter of the ring. The greater the diameter the smaller the fringe separation. Despite this fact, all rings exhibit the same optical axis and especially the central intensity lobes are perfectly overlapping. While for emission angles $|\alpha| > 0.5^\circ$ the dissimilar fringe separation creates a rather blurred intensity distribution, the central part of the beam shows an excellent beam quality with a well defined intensity maximum. The power scaling behavior of this central intensity peak is provided in Fig. 3.21 (j). The relative intensity is plotted as a function of the number of operating rings, starting from the center of the array. This demonstrates that pumping all six rings enables a 16-fold enhancement of the central peak intensity compared to the far field of the innermost ring. Since larger rings provide also more power this power scaling exhibits a non-linear behavior.

3.7 Influence of whispering gallery modes

Sound waves are capable of propagating along a curved interface with a reduced attenuation as discovered by Lord Rayleigh in the late 19th century [163]. More precisely, the intensity of a sound wave clinging to a circular wall decays with the inverse of the distance instead of the inverse square as in air. Hence, whisper between opposite sides of the St. Paul's Cathedral are better heard along the inner wall than along the direct path. This principle can also be applied to light waves [164, 165, 166].

3.7.1 Circular cavities

Light propagation along the inner perimeter of a circular cavity can be supported when the refractive index n_{eff} of the cavity is larger than the refractive index n_s of the surrounding medium. This condition enables total internal reflection and facilitates controlled light propagation. According to Snell's law, total internal reflection, as shown in Fig. 3.22, appears for

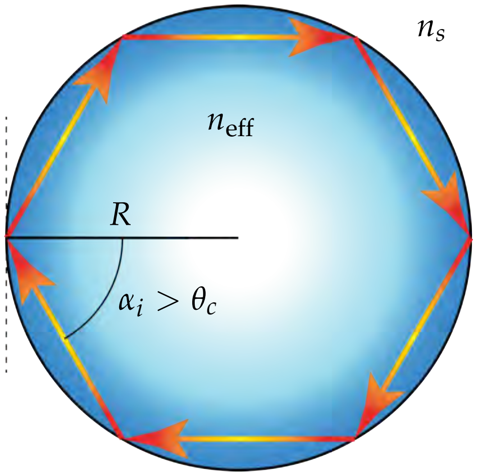

Figure 3.22: Total internal reflection in a circular cavity promoting whispering galley modes (WGMs).

$$\alpha_i > \theta_c = \arcsin\left(\frac{n_s}{n_{\text{eff}}}\right) \tag{3.7.1}$$

with the incidence angle α_i and the critical angle of total internal reflection θ_c. Lasing modes in such a resonator must fulfill the phase-matching round-trip condition. One round-trip length corresponds to an integer number m of wavelengths. The following resonance condition

$$m\frac{\lambda}{n_{\mathrm{eff}}} = 2\pi R \tag{3.7.2}$$

with the radius R can be obtained. Similar as for straight laser ridges in Eq. (2.3.36), the FSR for circular cavities reads

$$\mathrm{FSR} = |\Delta\lambda| = \frac{\lambda^2}{2\pi R n_g + \lambda}. \tag{3.7.3}$$

Compared to straight cavities in Fig. 2.11, whispering gallery modes (WGMs) of circular resonators do not exhibit a symmetric profile along the radial direction with respect to the waveguide center. Figure 3.23 provides an overview of the eigenmodes of a semiconductor ring waveguide. The electromagnetic eigenvalue problem is solved with

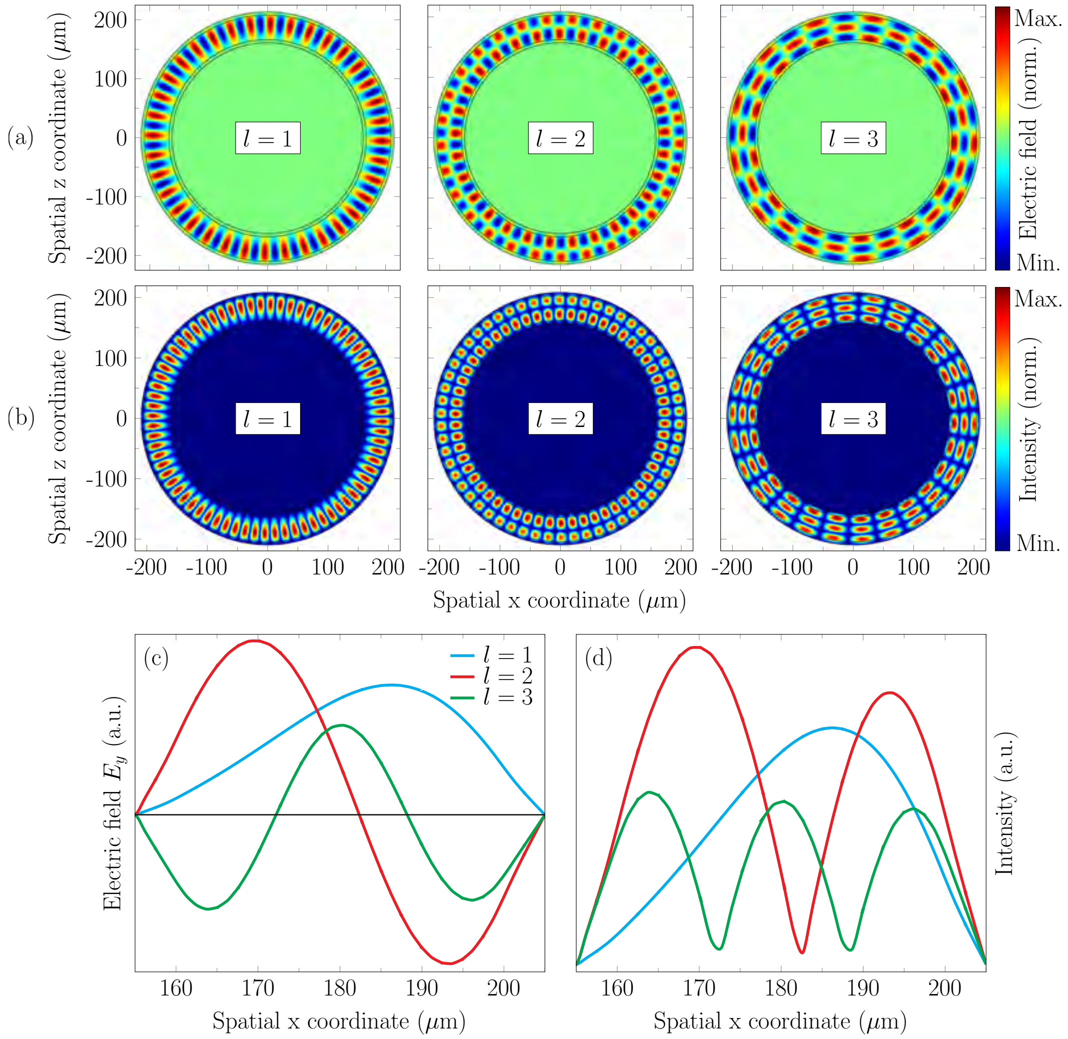

Figure 3.23: COMSOL simulation of WGMs for different order numbers l. (a) and (b) provide two dimensional mode distributions of the electric field and the intensity, respectively. (c) and (d) indicate the corresponding cross sections. The curvature of the waveguide introduces an asymmetry in the mode distribution.

the COMSOL Multiphysics® software [167] by implementing the finite-element-method. Each mode can be characterized by the order numbers m and l, determining the number of lobes in the tangential and radial direction, respectively. Fig. 3.23 (a) provides the out-of-plane electric field vector (E_y) for the three lowest radial order modes ($l = 1, 2, 3$). In Fig. 3.23 (b) the same (m, l) combinations are shown for the intensity of the corresponding modes. In order to investigate the spatial mode profiles, line scans of the electric field and the intensity are provided in Fig. 3.23 (c) and (d), respectively. Evidently, all modes are not symmetric in the radial direction with respect to the center of the waveguide and the fundamental $l = 1$ mode is pushed towards the outer wall of the ring resonator. [44]

For an analytical solution the wave equation from Eq. (2.3.9) can be written in a one-dimensional scalar form in cylindrical coordinates as follows

$$\left(\frac{\partial^2}{\partial r^2} + \frac{1}{r}\frac{\partial}{\partial r} + \frac{1}{r^2}\frac{\partial^2}{\partial \phi^2} + \frac{\partial^2}{\partial y^2} + k^2\right) E_y = 0 \tag{3.7.4}$$

with the azimuthal angle ϕ and the radial coordinate r. Utilization of the separation ansatz

$$E_y(r, \phi, y) = E_y^r(r) e^{\pm im\phi} e^{ik_y y} \tag{3.7.5}$$

yields the radial wave equation

$$\left(\frac{\partial^2}{\partial r^2} + \frac{1}{r}\frac{\partial}{\partial r} - \frac{m^2}{r^2} + q^2\right) E_y^r(r) = 0 \tag{3.7.6}$$

with $q^2 = k^2 - k_y^2$. Solutions of Eq. (3.7.6) are provided by Bessel functions $J_m(qr)$ of the first kind for the interior of the waveguide with $q \in \mathbb{R}$. Outside the waveguide $q \in \mathbb{I}$ and the corresponding solutions are given by modified Bessel functions $K_m(qr)$ of the second kind [168, 169]. An alternative approach describes the transformation of the coordinate system resulting in a straight waveguide [170, 171]. Such a conformal transformation defines

$$u = R_{\text{out}} \ln\left(\frac{r}{R_{\text{out}}}\right) \tag{3.7.7}$$

$$v = R_{\text{out}}\phi \tag{3.7.8}$$

with the outer radius R_{out}. The circular waveguide in (r, ϕ)-space corresponds to a straight one in (u, v)-space. The electric field $E_y(r, \phi, y)$ is equivalent to $F(u, v, y)$. This modifies the wave equation to

$$\left(\frac{\partial^2}{\partial u^2} + \frac{\partial^2}{\partial v^2} + q^2 e^{2u/R_{\text{out}}}\right) F(u, v) = 0 \tag{3.7.9}$$

where u depicts the lateral and v the propagation direction. Hence, the field can be written as $F(u, v) = F_1(u) \cdot F_2(v)$ with $F_2(v) = e^{ik_v v}$. In “radial” u-direction the wave equation reduces to

$$\left(\frac{\partial^2}{\partial u^2} + q^2 e^{2u/R_{\text{out}}} - k_v^2\right) F_1(u) = 0. \tag{3.7.10}$$

In Eq. (3.7.10) the term $q^2 e^{2u/R_{\text{out}}}$ takes the form of a potential in (u, v)-space when comparing this formula to the Schrödinger equation of quantum mechanics. It implies that for circular waveguides the refractive index increases exponentially with radial distance. Equation (3.7.10) can be solved using the WKB method [172] or the transfer matrix approach [173]. Especially for large radii the exponential refractive index gradient can be approximated as a linear function. In turn, this facilitates an analytical solution based on a linear combination of the Airy functions $\text{Ai}(Z)$ and $\text{Bi}(Z)$ with $Z = -(c + d \cdot u - k_v^2)/d^{2/3} \approx -q^2 e^{2u/R_{\text{out}}} + k_v^2$ and c and d being constants [174, 175].

3.7.2 Influence on the emission beam

The asymmetric mode profile of WGMs shown in Fig. 3.23 can have an effect on the outcoupled light. In turn, this effect can be exploited to gain information about the WGMs propagating inside the cavity. In the following the influence of WGMs on the far field of ring QCLs is investigated by means of a modified second order DFB grating. Therefore, the first and second order WGMs in ring QCLs are calculated using the conformal transformation method in combination with a linear approximation of the refractive index as described in section 3.7.1. Mode intensities along the radial coordinate for the first (solid) and second (dashed) order WGM are depicted in Fig. 3.24. The modified DFB grating is based on a dual grating configuration featuring two continuous π phase shifts. Abrupt grating π shifts were discussed in section 3.4. They flip the phase by 180° and create central intensity lobes in the far field of ring QCLs. Continuous π phase shifts are based on the same phase-flipping mechanism but are spread over a large area along the perimeter of the ring. They are realized by means of a dual grating structure as shown in Fig. 3.25 (a). It shows a ring QCL with a dual grating featuring two continuous π shifts. The cutout on the right illustrates the location of the WGM inside the waveguide. There, the inner part of the grating is defined to be π shifted and the outer part is unshifted. On the other side of the ring the situation is reverse. Furthermore, along the azimuthal angle α the dual grating exhibits a continuous ratio R_{cont} between π- and unshifted grating parts. In Fig. 3.25 (b) a SEM image of the dual grating with a balanced ratio is depicted. A descriptive comparison between a conventional (S), an abrupt π shift (A) and a continuous π shift (C) grating along the azimuthal coordinate α is provided in Fig. 3.26 (a). Without loss of generality the blue slits are assumed to be unshifted and the red slits are π shifted. A conventional second order DFB grating features a waveguide mode which has the same phase in every slit. Abrupt π shifts flip the phase for one half of the ring resonator. Consequently, left and right part of the ring in Fig. 3.12, corresponding to the upper and lower part of the

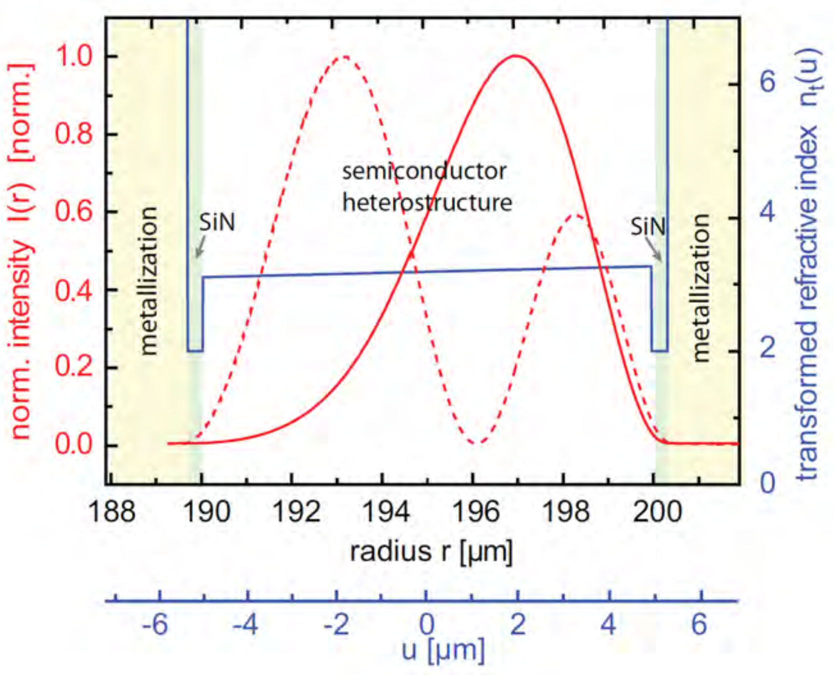

Figure 3.24: Calculated lateral mode distribution for the first (solid) and second (dashed) order radial modes in a ring QCL.
Reprinted with permission from [88]

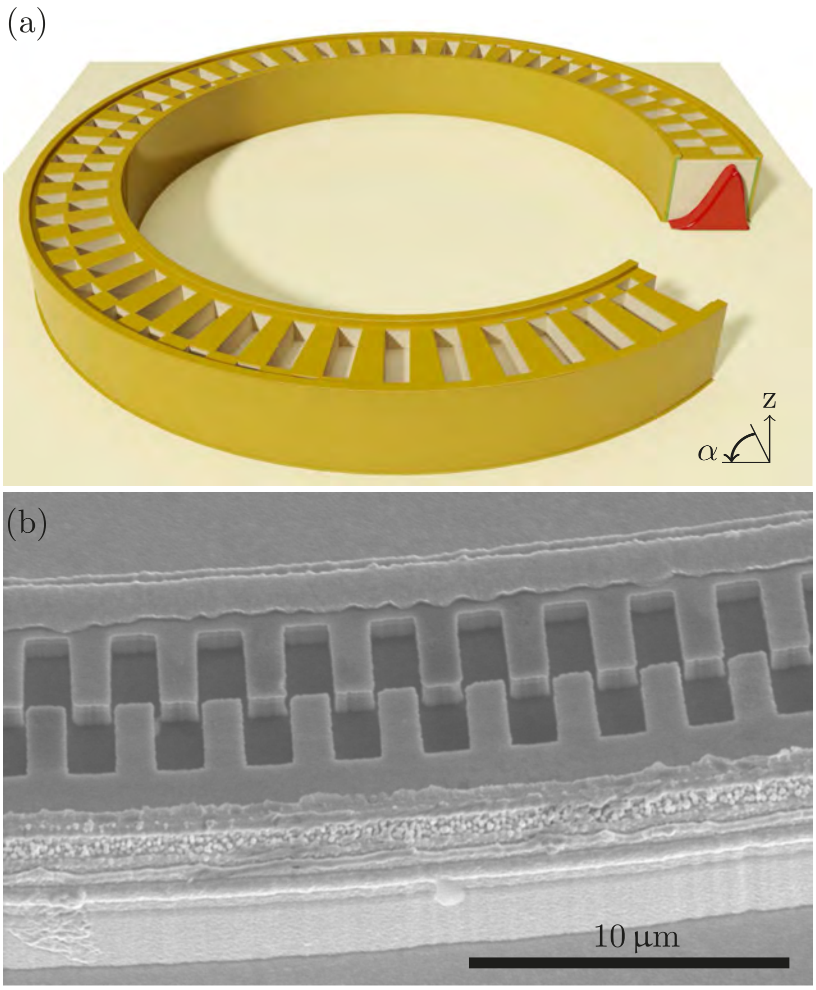

Figure 3.25: (a) Sketch of a ring QCL with a continuous π phase shift in the DFB grating. The latter enables investigations of the WGM (red) inside the laser cavity. (b) SEM image of the dual grating forming the continuous phase shift.
Reprinted with permission from [176]

grating in Fig. 3.26 (a), exhibit a phase difference of π. However, a distinct phase can be assigned to each azimuthal location α on the ring. In the case of the dual continuous π shift grating, this is not the case anymore. In fact, the phase for each α is a linear superposition of π- and unshifted grating components. The corresponding electric field vectors emitted by these grating components exhibit an antiparallel orientation as stated in section 3.4. When these antiparallel field vectors are emitted from opposing sides of the ring laser they interfere destructively in the far field. However, if they are emitted by neighboring slits from the same grating region, they annihilate each other already in the near field. This explains the dark spots in the near field at the location of abrupt grating π shifts. For a continuous π shift it is obvious that a complete annihilation of light occurs only for certain R_{cont} values at specific angles α. In order to identify these parameters a consideration of the WGM inside the waveguide is required. Figure 3.26 (b) illustrates the electric field of the WGM below the dual DFB grating. It is assumed that each grating slit couples out solely that part of the WGM which is located directly below this slit. Due to the asymmetry of WGMs, a balanced grating ratio $R_{\text{cont}} = 0.5$ shows no complete light annihilation but a domination of the outer mode part. Maximum light annihilation occurs when R_{cont} coincides with the center of mass (COM) of the WGM. The latter is defined as the radial distance at which the red and blue areas are equal.

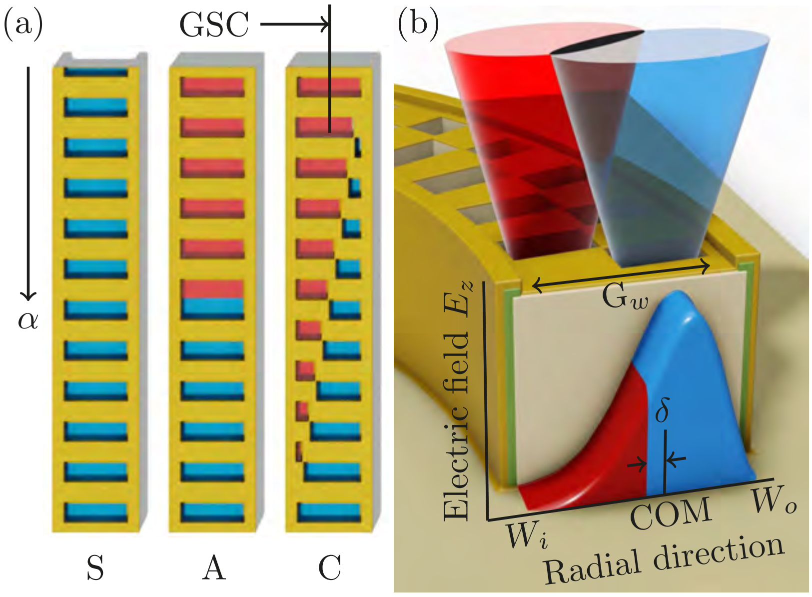

Figure 3.26: (a) Comparison between conventional (S), abrupt π phase shift (A) and continuous π phase shift (C) DFB gratings with the corresponding mode distribution indicated by the colored slits. (b) Working principle of the dual grating. Inner and outer part of the dual grating are phase shifted. Each part couples out this section of the WGM which is located directly below the respective grating element. As a result of the π phase shift, outcoupled light from the inner and outer part of the grating interferes destructively. Due to the asymmetry of the WGM a balanced grating with equal size for the outer and inner grating part does *not* result in total light annihilation but leads to a domination of the outer grating part. Based on this effect the dual grating is designed to enable a quantitative analysis of the location and shape of the WGM.
Reprinted with permission from [176]

From

$$\int_{W_i}^{\mathrm{COM}} E_z(r)dr \overset{!}{=} \int_{\mathrm{COM}}^{W_o} E_z(r)dr \tag{3.7.11}$$

it is clear that the WGM profile $E_z(r)$ determines the COM of the WGM. The locations of maximum light annihilation are depicted in Fig. 3.27 (a) by the black filled circles. Compared to abrupt π phase shifts with the strongest light annihilation at $\alpha = 90°$ and $\alpha = 270°$, they are shifted along the perimeter of the ring by a specific value $\Delta\alpha$. These modifications of the near field intensity pattern induce a rotational shift of the entire emission pattern. Since the locations of strongest light emission remain at $\alpha = 0°$ and $\alpha = 180°$, the total far field rotation is not equal to $\Delta\alpha$. A precise identification of the far field rotation necessitates a rigorous analysis of the spatially dependent near field amplitude. The latter depends on the WGM profile and the local grating ratio R_{cont}. It amounts to

$$E_{\mathrm{NF}}(\alpha) = A_B(\alpha)\sqrt{\alpha_{\mathrm{surf}}^B(\alpha)} - A_R(\alpha)\sqrt{\alpha_{\mathrm{surf}}^R(\alpha)} \tag{3.7.12}$$

with the blue and red areas of the WGM denoted by $A_B(\alpha)$ and $A_R(\alpha)$, respectively. The variables $\alpha_{\mathrm{surf}}^B(\alpha)$ and $\alpha_{\mathrm{surf}}^R(\alpha)$ determine the surface losses of the corresponding grating components. In Fig. 3.27 the electric near field amplitude from Eq. (3.7.12) is shown. In a first approximation the surface losses could be approximated as equal and constant. However, it is found that aspect ratio dependent etching (ARDE) of small slits must be taken into account. It results in an α-dependency of the surface

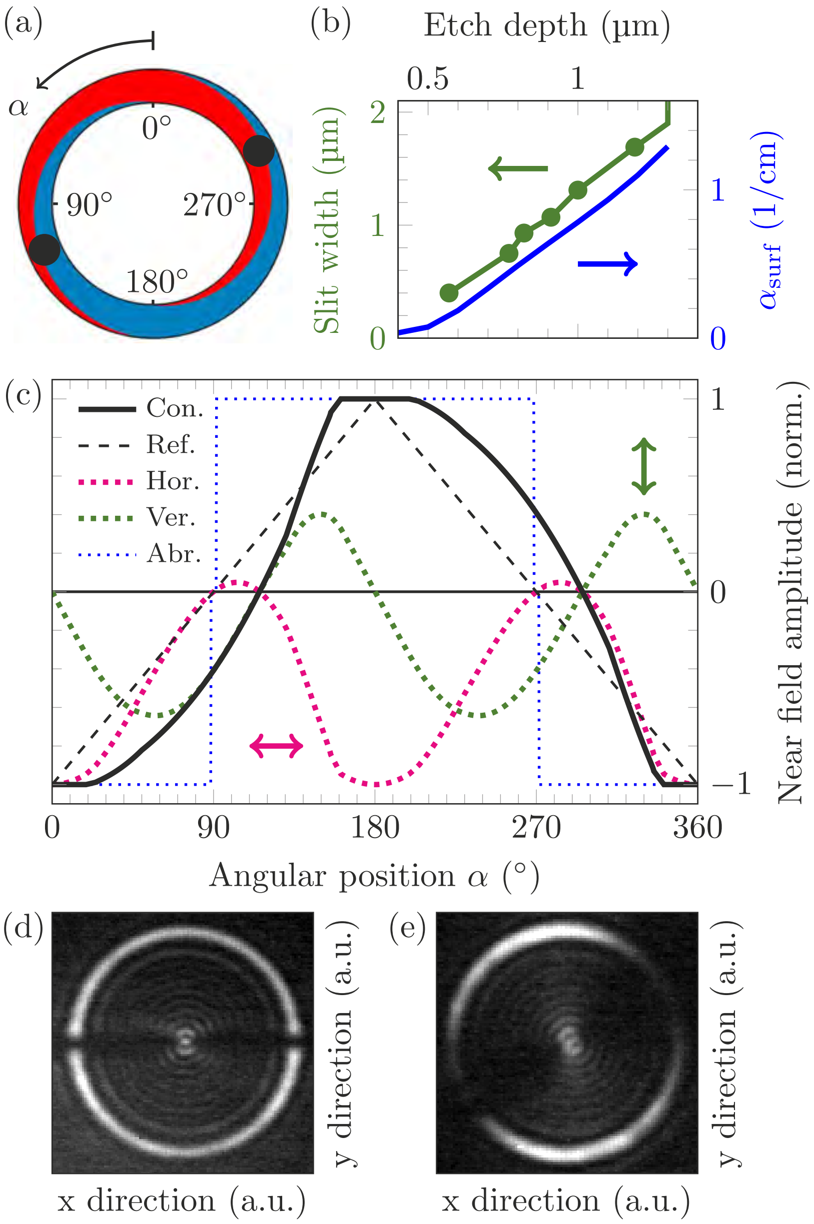

Figure 3.27: (a) Sketch of the dual DFB grating with the unshifted (blue) and π shifted (red) grating parts. (b) Slit width and surface losses as a function of the grating etch depth. (c) Calculated near field amplitudes for a continuous phase shift (black solid, Con.) grating and the corresponding horizontal (magenta dashed, Hor.) and vertical (green dashed, Ver.) polarization components. The hypothetical near field amplitude of a reference continuous phase shift with a centered and symmetric WGM is given by the black dashed line (Ref.). This illustrates that the asymmetry of the WGM induces a deviation from the linear to a curved behavior of the near field amplitude. For comparison the corresponding amplitude of an abrupt phase shift is given by the blue dotted line (Abr.). Measured near fields of an abrupt (d) and a continuous (e) π phase shift ring QCL confirm the theoretical near field amplitudes.
Reprinted with permission from [176]

losses. Figure 3.27 (b) demonstrates that in the given range from 0.5 μm - 1.4 μm the surface losses increase linearly with the etch depth. In addition the radial slit width depends linearly on the etch depth as well. Assuming constant total losses α_{tot} along the ring implies a linear dependency of the optical output power $P = \alpha_{\mathrm{surf}}/\alpha_{\mathrm{tot}}$ on the surface losses. Thus, the electric near field amplitude correlates with the square root of the corresponding surface losses and amounts to the expression in Eq. (3.7.12) which is represented in Fig. 3.27 (c) by the black solid line. Near field amplitudes for the horizontal and vertical polarization components amount to $E_{\mathrm{NF}}\cos(\alpha)$ and $E_{\mathrm{NF}}\sin(\alpha)$, respectively. In addition Fig. 3.27 (a) features theoretical near field amplitudes of an abrupt π shift represented by the blue dotted line. It possesses abrupt transitions from ± 1 to ∓ 1 at the phase shifts. This is also evident in the experimentally determined near fields of abrupt and continuous π shifts in Fig. 3.27 (d) and (e), respectively. Abrupt π phase shift ring QCLs exhibit clear grating phase shifts indicated by dark areas in the near field. In contrast, continuous π phase shifts feature a fade-out of the intensity. The curved shape of $E_{\mathrm{NF}}(\alpha)$ is directly caused by the asymmetry of the WGM. On the one hand it is modified by the α-dependent surface losses originating from aspect ratio dependent etching. On the other hand the flat parts at $0° \pm 19°$ and $180° \pm 19°$ occur due to shifted onsets of the dual grating region which can be attributed to the disappearance of the small slits in these areas during fabrication. Hence, the surface losses for the unshifted blue slits are composed of the following components

$$\alpha^{B}_{\mathrm{surf}}(\alpha) \quad = \quad \alpha^{B}_{\mathrm{surf},0}\cdot\begin{cases} 0, & \text{if } -\beta < \alpha < +\beta \\ \frac{\alpha-\beta}{\gamma-\beta}, & \text{if } +\beta < \alpha < +\gamma \\ 1, & \text{if } +\gamma < \alpha < -\gamma \\ \frac{\alpha+\beta}{\gamma+\beta}, & \text{if } -\gamma < \alpha < -\beta. \end{cases} \tag{3.7.13}$$

In a similar fashion the surface losses of the π shifted red slits amount to

$$\alpha^{R}_{\mathrm{surf}}(\alpha) \quad = \quad \alpha^{R}_{\mathrm{surf},0}\cdot\begin{cases} 0, & \text{if } 180° - \beta < \alpha < 180° + \beta \\ \frac{\alpha-\beta}{\gamma-\beta}, & \text{if } 180° + \beta < \alpha < 180° + \gamma \\ 1, & \text{if } 180° + \gamma < \alpha < 180° - \gamma \\ \frac{\alpha+\beta}{\gamma+\beta}, & \text{if } 180° - \gamma < \alpha < 180° - \beta. \end{cases} \tag{3.7.14}$$

The angles β and γ mark the transitions to the dual grating region and the onset of the influence of ARDE, respectively. For the used ring QCL these values are $\beta = 19.0°$ and $\gamma = 49.7°$. Applying Eq. (3.7.13) and (3.7.14) to Eq. (3.7.12) provides the α-dependent near field amplitude. The corresponding WGM areas $A_B(\alpha)$ and $A_R(\alpha)$ are numerically extracted from the shape of the WGM and the α-dependent locations of the blue and red grating slits. The calculated near field amplitude shows certain similarities to chirped gratings [130]. For the latter a slow variation of the grating periodicity in straight DFB lasers shifts the near field intensity towards the center of the device. This directs more light into one of the two far field lobes and creates an off-center single lobe emission beam. In contrast, the presented dual grating approach is not based on an alteration of the grating period but facilitates a continuous variation of the ratio between π and unshifted grating elements. As demonstrated in the corresponding far field patterns, this approach provides a central intensity maximum in terms of a local decrease of the near field amplitude in combination with π phase shifts at the locations of strongest light annihilation. For a straight second order chirped DFB laser a reversal of the grating chirp shifts the intensity into the other of the two far field lobes [130]. In the case of dual grating ring QCLs, inverting the grating geometry changes the rotation direction of the far field.

Such a rotated far field is shown in Fig. 3.28 (a). The central intensity maximum is part of the symmetric pattern with a counter clockwise rotated symmetry axis. This rotation originates from the dual grating and is not due to a rotation of the entire chip as demonstrated by the inset showing an abrupt π shift laser on the same chip.

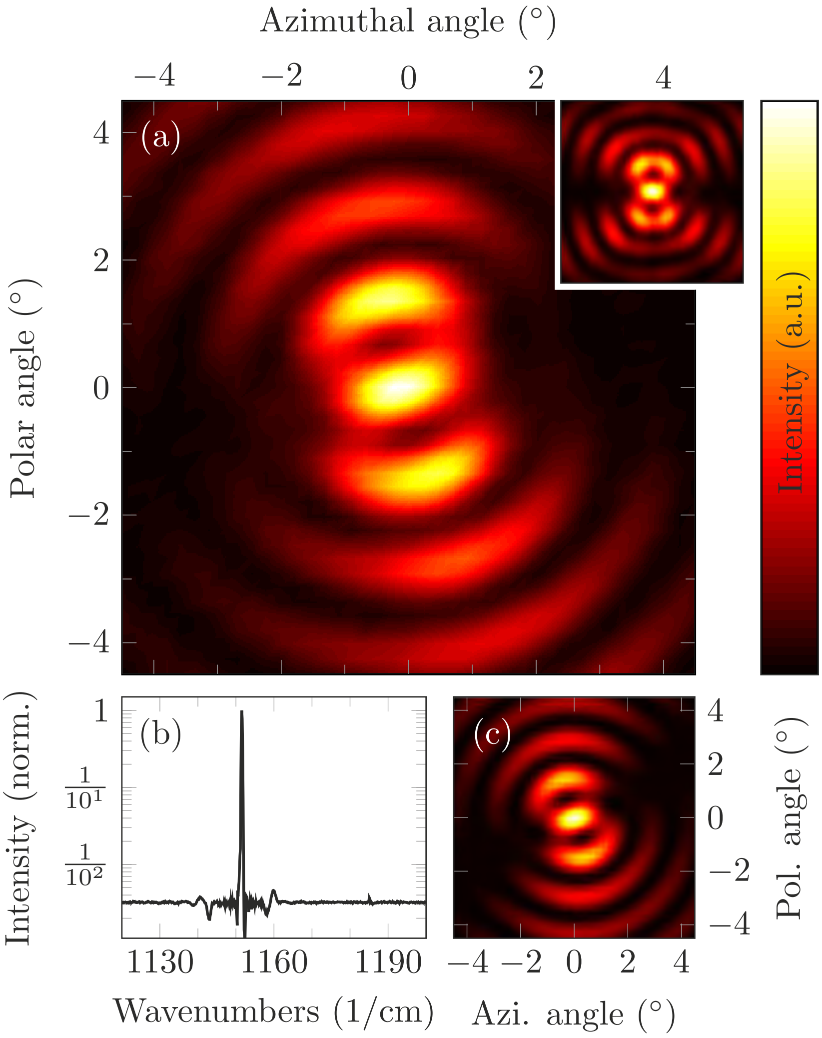

Figure 3.28: (a) Measured far field of a continuous phase shift ring QCL with a central intensity maximum. The locations of strongest light annihilation are circularly shifted compared to the abrupt phase shift shown in the inset. (b) The single mode spectrum verifies the formation of the far field due to one mode only. (c) Simulated far field based on the near field amplitude provided in Fig. 3.27 (c).
Reprinted with permission from [176]

Furthermore, the single mode spectrum in Fig. 3.28 (b) indicates that the displayed emission beam is produced by solely one mode in the waveguide. A comparison of the polarization purity $P = 10\log\left(p_{\parallel}/p_{\perp}\right)$ in both far fields yields values of $P_c = 1.67\,\mathrm{dB}$ and $P_a = -0.97\,\mathrm{dB}$ for the continuous and abrupt π shift, respectively. That is, the entire far field of the former emits more light polarized parallel to the polarization $p_{\parallel}$ of the central lobe. The rotated symmetry axis originates from the shifted near field pattern caused by the asymmetry of the WGM. Equation (3.7.12) defines the near field object function. The corresponding far field is calculated based on the two dimensional Fourier transform from section 3.2 and shown in Fig. 3.28 (c). Experimental and simulated far fields for the horizontal and vertical polarization components are provided in Fig. 3.29. An overall good agreement between simulation and experiment is found. In order to quantitatively determine the rotation of the experimental far field a reference far field was utilized. The near field amplitude of this reference far field is provided in Fig. 3.27 (a) by the black dashed line. It represents the values of $E_{\mathrm{NF}}(\alpha)$ for the same dual DFB structure but with a centered and symmetric mode profile. In this case the points of

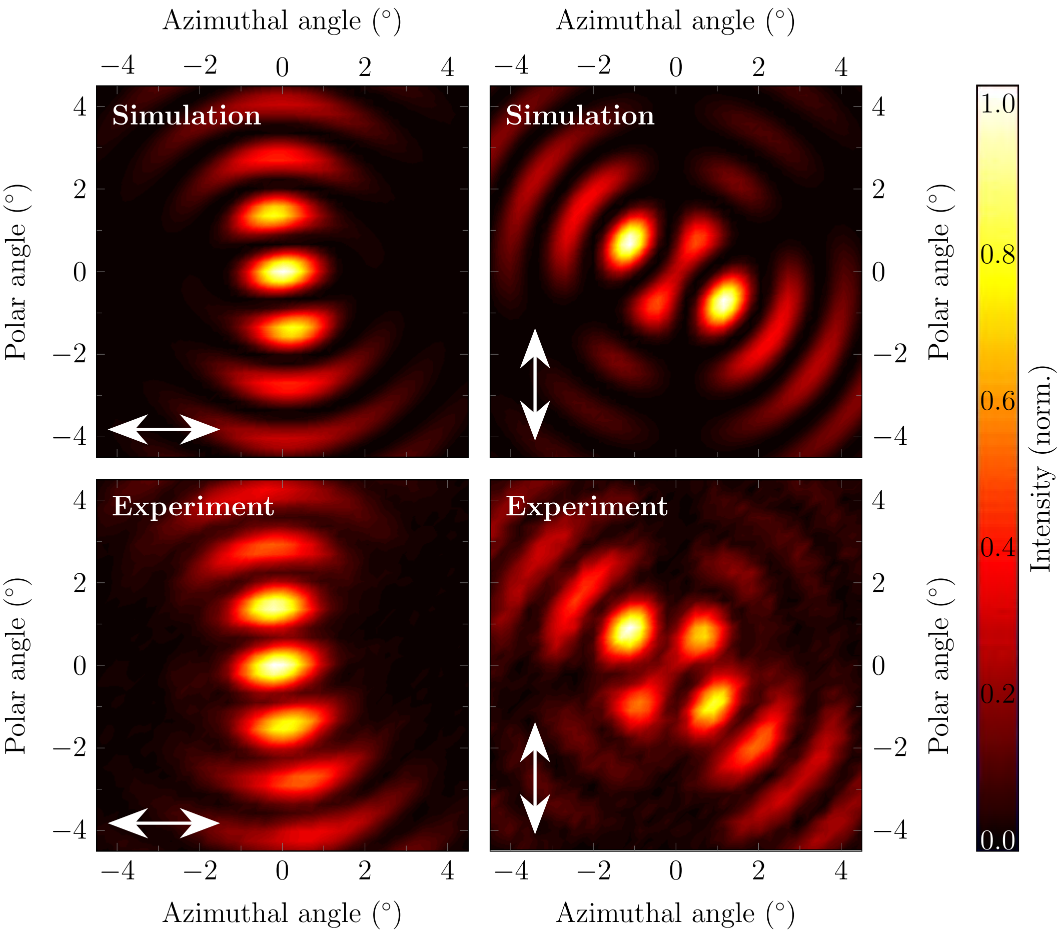

Figure 3.29: Horizontally (left column) and vertically (right column) polarized far field components of the calculated (top row) and measured (bottom row) emission beams in Fig. 3.28. The good agreement for both components supports the implemented theoretical approach to describe continuous phase shift lasers.

strongest light annihilation are congruent with the dark spots at the abrupt π shifts. The only difference is the dual grating structure producing a fade-out of the intensity towards the points of strongest light annihilation instead of an abrupt intensity drop. Hence, this calculated reference far field can be used to obtain the rotation of the experimental beam pattern. The former is rotated around the center point of the far field while for each rotation angle the two dimensional correlation coefficient with the experimental far field is calculated. This function is illustrated in Fig. 3.30 (a) by the solid curve. The angle at the maximum of this correlation coefficient indicates the rotation of the entire beam. For the laser beam shown in Fig. 3.28 (a) the red sinusoidal fit yields a rotation of the experimental far field of 13.9°. By using the same method but calculating the correlation coefficient between the reference and the theoretical far field in Fig. 3.28 (c), the rotation of the latter can be evaluated. It amounts to 15.0° which suggests an error between experimental and simulated far field of 1.1°. In the same manner a total number of 7 lasers were investigated. The corresponding grating parameters are displayed in Tab. 3.1. Rotation angles of the corresponding experimental and theoretical far fields are depicted in Fig. 3.30 (b). A linear relation between the far field tilt and the parameter

$$\delta = \mathrm{COM} - \mathrm{GSC} \tag{3.7.15}$$

is evident. It describes the spatial distance between the COM of the WGM and the

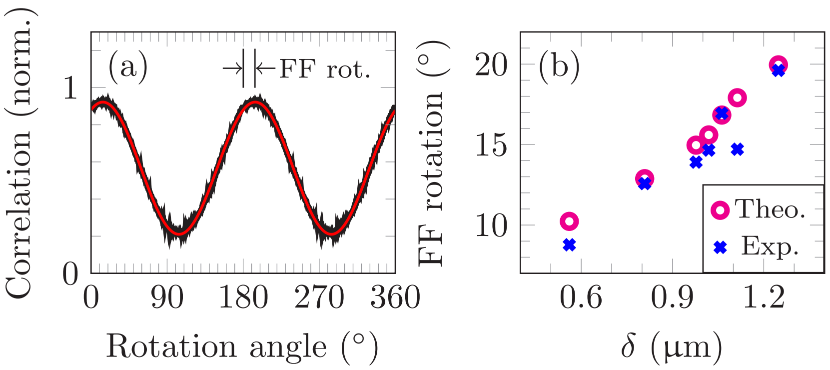

Figure 3.30: (a) Correlation function between the measured and the revolving reference far field. The latter is calculated based on the amplitude function given by the black dashed curve in Fig. 3.27 (c). The sinusoidal fit determines the rotation of the far field. (b) Far field rotation of the calculated (magenta circles) and experimentally obtained (blue crosses) laser beams as a function of the parameter δ denoting the spatial distance between center of mass (COM) of the WGM and the grating slit center (GSC) according to Fig. 3.26 (a).
Reprinted with permission from [176]

Laser	W_i	W_o	G_w	GSC	COM	δ
1	189	201	4.4	194.90	195.46	0.56
2	189	201	5.2	194.68	195.49	0.81
3	189	202	5.6	195.22	196.20	0.98
4	189	202	5.6	195.09	196.11	1.02
5	189	202	5.7	194.95	196.01	1.06
6	189	203	5.4	195.23	196.34	1.11
7	189	203	5.6	194.63	195.88	1.25

Table 3.1: Geometrical laser parameters in µm as described in Fig. 3.26. Inner and outer waveguide radii are given by W_i and W_o, respectively. The grating width is G_w and δ is defined as the spatial distance between the COM of the WGM and the GSC.
Reprinted with permission from [176]

grating slit center (GSC) as indicated in Fig. 3.26 (a). Hence, the location of the WGM relative to the grating determines the far field tilt. A linear fit yields an inverse slope of (67 ± 5) nm/° for the experimental and (62 ± 4)nm/° for the theoretical dataset.

In the course of laser beam characterization, several far fields showed a clockwise rotation. An example is provided in Fig. 3.31. At first glance, this behavior is counterintuitive since most of the light seems to originate from the locations of strongest light annihilation as illustrated in Fig. 3.26 (a). Verification of the laser spectrum in Fig. 3.31 (b) provides a suitable explanation. It consists of two distinct peaks at 1150/cm and 1180/cm. Polarization dependent spectra were recorded in order to connect the dual mode emission spectrum with the clockwise rotation of the far field. As demonstrated in section 3.2 the emitted polarization of a ring QCL is tangential. Figure 3.31 (c) denotes the height of both spectral peaks for different orientations of an external wire grid polarizer placed between laser and spectrometer. In combination with the assumption of tangential polarization, the peak height for each orientation of the polarizer can be related to the emitted near field intensity for a specific location on the ring. Thus, the emission characteristics can be extracted for both modes separately. It is found that

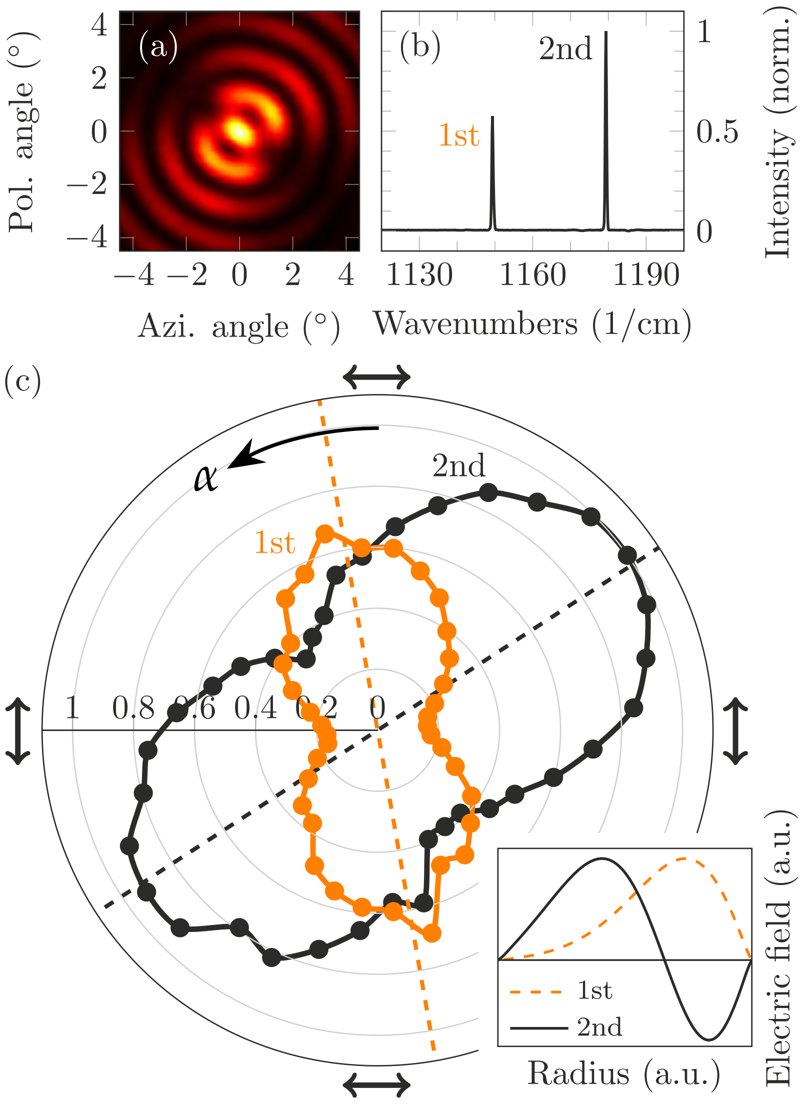

Figure 3.31: (a) Measured far field of a continuous π phase shift ring QCL exhibiting a counterintuitive clockwise rotation of the far field. (b) Spectral investigations demonstrate two emission modes roughly 30 /cm apart. (c) Polarization dependent spectra indicate that the mode at 1150 /cm produces a counterclockwise far field rotation while the second mode at 1180 /cm leads to the clockwise rotation. Hence, the spectral peaks at 1150 /cm and 1180 /cm can be attributed to the first and second order radial WGMs.
Reprinted with permission from [176]

the mode at 1150/cm features a counter clockwise rotated emission beam as previously discussed. However, the mode at 1180/cm clearly possesses a far field with a clockwise rotation. This suggests that the latter is generated by a second order radial WGM as depicted in the inset of Fig. 3.31 (c). The key point is the change of the polarity of the electric field along the radial coordinate for the second order WGM. When the grating ratio R_{cont} coincides with the zero crossing of the electric field of the second order WGM, the grating π shift cancels out the inverse polarities and facilitates constructive interference and maximum light emission at $\alpha \approx 123.5°$ indicated by the black dashed line in Fig. 3.31 (c). At around $\alpha \approx 45°$ the far field emitted by the second order WGM shows the lowest intensity. There, the electric field can be divided into three sections. The first section in radial direction has a positive electric field and the corresponding grating is unshifted. In the second section the grating is π shifted and the electric field is still positive. The third section features a negative electric field with a π shifted grating.

Hence, only the first and the third section are in phase and around $\alpha \approx 45°$ their areas equal the area of the second section which provides maximum light attenuation. In contrast, the brightest areas of the first order WGM are located at $\alpha \approx 10.1°$ as indicated by the orange dashed line. The measured far field in Fig. 3.31 (a) is a superposition of the first and second order far fields. [176]

The presented dual DFB grating approach incorporating continuous π phase shifts facilitates a connection between the WGM inside the waveguide and the emission beam of the ring laser. This technique is not limited to quantum cascade lasers but can be applied to all vertically emitting grating coupled high-index lasers. It is found that the rotation angle of the emitted far field describes the location of the WGM relative to the DFB grating and the rotation direction depicts the order of the WGM.

3.8 Linearly polarized far field

PREVIOUS sections predominantly deal with DFB grating modifications and the accompanying beam transformations. In section 3.1 the ability of ring QCLs to provide surface and substrate emission is discussed. The corresponding emission beams do not show any significant difference, i.e. the beam emitted through the substrate is basically identical with the surface beam. The results presented in sections 3.3 to 3.7 are valid for both emission directions. However, most of them depict the surface beam. In the following sections 3.8 to 3.10 the substrate beam is investigated. Several modifications of the substrate enable selective and systematic variations of the emission beam. In order to influence the light emitted towards the substrate, designed structures are deposited or etched into the bottom side of the laser chip.

As discussed in section 3.2 and 3.3, the natural polarization state in ring QCLs is tangential. Due to their rotational symmetry the contribution from the horizontal and vertical polarization component is identical. For π phase shifts it was found that the polarization component perpendicular to the polarization of the central lobe is slightly stronger for the entire emission beam. Nevertheless, all ring QCLs investigated in the previous sections exhibit significant light emission for all polarization components. Several applications, however, demand a linearly polarized beam with solely one distinct polarization direction. Due to the intersubband selection rule, discussed in section 2.2.3, edge emitting QCLs possess an inherent linear polarization but suffer from a rather large beam divergence as illustrated in Fig. 3.9 (b). In contrast, ring QCLs exhibit a collimated far field but contain all polarization components. A metallic on-chip wire grid polarizer, fabricated directly on the substrate of the QCL chip as sketched in Fig. 3.32 (a), can be utilized in order to create a linearly polarized and at the same time strongly collimated laser beam. The metallic wires are defined by electron beam lithography and are oriented along the horizontal x-direction. They consist of a 120 nm thick gold layer on top of a 15 nm thick titanium adhesion layer and have a width of 500 nm with a period of 1 μm resulting in a duty cycle of 50%. In this configuration the on-chip polarizer is transparent for light with the electric field vector oriented along the vertical y-direction and absorbs horizontally polarized light. The laser on the upper side of the semiconductor chip incorporates two π phase shifts in the DFB grating. This creates a linearly polarized central lobe in the far field. The on-chip polarizer extends this polarization characteristic to the entire beam by filtering out the horizontal component. In order to

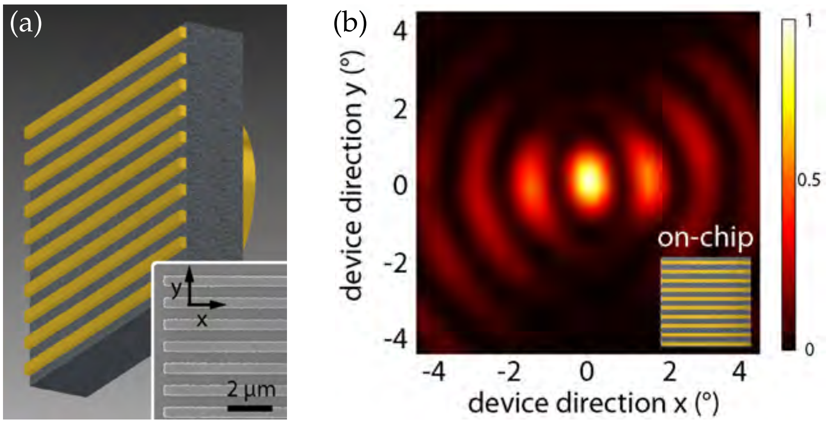

Figure 3.32: (a) Sketch of the on-chip polarizer. The inset shows the corresponding SEM image. (b) Obtained far field consisting mainly of the vertical polarization component.
Reprinted with permission from [149]

provide an adequate overlap between the emission beam and the on-chip polarizer, the latter is located on the substrate side utilizing a SEM and the corresponding coordinates of the ring laser on the surface side with respect to an edge of the chip. The resulting emission beam is provided in Fig. 3.32 (b). It depicts the far field interference fringes predominantly formed by the vertical polarization components emitted from the left and right side of the ring. An evaluation of the conducted efficiency study is described in Tab. 3.2. The corresponding far fields are indicated in Fig. 3.33. The upper row shows

Peak intensity			
Substrate	No polarizer	Horizontal polarization	Vertical polarization
Blank	100%	53%	64%
On-chip polarizer	60%	2%	47%
Total intensity			
Substrate	No polarizer	Horizontal polarization	Vertical polarization
Blank	100%	48%	33%
On-chip polarizer	28%	2%	21%

Table 3.2: Polarization dependent peak and total intensities of the substrate emitted light for a ring QCL with a blank substrate and a substrate with an on-chip wire grid polarizer.

the substrate emitted far fields of a π shift ring QCL with a blank substrate. These far fields are measured without (left) and with an *external* wire grid polarizer transmitting the horizontal (center) and vertical (right) polarization component. They are equivalent to the far fields in Fig. 3.14. With the on-chip polarizer directly fabricated on the bottom side of the very same device, the respective far fields in the lower row were obtained. Each far field is normalized to 1 for the sake of clarity. On the bottom right of each far field the orientation of the on-chip wire grid polarizer is shown. The white arrows indicate the polarization component transmitted by the *external* polarizer. In correspondence with Tab. 3.2 the peak and total intensity of the far field measured without external and on-chip polarizer is set to 100%. Prior to the fabrication of the on-chip polarizer the peak and total intensity of the respective polarization components amount to 53% and 48% for the horizontal polarization and to 64% and 33% for the vertical polarization. The different behavior for both components can be attributed to

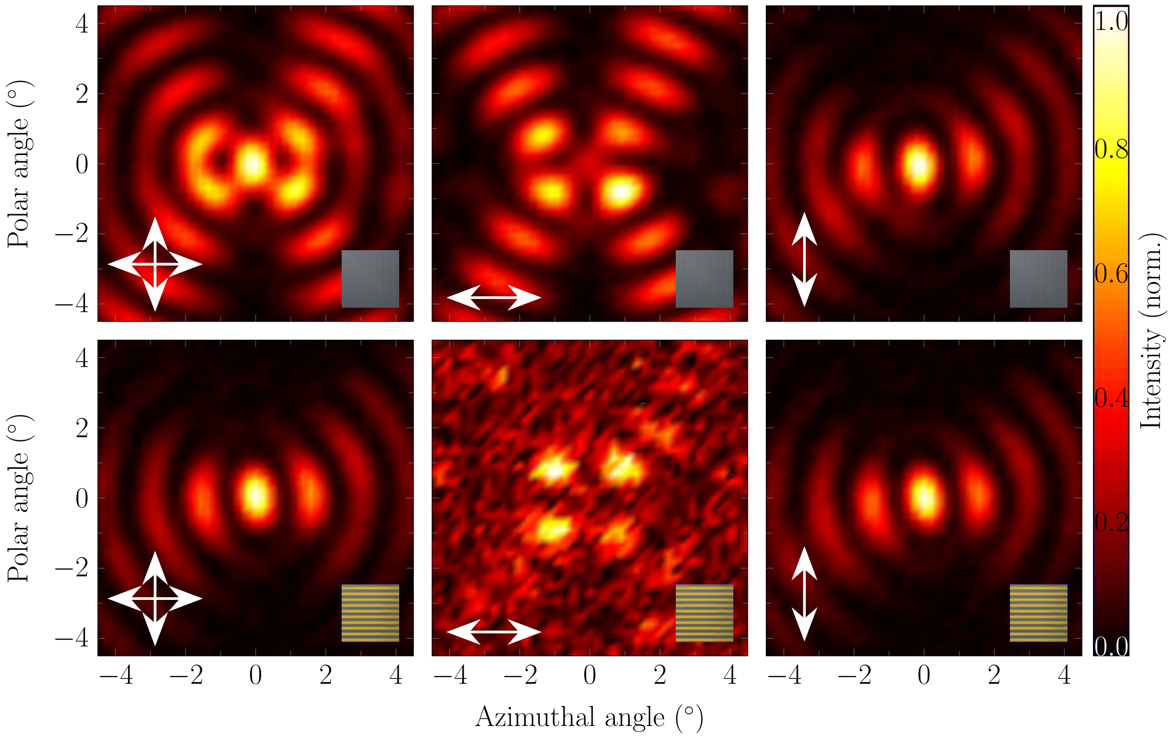

Figure 3.33: Measured far fields of a π shift ring QCL before (top row) and after (bottom row) fabrication of the on-chip polarizer. The white arrows denote the polarization components transmitted through an external polarizer placed in front of the MCT detector.

the fact that the entire far field exhibits more horizontal polarization whereas the central peak shows an excess of vertical polarization. Similar results were obtained for the same laser with an on-chip polarizer fabricated onto the substrate. In order to compare the efficiency of external and on-chip polarizer the percentages of the transmitted light intensity for the vertically polarized blank substrate and for the unpolarized on-chip polarizer have to be considered. For the peak intensity these values read 64% and 60%, respectively. The same values for the entire far field are 33% and 28%, respectively. According to these numbers the on-chip polarizer shows almost the same performance as the external wire grid polarizer for both the central peak as well as the entire laser beam. Thus, this on-chip polarizer facilitates a replacement of bulky external polarizers, resulting in a drastic size reduction of potential sensing setups. [149]

3.9 On-chip light collimation

Plenty of applications in optics require as much light as possible in the center of the laser beam with a preferably small beam divergence. Instead of gold wires for polarizing purposes, other structures can be fabricated on or into the substrate side of the chip in order to modify the emission beam of ring QCLs. The latter impress with their collimated beam profile. However, due to their circular emitting area, interference between opposing sides of the ring create interference fringes in the far field. A significant amount of power is directed into interference fringes emitted under larger angles. In order to reduce these off-axis components of the light beam, a narrower envelope function is beneficial. According to section 3.2 this can be realized by increasing the width of waveguide. However, this will not only increase the total power consumption but also the threshold current. Therefore, other approaches for a further collimation of the emission beam of ring QCLs are desirable.

3.9.1 Focusing metasubstrate

In the following the design and realization of a flat dielectric on-chip lens is presented. It is based on sub-wavelength holes etched directly into the substrate forming a gradient refractive index metamaterial for the collimation of light. Since this metamaterial is directly fabricated into the substrate, it is referred to as metasubstrate. The latter is implemented for conventional and π phase shift ring QCLs. Figure 3.34 (a) depicts a sketch of the surface (left) and substrate (right) side of the laser chip. The former exemplary shows a π shift ring QCL and the gradient index metasubstrate is located directly below this laser on the other side of the chip. The working principle of this collimation element is illustrated in Fig. 3.34 (b). It shows a sketch of the cross section of the laser substrate. Its location is indicated by the black line in the inset which shows a sketch of the bottom view of the laser chip. From the ring waveguide on the surface side on the right the emitted light forms a spherical wavefront indicated by the blue dashed arcs. Two exemplary light rays emitted under angles α and $\alpha = 0°$ are sketched, whereby the former perceives a longer optical path. The fundamental concept of the metasubstrate is that light rays emitted under different angles cover the *same* optical path in the substrate and metasubstrate *combined*. Thus, path differences within the substrate are compensated in the metasubstrate. This flattens the wavefront and makes the area of the metasubstrate the emitting area of the beam. From this point onwards, spherical wavefronts emerge according to the Huygens-Fresnel principle. Due to the increased emitting area the laser beam exhibits a smaller divergence of the far field's envelope compared to the initial beam of the laser. From geometrical considerations it is clear that identical optical path lengths, which provide the flattening of the wavefront, require

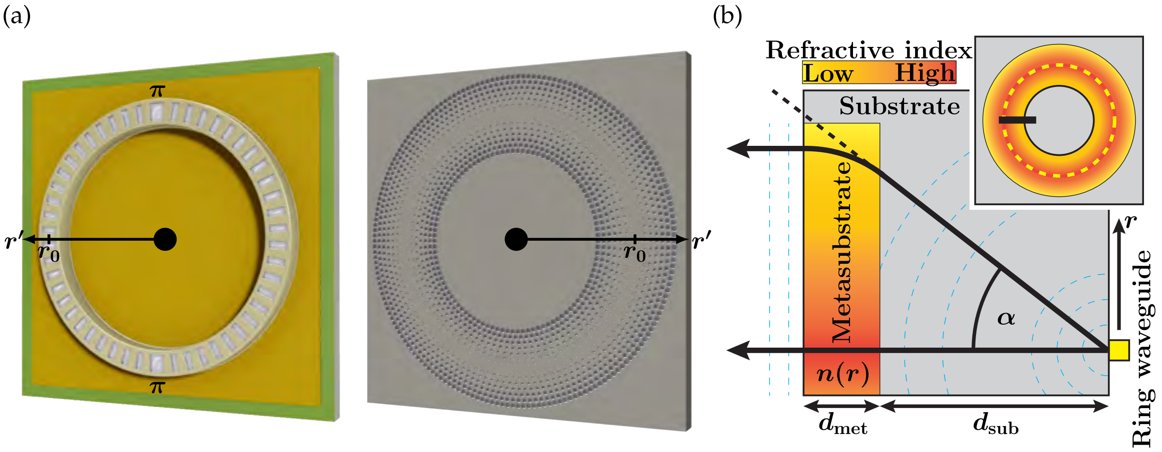

Figure 3.34: (a) Sketch of the ring laser (left) on the surface of the chip and the metasubstrate (right) fabricated directly below the laser on the other side of the semiconductor chip. (b) Working principle of the metasubstrate. The compensation of the longer optical path lengths of rays emitted under larger angles α flattens the wavefront and makes the entire metasubstrate the emitting area.
Reprinted with permission from [150, 177]

$$n_0\left(d_{\text{sub}} + d_{\text{met}}\right) \overset{!}{=} s(\alpha)n_0 + m(\alpha)n(r) \tag{3.9.1}$$

with the refractive index $n_0 = 3.06$ of the InP substrate [178], the substrate thickness d_{sub} and the thickness of the metasubstrate d_{met}. The parameters $s(\alpha)$ and $m(\alpha)$ are the angle dependent path lengths in the substrate and metasubstrate, respectively. The desired function of the refractive index is given by $n(r)$. Based on geometric and trigonometric basic knowledge in combination with Snell's law $s(\alpha)$ and $m(\alpha)$ can be rewritten such that Eq. (3.9.1) yields

$$n_0\left(d_{\text{sub}} + d_{\text{met}}\right) \overset{!}{=} n_0\sqrt{d_{\text{sub}}^2 + r^2} + \arcsin\left(\frac{n_0 r}{n(r)\sqrt{d_{\text{sub}}^2 + r^2}}\right) n(r). \tag{3.9.2}$$

This is a non-trivial equation with a numerical solution only. Nonetheless, for small metasubstrate thicknesses $d_{\text{met}} \ll d_{\text{sub}}$ and small angles α, the light path within the metamaterial can be approximated by $m(\alpha) \approx d_{\text{met}}$. This simplifies Eq. (3.9.2) and provides the following expression for the required refractive index

$$n(r) = n_0\left(1 + \frac{d_{\text{sub}}}{d_{\text{met}}} - \frac{\sqrt{d_{\text{sub}}^2 + r^2}}{d_{\text{met}}}\right) \tag{3.9.3}$$

as a function of the radial coordinate $r = r' - r_0$ with r_0 being the radius of the waveguide center as shown in Fig. 3.34 (a). Equation (3.9.3) demonstrates that the only variable parameter is the thickness d_{met} of the metasubstrate. The latter is defined by the etch depth of the holes. For a specific etch depth the refractive index gradient is immutable. Figure 3.35 presents the refractive index gradient from Eq. (3.9.3) for different etch depths ranging from $1\,\mu$m to $6\,\mu$m. It is striking that the etch depth determines the radial width and therefore the size of the metasubstrate. Since refractive indices below 1 are not feasible, the width of the metasubstrate for each etch depth is given by the radial distance w between the points where $r(-w/2) = r(+w/2) = 1$. As a consequence the

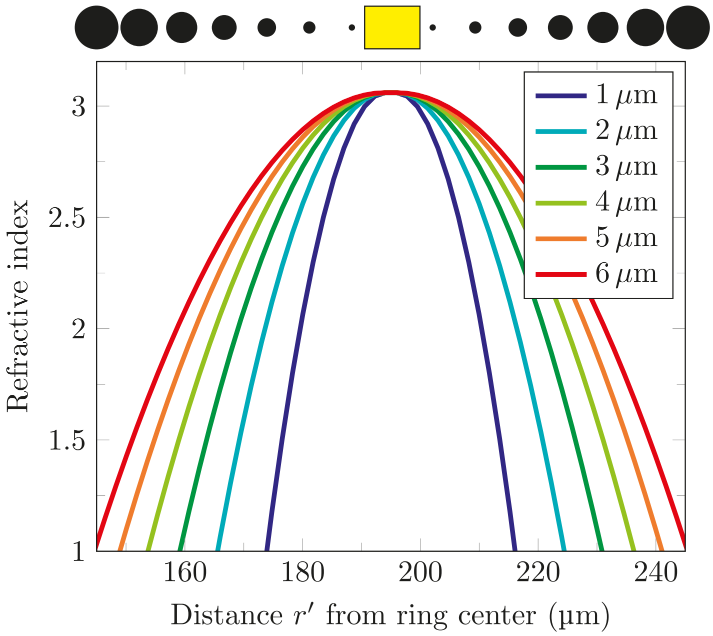

Figure 3.35: Refractive index gradient for different etch depths from $1\,\mu$m to $6\,\mu$m. A deeper etch depth provides a larger metasubstrate area which in turn is capable of collecting and collimating more light. The size of the metasubstrate is mainly limited by total internal reflection at the semiconductor-air interface.
Reprinted with permission from [150]

etch depth directly correlates with the size of the metasubstrate and therefore also with the total amount of collected and collimated light. Thus, a larger etch depth increases the efficiency of the metasubstrate. However, the enlargement of the metasubstrate encounters a fundamental limit when α is larger than the critical angle of total internal reflection θ_c. The inherent dependency of the refractive index gradient $n(r)$ on the etch depth d_{met} also implies that the final etch depth has to be well-known prior to the design and fabrication of the metasubstrate. The here presented metamaterials for both conventional and π shift ring QCLs possess a nominal etch depth of 4.2 μm. It is reduced for hole diameters less than 1.5 μm due to aspect ratio dependent etching (ARDE), which results in an increase of the local refractive index. In order to compensate for this effect, the respective holes of the metamaterial are designed to be larger and fit the required local refractive index. With a constant hole period $p_h = 1.8\,\mu$m the hole diameter $d_h(r)$ obeys

$$n_0\left(p_h - d_h(r)\right) + d_h(r) = p_h n(r). \tag{3.9.4}$$

The hole diameter corrected for ARDE is obtained by equalizing Eq. (3.9.3) and (3.9.4) and using the variable etch depth

$$d_{\text{met}} = u + v d_h \tag{3.9.5}$$

with the ARDE parameters $u = -0.79\,\mu$m and $v = 3.08$ obtained by focused ion beam milling and subsequent inspection of the vertical cross sections of the metasubstrate of a test sample. This ARDE study is summarized in the inset of 3.36. The derivation mentioned above leads to a quadratic equation and yields the following solutions for the ARDE corrected hole diameter

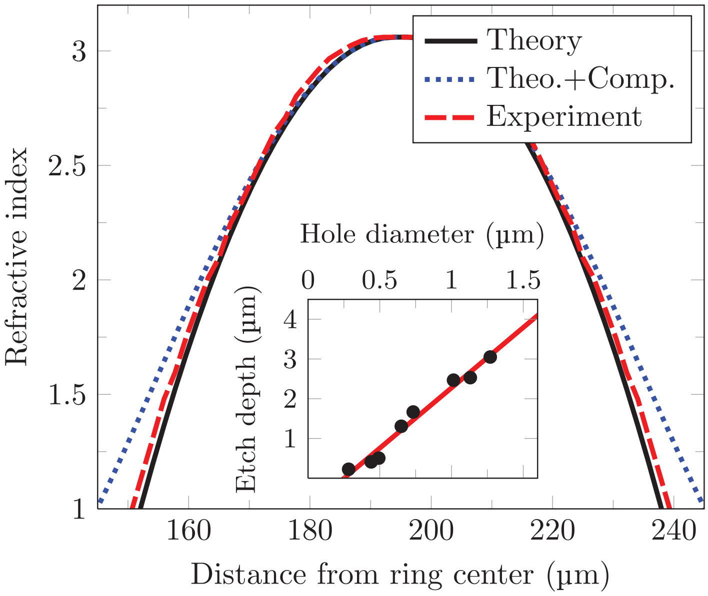

Figure 3.36: Required (black solid) and experimentally obtained (red dashed) refractive index gradient. In order to compensate for isotropic etching of the thin walls at the outer regions of the metasubstrate a compensation function is applied as indicated by the blue dotted curve. The inset describes the ARDE which was taken into account in this study.
Reprinted with permission from [177]

$$\begin{aligned} d_h(r)^{\pm} &= \frac{1}{2(v-n_0 v)}\Bigg\{-u + n_0 u + p_h v \pm \sqrt{\left(u - n_0 u - p_h v\right)^2 + \ldots} \\ &\qquad \ldots + 4(v - n_0 v)\left[p_h u + \left(1 - \frac{\sqrt{d_{\text{sub}}^2 + r^2}}{d_{\text{sub}}}\right) p_h d_{\text{sub}} n_0\right]\Bigg\} \end{aligned} \tag{3.9.6}$$

whereof only one solution is physically meaningful. Application of Eq. (3.9.6) facilitates to create a detailed map of the metasubstrate allowing to assign well-defined hole diameters to specific locations on the substrate interface. Theoretical and experimentally realized refractive index gradients are presented in the main part of Fig. 3.36. The black solid curve depicts the required refractive index gradient calculated by Eq. (3.9.3) in combination with the ARDE correction. It was found that the thin walls between the large holes at the borders of the metasubstrate suffer from isotropic etching. Thus, these thin walls are etched faster than expected from theory, which reduces the local refractive index. An empirical correction function $f_c(r) = 1.2 \cdot 10^{-7} \cdot r^4\, \mu\text{m}^{-4}$ was defined so as to compensate for this effect. Due to the quartic dependence on r this correction functions shows little effect in the center of the metasubstrate but significantly increases the local refractive index for larger values of r. The blue dotted curve in Fig. 3.36 represents the modified refractive index $n(r) + f_c(r)$. From the experimentally determined refractive index gradient, given by the red dashed curve, it is evident that the application of the correction function represents a valid approach. In order to obtain the refractive index gradient for the real structure, the hole diameters were measured using a SEM. For small values of r, i.e. $170\,\mu\text{m} < r' < 220\,\mu\text{m}$, the theoretical, modified theoretical and experimental refractive index gradients overlap. However, for larger r values the expected local reduction of the real refractive index is evident by the discrepancy between the blue dotted and red dashed curve. A correct estimation of $f_c(r)$ verified by the congruence of the black solid and red dashed curve, i.e. the conformity between theory and experiment. SEM images of this metasubstrate are depicted in Fig. 3.37. The main figure shows a top view of a section of the metasubstrate. In the center the yellow shaded area indicates the location of the ring waveguide on the other side of the chip. Hole sizes increase from 250 nm in the center of the metamaterial to $1.4\,\mu\text{m}$ in the outer region, i.e. the refractive index decreases. A total width of $w \approx 80 - 90\,\mu\text{m}$ is obtained. The inset provides a view under an angle of 45° in order to visualize the etch depth of the holes. As mentioned above, the goal of the application of this metasubstrate is to collimate the beam and increase the local intensity in the center of the beam. However,

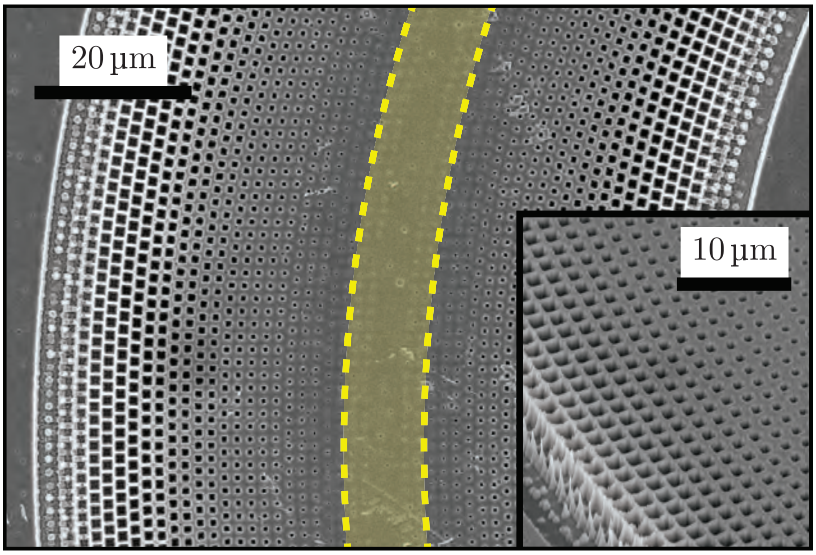

Figure 3.37: SEM image of the metasubstrate. The yellow shaded area indicates the location of the ring waveguide on the other side of the chip. The inset provides a three dimensional view of the metasubstrate.
Reprinted with permission from [177]

this implicates that the total emitted output power is unchanged and solely the light distribution is affected. Figure 3.38 verifies that the metasubstrate does not influence the overall performance of the ring laser. Exemplary the LI curves of a conventional ring QCL are shown, which were recorded before and after the fabrication of the metasubstrate. They show the same threshold current, slope efficiency and output power. Furthermore, the laser mode is unaltered and emits around 1137 /cm as indicated in the inset of Fig. 3.38. The unaltered behavior of the laser ensures that the following changes in the beam profile are generated by the metasubstrate only. [150, 177]

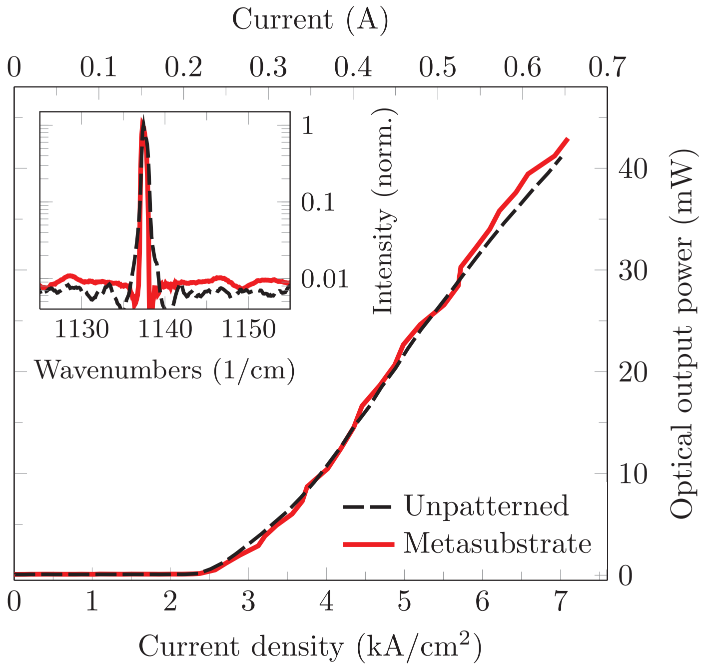

Figure 3.38: LI and spectra (inset) of the ring laser before and after fabrication of the metasubstrate. The latter does neither influence the overall output power nor the spectral performance of the ring QCL.
Reprinted with permission from [177]

3.9.2 Intensity enhancement

The compensation of the optical path lengths and the consequential increase of the emitting area induces a decrease of the envelope function of the emission beam. Conservation of energy dictates that light is not lost but simply shifted within the far field. Quantifying the collimation effect demands the consideration of the respective emitting area. Figures 3.39 (a) and (b) describe the near field object functions for both polarization components of a π shift ring QCL without and with the metasubstrate, respectively. The former represents the ring waveguide whereas the latter depicts the size of the entire metasubstrate which is assumed to be the emitting area. These object functions were utilized to calculated the theoretical far field patterns based on a two dimensional Fourier transform as described in section 3.2. In order to meet the criteria of energy conservation, the overall emitted light intensity is kept constant within the critical angle $\alpha_c = \arctan(w/d_{\text{sub}})$ of the metasubstrate. That is the maximum angle under which the light is influenced by the metamaterial. One dimensional cross sections of the far field patterns recorded before and after the fabrication of the metasubstrate are provided in Fig. 3.39 (c) by the red and blue curve, respectively. The corresponding two dimensional emission beams are shown in the insets on the right. From the cross section plots

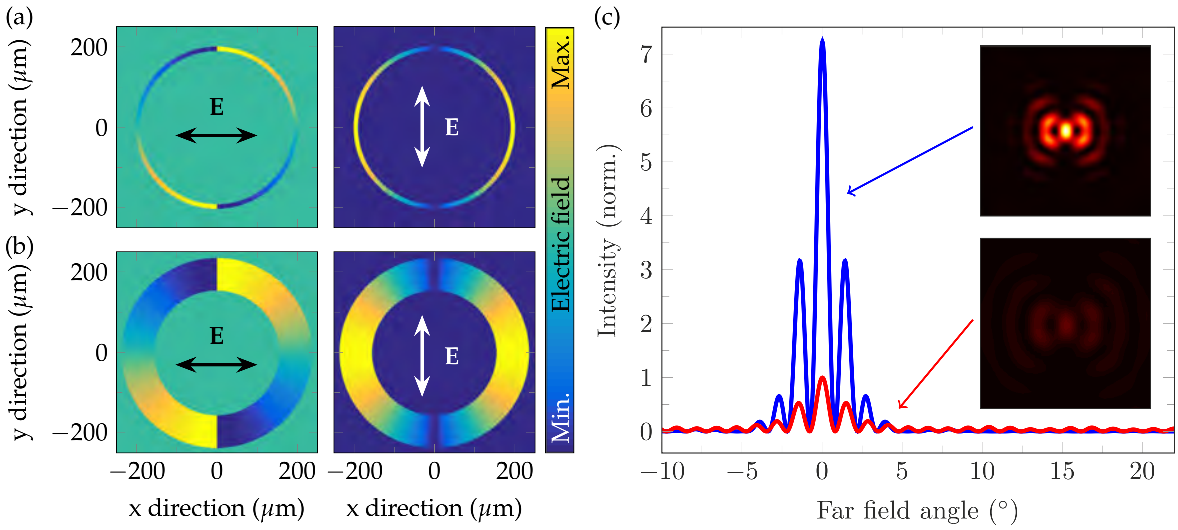

Figure 3.39: Near field object functions of both polarization components for (a) a π phase shift ring QCL and (b) the monolithic light collimating metasubstrate. (c) Calculated far fields of a π shift ring QCL without (red) and with a light collimating metasubstrate on the back side of the chip. The insets indicate the two dimensional far fields.
Reprinted with permission from [150]

a peak intensity increase to a value of 724% is obtained. This is also reflected in the two dimensional far fields sharing the same color scale bar. Thus, the metasubstrate device exhibits a brighter beam. Identical calculations were performed for conventional ring QCL as well. In contrast to the π shift laser a central intensity minimum is existent as indicated in Fig. 3.40. Theoretical (blue dashed) and experimental far fields before (black dashed) and after (red solid) metasubstrate fabrication are displayed in Fig. 3.40 (a). The initial far field recorded with the unpatterned substrate is normalized to one. With reference to the latter the metasubstrate far field exhibits a peak value of 617%. The maximum theoretical value amounts to 683%. Although the envelope functions are identical, this value is lower than the respective theoretical peak intensity of 724% of the π shift laser. This is due to the fact that the π shift laser possesses its intensity maximum in the center of the beam and therefore the peak value coincides with the peak of the envelope function. For the conventional ring laser the height of the central intensity lobes is limited by the envelope function, which at these angles is lower than at the center of the beam. Experimental and theoretical far fields show an overall good agreement. However, the theoretical peak intensity is not fully reached for the innermost intensity ring. In contrast, the intensity of the subsequent rings is higher in the experimental far field. Three possible explanations can be considered. (i) The far fields were recorded using an MCT detector with a size of 1 mm × 1 mm on a two dimensional translational stage. Hence, the relatively large detector area allows interference from light rays emitted under slightly different angles. This results in a blurring effect. (ii) The theoretical approach presented in Fig. 3.34 (b) is based on a point source. However, the real laser possesses a waveguide width of 10 μm. Thus, light rays emitted under the same angle but from different locations in the waveguide exhibit a slightly different refractive index in the metasubstrate. As a consequence, these rays are not deflected accordingly which broadens the intensity distribution. (iii) Finally, processing imperfections of the metasubstrate can lead to similar alterations of the beam. In order to eliminate the possibility that the additional treatment of the substrate during metasubstrate fabrication has any effect on the beam quality, far fields of a neighboring reference device were

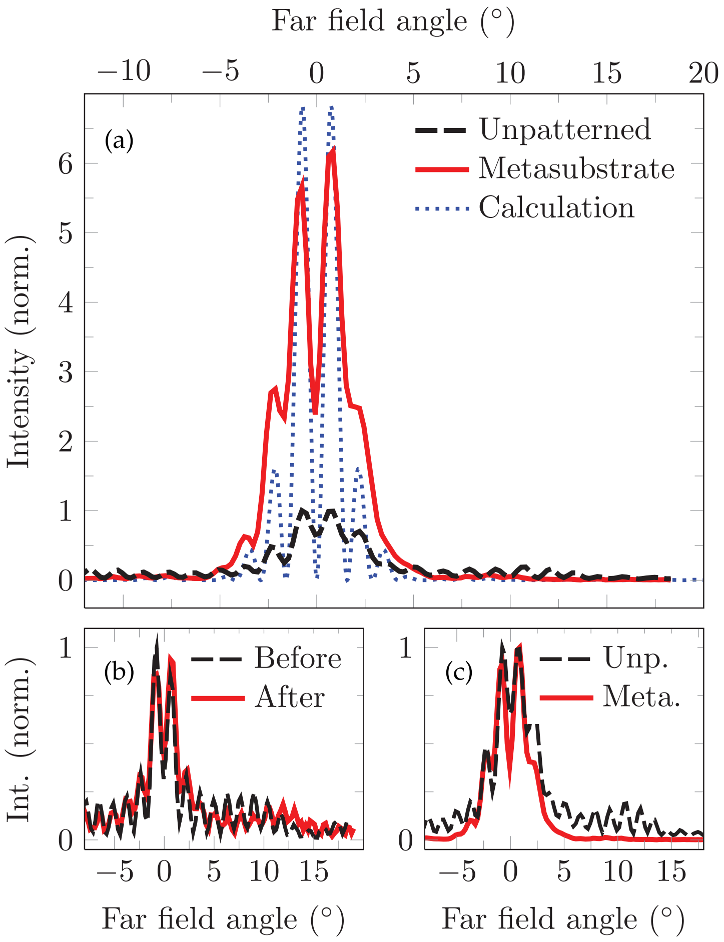

Figure 3.40: (a) Measured far field cross sections of a ring QCL before (black dashed) and after (red solid) metasubstrate fabrication. A peak intensity increase to 673% is observed. This is close to the theoretical maximum given by the blue dotted curve. (b) Measured far fields of a reference device with no metasubstrate. (c) Normalized far fields shown in (a) illustrating the light collecting principle of the metasubstrate.
Reprinted with permission from [177]

recorded. As shown in Fig. 3.40 (b), no significant change is evident. According to the theoretical approach describing the metasubstrate, the working principle is based on a shift of the emitted light intensity from larger far field angles to the center of the beam and thus narrowing the envelope function. Figure 3.40 (c) can be considered as a visual aid for this effect. It shows both experimental far fields from Fig. 3.40 (a) normalized to unity. It is apparent that the initial beam of the unpatterned device exhibits interference fringes at least up to far field angles of ±18°. In contrast, the metasubstrate far field has only $2-3$ interference fringes within ±5° and negligible light intensity for larger angles. This verifies that the metasubstrate collects the light emitted under relatively large angles and shifts its intensity towards the center of the beam. At first glance the rather large intensity increase in Fig. 3.40 (a) is unproportional to the small height of the interference fringes at larger far field angles. However, it must be considered that the larger the far field angle the greater the two dimensional interference ring. Hence, these interference rings contain more intensity than inferred from the one dimensional cross section. Two dimensional experimental emission beams of a conventional (left column) and a π shift ring QCL (right column) measured before (top row) and after (bottom row) metasubstrate fabrication are depicted in Fig. 3.41. The color scale bar is normalized with respect to the corresponding peak values of the metasubstrate far fields. Hence, the

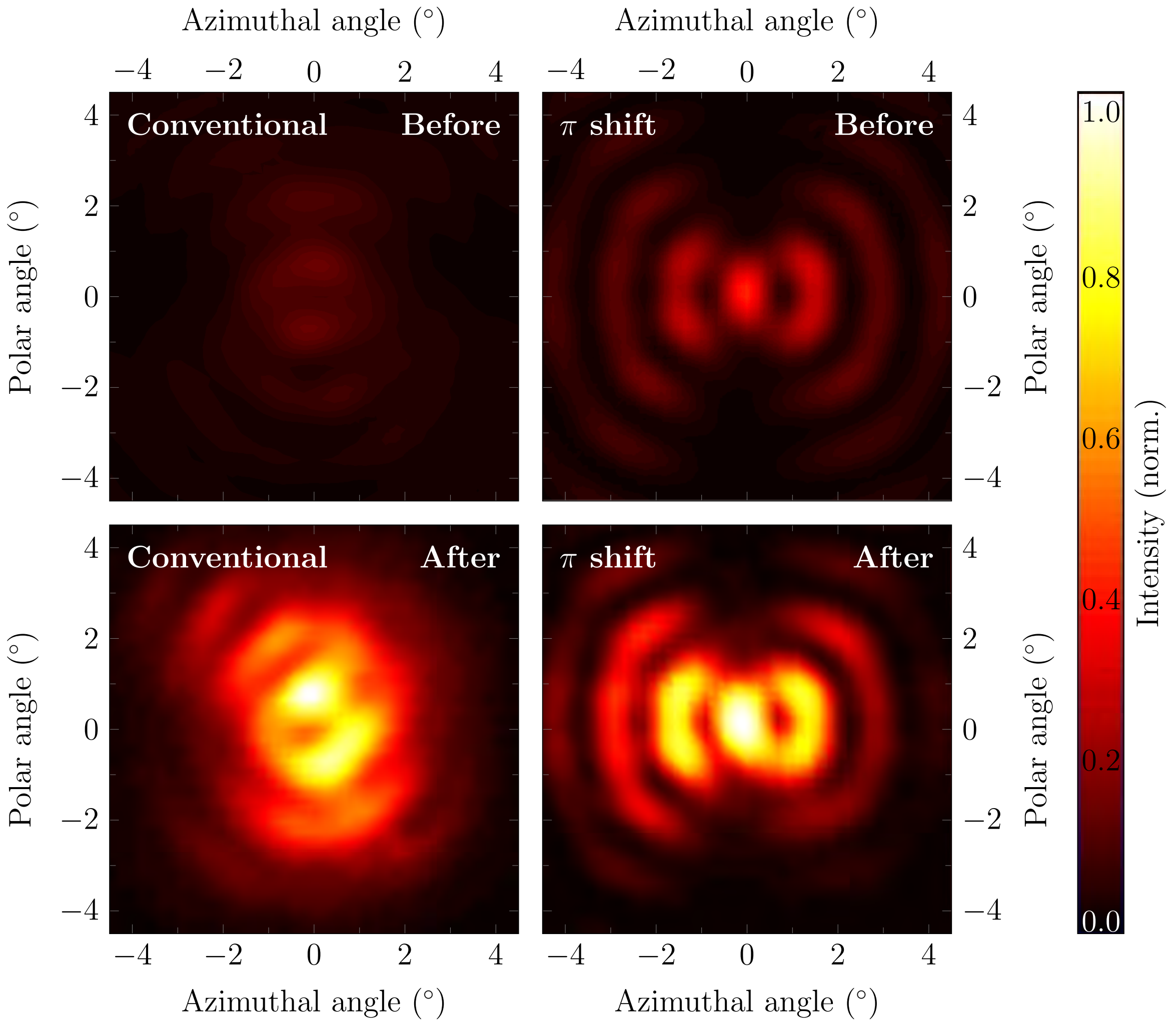

Figure 3.41: Two dimensional beam patterns before (top row) and after (bottom row) metasubstrate fabrication of a conventional (left column) and a π shift (right column) ring QCL. The far fields recorded with the metasubstrate are scaled to unity and the corresponding far fields prior to the metasubstrate fabrication share the same color bar in order to visualize the increase of the peak intensity generated by the metasubstrate.
Reprinted with permission from [150]

direct effect of the metasubstrate on the two dimensional emission beams is emphasized. [150, 177]

In comparison to similar approaches for light collimation this approach exhibits major advantages. Plasmonic antenna arrays [179] have proven to be versatile optical tools for reshaping the wavefront. They facilitate arbitrary light deflection [180] and polarization selection as well as collimation of light [118] and the possibility to shift the wavefront in order to obtain beams carrying an orbital angular momentum [181]. However, the demonstrated plasmonic metasurfaces operate with a rather low efficiency of around 1% [182]. In contrast dielectric metamaterials affect all of the light propagating through them and in the here presented approach efficiencies close to unity are achieved. In a different approach a nanopore array [183] is fabricated directly into the substrate side of a vertically emitting straight DFB QCL. This method also increases the emitting area of the laser. However, scattering processes inside the nanopore layer destroys the coherence of the beam. As a consequence the far field pattern shows no interference fringes. Furthermore, scattering losses reduce the theoretically achievable peak intensity.

3.10 Orbital angular momentum emitter

Building on the concept in section 3.9 various beam modifications can be implemented. In this section a metasubstrate imparting an orbital angular momentum (OAM) to the emission beam is introduced. The first experimental demonstration that light can possess and transfer angular momentum dates back to 1936 and was conducted by Beth [184]. In this experiment circularly polarized light induced a rotation of a quartz wave plate. Unlike for solid bodies the angular momentum of light is not only described by an orbital part but also includes a spin angular momentum (SAM). As evident from the following discussion the latter is associated with the polarization of the beam whereas OAM beams exhibit a helical wavefront. They are promising tools utilized in various fields including micromanipulation of microscopic particles [185], telecommunications with data rates already reaching 2.5 Tbits/s [186] and sensing of chiral molecules [187].

3.10.1 Separation of the angular momentum of light

The main task for the analysis of the OAM is the separation of the total angular momentum J into the SAM part S and OAM part L. Therefore, the continuity equation of the linear momentum P has to be considered. It reads $\frac{\partial}{\partial t}\rho_k^P + \frac{\partial}{\partial x_i} j_{ik}^P = q_k^P$ using the notation in components. From the definition of the Lorentz force in combination with Maxwell's equations it is possible to identify $q_k^P = -\rho E_k - \epsilon_{klm} j_l B_m$ as the source density, $\rho_k^P = \frac{\mu_0}{c^2} S_k = \varepsilon_0 \epsilon_{klm} E_l B_m$ as the linear momentum density and $j_{ik}^P = \varepsilon_0(\frac{1}{2}E^2\delta_{ij} - E_i E_k) + \frac{1}{\mu_0}(\frac{1}{2}B^2\delta_{ik} - B_i B_k)$ as the momentum flux density. According to conventional notation δ_{ij} and ϵ_{klm} are the Kronecker delta and the Levi-Civita operator, respectively. Furthermore, S_k describes the k-th component of the Poynting vector. According to the vectorial definition of the angular momentum $\mathbf{J} = \mathbf{r} \times \mathbf{P}$, the angular momentum density, the angular momentum flux density and the corresponding source density read

$$\begin{aligned} \rho_k^J &= \epsilon_{klm} x_l \rho_m^P && (3.10.1) \\ j_{ik}^J &= \epsilon_{ijl} x_j j_{lk}^P && (3.10.2) \\ q_k^J &= \epsilon_{klm} x_l q_m^P. && (3.10.3) \end{aligned}$$

Thus, it is possible to write the continuity equation for the angular momentum by using the quantities from the linear momentum

$$\epsilon_{ijk} x_j \left(\frac{\partial}{\partial t}\rho_k^P + \frac{\partial}{\partial x_l} j_{kl}^P - q_k^P \right) = 0, \tag{3.10.4}$$

which means that the continuity equation for the angular momentum is always fulfilled if the corresponding equation for the linear momentum is fulfilled. In free space the source density vanishes and $q_k^J = 0$, which leaves the terms for the angular momentum density and the angular momentum flux density in the continuity equation. Due to the existence of SAM in light beams a clear separation of the total angular momentum $J = L + S$ into orbital and spin parts is *not* straightforward. However, it was shown [188] that by using the angular momentum flux density

$$j_{il}^J = \epsilon_{ijk} x_j \left[\frac{1}{2}\delta_{kl} \left(\epsilon_0 E^2 + \frac{1}{\mu_0} B^2 \right) - \varepsilon_0 E_k E_l - \frac{1}{\mu_0} B_k B_l \right] \tag{3.10.5}$$

this goal can be achieved. The angular momentum flux describes the "amount" of angular momentum crossing a surface per unit time. In the paraxial approximation with the axis of the beam in z-direction [189] the angular momentum flux density is given by

$$j^J_{33} = y\left(\varepsilon_0 E_x E_z + \frac{1}{\mu_0} B_x B_z\right) - x\left(\varepsilon_0 E_y E_z + \frac{1}{\mu_0} B_y B_z\right). \tag{3.10.6}$$

The total angular momentum flux $M_{zz} = \iint j^J_{33} dxdy$ through the plane perpendicular to the z-direction is obtained by integration over the entire plane. This task is simplified by using the complex field amplitudes

$$\begin{aligned} E_i &= \Re\left[\varepsilon_i e^{-i\omega t}\right] & (3.10.7)\\ B_i &= \Re\left[\beta_i e^{-i\omega t}\right] & (3.10.8) \end{aligned}$$

in combination with the corresponding Maxwell equations

$$\begin{aligned} \varepsilon_j &= \frac{-c^2}{i\omega}\epsilon_{jkl}\frac{\partial}{\partial x_k}\beta_l & (3.10.9)\\ \beta_j &= \frac{1}{i\omega}\epsilon_{jkl}\frac{\partial}{\partial x_k}\varepsilon_l. & (3.10.10) \end{aligned}$$

The latter formulas enable the elimination of the z-components of the electric and magnetic field in the equation for the angular momentum flux density in Eq. (3.10.6) which results in

$$\begin{aligned} j^J_{33} = \frac{c^2\varepsilon_0}{2\omega}\Re\Bigg[\frac{1}{i}\Bigg(& y\varepsilon_x\frac{\partial}{\partial x}\beta^*_y - y\varepsilon_x\frac{\partial}{\partial y}\beta^*_x + y\beta^*_x\frac{\partial}{\partial x}\varepsilon_y - y\beta^*_x\frac{\partial}{\partial y}\varepsilon_x - \ldots\\ & \ldots - x\varepsilon_y\frac{\partial}{\partial x}\beta^*_y + x\varepsilon_y\frac{\partial}{\partial y}\beta^*_x - x\beta^*_y\frac{\partial}{\partial x}\varepsilon_y + x\beta^*_y\frac{\partial}{\partial y}\varepsilon_x\Bigg)\Bigg]. \end{aligned} \tag{3.10.11}$$

Terms including electric and magnetic field of the same component can be combined according to the product rule for derivatives. It is straightforward to calculate the integral for the total angular momentum flux using integration by parts. Two types of expressions occur in Eq. (3.10.11). Terms with equal components are integrated as follows

$$\begin{aligned} \iint -x_2\frac{\partial}{\partial x_2}\left(A_1A_2\right)dx_1dx_2 &= \int\left\{\left[-x_2A_1A_2\right]^{+\infty}_{-\infty} + \int A_1A_2dx_2\right\}dx_1\\ &= \iint A_1A_2dx_1dx_2 & (3.10.12) \end{aligned}$$

and all other terms obey

$$\begin{aligned} \iint x_2A_1\frac{\partial}{\partial x_1}A_2dx_1dx_2 &= \int\left\{\left[x_2A_1A_2\right]^{+\infty}_{-\infty} + \int x_2A_2\frac{\partial}{\partial x_1}A_1dx_1\right\}dx_2\\ &= -\iint x_2A_2\frac{\partial}{\partial x_1}A_1dx_1dx_2 & (3.10.13) \end{aligned}$$

with the parameters $x_{1/2} = x, y$ and $A_{1/2} = \varepsilon_x, \varepsilon_y, \beta^*_x, \beta^*_y$. Using these integral equalities it is possible to rewrite all expressions of $\iint j^J_{33}dxdy$. Terms with equal components assume the shape of the integral after integration by parts while all other terms are expressed by a combination of the respective integral before and after integration by parts, i.e. only half of each term is integrated by parts and the other half is unchanged. Application of this simple trick enables the angular momentum flux to assume the following shape

$$\begin{aligned} M_{zz} &= \frac{c^2\varepsilon_0}{2\omega}\Re\left\{\frac{1}{i}\iint\left[\varepsilon_x\beta_x^* + \varepsilon_y\beta_y^* + \frac{1}{2}\varepsilon_x\left(y\frac{\partial}{\partial x} - x\frac{\partial}{\partial y}\right)\beta_y^* + \ldots\right.\right. \\ &\quad \ldots + \frac{1}{2}\beta_x^*\left(y\frac{\partial}{\partial x} - x\frac{\partial}{\partial y}\right)\varepsilon_y + \frac{1}{2}\varepsilon_y\left(x\frac{\partial}{\partial y} - y\frac{\partial}{\partial x}\right)\beta_x^* + \ldots \\ &\quad \left.\left.\ldots + \frac{1}{2}\beta_y^*\left(x\frac{\partial}{\partial y} - y\frac{\partial}{\partial x}\right)\varepsilon_x\right] dxdy\right\}. \end{aligned} \tag{3.10.14}$$

Equation (3.10.14) clearly provides the opportunity to switch to polar coordinates and apply $\frac{\partial}{\partial\varphi} = x\frac{\partial}{\partial y} - y\frac{\partial}{\partial x}$. Finally, the angular momentum flux yields

$$\begin{aligned} M_{zz} &= \underbrace{\frac{c^2\varepsilon_0}{4\omega}\Re\left\{\frac{1}{i}\iint\left[\varepsilon_y\frac{\partial}{\partial\varphi}\beta_x^* + \beta_y^*\frac{\partial}{\partial\varphi}\varepsilon_x - \varepsilon_x\frac{\partial}{\partial\varphi}\beta_y^* - \beta_x^*\frac{\partial}{\partial\varphi}\varepsilon_y\right]\rho d\rho d\varphi\right\}}_{\text{OAM}} + \ldots \\ &\quad \ldots + \underbrace{\frac{c^2\varepsilon_0}{2\omega}\Re\left\{\frac{1}{i}\iint\left[\varepsilon_x\beta_x^* + \varepsilon_y\beta_y^*\right]\rho d\rho d\varphi\right\}}_{\text{SAM}}. \end{aligned} \tag{3.10.15}$$

From Eq. (3.10.15) the separation into SAM and OAM is evident. The second term describes the polarization characteristics and is therefore associated with the SAM. An explicit dependency on the azimuthal coordinate φ suggests that the first term represents the OAM. This separation gets even clearer by applying transformations which should only influence the SAM *or* OAM. A birefringent optical element possesses different refractive indices n_s and n_f for the two orthogonal polarization states and induces the transformations $\varepsilon_{x/y} \to \varepsilon_{x/y}e^{in_{f/s}kL}$ and $\beta_{x/y}^* \to \beta_{x/y}^* e^{in_{s/f}kL}$ on the electric and magnetic field, respectively. Substitution of these transformations in Eq. (3.10.15) reveals that it solely influences the SAM. On the other hand, an optical element introducing an azimuthal phase change is characterized by the transformation $\varepsilon_{x/y}/\beta_{x/y}^* \to \varepsilon_{x/y}/\beta_{x/y}^* e^{im\varphi}$. The explicit behavior on the azimuthal coordinate φ demonstrates that such a transformation only has an effect on the OAM. Thus, the total angular momentum flux is built up of independent spin and orbital components which suggests that the conducted separation is justified. [188, 190, 191]

Strictly speaking, this analysis for the calculation of M_{zz} is only valid in the paraxial approximation which allows to write the propagation constant from the Helmholtz equation (Eq. (2.3.9)) in a simplified way. Series expansion of k_z yields

$$k_z = \sqrt{k^2 - k_x^2 - k_y^2} \approx k - \frac{k_x^2 + k_y^2}{2k} \tag{3.10.16}$$

which connotes a small inclination angle between k_z and the optical axis. A solution of the Helmholtz equation can be expected from the ansatz

$$\Psi(\mathbf{r}) = u(\mathbf{r})e^{ikz}. \tag{3.10.17}$$

Substitution into the Helmholtz equation in combination with the derivation rule $(fg)'' = f''g + 2f'g' + fg''$ produces

$$e^{ikz}\left(\frac{\partial^2}{\partial x^2}u(\mathbf{r}) + \frac{\partial^2}{\partial y^2}u(\mathbf{r}) + \frac{\partial^2}{\partial z^2}u(\mathbf{r}) + 2ik\frac{\partial}{\partial z}u(\mathbf{r}) - u(\mathbf{r})k^2 + u(\mathbf{r})k^2\right) = 0. \tag{3.10.18}$$

If the function $u(\mathbf{r})$ is slowly varying, the second derivative in z can be neglected which represents the paraxial approximation. The resulting wave equation is given by

$$\frac{\partial^2}{\partial x^2}u(\mathbf{r}) + \frac{\partial^2}{\partial y^2}u(\mathbf{r}) + \frac{\partial^2}{\partial z^2}u(\mathbf{r}) + 2ike^{ikz}\frac{\partial}{\partial z}u(\mathbf{r}) = 0. \tag{3.10.19}$$

A complete set of solutions to Eq. (3.10.19) is given by the Hermite-Gaussian beams $u_n^{\mathrm{HG}}(x,z)$. They feature rectangular symmetry and are therefore not capable of carrying OAM. Passing on to cylindrical coordinates the wave equation reads

$$\left(\frac{1}{\rho}\frac{\partial}{\partial \rho} + \frac{\partial^2}{\partial \rho^2}\frac{1}{\rho^2}\frac{\partial^2}{\partial \varphi^2} + 2ik\frac{\partial}{\partial z}\right)u(\mathbf{r}) = 0 \tag{3.10.20}$$

and the set of solutions is given by the rotationally symmetric Laguerre-Gaussian beams

$$u_{mp}^{\mathrm{LG}}(\rho,\varphi,z) \sim L_p^{|m|}e^{im\varphi}. \tag{3.10.21}$$

The latter consist of concentric intensity rings. Their number is determined by the mode index p. The other mode index m describes the helical wavefront of the beam [192]. Hence, the azimuthal phase structure of the beam is defined by the term $e^{im\varphi}$ which provides the beam with an OAM. It is found that *all* beams with a phase factor of $e^{im\varphi}$ have a well-defined OAM. Bessel beams represent a complete set of solutions to the wave equation. They belong to the category of diffraction-free beams [193] and their radial, azimuthal and axial components can be separated as follows

$$u_m^{\mathrm{B}}(\rho,\varphi,z) = J_m\left(\kappa\rho\right)e^{im\varphi}e^{i(k_z-k)z} \tag{3.10.22}$$

with $\kappa = \sqrt{k_x^2+k_y^2}$. Due to the appearance of $e^{im\varphi}$, Bessel beams can also carry OAM. Furthermore, these beams can be used to extend the property of well-defined OAM to the non-paraxial case. By reason of their completeness it is possible to expand the Laguerre-Gaussian beams using Bessel beams

$$u_{mp}^{\mathrm{LG}}(\rho,\varphi,z) = \int_0^\infty d_{mp}(\kappa)J_m(\kappa\rho)e^{im\varphi}e^{-i\kappa^2z/2k}d\kappa \tag{3.10.23}$$

with the mode function $d_{mp}(\kappa)$ [189]. The non-paraxial version of this beam is simply given by inserting the exact value for k_z. The resulting beam formula reads

$$\hat{u}_{mp}^{\mathrm{LG}}(\rho,\varphi,z) = \int_0^k d_{mp}(\kappa)J_m(\kappa\rho)e^{im\varphi}e^{i\sqrt{k^2-\kappa^2}z}d\kappa. \tag{3.10.24}$$

In contrast to the paraxial approximation the integral in the non-paraxial beam covers only values of κ between zero and k. Using this notation the non-paraxial beam still possesses the azimuthal term $e^{im\varphi}$. Therefore, a separation into SAM and OAM is justified and the beam can carry well-defined OAM. Comparison of the orbital angular momentum flux and the energy flux reveals that their ratio amounts to m/ω. Since each photon can be associated with the energy $\hbar\omega$ this implies that every single photon in a beam with a helical wavefront carries OAM. Integration of the azimuthal phase along the azimuthal direction indicates that the mode number

$$m = \frac{1}{2\pi}\oint \nabla\mathbf{S}\cdot d\mathbf{l} \tag{3.10.25}$$

can be associated with the topological charge. In Eq. (3.10.25) $d\mathbf{l}$ is the line element of the integral and $S = m\varphi$ is the azimuthal phase. The topological charge describes the number of phase discontinuities along the azimuthal integration path. [188, 191]

3.10.2 Generation of helical wavefronts

Compared to SAM with only two orthogonal polarization states, OAM basically exhibits an unlimited number of orthogonal states, i.e. the topological charge m can assume every integer number in the orbital term $e^{im\varphi}$. This represents major advantages for encoding information via OAM rather than SAM. However, these advantages come along with the necessity to generate and measure the various OAM states. Detection of OAM states is versatile. Two popular examples are the observation of rotating particles [194] and counting the number of spiral interference fringes [195]. The former is based on the fact that SAM induces a rotation of a microscopic particle around its own axis while OAM forces the particle on a trajectory around the central axis of the beam. The latter approach describes the interference of a plane wave reference beam with the OAM beam. Fringes occur in the interference pattern due to differences in the relative phase between both beams. The number of fringes corresponds to the topological charge m [196]. Two of the most common techniques for the generation of OAM beams are spiral phase plates [197] with a varying optical thickness along φ and pitchfork holograms [198] resembling diffraction gratings. In dependence on spiral phase plates it was demonstrated that plasmonic metasurfaces [199] are capable of generating OAM beams. On-chip generation of OAM laser beams in the near-infrared was realized by implementing spiral phase plates [200] and off-resonance gratings [201]. In this section on-chip generation of MIR light beams emitted from ring QCLs is demonstrated.

The employed approach utilizes the ring QCL on the surface side of the chip which emits light towards the substrate. The latter is modified in the form of an OAM metasubstrate which in turn manipulates the emitted light and creates an OAM beam. This principle is similar to the light collecting metasubstrate in section 3.9. The main difference is that the OAM metasubstrate does not exhibit a refractive index gradient in radial but in azimuthal direction. Essentially, it is a combination of spiral phase plate and metamaterial created by means of etching sub-wavelength holes into the structure. A sketch of the surface and substrate side of this device is provided in Fig. 3.42. As the hole size of the OAM metasubstrate decreases with the azimuthal coordinate, the refractive index is increasing which forms a linear refractive index gradient. The main advantage with respect to conventional spiral phase plates is that no gray scale lithography is necessary and only a single exposure is required. Therefore, the here presented

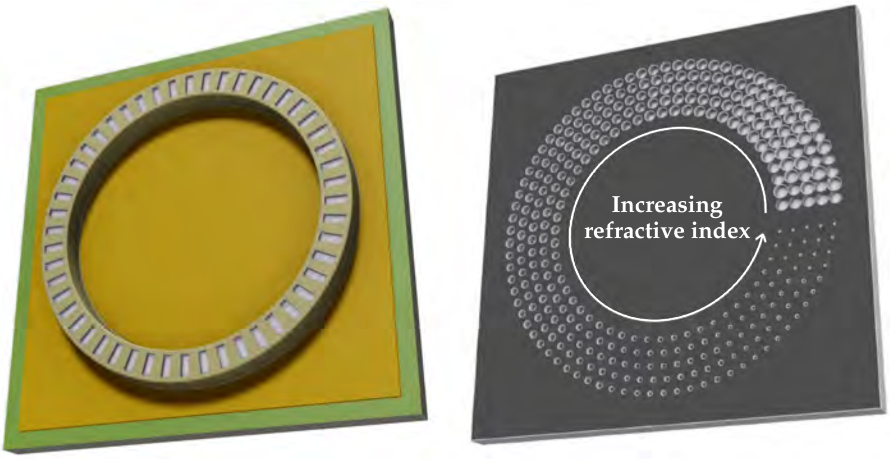

Figure 3.42: Sketch of a ring QCL (left) equipped with an OAM metasubstrate (right). Differently sized holes are etched into the substrate and create a circular refractive index gradient. Reprinted with permission from [150]

OAM metasubstrate is reproducible and robust in the face of varying processing parameters, e.g. exposure and developing time. Figures 3.43 (a) - (c) indicate fabricated OAM metasubstrates with topological charges of $m = +1, -1$, and $+2$. Without loss of generality positive topological charges correspond to a counter clockwise increase of the refractive index. A key condition is the step height of the discontinuity of the OAM metasubstrate. It is defined by the etch depth and has to amount to $\lambda/(n_0 - 1)$. The number of discontinuities is determined by the topological charge $|m|$. In the case of a reduced or increased step height, fractional OAM beams are created. In Fig. 3.43 (d) a closeup view of the metasubstrate is shown, enabling a thorough evaluation of the hole design. For each of the given metasubstrates the refractive index gradient was measured according to the technique in section 3.9 which also includes ARDE. The experimental results along with the ideal gradient as a function of the azimuthal coordinate are indicated in Fig. 3.43 (e). An overall good agreement between the fabricated metamaterial and the ideal structure can be observed. In combination with an accurate etch depth, which was found to be $d_{\text{met}} = 4.32\,\mu\text{m} = 1.014 \cdot \lambda/(n_0 - 1)$, as shown in Fig. A.2 (b), with a mean emission wavelength of $\lambda = 8.77\mu\text{m}$ and the refractive index $n_0 = 3.06$ of InP [178], this represents a feasible approach for creating OAM beams. In appendix A.4 detailed SEM images of the etched holes at different locations of an $m = +1$ metasubstrate are provided.

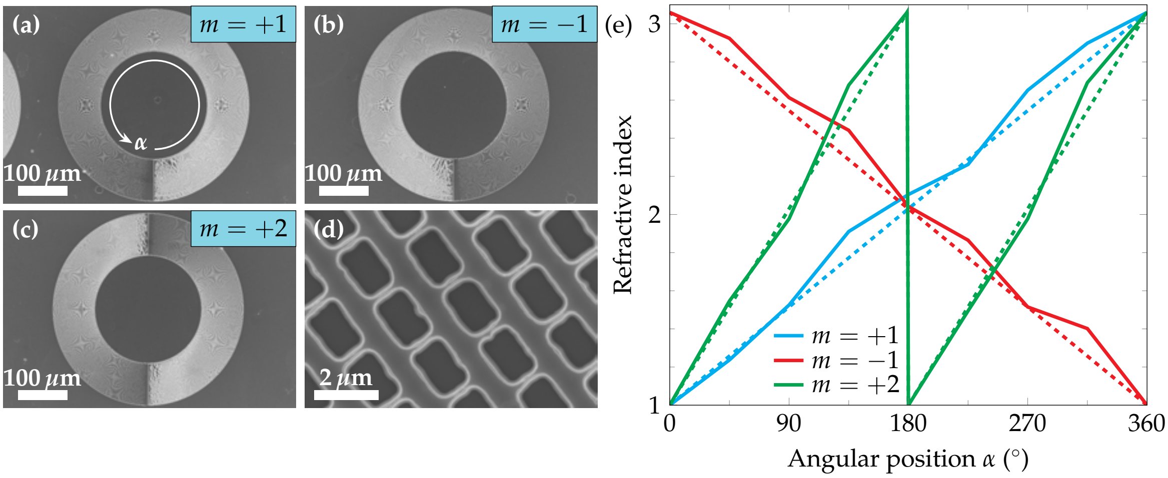

Figure 3.43: SEM images of OAM metasubstrates for the generation of beams with topological charges of $m = +1$ (a), $m = -1$ (b) and $m = +2$ (c). (d) Magnified SEM image showing the structure and geometry of the etched holes. (e) Required (dashed) and realized (solid) refractive index gradients of the metasubstrates in (a) - (c).

Depending on the existence and topological charge of the OAM the light beam alters its shape. Laguerre-Gaussian beams feature a central intensity minimum for $|m| = 1$. Increasing the topological charge also enlarges the area of this central dark spot in the beam [191, 200]. In the following the behavior of ring QCL beams under the influence of OAM is investigated. The metasubstrate in Fig. 3.43 (a) with a topological charge of $m = +1$ is fabricated below a ring QCL. Far fields for the surface and substrate emission before and after fabrication of the metamaterial are presented in Fig. 3.44. Prior to the fabrication of the OAM metamaterial the substrate of the chip is blank. Therefore, surface and substrate emission show identical interference patterns with a central intensity minimum in the far field. Application of the OAM metasubstrate does not influence the surface emission. However, a radical change in the substrate emission is observed. The central minimum is exchanged by a central intensity peak and

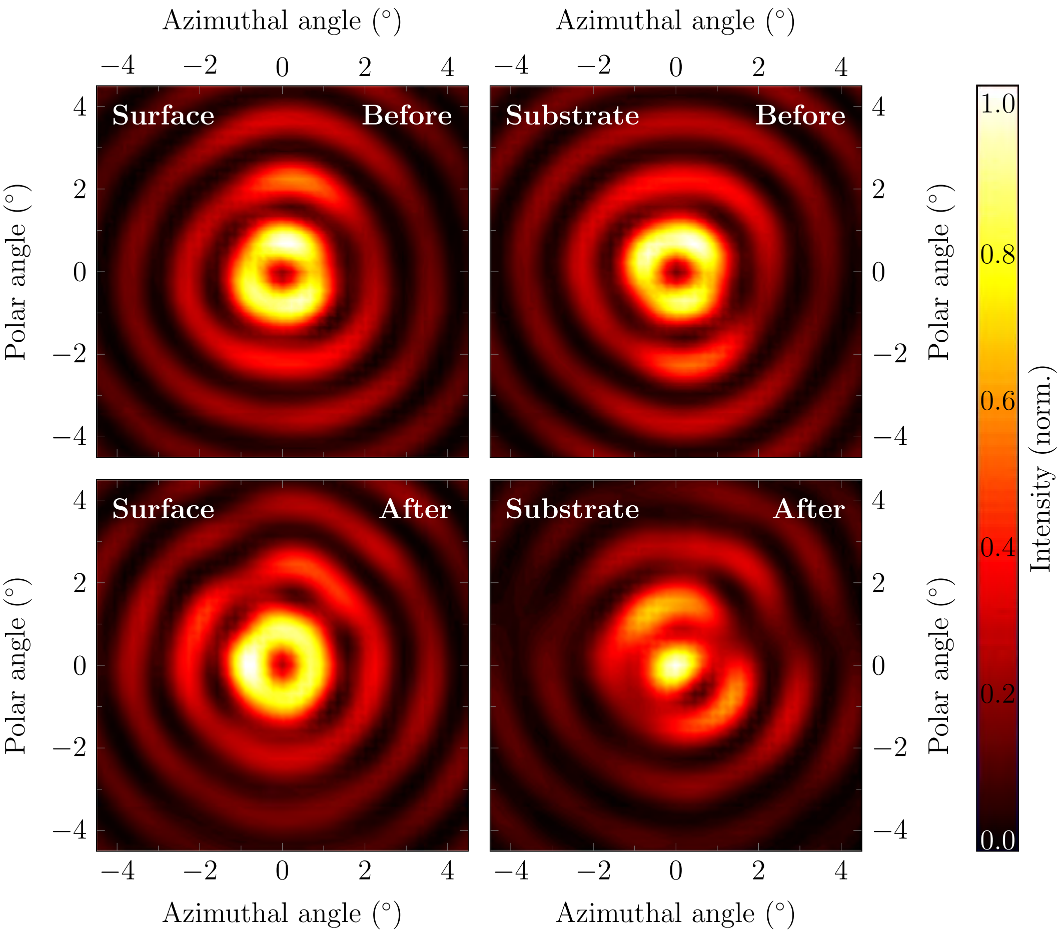

Figure 3.44: Experimentally measured surface (left column) and substrate (right column) far fields of a ring QCL before (top row) and after (bottom row) the fabrication of the OAM metasubstrate. The surface emission exhibits no significant change. In contrast, the substrate emission shows a metasubstrate induced transformation from a central intensity minimum to a central maximum.

the subsequent interference fringes are located at emission angles which correspond to minima of the surface far field, i.e. minima and maxima are exchanged similar to the far field in Fig. 3.15. Furthermore, rotational symmetry is maintained and stable single mode emission around 1131 /cm is guaranteed for all four emission beams. Throughout this dissertation several approaches and techniques have been demonstrated to create central lobe emission beams. Abrupt and continuous π phase shifts were used to switch phase and polarization vectors. These approaches induced dark parts in the far fields. Off-centered DFB gratings were successfully implemented in order to generate rotationally symmetric far field pattern. This is explained by a time depending behavior of the mode inside the waveguide. Only this time depending analysis is capable to produce the rotationally symmetric central lobed far field. The latter is quite similar to the OAM far field in Fig. 3.44. However, it can be explained without a time depending behavior of the mode. Figure 3.45 provides an illustrative exemplification of the formation of the far field. The curved waveguide with the grating is displayed in a straight fashion along the azimuthal coordinate α. The left sketch represents the emission through a blank substrate resulting in horizontal wavefronts. Blue and red wavefronts exhibit a phase difference of π. Due to the curvature of the waveguide opposing sides of the ring (e.g. at 90° and 270°) emit antiparallel polarization vectors. In the far field these will interfere destructively and create the central intensity minimum. Due to the re-

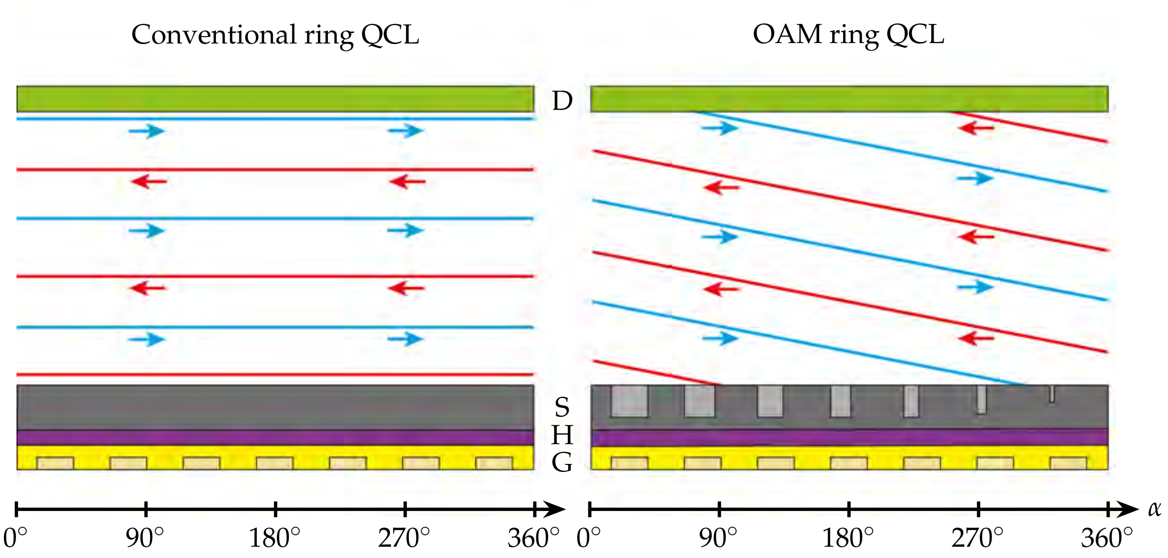

Figure 3.45: Wavefront analysis in which the colored arrows denote the emitted polarization vectors. The conventional ring QCL exhibits flat wavefronts which result in destructive interference and a central intensity minimum. The OAM metasubstrate introduces an inclination of the wavefront resulting in constructive interference and a central intensity maximum. Detector (D), substrate (S), heterostructure (H) and grating (G) are labeled accordingly.

fractive index gradient the laser containing the OAM metasubstrate produces oblique wavefronts. A proper etch depth in combination with an accurate refractive index profile ensures a precise alignment of opposing polarization vectors. Light emitted from the ring location $\alpha = 90°$ escapes the chip half of the light's oscillation period faster than light at $\alpha = 270°$. Thus, photons from $\alpha = 90°$ will interfere with photons at $270°$ of the preceding wavefront. Since these photons are phase shifted by a value of π their polarization vectors assume a parallel orientation which results in constructive interference and a central intensity maximum in the far field. As evident from Fig. 3.45 this approach is valid for the entire ring and constructive interference is ensured between all locations on the ring with an azimuthal distance of $\Delta\alpha = 180°$. Hence, a central intensity maximum in the far field is an unambiguous representation of a ring QCL beam carrying OAM. A summary of the effect of all OAM metasubstrates in Fig. 3.43 (a) - (c) with topological charges $m = +1, -1$, and $+2$ on the emission beam is provided in Fig. 3.46. The substrate emitted far fields with a topological charge of $m = \pm 1$ exhibit a central intensity maximum as previously discussed. The respective surface emission shows the conventional interference pattern with a central minimum. For the $m = +2$ metasubstrate the far field possesses in turn a central intensity minimum. An $|m| = 2$ OAM metasubstrate contains two discontinuities and hence features a steeper refractive index gradient. Consequently, the emitted wavefronts are more sloped. In accordance with the sketch in Fig. 3.45, light emitted at $\alpha = 90°$ in the red wavefront interferes with light emitted at $\alpha = 270°$ in the preceding red wavefront with a phase difference of 2π. Hence, the polarization vectors show an antiparallel orientation and the far field possesses a central intensity minimum. This matter of fact implies that from this simple analysis of the far field beams with $m = 0$ and $|m| = 2$ show central intensity minima.

The descriptive explanation of the far field behavior under influence of the OAM metasubstrate provided in Fig. 3.45 enables a qualitative understanding of the mechanism behind the formation of the far field. In addition, a quantitative theoretical investigation based on two different approaches was utilized to simulate the OAM emission

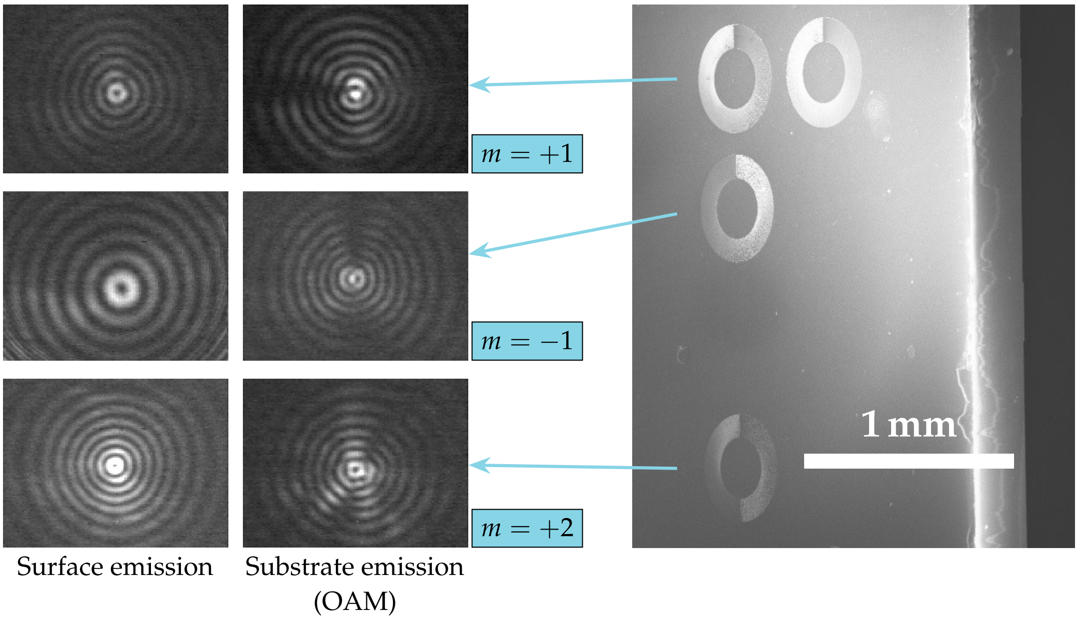

Figure 3.46: Surface and substrate emission of three ring QCLs equipped with OAM metasubstrates generating topological charges of $m = +1, -1, +2$. SEM images of the corresponding metasubstrates are provided in the right image taken under a viewing angle of 45°. OAM metasubstrates with $|m| = 1$ generate central intensity maxima whereas $|m| = 2$ metasubstrates create central minima. This can be explained by the doubled angle of inclination of the wavefront which provides destructive interference for $|m| = 2$.

beams. The first approach is based on a numerical model featuring 128 azimuthally oriented independent dipoles [115]. The second approach is based on a vectorial ray-based diffraction integral [202]. A comparison of the simulated far fields for $|m| = 0, 1, 2$ is provided in Fig. 3.47. Both models deliver similar results for all investigated m-values.

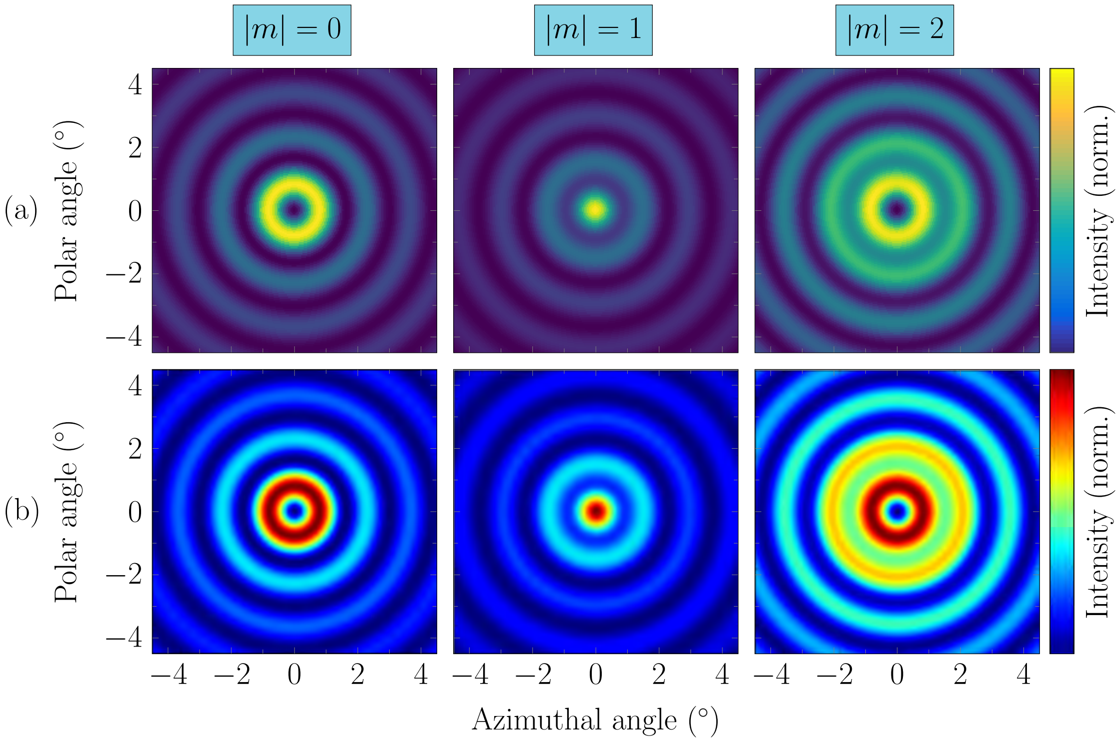

Figure 3.47: Far field patterns for $|m| = 0, 1, 2$ calculated with a dipole model (a) and ray-based diffraction integrals (b).

Topological charges of $m = 0$ and $|m| = 2$ feature a far field with an intensity minimum whereas topological charges of $|m| = 1$ result in a central intensity maximum. Based on the second theoretical approach using vectorial diffraction integrals, ring QCL emission beams with topological charges of $|m| = 0$ and $|m| = 1$ are compared with Gaussian beams with $|m| = 1$ in Fig. 3.48. Corresponding far fields are provided in Fig. 3.48 (a).

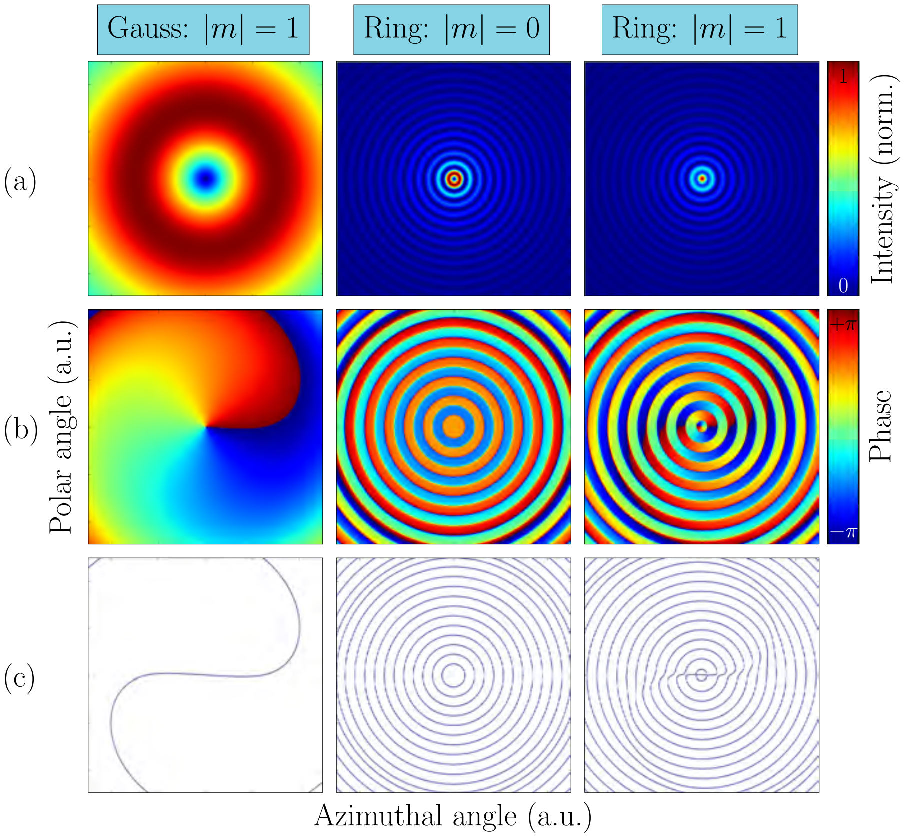

Figure 3.48: (a) Far field patterns of a Gaussian beam, a conventional ring QCL beam and a ring QCL beam carrying an OAM of $|m| = 1$. (b) Phase structure of all three beams. Ring QCLs exhibit a phase difference of π between adjacent interference fringes. The OAM phase structure of a ring laser beam is a superposition of the conventional phase and the OAM spiral phase pattern. (c) Iso-phase lines of the corresponding beams.

The Gaussian beam shows the characteristic donut shape while the ring laser far fields exhibit concentric intensity rings with a central minimum and maximum for the conventional and OAM carrying beam, respectively. Figure 3.48 (b) illustrates the phase of each beam. The OAM carrying Gaussian beam is characterized by a spiral phase pattern whereas for the conventional ring laser a phase difference of π between adjacent interference fringes is observed. At the same time the phase along one interference fringe ring is constant. Ring QCLs carrying OAM possess a phase pattern which is a superposition of the conventional and the spiral phase pattern as shown in the right graph of Fig. 3.48 (b). This superposition is also evident in the iso-phase lines shown in Fig. 3.48 (c). These lines indicate the locations of a phase value of zero.

CHAPTER 4

PHOTONIC SENSING

Prior to the first demonstration of QCLs in 1994 [48] mostly lead salt lasers [203] were utilized for spectroscopic applications in the MIR. Especially the successful realization of room temperature CW QCLs in 2002 [204] paved the way for the widespread use of QCLs in high-resolution spectroscopy and chemical sensing applications [205]. The versatility of QCLs allows implementation in different setups as well as combination with various spectroscopic techniques. Figure 4.1 gives an overview of several spectroscopic techniques utilizing QCLs. Chirped laser dispersion spectroscopy [211] is used to measure the dispersion instead of the absorption of substances in the MIR. In cavity ring-down spectroscopy [207] the light emitted from a QCL is bounced back and forth between two high reflecting mirrors while the decay time yields information about the analyte between both mirrors. Transformation of optical into acoustic information is achieved in quartz-enhanced photo-acoustic spectroscopy [208]. Medical applications could benefit from

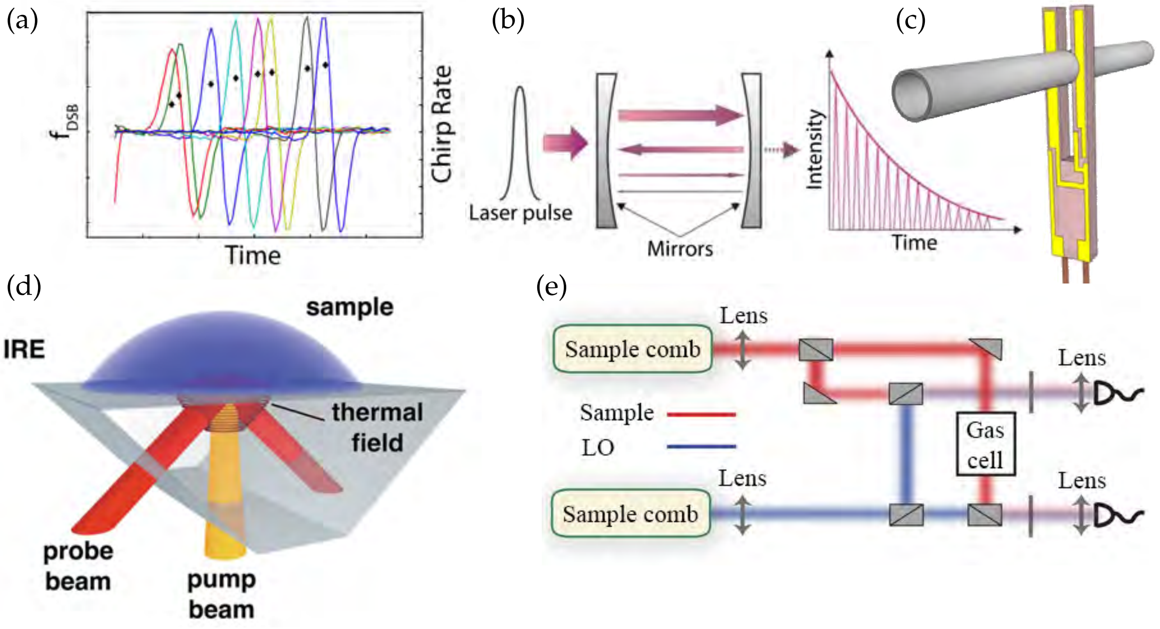

Figure 4.1: Overview of spectroscopic techniques utilizing QCLs. (a) Chirped laser dispersion spectroscopy. (b) Cavity ring-down spectroscopy. (c) Quartz-enhanced photo-acoustic spectroscopy. (d) Photothermal deflectometry. (e) Frequency comb spectroscopy. Reprinted with permission from [206, 207, 208, 209, 210]

QCLs implemented in a photothermal deflectometry [209] setup. Eventually, quantum cascade frequency combs [210] have been realized and implemented for chemical sensing.

In this chapter the suitability of ring QCLs for spectroscopic sensing applications is demonstrated. Due to their small footprint and vertically emitting nature they are ideal light sources for integration into compact hollow waveguides for gas sensing as shown in section 4.1. Utilization of CW ring QCLs at cryogenic temperatures facilitates a heterodyne detection scheme and provides insights into the thermal and electronic characteristics of these lasers. Preliminary results are provided in section 4.2. In the final section 4.3 of this chapter a unique on-chip sensor system based on bi-functional surface emitting and detecting quantum cascade structures for remote sensing is demonstrated.

4.1 Substrate-integrated hollow waveguides

CHEMICAL species in the gas phase are typically analyzed by laser spectroscopy in an open-path measurement or by using a closed gas cell. Conventional cells suffer from several disadvantages including a relatively large size accompanied by a huge gas volume. Furthermore, the limited robustness and portability as well as the requirement for optical alignment especially for multi-pass gas cells restricts the possible fields of application. A novel and innovative concept for miniaturized sensing systems is the substrate-integrated hollow waveguide (iHWG) [212]. It represents a combination of optical waveguide and gas cell with a significantly smaller gas volume than conventional cells. This allows for fast sample transition times, i.e. a fast gas exchange. In addition, a higher volumetric optical efficiency than in long-path or multi-pass gas cells can be achieved. These excellent characteristics facilitate application of iHWGs in compact and efficient sensing tools for environmental monitoring [213, 214], process analytics [215, 216] and medical applications such as breath diagnostics [217, 218]. Due to their vertically emitting nature and collimated rotationally symmetric beam, ring QCLs are ideal light sources to be used in combination with iHWGs. In this study a prototype sensor based on direct absorption spectroscopy is demonstrated. It comprises a dual-color ring QCL and a compact iHWG. A photograph of the respective sensing setup is provided in Fig. 4.2. The light emitted from the ring laser on the left is collimated by a ZnSe lens for optimum coupling to the iHWG. The latter is fabricated from brass and has a total optical path length of 15 cm. The rectangular cross section of the optical channel occupies an area of $2.0\,\mathrm{mm}^2$ resulting in a total gas volume of $300\,\mathrm{mm}^3$ excluding the gas transfer lines. Copper and gold layers are deposited on the polished inner walls of the iHWG for high reflectivity and efficient waveguiding. Front and back end of the cell are sealed with BaF_2 windows. Subsequent to traversing the iHWG, the light is detected by a liquid nitrogen cooled MCT detector. The latter contains a $4\,\mathrm{mm}^2$ large detector element which is directly attached to the iHWG. Due to the non-imaging nature of the iHWG, the exiting light exhibits a rather broad divergence angle which reduces the collected light with an increasing distance between MCT and iHWG. The utilized ring QCL features a continuous π phase shift grating as described in section 3.7. Depending on the driving current the laser provides single or dual mode emission as depicted in Fig. 4.3 (a). In dependence on the analysis carried out in section 3.7 these modes can be associated with the first and second order radial WGMs. Therefore, their spectral lines are well-separated which enables simultaneous detection of two different analytes, namely furan and 2-methoxyethanol vapor. In Fig. 4.3 (b) the light-

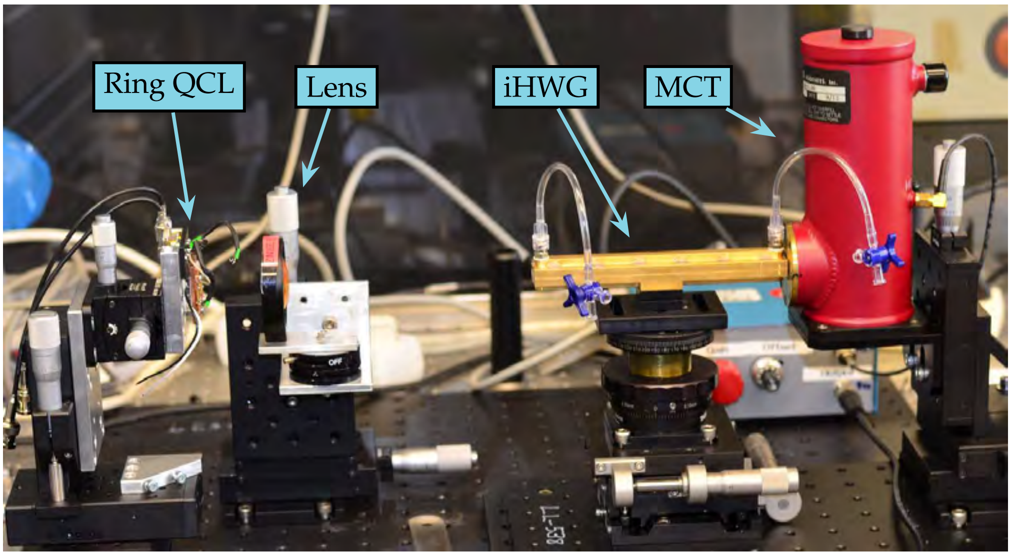

Figure 4.2: Experimental setup including a ring QCL and an iHWG. The light emitted from the ring QCL is coupled to the iHWG via a ZnSe lens. An MCT detector is placed at the other side of the iHWG.

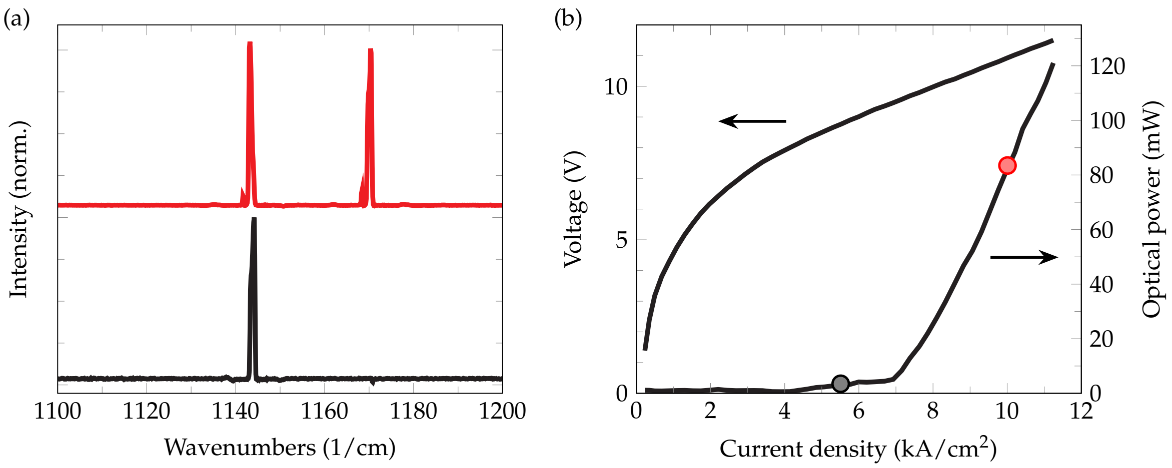

Figure 4.3: (a) Spectra of the dual color ring QCL recorded at 5.5 kA/cm^2 (black) and 10.0 kA/cm^2 (red). The single mode emission at lower driving currents gives way to the dual color emission at higher driving currents. (b) LIV curve of the laser device. The black and red dots mark the operation points at which the spectra in (a) were taken.
Reprinted with permission from [219]

current-voltage (LIV) characteristics of the laser is shown. Between lasing threshold at 4 kA/cm^2 and 7 kA/cm^2 the LI shows a rather linear behavior. In this region the laser exhibits single mode emission at 1144 /cm. At 7 kA/cm^2 a sharp kink in the LI marks the onset of the second order radial WGM. For the rest of the shown LI the laser is in the dual mode regime, simultaneously emitting at 1144 /cm and 1170 /cm. Black and red dots indicate the operation point of the recorded spectra in Fig. 4.3 (a) at 5.5 kA/cm^2 and 10 kA/cm^2, respectively. The dual color emission is given in Fig. 4.4 together with the absorption spectra of furan and 2-methoxyethanol. Furan exhibits a higher absorption at 1170 /cm than at 1144 /cm whereas 2-methoxyethanol shows the reverse behavior with a stronger absorption at 1144 /cm. Several mixtures of furan and 2-methoxyethanol were investigated at the two different driving currents indicated in Fig. 4.3 (b). The results are provided in Fig. 4.5. It shows the measured signal of the ring QCL - iHWG system for a changing furan concentration in 2-methoxyethanol. Fig-

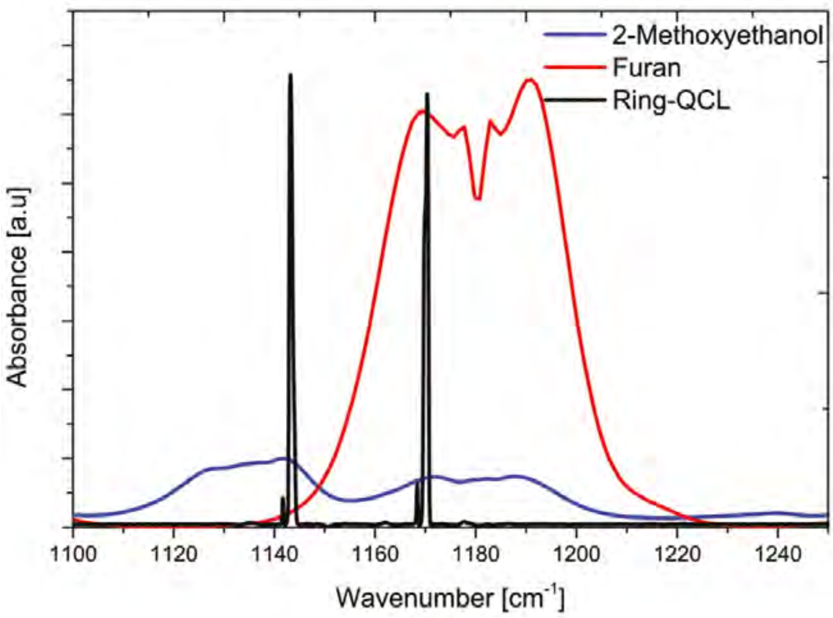

Figure 4.4: Spectrum of the dual color ring QCL on top of the absorption spectra of 2-methoxyethanol and furan showing higher absorption at 1144 /cm and 1170 /cm, respectively.
Reprinted with permission from [219]

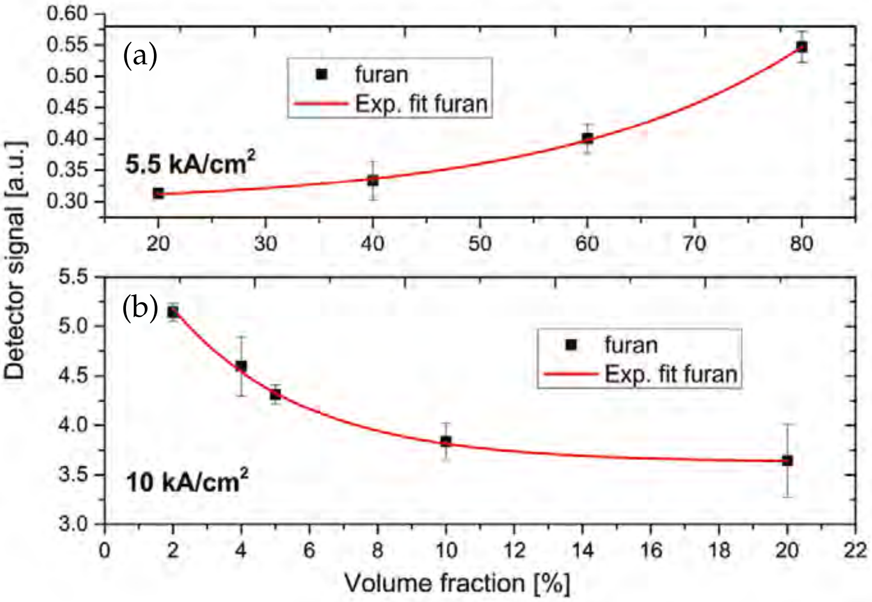

Figure 4.5: Measured detector signal for different mixing ratios between 2-methoxyethanol and furan recorded with single mode emission at 5.5 kA/cm^2 (a) and dual mode emission at 10.0 kA/cm^2 (b). Due to the inverse behavior of the two substances at both emission wavelengths, an increasing and decreasing detector signal is obtained for rising furan concentrations in (a) and (b), respectively.
Reprinted with permission from [219]

ures 4.5 (a) and (b) depict the detector signal for laser driving currents of 5.5 kA/cm^2 and 10 kA/cm^2, respectively. At the former operation point only the spectral line at 1144 /cm is active where 2-methoxyethanol shows a stronger absorption than furan. Hence, an increase of the furan concentration which corresponds to a decrease of the 2-methoxyethanol concentration enhances the detector signal. The experimental data shows a good agreement with the exponential fit according to Beer-Lambert's law. For the operation point at 10 kA/cm^2 both spectral lines are active. Since the maximum absorption of furan is stronger in this wavelength range than for 2-methoxyethanol, it will dominate the absorption behavior of the mixture. Thus, for increasing furan concentrations the detector signal is decreasing. Experiment and theoretical prediction of the Beer-Lambert law exhibit a good agreement. In conclusion, depending on the laser driving current a change in the two component mixture induces an increase or decrease of the detector signal. Hence, the two vapor phase analytes were successfully detected and quantified. This study represents a proof-of-principle for combining ring QCLs and iHWG. As evident from the experimental setup shown in Fig. 4.2 the system is rather large and does not exploit the entire miniaturization potential, yet. Ongoing investigations focus on a direct integration of laser and detector on the iHWG. Such a compact, robust and versatile sensor could be used in various fields and even enable completely novel applications requiring small and lightweight sensor systems. [219]

4.2 Heterodyne phase-sensitive detection

UTILIZATION of single mode CW QCLs enables efficient tunable laser spectroscopy. The latter is characterized by a systematic variation of the injected laser current. The operation speed for such a current modulation is fundamentally limited by the picosecond intersubband carrier lifetimes which theoretically allow modulation bandwidths up to the THz regime [220]. A modulation of the laser driving current induces a change in the refractive index and therefore shifts the emission wavelength of the laser. Two main effects contribute to this effect. Joule heating as well as a strong light-carrier interaction due to increased carrier densities influence the refractive index of the active region. They are associated with thermal and electronic tuning, respectively. Since the former is a rather slow process it dominates in the low frequency domain where the temperature is capable of following the modulation current. In the high frequency domain the current modulation is too fast for the temperature and only the electronic condition inside the active region contributes to the change of the refractive index. Hence, electronic tuning dominates at high modulation frequencies.

A current modulation can be quantitatively described by

$$I_L(t) = I_0 + \Delta I \cos\left(2\pi f_M t\right) \tag{4.2.1}$$

with the modulation frequency f_M, the DC current I_0 and the current modulation amplitude ΔI. Assuming a non-zero slope-efficiency such a current modulation induces also a modulation of the emitted power

$$P_L(t) = P_0 + \Delta P \cos\left(2\pi f_M t - \Phi_{IM}\right) \tag{4.2.2}$$

with the average power P_0, the power amplitude ΔP and the intensity modulation (IM) phase shift Φ_{IM} between modulated current and modulated power. Due to the varying refractive index Eq. (4.2.1) is accompanied by the following modulation of the emitted frequency

$$f_L(t) = f_0 + \Delta f \cos\left(2\pi f_M t - \Phi_{IM} + \Theta\right) \tag{4.2.3}$$

with the center frequency f_0, the frequency amplitude Δf and the phase shift Θ between IM and frequency modulation (FM). A systematic variation of the emission frequency is equivalent to a beat note signal originating from several emitters with distinct frequencies given by $f_0 \pm f_M$. This results in the formation of sidebands around the center frequency. Utilization of such a light source for the detection of chemical species with sharp absorption features introduces favorable properties. In the vicinity of a molecular absorption line the real part of the refractive index assumes the slope shown in Fig. 4.6 (a) [221]. Its mathematical representation is given by

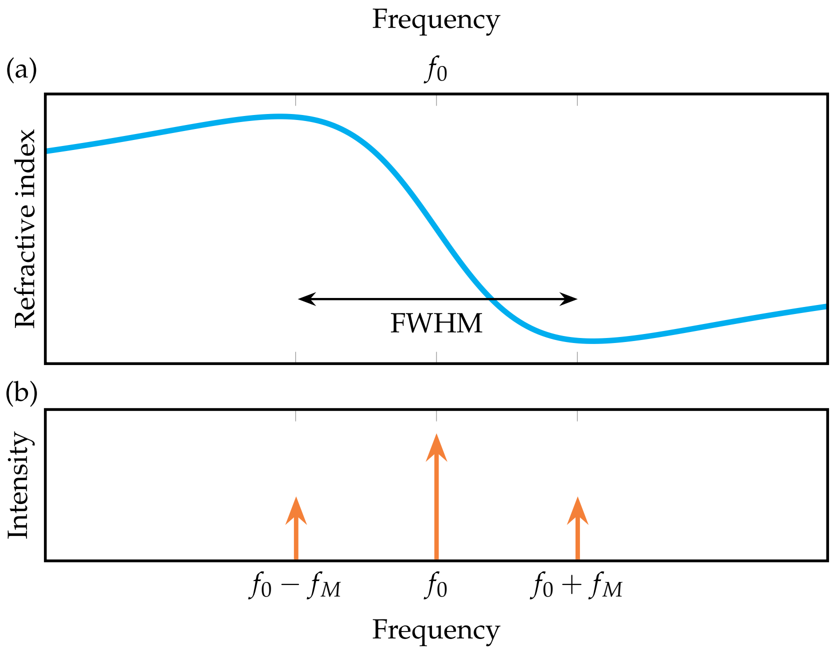

Figure 4.6: (a) Refractive index in the vicinity of a molecular absorption line. (b) Emission spectrum of a current-modulated laser with the central laser frequency f_0 and two distinct sidebands. Reprinted with permission from [222]

$$n(f) = n_0 + x_s \frac{f_0 - f}{(f_0 - f)^2 + (\mathrm{FWHM}/2)^2} \tag{4.2.4}$$

with the center frequency f_0 of the molecular transition and the variable x_s describing the spectral line. Precise spectral alignment of the central laser frequency and its sidebands, as shown in Fig. 4.6 (b), facilitates the determination of the refractive index shape. A matching of the location of the sidebands for a maximum refractive index difference is possible via tuning of the modulation frequency. While propagating through the medium the different emission lines experience different refractive indices and therefore travel at different speeds. In turn, this corresponds to a change in the relative phase between the emission lines. In the low concentration approximation this beat note phase can be written as [222]

$$\Theta = \frac{f_0 L}{2c} \left[n(f_0 + f_M) - n(f_0 - f_M) \right] \tag{4.2.5}$$

with the light-analyte interaction path length L. Hence, the measurement of the beat note phase enables a quantitative determination of the species concentration. This sensing technique is referred to as heterodyne phase-sensitive detection (HPSD) and measures the refractive index of the analyte which is in contrast to conventional sensing methods based on absorption according to the Beer-Lambert law [223, 224, 225]. [222, 226]

Furthermore, probing the IM and FM properties of a laser provides detailed information about its thermal and electronic characteristics. With this goal in mind a current modulated ring QCL was operated in CW mode at liquid nitrogen temperatures. A 10 cm long gas cell filled with 0.4% of CH_4 in N_2 was utilized for the following experiments. Figure 4.7 shows the amplitude (a) and the FM-IM phase (b) recorded with an MCT detector for a modulation frequency of $f_M = 100\,\mathrm{MHz}$ and a DC current of $I_0 = 200\,\mathrm{mA}$. The signal from the MCT was fed into a mixer and down-mixed to 100 kHz. The latter was then detected via a lock-in amplifier. Two absorption features of the gas are evident in Fig. 4.7. Only the larger feature at 1322.08 /cm was fitted and used for the following analysis. Several modulation frequencies from 1 − 150 MHz were implemented for different operation points (DC currents) of the laser. The latter required an adjustment of the operation temperature in order to spectrally compensate the temperature effect of the DC current. Details are provided in Tab. 4.1. Figure 4.8 provides the ratio $\Delta f/m = \Delta f/(\Delta P/P_0)$ (a) between absolute frequency modulation and normalized intensity modulation as well as the FM-IM phase shift Θ (b) for all DC currents and modulations frequencies. Between 150 MHz and 30 MHz no significant change is evident. However, below 20 MHz the rise in the FM-IM ratio in combination with the changes of the phase implies the onset of thermal tuning in the ring QCL. The here presented measurements represent a feasibility study and form the basis for ongoing investigations of the tuning characteristics of ring QCLs. Especially potential differences in the tuning behavior between straight ridge-type QCLs and circular ring QCLs are subject of current research studies. [222, 226]

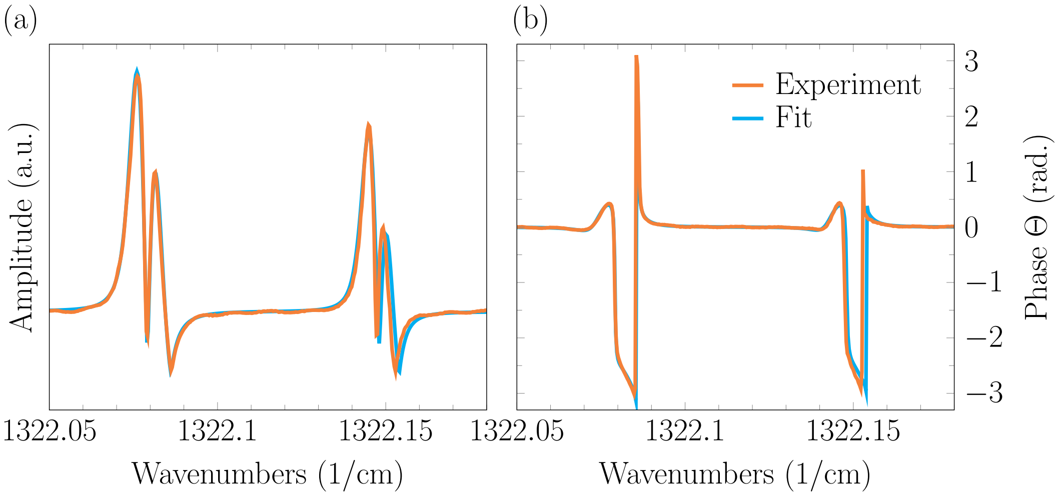

Figure 4.7: Obtained amplitude (a) and FM-IM phase (b) of an exemplary measurement with a modulation frequency of 100 MHz and a DC current of 200 mA. Experimental data (orange) and fit (blue) are in good agreement. Two distinct absorption features at 1322.08 /cm and 1322.15 /cm are observed. For the following analysis, summarized in Fig. 4.8, only the first feature at 1322.08 /cm was considered.

DC current	65 mA	101 mA	150 mA	200 mA
Temperature	118 K	110 K	100 K	88 K

Table 4.1: Laser submount temperatures at different DC currents were utilized in order to compensate for the spectral shift introduced by thermal effects of the DC current.

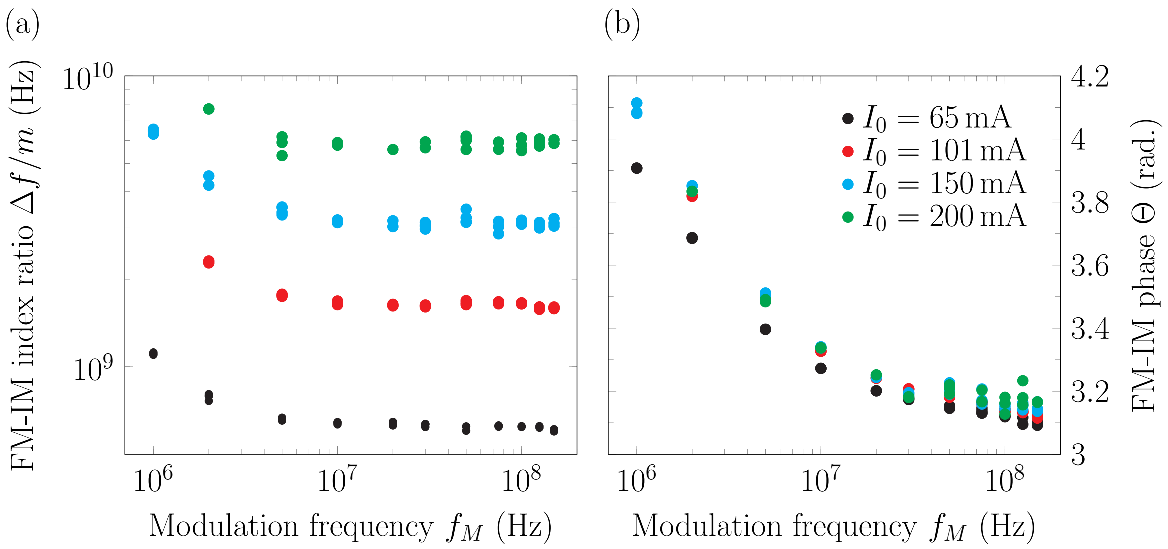

Figure 4.8: FM-IM index ratio (a) and FM-IM phase shift (b) as a function of the modulation frequency f_M for different DC currents ranging from 65 mA to 200 mA. The FM-IM index ratio shows a steady scaling with the DC current. Both, index ratio and phase, exhibit an increase for modulation frequencies below 20 MHz which indicates the onset of thermal tuning in ring QCLs.

4.3 Remote sensing

Several spectroscopic sensing techniques utilizing QCLs have been introduced in Fig. 4.1. The latter impressively demonstrates the versatility of QCLs. However, most spectroscopic applications are based on the same fundamental sensing setup. It consists of a light source, a light-analyte interaction region and a separate external detector. In this section an innovative concept is introduced combining light source and detector on a single chip. Wavelength-matching between the monolithic laser and detector is achieved by implementing bi-functional quantum cascade heterostructures [227]. Sensing systems based completely on quantum cascade technology [228] have already been demonstrated. However, in such sensor system laser and detector components originate from dissimilar growths and are placed on different chips which does not fully exploit the potential of quantum cascade systems. The first quantum cascade on-chip sensor for liquids was published by Schwarz et al. in 2014 [229]. Based on this heterostructure surface emitting and detecting gas sensors [230] have been developed in the course of this dissertation. The design and realization as well as proof-of-principle gas sensing measurements are provided in section 4.3.3. Building on this approach an innovative sensor concept is introduced in section 4.3.4. It features two commutable surface emitting and detecting ring quantum cascade laser/detector structures for efficient sensing of chemical substances [231]. Both rings can be alternately operated as laser and detector which not only facilitates compact chemical sensors but also enables a versatile and efficient implementation in various spectroscopic sensing applications. In the following sections 4.3.1 and 4.3.2 introductions of QCDs and bi-functional heterostructures are provided.

4.3.1 Quantum cascade detectors

Imaging and sensing applications are the major forces behind the advancement of infrared detector technology. Especially quantum cascade detectors (QCDs) have recently emerged from unexplored intersubband devices to sophisticated infrared detectors used in complex systems for imaging [232] and spectroscopic sensing [228]. They emerged from quantum well infrared photodetectors (QWIPs) and consist of a semiconductor heterostructure enabling tailorable absorption characteristics similar to QCLs. In contrast to photoconductive QWIPs, QCDs do *not* require an external bias voltage which reduces the dark current. QWIPs were first demonstrated in 1987 by Levine [57]. They consist of a series of quantum wells as shown in Fig. 4.9 (a). In the bound-to-quasibound scheme each quantum well possesses two energy levels. The detection energy is given by the energetic separation of these two levels. Incoming radiation lifts electrons from the lower energy level to the upper level which is in resonance with the barrier edge for efficient electronic extraction. This concept for infrared detectors enabled a myriad of applications [59, 233]. In principle, photovoltaic QWIPs [234, 235] can be operated without external bias and exhibit superior noise properties with no dark current and enable higher photon fluxes than photoconductive QWIPs. This is enabled by the built-in inversion asymmetry which plays the role of an internal field. The latter defines the predominant direction of the electron motion. For symmetric photoconductive QWIPs this task is undertaken by the applied electric field.

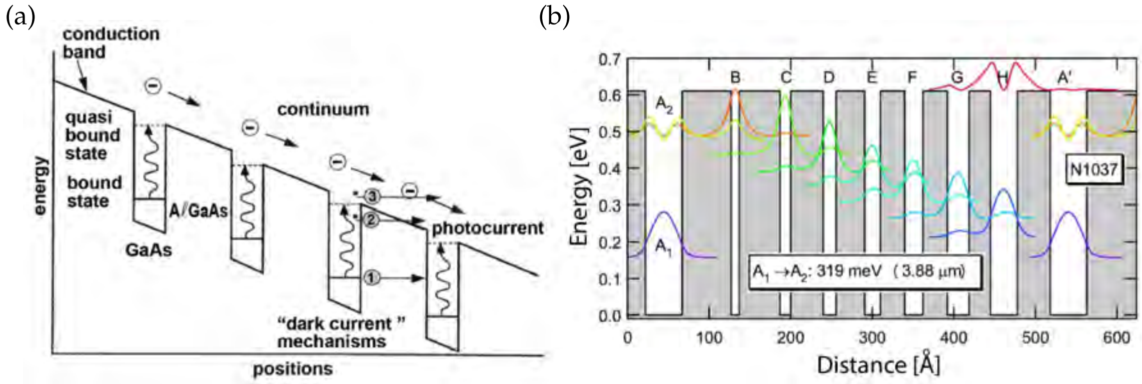

Figure 4.9: Working principle of QWIPs (a) and QCDs (b). In a QWIP electrons in a quantum well are excited to an upper quasi bound level by incoming radiation. This upper level is resonant with the conduction band edge which facilitates coupling to the continuum and efficient carrier extraction by the applied voltage. A QCD operates without external bias and therefore exhibits no dark current. An electron is excited from level A_1 to A_2 by an incoming photon before it cascades from quantum well B to H where it enters the first quantum well A_1' of the next active region of the QCD.
Reprinted with permission from [59, 233]

In 2002 Hofstetter et al. demonstrated that a quantum cascade laser heterostructure is capable of detecting light when unbiased [236]. This discovery paved the way for the first designed QCD in 2004 [237]. Nowadays, QCDs are deployed for applications in the MIR [60], near-infrared [238] and THz [239] spectral region. The schematic in Fig. 4.9 (b) depicts the heterostructure and energy levels with the respective wavefunctions of a QCD period. The optical transition occurs in the thick doped quantum well from level A_1 to A_2. Subsequently, the electrons follow the undoped extraction cascade from quantum well B to H. This implementation introduces an asymmetry to the heterostructure which induces a predominant direction for the motion of the photoexcited electrons resulting in a net photocurrent. Since no external field is necessary to obtain this electronic flow, no dark current noise is present. Similar as in QCLs, the thickness of the quantum wells as well as their material composition determine the energetic levels and therefore the wavelength at which the QCD is sensitive. A figure of merit for QCDs is the responsivity

R. It is defined as the ratio

$$R = \frac{I_s}{P_s} = \frac{e\eta g_p}{h\nu} = \frac{\lambda e\eta g_p}{hc} \tag{4.3.1}$$

between generated output current I_s and incoming radiation power P_s. In this notation e is the electronic charge, η is the absorption efficiency and

$$g_p = \frac{p_e}{N_p p_c} \tag{4.3.2}$$

is the detector gain with the extraction probability p_e, the capture probability p_c and the number of periods N_p. For QCDs a common assumption is $p_c = 1$. According to Eq. (4.3.2) the detector gain is inversely proportional to the number of periods which is in contrast to the behavior of the lasing gain in QCLs as discussed in section 2.2.6. Since one absorbed photon only carries an electron from one period to the next, a total number of N_p photons is necessary to enable a single electron to traverse the entire heterostructure and contribute to the measurable detector current. Based on Eq. (4.3.2) as few periods as possible seem to be desirable for QCDs. However, increasing N_p delivers a higher device resistance which is beneficial for the detectivity

$$D^* = \frac{R_{\text{max}}}{I_n}\sqrt{A\Delta f_{\text{QCD}}} \tag{4.3.3}$$

due to a lower Johnson noise. In Eq. (4.3.3) the maximum responsivity is denoted by R_{max}, the noise current is given by I_n, the detector area is A and the measurement bandwidth is identified by Δf_{QCD}. Above the background limited infrared performance temperature the detectivity can be expressed as

$$D^*_J = R_{\text{max}}\sqrt{\frac{AR_0}{4k_bT}} \tag{4.3.4}$$

with the differential devices resistance R_0.

The intersubband selection rule discussed in section 2.2.3 holds not only for QCLs but for QCDs as well. Hence, normal incident light cannot be detected efficiently [240]. Thus, coupling strategies like the 45° mesa, the Brewster angle configuration [241] or grating couplers [242] have to be exploited. In recent years advanced approaches including the application of photonic crystals [243], metamaterials [244] and plasmonic lenses [245] as well as scattering induced coupling [246] of normal incident light to the QCDs active region have been demonstrated. [61, 62, 241, 247]

4.3.2 Introduction to bi-functional heterostructures

Realization of efficient ultra-compact optical sensors requires the implementation of emitter and detector on a single chip. Although wafer bonding techniques [248, 249] represent a valid approach, a more elegant solution is the creation of a bi-functional semiconductor chip which enables wavelength-matched emission and detection from monolithically integrated lasers and detectors. Such concepts were already realized decades ago for band gap devices [250]. However, it was only recently that a successful implementation was realized for quantum cascade structures [227]. When biased they provide laser emission whereas the unbiased device is a detector. The main obstacle in designing a bi-functional quantum cascade device is the wavelength mismatch between laser and detector mode.

Since in unbiased detector operation the optical transition occurs between the upper laser level and an extraction level instead of the energetically elevated lower laser level, this results in a blue shift of the detector spectrum. A reduction of the coupling between lower laser level and extraction levels through thicker barriers as well as an additional narrow well between injector and active well can compensate this energy shift. A red shift of the optical transition is observed when the narrow well level is strongly coupled to the upper laser level, as is the case in the detector mode. In the lasing configuration this narrow well level shifts to higher energies which reduces the coupling and consequently results in an effective red shift of the detector transition. Fine tuning of the width of the narrow well allows for a matching of laser and detector spectrum for specified operation temperatures. Figure 4.10 (a) indicates the wavelength overlap between laser and detector at room temperature. Combination of bi-functional laser/detector devices with a waveguiding structure on a single chip as illustrated in Fig. 4.10 (b) facilitates the realization of lab-on-a-chip sensors for the analysis of liquid species [229, 252].

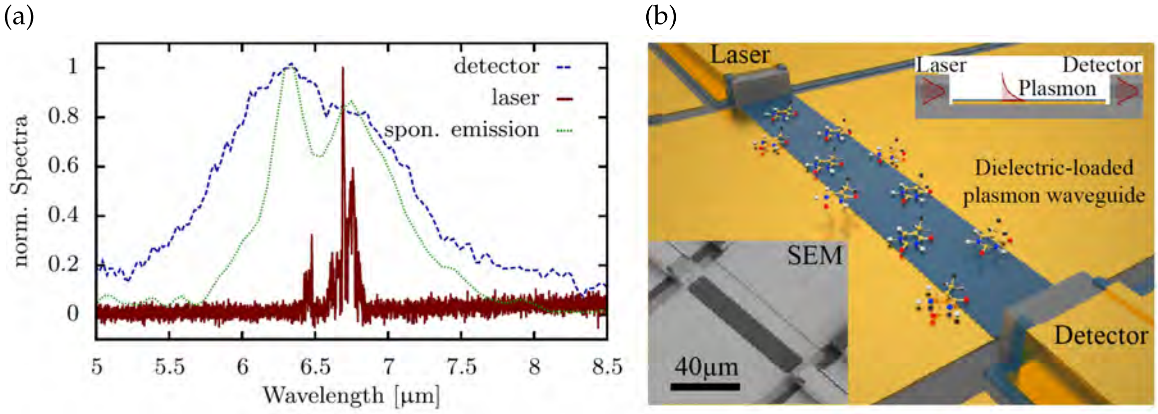

Figure 4.10: (a) Laser (brown solid) and detector (blue dashed) spectra as well as spontaneous emission (green dotted) of a bi-functional quantum cascade device with a designed wavelength overlap. (b) On-chip sensor for liquids consisting of a monolithic quantum cascade laser and detector. The insets depict a SEM image of the sensor and a schematic of its working principle.
Reprinted with permission from [229, 251]

4.3.3 Surface active transceiver

As a result of the limited size of typical semiconductor chips, the sensing approach presented in section 4.3.2 is not feasible for gaseous analytes which usually require larger light-analyte-interaction paths on the order of centimeters or meters. Although photonic on-chip gas sensing [253] is possible, it requires complex chip designs in combination with precise control of the light on the chip. Hence, such approaches are not accessible for quantum cascade material systems, yet. An alternative approach for “quasi” on-chip gas sensing is to outsource the analyte-interaction zone from the chip while keeping the monolithic laser and detector. Following this approach vertically emitting and detecting devices provide several advantages over facet emitters, e.g. the possibility for two dimensional integration. In this section the first prototype of a surface active on-chip gas sensor based on bi-functional quantum cascade heterostructures is demonstrated. A SEM image of this surface transceiving device is depicted in Fig. 4.11 (a). It consists of a ring QCL surrounding a circular detector element. The ring laser facilitates light outcoupling via a second order DFB grating shown in Fig. 4.11 (b). The detector centered within the ring laser is capable of normal incident light absorption via a metal

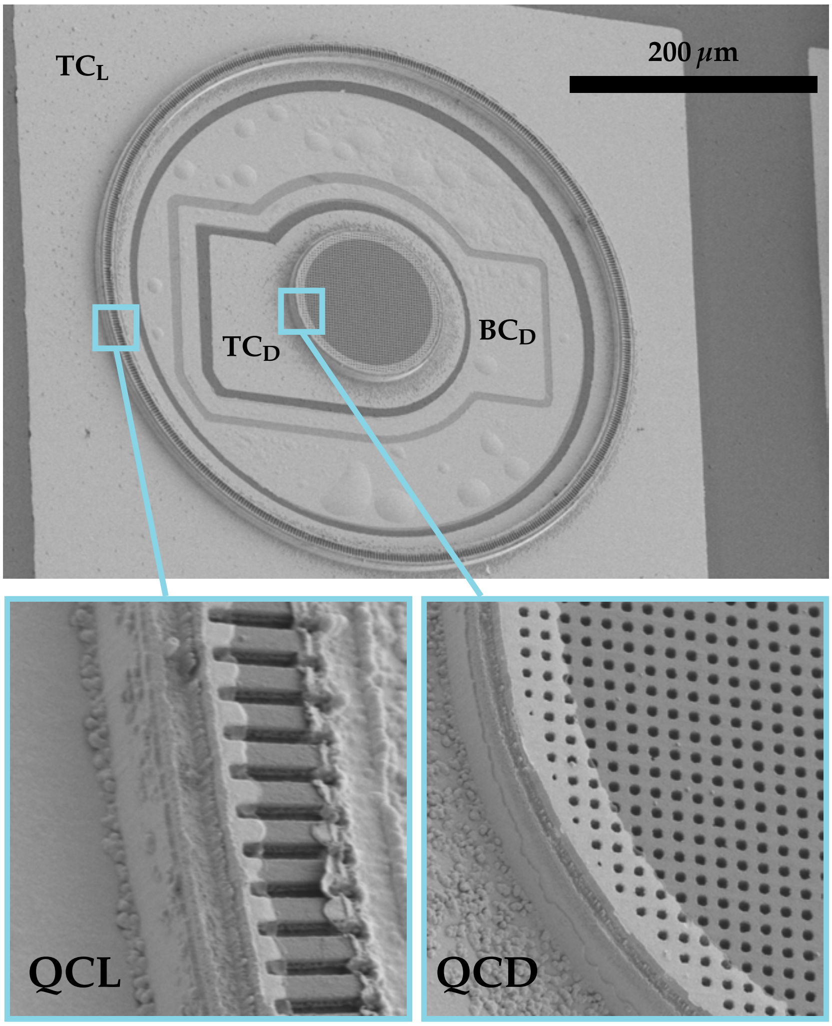

Figure 4.11: SEM images of the surface active transceiver. The ring QCL provides light emission via the second order DFB grating and the centered disk QCD facilitates detection of vertically incident light via the metal hole grating.

hole grating presented in Fig. 4.11 (c). Its period is 2 μm and the diameter of each hole amounts to roughly 1 μm, resulting in a duty-cycle of 50%. In addition to optical coupling, the metal hole grating also serves as part of the detector's extended top contact marked by $\mathrm{TC_D}$ in Fig. 4.11 (a). Its bottom contact is labeled $\mathrm{BC_D}$. The laser top contact is given by $\mathrm{TC_L}$ and its bottom contact is formed by the InP substrate. This configuration ensures potential stability for the detector. Prior to a simultaneous operation of laser and detector, both devices were characterized separately. The corresponding measurement setups are depicted in Fig. 4.12 (a). For characterization of the ring laser the semiconductor chip is placed in front of a ZnSe lens which couples the emitted light to an FTIR spectrometer. Spectral information as well as power characteristic of the laser are obtained by focusing the light onto a calibrated deuterated triglycine sulfate (DTGS) detector inside the spectrometer. Characterization of the detector requires the utilization of a rotating chopper and the integrated broadband globar source of the FTIR. Laser and detector spectra recorded at 80 K are provided in Fig. 4.12 (b) and demonstrate the spectral overlap around 6.5 μm. While the laser produces single mode emission at 1514 /cm, the detector features a rather broad absorption spectrum with measurable sensitivity from 1350 /cm to 1700 /cm with a peak responsivity of 2.4 mA/W at 1566 /cm measured at 80 K. The on-chip sensing scheme is sketched in Fig. 4.13 (a). In Fig. 4.13 (b) the power characteristics of the ring QCL are investigated

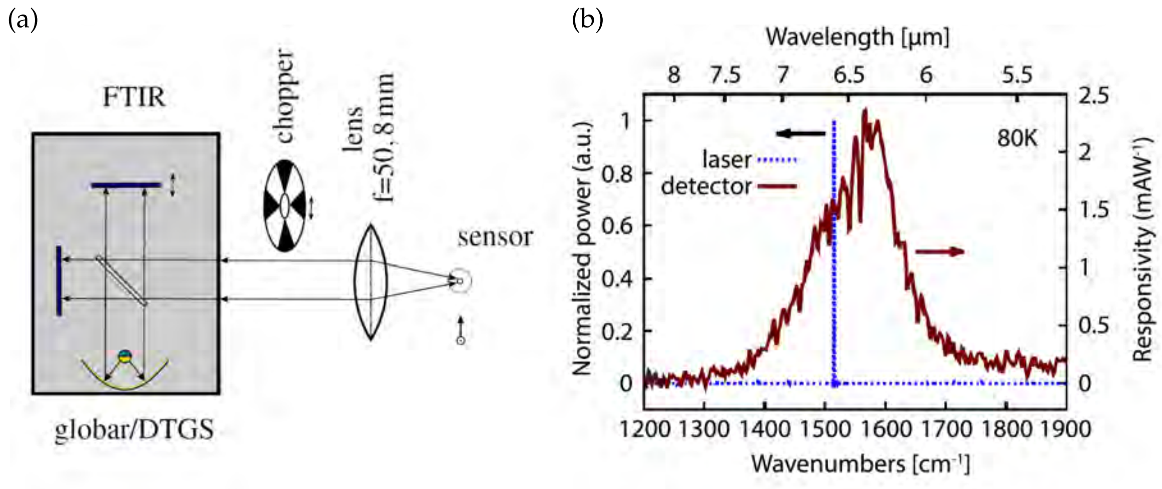

Figure 4.12: (a) Setup utilized for the characterization of the surface active transceiver. (b) Spectra of the ring laser (blue dotted) and disk detector (brown solid) recorded at 80 K with a wavelength overlap at 6.5 μm.
Reprinted with permission from [230]

by means of the external DTGS detector associated with the blue dotted curve and the on-chip detector represented by the brown solid line. Light emitted from the sensor chip

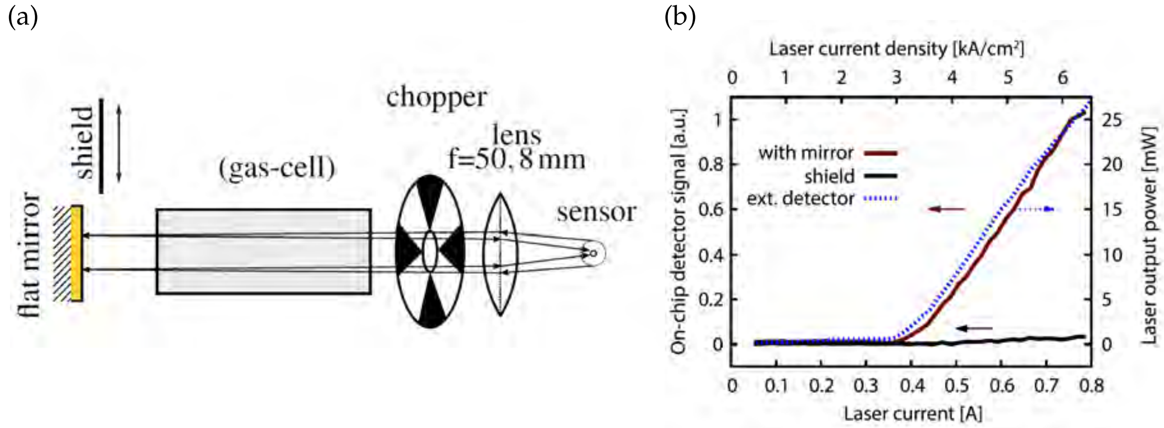

Figure 4.13: (a) Sensing setup. Light emitted from the ring laser is collimated by a lens and propagates through the gas cell before it is back-reflected by the flat gold mirror and takes the initial path back to the sensor chip where it is detected by the disk detector. (b) LI curves recorded with an external DTGS detector (blue dotted) and the on-chip detector (brown solid). In order to verify that the measured signal originates from the back-reflected light, the mirror was covered with a low reflecting shield. The corresponding LI curve is given by the black solid line and shows a negligible detector signal.
Reprinted with permission from [230]

is collimated by a ZnSe lens with a focal distance of $f = 50.8\,\text{mm}$. Subsequently, the light is modulated by a rotating chopper which is required in order to filter the crosstalk between laser and detector. Back-reflection from the flat gold mirror forces the laser beam to reversely propagate on its initial path back through the chopper and the lens before it impinges on the sensor chip. The recorded LI of the laser exhibits a threshold current density of $3\,\text{kA/cm}^2$ which is perceived in both detection schemes. Furthermore, the power behavior of the laser for all applied currents is successfully identified by the on-chip detector demonstrating a good agreement with the DTGS measurement. In order to eliminate the possibility of electrical contributions (crosstalk) to the detector signal the LI was recorded with an absorbing shield blocking the mirror and therefore preventing back-reflection of light to the sensor chip. The respective detector signal as a function of the applied current recorded in this configuration is given by the black solid curve in Fig. 4.13 (b) and exposes a negligible signal. In addition to residual electrical crosstalk, the remaining signal can arise due to reflections from the gas cell. Hence, the previously obtained detector signal associated with the brown curve in Fig. 4.13 (b) can be mainly attributed to an optical signal from the back-reflected light which verifies the working principle of this sensor. Proof-of-concept gas measurements were conducted using this on-chip laser/detector system. Therefore, a gas cell with a length of 10 cm was placed between mirror and chopper as indicated in Fig. 4.13 (a). Isobutane/nitrogen and propane/nitrogen mixtures were investigated. Absorbance spectra of these two alkanes, taken from the Pacific Northwest National Laboratory (PNNL) database [254], are provided in Fig. 4.14 (a). Nitrogen is assumed not to show any

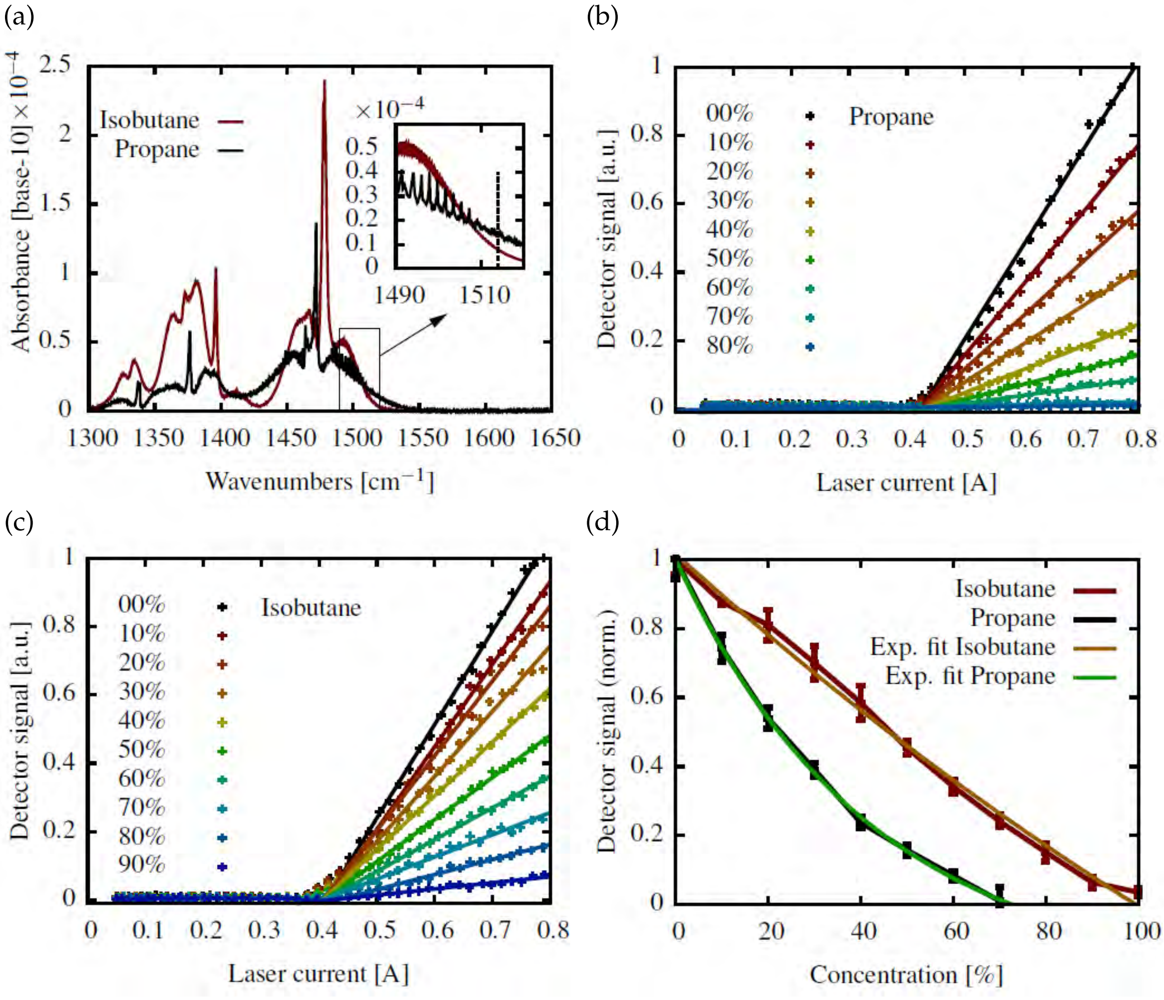

Figure 4.14: (a) Absorption spectra of isobutane and propane. The inset shows a magnified section of the spectra around the laser emission wavelength given by the black dashed vertical line. (b) and (c) provide LI curves recorded for different gas concentrations of propane and isobutane, respectively. A higher gas concentration decreases the detector signal along the entire range of the LI curve. (d) Measured detector signal (data points) and exponential fits (solid lines) for both gases as a function of the concentration. Since propane exhibits a higher absorbance at the laser emission wavelength the detector signal shows a stronger decline with increasing gas concentration.
Reprinted with permission from [230]

absorption in this wavelength range. At the emission wavelength of the laser, indicated by the vertical dashed line in the inset of Fig. 4.14 (a), propane exhibits a stronger absorption than isobutane. The experimental procedure for the analysis of both gases stipulates the recording of the entire LI from 0 A to 0.8 A for different gas concentrations. The laser is operated in pulsed mode with a pulse length of 100 ns and a repetition rate of 20 kHz at 80 K. Within the cell the gases are kept at room temperature and ambient pressure. A constant flow rate of 3 L/min was ensured. Results of these measurements are presented in Fig. 4.14 (b) and (c) for propane and isobutane, respectively. Increasing the gas concentration induces a decline of the measured on-chip detector signal at every operation point above the lasing threshold. In order to quantify the experimental results symbolized by the "+" signs, linear fits for currents between 0.44 A and 0.8 A for every recorded LI are obtained. The fit values at 0.8 A were utilized to express the detector signal as a function of the gas concentration as shown in Fig. 4.14 (d). Experimental data and exponential fits according to the Beer-Lambert law are in agreement within the specified errors of the experiment. Since propane exhibits a stronger absorption at the laser emission wavelength, the measured detector signal shows a faster decline with increasing gas concentration than for isobutane. [230]

The performance of the here presented on-chip sensor strongly depends on the light pattern incident on the chip after reflection from the flat gold mirror. However, this information is not readily obtained since placing a camera or detector element between semiconductor chip and lens to capture the light reflected from the mirror would block the initial laser beam. Therefore, the setup shown in Fig. 4.13 (a) was mirrored along the mirror plane, as shown in Fig. 4.15, in order to replicate the beam in a non-reflecting fashion, which allows to obtain the intensity distribution with a bolometer camera. The mirror was removed from the original setup and replaced by a second lens which is identical to the first one. The second lens collimates the parallel beam and creates a beam pattern onto the bolometer camera which is in good approximation identical

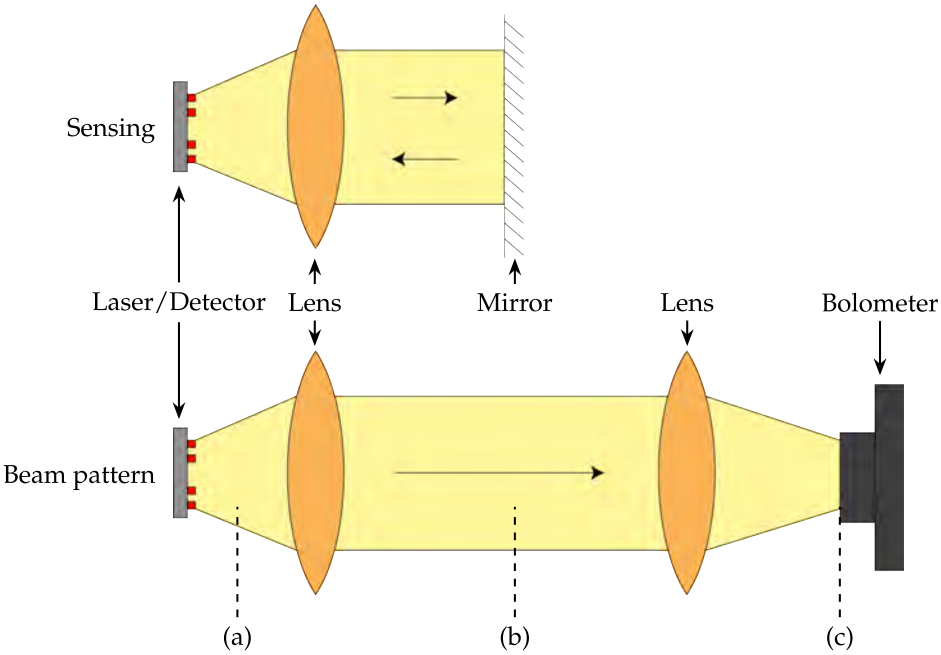

Figure 4.15: Sensing setup compared with the mirrored setup for the investigation of the beam pattern incident on the sensor chip. The mirror in the sensing setup is replaced by a second lens which projects the beam pattern on the bolometer camera. (a), (b) and (c) denote the planes at which the intensity patterns in Fig. 4.16 were recorded.

to the beam incident on the sensor chip in the original setup. Figure 4.16 depicts the beam patterns recorded at different locations in the setup. Without any optical components, directly after the semiconductor chip (a), the beam consists of concentric intensity rings as discussed in section 3.2. The large ring-shaped intensity accumulation at ±4° originates from reflections at the cryostat window. In the mirror plane (b) the beam features a ring intensity pattern with a diameter of roughly 2 mm and stray light in its center. Figure 4.16 (c) shows the beam profile recorded after the second lens at a distance equal to the distance between sensor chip and first lens. Hence, this beam pattern describes the intensity distribution incident on the detector when utilizing the sensing setup in Fig. 4.13 (a). Again the beam mainly consists of a ring shaped intensity pattern with a diameter of $8-12$ pixels of the bolometer camera. Considering the pixel pitch of $52\,\mu$m this results in a diameter of $416-624\,\mu$m which roughly corresponds to the $400\,\mu$m diameter of the ring QCL. Consequently, most of the emitted light is *not* incident on the centered detector element. Mainly, the central peak of the intensity distribution, originating from parasitic reflections, contributes to the measured detector signal. Optimization of the detector geometry is capable of significantly improving the sensor performance. [230]

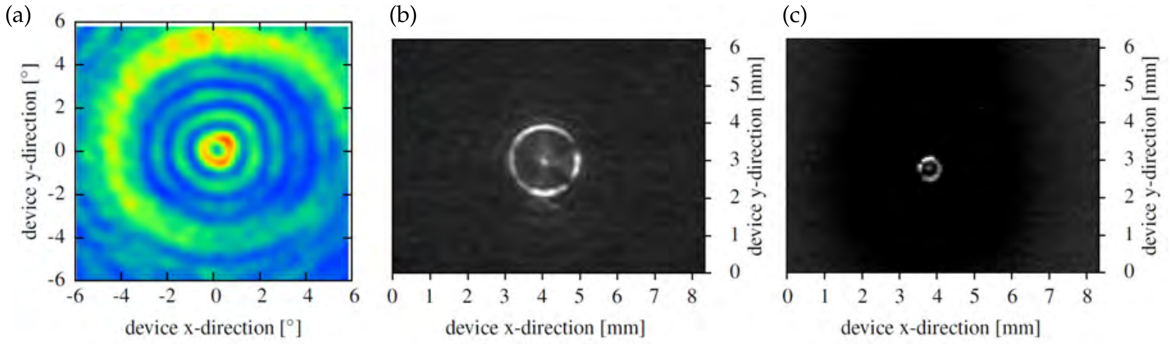

Figure 4.16: Beam patterns recorded at the planes specified in Fig. 4.15. (a) The light distribution is recorded without any optical elements and consists of concentric intensity rings. The large intensity ring at around ±4° is caused by reflections at the cryostat window. (b) Laser beam in the mirror plane forming a ring shaped intensity pattern. (c) Beam pattern focused on the bolometer camera. The ring shaped intensity distribution represents the laser beam incident on the sensor chip in the sensing setup. The intensity ring possesses a diameter of roughly the diameter of the ring QCL. Consequently, most of the emitted light is *not* incident on the centered disk detector.
Reprinted with permission from [230]

4.3.4 Commutable laser/detector sensor

As described in the introduction of this chapter, conventional sensing setups consist of a light source, a light-analyte-interaction region and a separate external detector. In this configuration QCLs find plenty of applications and are implemented in combination with various spectroscopic techniques. The gas sensor prototype presented in section 4.3.3 marks the first step towards compact integrated sensor systems with a revolutionary operation principle. Integration of laser and detector elements on a single chip facilitates a significant miniaturization of optical sensors and enables unprecedented applications in environmental monitoring as well as medical and biochemical applications. In this final section a highly integrated surface active sensor is demonstrated. Based on the sensor concept introduced in the previous section it provides an improved detector geometry which is matched to the emission beam pattern. Therefore, the laser-detector coupling is drastically enhanced which not only results in room temperature operation but also facilitates precise gas sensing measurements with detection limits in the parts-per-million (ppm) range.

A sketch of this sensor is provided in Fig. 4.17. Two concentric ring structures featuring second order DFB gratings are monolithically integrated on a single chip. The grating enables not only vertical light emission but also detection of normal incident light. The diameters of the inner and outer ring are 330 μm and 400 μm, respectively. Each ring possesses own top (TC) and bottom (BC) contacts to filter the electrical crosstalk. This is crucial in order to enable alternating operation of both rings in the lasing and detection mode, i.e. both rings can be used as laser *and* detector. Figure A.4 in appendix A.6 depicts a SEM image of the entire device. A closeup SEM image of the ring waveguides and the DFB gratings is provided in the inset of Fig. 4.17. The spectral performance of inner and outer ring at room temperature is indicated in the lower and upper panel in Fig. 4.18, respectively. Both rings show single mode lasing around 1484 /cm. In contrast, their broadband absorption feature in the detector mode covers the wavelength range from 1200 /cm to 1700 /cm with a room temperature peak responsivity of 1.2 mA/W at 1481 /cm. This precise spectral overlap facilitates efficient optical coupling between laser and detector. The capability to switch between lasing and detection mode renders the differentiation between laser and detector needless and creates a sensor system with commutable laser/detector elements. The basis for this permutability is the second order DFB grating. As discussed in section 2.3.2 and 3.1.1 it provides optical feedback to the laser and enables vertical light outcoupling. Normal incident light is refracted

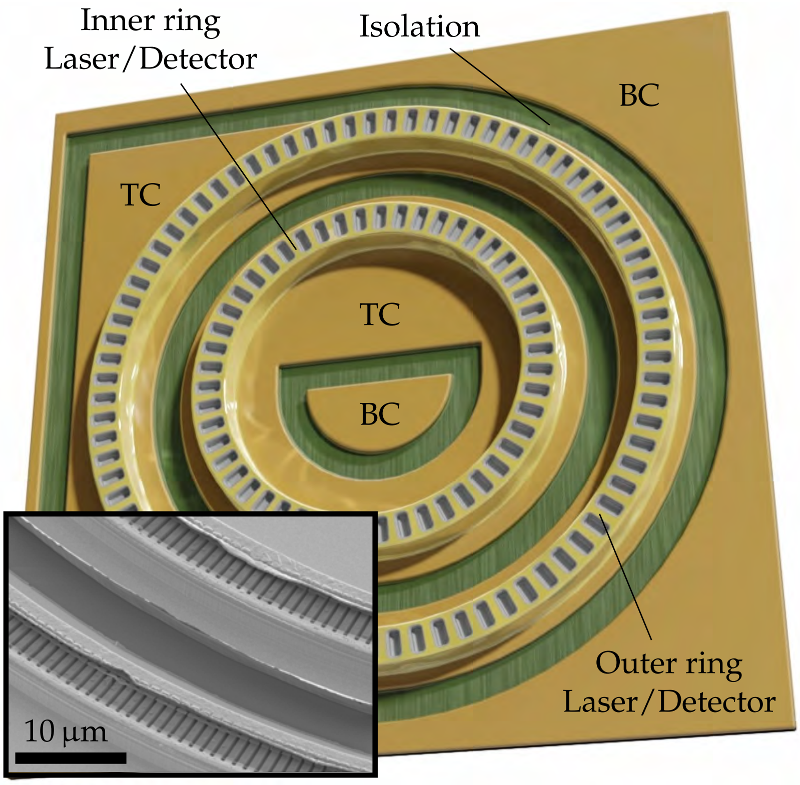

Figure 4.17: Sketch of the commutable on-chip sensor consisting of two concentrically aligned ring structures with a second order DFB grating for light emission and detection. The inset shows a SEM image of both ring waveguides with their DFB gratings.
Reprinted with permission from [231]

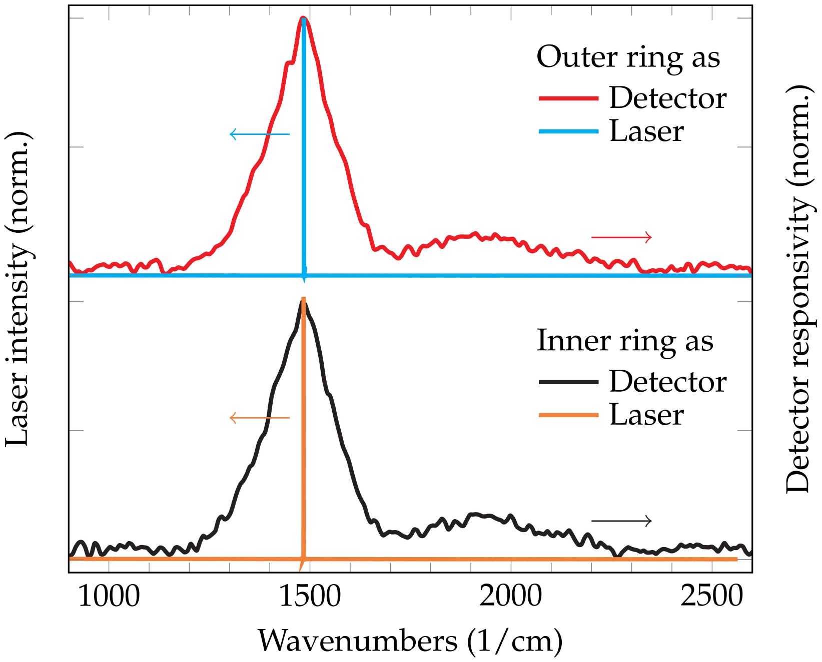

Figure 4.18: Laser and detector spectra of the commutable sensor system. The upper panel shows the performance of the outer ring operated as a detector (red) and a laser (blue). Similarly, the lower panel indicates the detector (black) and laser (orange) performance of the inner ring. Due to the utilization of bi-functional quantum cascade heterostructures a perfect wavelength overlap is achieved.
Reprinted with permission from [231]

by the grating and coupled to the quantum cascade active zone. As DFB gratings are rather unconventional coupling tools for QCDs a thorough investigation of the spectrum as well as performance simulations were conducted. Figure 4.19 shows the absorption spectra of a facet illuminated ridge detector and a normal incidence DFB ring detector, both fabricated from the same wafer. While the main absorption peak around 1500 /cm exhibits an identical shape, the other spectral regions present a reduced responsivity of the DFB detector. The origin of this matter of fact lies in the DFB grating itself. The measurement of the presented detector spectra in Fig. 4.19 were conducted according to the setup in Fig. 4.12 (a). Light emitted from a globar is collected by a lens with a focal length of 38 mm and focused on the ring detector. Considering the globar beam diameter of 32 mm prior to propagation through the lens, results in a maximum incidence angle of $\alpha_m = \pm 23°$, i.e. light rays under all angles between $-23°$ and $+23°$ with respect to the surface normal are incident on the detector. According to the grating equation

$$\sin(\alpha) = \frac{\lambda_\alpha}{\Lambda} - n \tag{4.3.5}$$

with the grating period Λ and the refractive index n, different wavelengths λ_α are efficiently coupled under different angles. Therefore, the value of α_m determines the maximum and minimum wavelengths coupled by the grating. They are given by

$$\lambda_{\alpha_m^+} = \lambda_0 + \Lambda \cdot \sin(+\alpha_m) \approx 7.5629\,\mu\text{m} \tag{4.3.6}$$

$$\lambda_{\alpha_m^-} = \lambda_0 + \Lambda \cdot \sin(-\alpha_m) \approx 5.9141\,\mu\text{m} \tag{4.3.7}$$

with the vacuum wavelength λ_0. Conversion into wavenumbers yields

$$\nu_{\alpha_m^+} = 1322/\text{cm} \tag{4.3.8}$$

$$\nu_{\alpha_m^-} = 1691/\text{cm}. \tag{4.3.9}$$

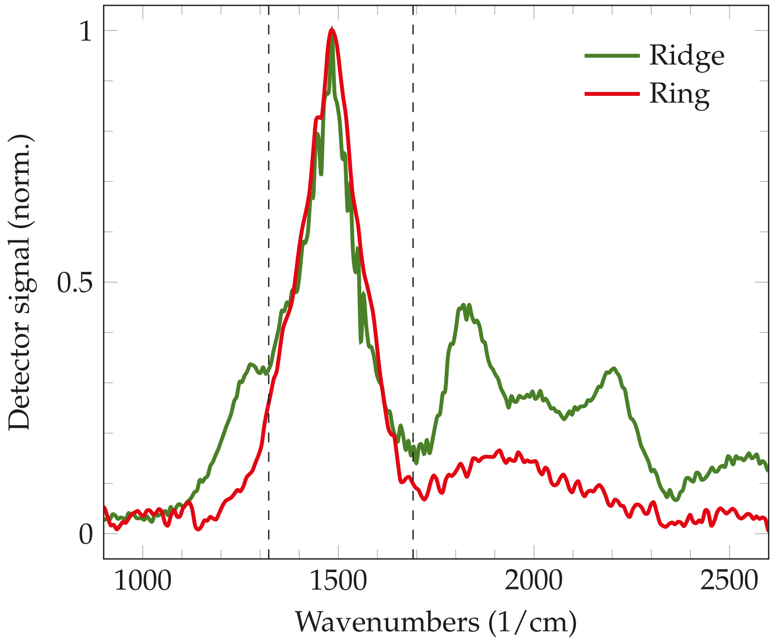

Figure 4.19: Comparison between a conventional ridge detector (green) and a DFB ring detector (red) fabricated from the same semiconductor material. While the main peak shows a good agreement, the ring detector exhibits a reduced detector signal for smaller and larger wavenumbers. This effect can be attributed to the coupling characteristics of the DFB grating. The area between the vertical black dashed lines indicates the wavelength region at which the DFB grating is capable of coupling light incident under $\alpha_m = \pm 23°$ to the active region.
Reprinted with permission from [231]

These values are indicated in Fig. 4.19 by the vertical dashed lines. Within these lines the grating facilitates efficient coupling and therefore shows a good agreement with the ridge detector. For higher and lower wavenumbers the grating equation is not fulfilled which results in a reduction of the detector signal. Residual sensitivity of the detector outside the dashed lines can be attributed to scattering effects at the grating. From DFB lasers it is known that the properties of the grating can strongly influence the laser performance. In order to theoretically investigate a similar behavior of DFB QCDs, COMSOL® [167] simulations with varying grating parameters were conducted. Figure 4.20 (a) illustrates the magnitude of the electric field aligned in vertical direction inside the heterostructure for normal incident light with a wavelength corresponding to the laser emission wavelength. Based on this simulation the grating efficiency in detector operation was calculated for various sets of grating parameters with varying grating depth and duty-cycle. The results of this investigation are presented in the upper panel of Fig. 4.20 (b). The respective theoretical laser characterization in the lower panel is obtained using rigorous Floquet-Bloch theory based on coupled wave theory [89]. Surprisingly, detector and laser performance exhibit a similar dependence on the grating parameters. This facilitates the selection of a suitable combination of grating parameters which allows to simultaneously reach maximum performance for the laser and detector operation. The chosen combination for the here presented sensor is a grating depth of $1\,\mu$m and a duty-cycle of 65%.

The commutable laser/detector system is implemented in the setup illustrated in Fig. 4.21. It is quite similar to the setup described in Fig. 4.13 (a) with the main exception being the utilization of a room temperature stage instead of a cryostat for the sensor

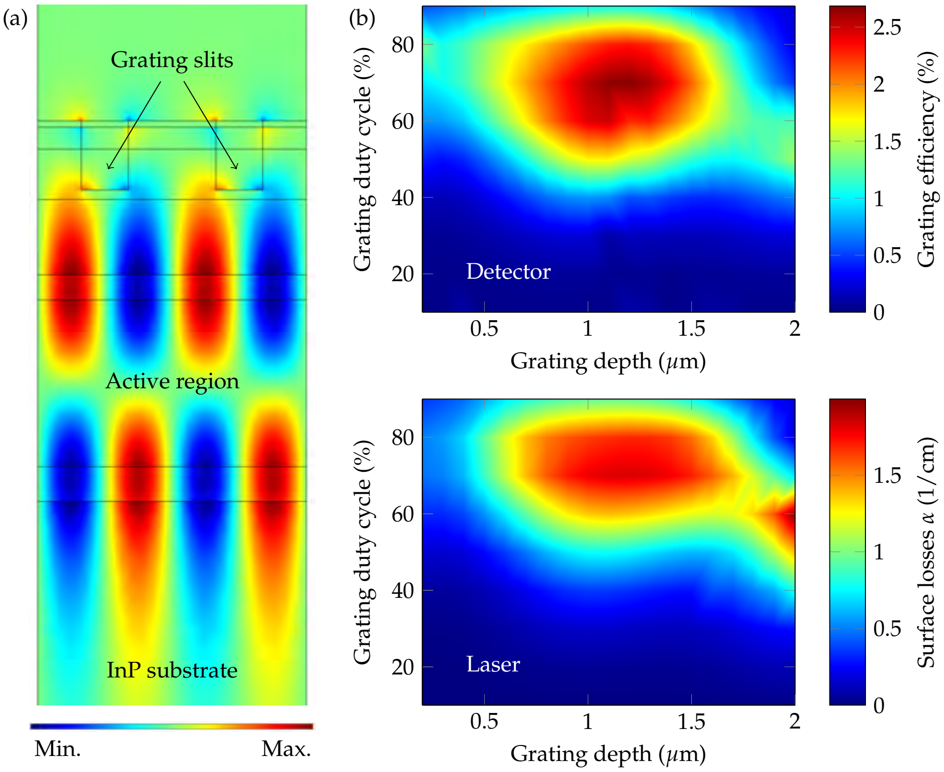

Figure 4.20: (a) COMSOL simulation of the DFB detector. Field distribution of E_y for normal incident light with a wavelength corresponding to the laser emission wavelength. (b) Grating study. Detector (top) and laser (bottom) performance calculated for different grating parameters. The presented sensor was fabricated with a grating duty-cycle of 65% and a grating depth of 1.0 μm which enables maximum performance in the detector as well as the laser mode. Reprinted with permission from [231]

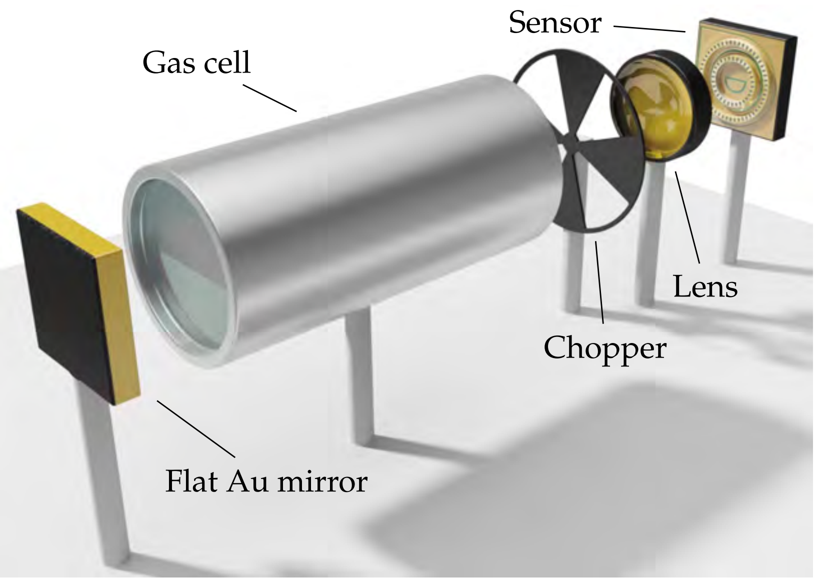

Figure 4.21: Sketch of the sensing setup. Light emitted from one of the rings is collimated by the lens and is guided through the chopper and the gas cell before it is back-reflected by a flat gold mirror. The laser beam propagates on its initial path back to the sensor chip where it is detected by the other ring.
Reprinted with permission from [231]

mounting. Light is emitted from one of the two rings, propagates through the lens, the chopper and the gas cell before it is back-reflected by the flat gold mirror following its initial path back to the sensor chip. There it is detected by the other ring. Its signal is pre-amplified with a conversion factor of 1 V/200 nA prior to quantitative analysis using a lock-in amplifier triggered by the chopper spinning at 300 Hz. The commutability of the two rings facilitates two operation modes. In the first operation mode (i) the inner ring assumes the role of the detector while the outer ring acts as the laser. In the second operation mode (ii) laser and detector exchange their roles. Prior to the sensing experiments both operation modes were characterized and compared to an external detection scheme. These results are shown in the LI curves in Fig. 4.22. Solid lines depict the LI measured with the on-chip detection scheme while the dashed lines are recorded with an external DTGS detector. Blue and orange curves represent laser operation of the outer and inner ring, respectively. A good agreement between on-chip and external detection scheme is found. Minor discrepancies can originate from unbalanced on-chip coupling efficiencies. The different threshold currents are attributed to the differently sized rings. Variations in the DFB grating period will only have a weak and negligible effect on the broad detector spectra. Figure 4.19 as well as Eq. (4.3.5) indicate that the grating period merely influences the lower and upper wavelength limits for efficient grating coupling. However, the peak of the absorption spectrum is mainly determined by the quantum cascade heterostructure and shows no significant dependence on the grating. The situation is entirely different for the DFB laser. Due to its narrowband emission, a variation of the grating period selects a different mode which significantly changes the emission spectrum. The presented sensor features two ring structures with different grating periods resulting in single mode emission at 1484.3 /cm and 1483.3 /cm for the outer and inner ring, respectively. Simultaneously, the two different grating periods do not alter the absorption spectra significantly as evident from Fig. 4.18. A closeup of the recorded laser spectra is depicted in Fig. 4.23 together with the absorption spectra of isobutene and isobutane which were utilized for the proof-of-principle experiments.

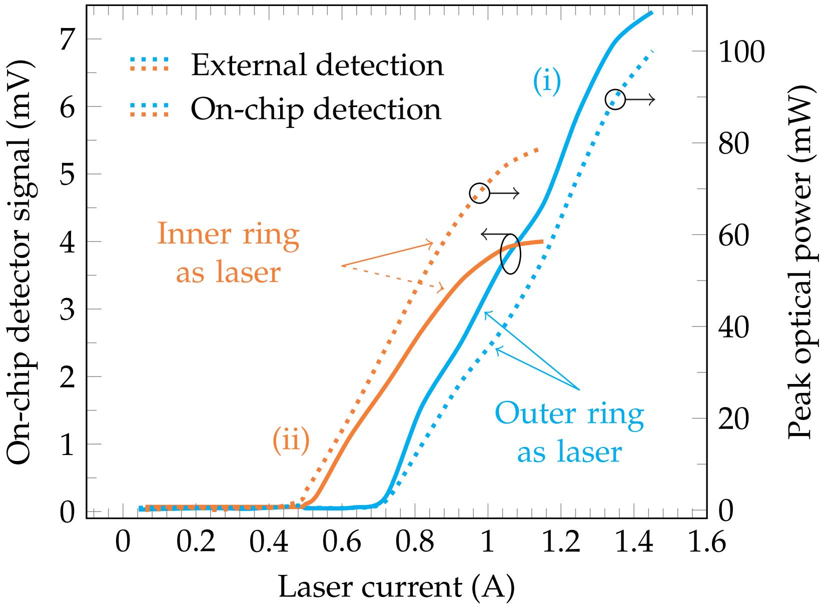

Figure 4.22: LI curves measured with an external (dotted) and the on-chip (solid) detection scheme. The on-chip sensor can be operated in two inverse modes: (i) Inner ring as detector and outer ring as laser. (ii) Outer ring as detector and inner ring as laser. Both operation modes show a good agreement with the external detection scheme utilizing a calibrated DTGS detector.
Reprinted with permission from [231]

The latter are taken from the PNNL database [254]. At the laser emission wavelengths

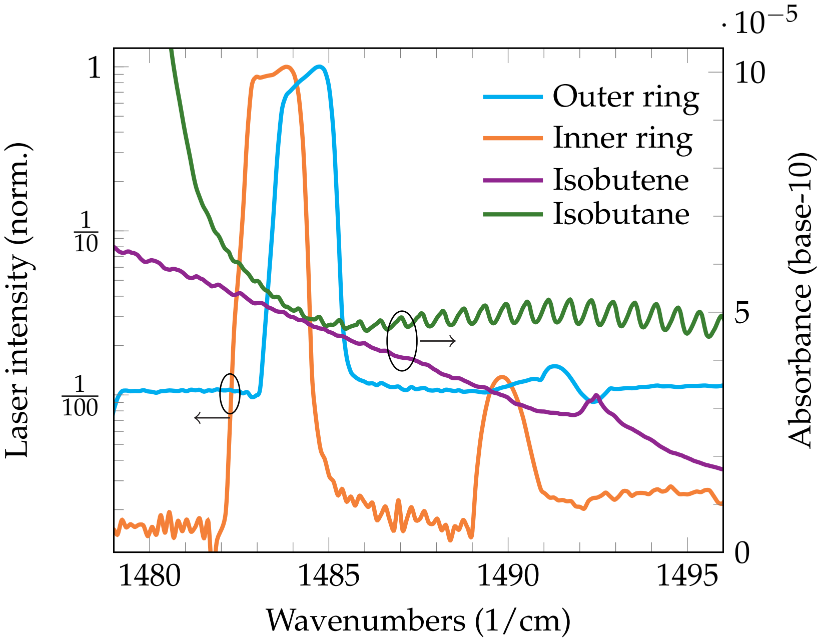

Figure 4.23: Laser spectra of both rings on top of the absorbance spectra of isobutene and isobutane according to the PNNL database [254]. Different DFB grating periods induce a relative shift of the emission wavelength between both lasers. At the emission wavelength of the outer ring both gases show a similar absorbance behavior. In contrast, at the emission wavelength of the inner ring isobutane exhibits a stronger absorption.
Reprinted with permission from [231]

both analytes exhibit similar absolute absorbance values. However, isobutane possesses a quadratic-like increase of the absorbance towards smaller wavenumbers whereas the absorbance of isobutene is characterized by a linear behavior. The goal of the following study is to positively distinguish these two substances using the commutable on-chip sensor. The latter was operated in both on-chip modes and the respective lasers were driven by 100 ns pulses with a repetition rate of 40 kHz. During each pulse the laser line shifts around 1.4 /cm. Gas flow through the cell was set to 1 L/min. A total of 120 datapoints were measured for each considered gas concentration in nitrogen with a lock-in time constant of 0.5 s. In Fig. 4.24 (a) and (b) the normalized transmittance versus gas concentration is plotted for isobutene and isobutane, respectively. Within the detectable concentration range from $0-16\%$ an excellent agreement between the experimental data, given by the points and error bars, and the theoretical prediction of the Beer-Lambert law, associated with the solid lines, is evident. In order to enable comparability to the PNNL database spectra, absorbance values from this analysis are calculated for 1 ppm-m and specified in the top right corner of each graph. For the isobutene study absorbances of $4.75 \cdot 10^{-5}$ and $5.07 \cdot 10^{-5}$ for the first and second operation mode could be extracted, respectively. Accordingly, the isobutane study revealed absorbance values of $4.78 \cdot 10^{-5}$ and $5.49 \cdot 10^{-5}$. It is striking that in the first operation mode with the outer ring as the laser, both gases exhibit a very similar absorption which agrees with the PNNL database in Fig. 4.22. Switching to the second operation mode with the inner ring as the laser introduces a significantly higher absorption for isobutane which concurs with the PNNL spectra as well. Extracted 3σ limits of detection (LOD) for both gases analyzed with both operation modes are provided in Tab. 4.2 together with the respective maximum detector voltage. Due to the higher output power of the outer laser a lower LOD is expected for the first operation mode. Although, this applies for the isobutane measure-

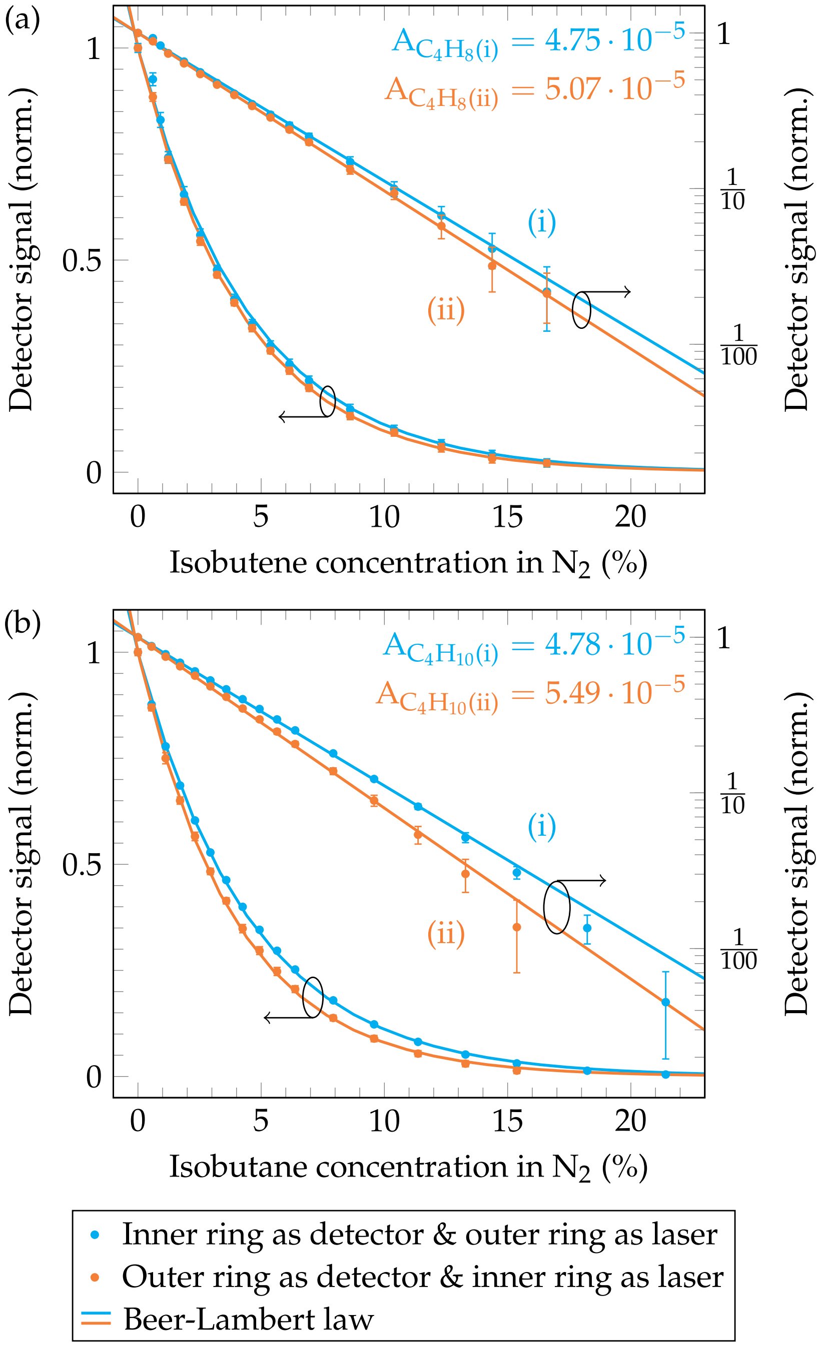

Figure 4.24: Transmittance as a function of the gas concentration for isobutene (a) and isobutane (b). Experimental data is given by the data points and corresponding error bars. Fitting curves based on the Beer-Lambert law are provided by the solid lines. Absorbance fit parameters are indicated in the top right corner of each graph. In addition to a good agreement with the Beer-Lambert law over a wide concentration range, these experimental absorbance values are consistent with the PNNL database.
Reprinted with permission from [231]

ment, the isobutene study exhibits an opposite behavior. From Tab. 4.2 it is evident that this is caused by a rather low detector voltage which is attributed to a suboptimal alignment of the components in the sensing setup. However, a 3σ LOD of below 400 ppm is achieved for the isobutane study. These values are obtained with a total light-analyte interaction path length of 20 cm without temperature stabilization of the sensor. These results demonstrate the capability of the sensor to distinguish and positively quantify two gases with similar absorption characteristics. In order to investigate the long-term

Limit of detection		
Laser	Isobutane	Isobutene
Outer ring	397 ppm	1458 ppm
Inner ring	1015 ppm	1093 ppm
Peak detector voltage		
Laser	Isobutane	Isobutene
Outer ring	7.405 mV	2.387 mV
Inner ring	4.012 mV	3.738 mV

Table 4.2: Limit of detection and corresponding peak detector voltage achieved in both sensor configurations for both gases.

stability of this sensor a one hour measurement with pure nitrogen flowing through the gas cell was taken and an Allan variance analysis [255] was conducted and the resulting Allan plot is provided in Fig. 4.25. It clearly demonstrates the good stability of the sensor with a domination of white noise and an optimum operation point at an averaging time around 300 s. All measurements presented in this section were obtained with an averaging time of 60 s. [231]

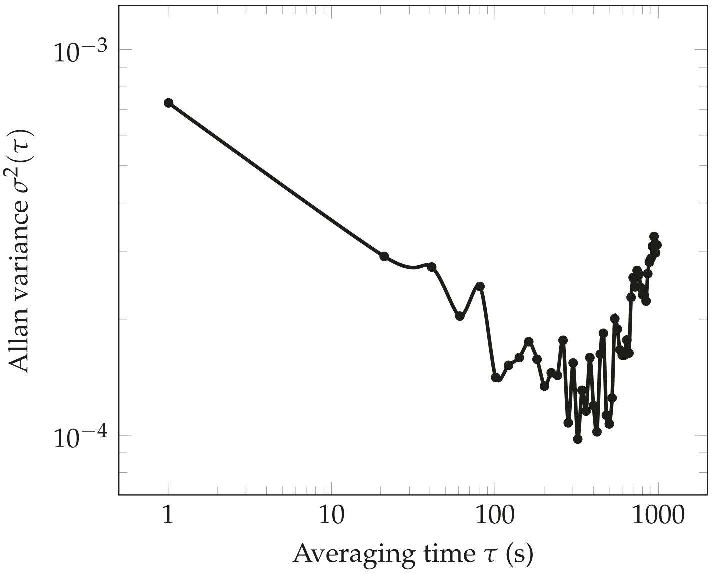

Figure 4.25: Allan variance plot based on a long term measurement with pure nitrogen flowing through the gas cell. An optimum averaging time for the sensor of 300 s is found.
Reprinted with permission from [231]

The demonstrated monolithic laser/detector system represents a compact and efficient highly integrated remote sensor for MIR applications. Surface emission and detection enables gas sensing and facilitates potential two dimensional array integration as suggested in Fig. A.7 in appendix A.6. In particular, the distinction between laser and detector becomes obsolete providing versatile commutable sensor systems. The latter are ideal candidates for spectroscopic applications requiring ultra-compact and efficient sensors.

CHAPTER 5

CONCLUSION

Within the framework of this dissertation beam modifications of ring QCLs were designed, realized and successfully implemented. They provide enhanced light outcoupling as well as a deeper understanding of the corresponding mechanisms. **Integrated phase shifts** in the DFB grating facilitate constructive interference of light emitted from opposing sides of the ring which consequently produces central lobed emission beams. In addition, these phase shifts were used to characterize the WGMs traveling inside the waveguide by means of a novel **dual DFB grating**. A simple analysis of the emitted far field provides detailed information about the location as well as the radial order of the WGM. Monolithic metamaterials, referred to as **metasubstrates**, are fabricated directly into the back side of the semiconductor chip. They consist of differently sized sub-wavelength holes and form a refractive index gradient. This facilitates **collimated laser beams** as well as the creation of twisted wavefronts carrying **OAM**.

The second part of this dissertation is dedicated to spectroscopic sensing applications and demonstrates the usability of ring QCLs in such setups. Combination of substrate integrated **iHWGs** with ring QCLs lay the groundwork for compact gas sensors requiring small sample volumes. **Heterodyne phase-sensitive detection** techniques were effectively implemented with CW ring QCLs and revealed the onset of thermal tuning in these lasers. Finally, a **surface active transceiver** based on bi-functional quantum cascade heterostructures featuring a ring laser and a disk detector is presented. The knowledge acquired from the implementation of this prototype forms the basis of the innovative **on-chip sensor** consisting of two **commutable ring-shaped laser/detector** units. These type of sensors could pave the way for ultra-compact sensor systems.

5.1 Outlook

Based on the topics presented in this dissertation, several prospective ideas in the field of beam modifications and sensing applications could be pursued.

Collimated OAM emission beam

On-chip metasubstrates were utilized for the collimation of ring QCL emission beams in section 3.9 as well as for the generation of OAM beams in section 3.10. The former creates a radial refractive index gradient while the latter requires a gradient in the azimuthal direction. Combining both approaches would facilitate collimated OAM beams generated with a single monolithic metamaterial. Such a two dimensional refractive index gradient requires larger etch depths and thus novel processing techniques have to be developed. An alternative approach would be the utilization of plasmonic metasurfaces which provide a higher design freedom.

Bi-functional Matryoshka array

A commutable on-chip sensor with two concentric ring quantum cascade laser/detectors is demonstrated in section 4.3.4. This sensor is a tiny spectroscopy system with laser and detector integrated on the same chip. Due to different DFB grating periods it features emission *and* detection of two different wavelengths. An extension of this concept to multiple concentric ring structures as described in section 3.6 would significantly enhance the performance and versatility of the sensor. One of these concentric rings could be used as a laser while all the others assume the role of the detector. This procedure would increase the detection efficiency and provide as many wavelengths as ring lasers. The major obstacle is the electrical contacting of the devices as well as their electrical isolation to suppress crosstalk. Flip-chip bonding techniques in combination with etching of deep trenches between the ring lasers represent possible solutions.

Self-mixing

The working principle of the commutable on-chip sensor is based on the detection of back-reflected light. One ring is operated as a laser while the other ring detects the incoming radiation. From Fig. 4.16 (c) it can be assumed that the back-reflected light illuminates a rather broad area on the sensor chip. Thus, only a finite portion of the back-reflected laser light can be measured with the detector ring. Most likely, MIR radiation is also incident on the lasing ring itself. Consequently this light is coupled into the waveguide by the DFB grating where it alters the optical and electrical characteristics of the laser. This effect is referred to as self-mixing and was already demonstrated for facet emitting QCLs [256]. A combination of the sensing scheme presented in section 4.3.4 with the self-mixing effect would provide a more efficient use of the back-reflected light and create a high-sensitivity sensor. In addition to the detector signal, perturbations in the laser voltage could provide information about the attenuation of the laser beam.

On-chip sensor with phase-sensitive detection

As discussed in section 4.3.4 the commutable on-chip sensor is based on molecular absorption of light described by the Beer-Lambert law. One of the main limitations of this sensor concept is caused by electrical crosstalk which significantly increases the noise level of the detector. One approach to weaken this effect could be the application of heterodyne phase-sensitive detection techniques, as described in section 4.2, which exhibit a high immunity to power fluctuations [211]. Such a concept would require CW laser operation with a current modulation as well as phase-sensitive detection using the on-chip detector.

APPENDIX

A.1 Growth sheets

Throughout this dissertation two different semiconductor heterostructures were used. For the sensing experiments the bi-functional quantum cascade heterostructure C0120 was implemented. For all other experiments in this dissertation the P51 heterostructure came into operation. In the following growth sheets for both heterostructures are provided. The first column shows the doping type, the second column specifies the material of the layer, the third column determines the actual doping value and the forth column indicates the thickness of each layer.

Type	Material	Doping	Thickness	
n^{++}	InGaAs	$1 \cdot 10^{20}\,\mathrm{cm}^{-3}$	10 nm	
n	InGaAs	$8 \cdot 10^{18}\,\mathrm{cm}^{-3}$	350 nm	
n	$\mathrm{InGa}_{0.5x}\mathrm{Al}_{0.5(1-x)}\mathrm{As}$ grading V	$2 \cdot 10^{17}\,\mathrm{cm}^{-3}$	25 nm	
n	InAlAs	$2 \cdot 10^{17}\,\mathrm{cm}^{-3}$	800 nm	
n	InAlAs	$1 \cdot 10^{17}\,\mathrm{cm}^{-3}$	1200 nm	
n	$\mathrm{InGa}_{0.5x}\mathrm{Al}_{0.5(1-x)}\mathrm{As}$ grading IV	$1 \cdot 10^{17}\,\mathrm{cm}^{-3}$	25 nm	
n	InGaAs	$5 \cdot 10^{16}\,\mathrm{cm}^{-3}$	400 nm	
n	$\mathrm{InGa}_{0.5x}\mathrm{Al}_{0.5(1-x)}\mathrm{As}$ grading VI	$1.5 \cdot 10^{17}\,\mathrm{cm}^{-3}$	26.0 nm	
n	$\mathrm{InGa}_{0.5x}\mathrm{Al}_{0.5(1-x)}\mathrm{As}$ grading II	$2 \cdot 10^{17}\,\mathrm{cm}^{-3}$	13.4 nm	Repeat 35×
undoped	Active region		62.1 nm	
n	$\mathrm{InGa}_{0.5x}\mathrm{Al}_{0.5(1-x)}\mathrm{As}$ grading III	$5 \cdot 10^{17}\,\mathrm{cm}^{-3}$	49.8 nm	
n	InGaAs	$5 \cdot 10^{16}\,\mathrm{cm}^{-3}$	550 nm	
n	$\mathrm{InGa}_{0.5x}\mathrm{Al}_{0.5(1-x)}\mathrm{As}$ grading I	$1 \cdot 10^{17}\,\mathrm{cm}^{-3}$	25 nm	
n	InP substrate	$1 \cdot 10^{17}\,\mathrm{cm}^{-3}$	$\sim 350\,\mu\mathrm{m}$	

Table A.1: C0120 growth sheet.

The total thickness of the C0120 structure amounts to 6.1033 µm on top of a low doped InP substrate with a thickness of approximately 350 µm. The active region consists of an alternating sequence of AlInAs and GaInAs layers. The corresponding thicknesses in Å from top to bottom are 31/**22**/28/**21**/44/**18**/17/**56**/24/**48**/26/**43**/26/**37**/18/**35**/19/**34**/20/**32**/22, with the bold values corresponding to the GaInAs layers.

Type	Material	Doping	Thickness	
n^{++}	InGaAs	$1 \cdot 10^{20}\,\text{cm}^{-3}$	10 nm	
n	InGaAs	$8 \cdot 10^{18}\,\text{cm}^{-3}$	350 nm	
n	InGa$_{0.5x}$Al$_{0.5(1-x)}$As grading V	$2 \cdot 10^{17}\,\text{cm}^{-3}$	25 nm	
n	InAlAs	$2 \cdot 10^{17}\,\text{cm}^{-3}$	800 nm	
n	InAlAs	$1 \cdot 10^{17}\,\text{cm}^{-3}$	1500 nm	
n	InGa$_{0.5x}$Al$_{0.5(1-x)}$As grading IV	$1 \cdot 10^{17}\,\text{cm}^{-3}$	25 nm	
n	InGaAs	$5 \cdot 10^{16}\,\text{cm}^{-3}$	300 nm	
n	InGa$_{0.5x}$Al$_{0.5(1-x)}$As grading VI	$1 \cdot 10^{17}\,\text{cm}^{-3}$	13.9 nm	
n	InGa$_{0.5x}$Al$_{0.5(1-x)}$As grading II	$2 \cdot 10^{17}\,\text{cm}^{-3}$	32.2 nm	Repeat 35×
undoped	Active region		27.5 nm	
n	InGa$_{0.5x}$Al$_{0.5(1-x)}$As grading III	$1 \cdot 10^{17}\,\text{cm}^{-3}$	13.7 nm	
n	InGaAs	$5 \cdot 10^{16}\,\text{cm}^{-3}$	500 nm	
n	InGa$_{0.5x}$Al$_{0.5(1-x)}$As grading I	$1 \cdot 10^{17}\,\text{cm}^{-3}$	25 nm	
n	InP substrate	$1 - 4 \cdot 10^{17}\,\text{cm}^{-3}$	$\sim 350\,\mu$m	

Table A.2: P51 growth sheet.

The total thickness of the P51 structure amounts to 5.6521 µm on top of a low doped InP substrate with a thickness of approximately 350 µm. The active region consists of an alternating sequence of AlInAs and GaInAs layers. The corresponding thicknesses in Å from top to bottom are 44/**18**/9/**57**/11/**54**/12/**45**/25, with the bold values corresponding to the GaInAs layers.

A.2 Cleanroom fabrication

In the following the detailed processing parameters for the fabrication of Ring-QCLs are given in chronological order. In addition, the manufacturing processes of the on-chip polarizer and the metasubstrates are presented.

Definition of the surface DFB grating with EBL

- Spin coating with PMMA resist AR-P679.04 for 35 s at 2000 rpm and subsequent baking for 5 min at 170 °C.
- EBL exposure with a dose of $\sim 80\,\mu\text{Cb/cm}^2$ and an acceleration voltage of 10 kV. This results in an emission current of 160 pA. The aperture is 30 µm and the write field is 500 × 500 µm.

- Developing with AR600-56 developer for 30 − 40 s and subsequent rinsing with isopropanol.

Evaporation of the grating

- Evaporation of a 15 nm Ti adhesion layer followed by a 50 nm Au layer below a 100 nm Ni layer. The Ni layer exhibits a rather high rigidity which facilitates the utilization of this metal mask for the etching of the grating *and* the waveguide. Typical evaporation rates are 30 pm/s for Ti and 30 − 100 pm/s for Au and Ni.
- Lift-Off in N-Methyl-2-pyrrolidone for 1 h at 120 °C and subsequent cleaning with isopropanol.

Etching of the grating

- Preconditioning of the chamber without sample but with carrier for 60 min with the process parameters given below.
- Grating depth of 1.2 − 1.7 μm etched by RIE with a silicon carrier utilizing gas flows of 5 sccm for $SiCl_4$ and 40 sccm for Ar. The working pressure is $2.67 \cdot 10^{-3}$ mbar. The RF power is 200 W and the process temperature is 250 °C. Typical etch rates range from 80 − 120 nm/min.

Definition of hard mask for the protection of the grating slits

- Deposition of 1.0 − 1.2 μm SiN with PECVD utilizing gas flows of 700 sccm for 2 % SiH_4/N_2 and 18 sccm for NH_3. The working pressure is 1.33 mbar. The RF power is 9 W and the process temperature is 300 °C. Typical deposition rates range from 8 − 10 nm/min.
- Optical lithography with AZ5214 (1:0) photoresist, spin coated with 4000 rpm for 35 s and subsequent baking for 60 s at 100 °C. Exposure of the ring waveguides for 4 s and developing in AZ351B (1:4) for 8 − 11 s with subsequent neutralization in water.
- SiN hard mask etching with RIE utilizing a gas flow of 40 sccm for SF_6 and a quartz carrier. The working pressure is $2 \cdot 10^{-2}$ mbar. The RF power is 60 W and the process temperature is 30 °C. The process is finished after the SiN around the ring waveguides is etched away. Typical etch rates range from 120 − 180 nm/min.
- Removal of excess photoresist via plasma oxidation for 10 min at 1 mbar and a power of 300 W followed by a acetone bath for 1 − 10 min at 100 °C and subsequent cleaning with isopropanol.

Etching of the ring waveguide

- Preconditioning of the chamber without sample but with carrier for 60 min with the process parameters given below.
- Waveguide depth of 6 − 9 μm etched by RIE with a silicon carrier utilizing gas flows of 5 sccm for $SiCl_4$ and 40 sccm for Ar. The working pressure is $2.67 \cdot 10^{-3}$ mbar. The RF power is 200 W and the process temperature is 250 °C. Typical etch rates range from 80 − 120 nm/min.

- Removal of excess SiN with RIE utilizing gas flows of 40 sccm for SF_6 and a quartz carrier. The working pressure is $2 - 6 \cdot 10^{-2}$ mbar. The RF power is 60 W and the process temperature is 30 °C. Typical etch rates range from $120 - 200$ nm/min.

Electrical isolation

- Deposition of $250 - 320$ nm SiN with PECVD utilizing gas flows of 700 sccm for 2 % SiH_4/N_2 and 18 sccm for NH_3. The working pressure is 1.33 mbar. The RF power is 9 W and the process temperature is 300 °C. Typical deposition rates range from $8 - 10$ nm/min.

- Optical lithography with ma-P1275 (1:0) photoresist, spin coated with 9000 rpm for 35 s and subsequent baking for 5 min at 100 °C. Exposure of the isolation pattern for $8.5 - 9$ s and developing in maD331 (1:0) for $25 - 40$ s with subsequent neutralization in water.

- Opening of the isolation on top of the grating by RIE etching with a quartz carrier utilizing a gas flow of 40 sccm for SF_6 and a quartz carrier. The working pressure is $2.67 \cdot 10^{-3}$ mbar. The RF power is 60 W and the process temperature is 30 °C. Typical etch rates range from $120 - 180$ nm/min.

- Removal of excess photoresist via plasma oxidation for 10 min at 1 mbar and a power of 300 W followed by a acetone bath for $1 - 10$ min at 100 °C and subsequent cleaning with isopropanol.

Extended electrical contact

- Optical lithography with an adhesion layer of HMDS, spin coated with 4000 rpm for 35 s and subsequent baking for $10 - 13$ s at 100 °C. Thereafter, spin coating of ma-P1275 photoresist with 8000 rpm for 35 s and subsequent baking for 5 min at 100 °C. Exposure of the contact pattern for $10 - 13$ s and developing in maD331 (1:0) for $30 - 55$ s with subsequent neutralization in water.

- Cleaning of the sample surface using the N_2 plasma in the sputter machine for $3 \times 30\,s$ at 25 W.

- Sputtering of the extended contact layer with an adhesion layer of Ti for 2×30 s at 50 W and a gold layer for 20×30 s at 25 W. Typical deposition rates are 10 nm/min for Ti and 33 nm/min for Au. The working pressure is set to $8 \cdot 10^{-3}$ mbar. The following lift-off process in acetone for 2 h at 80 °C with subsequent cleaning in isopropanol electrically separates the rings and removes the excess gold from the grating in order to ensure surface light emission.

Fabrication of the on-chip wire grid polarizer

- Spin coating with PMMA resist AR-P679.04 for 35 s at 2000 rpm and subsequent baking for 5 min at 170 °C.

- EBL exposure with a dose of $\sim 80 - 90\,\mu$Cb/cm^2 and an acceleration voltage of 10 kV. This results in an emission current of 160 pA. The aperture is 30 μm and the write field is $500 \times 500\,\mu$m.

- Developing with AR600-56 developer for $45 - 50\,\mathrm{s}$ and subsequent rinsing with isopropanol.
- Evaporation of a 15 nm Ti adhesion layer followed by a $120 - 150\,\mathrm{nm}$ Au layer. Typical evaporation rates are 30 pm/s for Ti and $30 - 100\,\mathrm{pm/s}$ for Au.
- Lift-Off in N-Methyl-2-pyrrolidone for 1 h at 120 °C and subsequent cleaning with isopropanol.

Fabrication of the collimating and OAM metasubstrates

- Deposition of $430 - 450\,\mathrm{nm}$ SiN with PECVD utilizing gas flows of 700 sccm for 2 % SiH_4/N_2 and 18 sccm for NH_3. The working pressure is 1.33 mbar. The RF power is 9 W and the process temperature is 300 °C. Typical deposition rates range from $8 - 10\,\mathrm{nm/min}$.
- Spin coating with PMMA resist AR-P679.04 for 35 s at 2000 rpm and subsequent baking for 5 min at 170 °C.
- EBL exposure with a dose of $\sim 90\,\mu\mathrm{Cb/cm^2}$ and an acceleration voltage of 10 kV. This results in an emission current of 160 pA. The aperture is $30\,\mu\mathrm{m}$ and the write field is $500 \times 500\,\mu\mathrm{m}$.
- Developing with AR600-56 developer for 60 s and subsequent rinsing with isopropanol.
- Etching of holes in SiN hard mask with RIE utilizing a gas flow of 40 sccm for SF_6 and a quartz carrier. The working pressure is $2 \cdot 10^{-2}\,\mathrm{mbar}$. The RF power is 60 W and the process temperature is 30 °C. Typical etch rates range from $120 - 180\,\mathrm{nm/min}$.
- Removal of excess photoresist via plasma oxidation for 5 min at 1 mbar and a power of 300 W followed by a acetone bath for $1 - 10\,\mathrm{min}$ at 100 °C and subsequent cleaning with isopropanol.
- Preconditioning of the chamber without sample but with carrier for 60 min with the process parameters given below.
- Etch depth of the holes of $3.8\,\mu\mathrm{m}$ etched by RIE with a silicon carrier utilizing gas flows of 5 sccm for $SiCl_4$ and 40 sccm for Ar. The working pressure is $2.67 \cdot 10^{-3}\,\mathrm{mbar}$. The RF power is 200 W and the process temperature is 250 °C. Typical etch rates range from $80 - 120\,\mathrm{nm/min}$.

A.3 Dual grating exploration

Figure A.1 (a) and (b) depict cuts through a ring QCL waveguide with a dual second order DFB grating. These cuts were realized by means of a focused ion beam. In Fig. A.1 (b) the differently shaded area at the "facet" of the waveguide indicates the active region of the QCL.

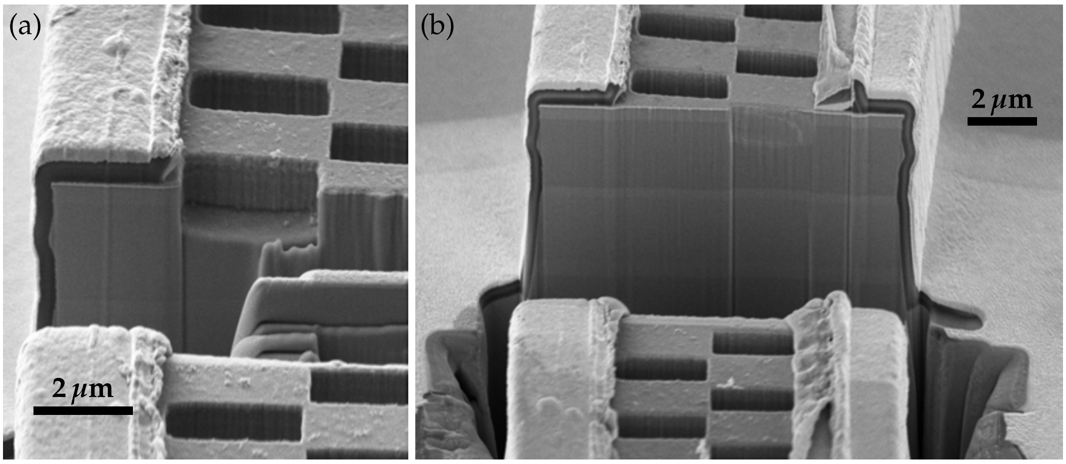

Figure A.1: SEM image of a cut through a dual grating ring QCL.

A.4 OAM metasubstrate

Refractive index profiles of the OAM metasubstrates are provided in Fig. 3.43 (e). These were obtained by a thorough investigation of the hole size using a SEM. In addition, ARDE was taken into account according to Fig. 3.36. Exemplary SEM images of an $m = +1$ metasubstrate are shown in Fig. A.2. In Fig. A.2 (a) the entire metasubstrate is displayed and the locations of the magnified images shown in Fig. A.2 (b) - (i) are indicated.

A.5 Sensing with ring QCLs and iHWGs

Ring QCLs in combination with iHWGs were demonstrated in section 4.1. In November 2016 the paper describing this prototype sensor setup made it on the cover of Analyst. The cover image is provided in Fig. A.3.

A.6 Remote gas sensor

In section 4.3.4 a novel sensing concept with laser and detector integrated on the same chip was demonstrated. Figure A.4 provides a SEM images of this on-chip sensor and also illustrates how this sensor is electrically contacted. Four bonding wires are connected with the top and bottom contact of each ring in order to ensure potential stability.

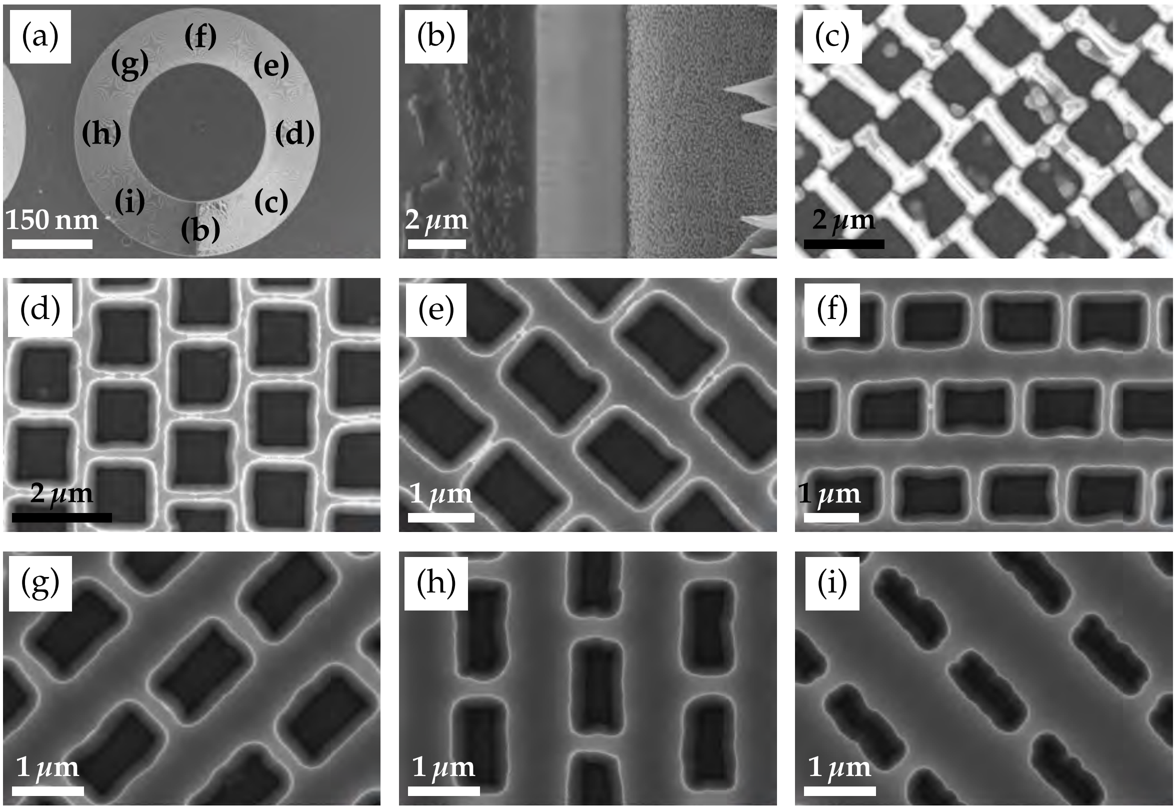

Figure A.2: SEM images of an OAM metasubstrate. In (a) the locations of the images (b) - (i) are displayed.

The research provided in section 4.3.4 was published in ACS Photonics. The corresponding graphical TOC entry is shown in Fig. A.5. Light emitted from one of the rings is attenuated by the molecules before it is back-reflected by the mirror, again attenuated and then detected on the sensor chip by the other ring. In this sketch the molecules are not to scale.

A sketch of the gas sensing setup is provided in Fig. 4.21. A photograph of the actual sensing setup is given in Fig. A.6. The latter demonstrates the compactness of the entire setup including light source, lens, chopper, gas cell and mirror. In the background the gas mixing system is visible.

The concluding words in section 4.3.4 describe the possibility of two dimensional array integration of these ultra-compact on-chip sensors. Figure A.7 shows a SEM image of such an array. By applying different DFB grating periods to the ring lasers a multi-color on-chip sensor is viable.

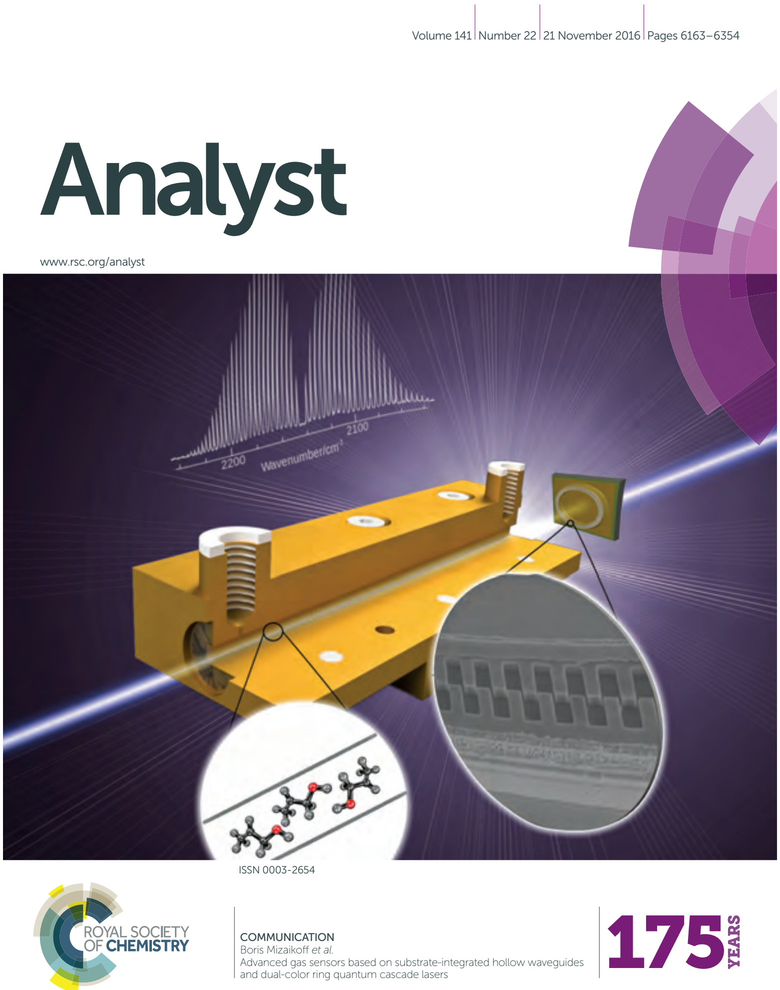

Volume 141 | Number 22 | 21 November 2016 | Pages 6163–6354

Analyst

www.rsc.org/analyst

ISSN 0003-2654

ROYAL SOCIETY OF CHEMISTRY

COMMUNICATION
Boris Mizaikoff *et al.*
Advanced gas sensors based on substrate-integrated hollow waveguides and dual-color ring quantum cascade lasers

175 YEARS

Figure A.3: Analyst cover showing a ring QCL in combination with an iHWG. Reprinted with permission from [219]

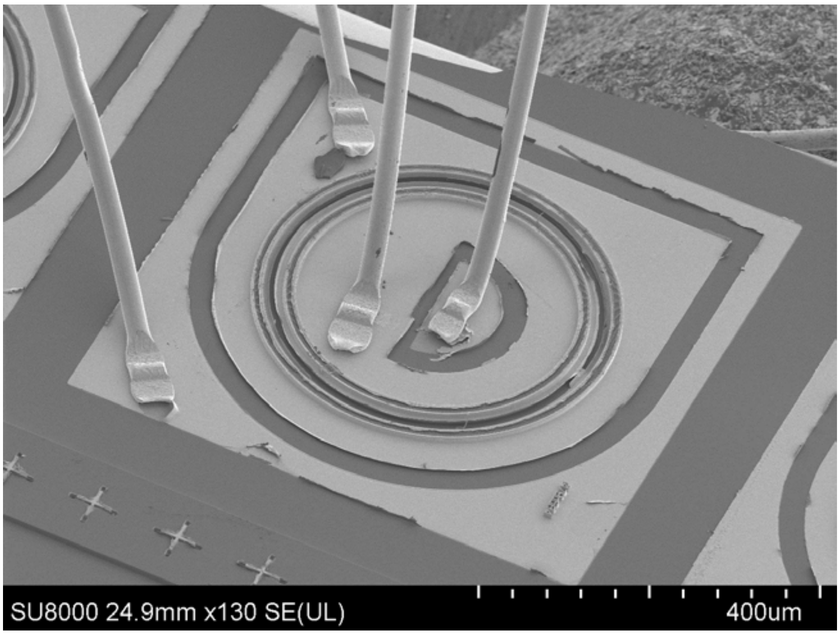

Figure A.4: SEM image of the commutable on-chip sensor with two concentric ring structures.

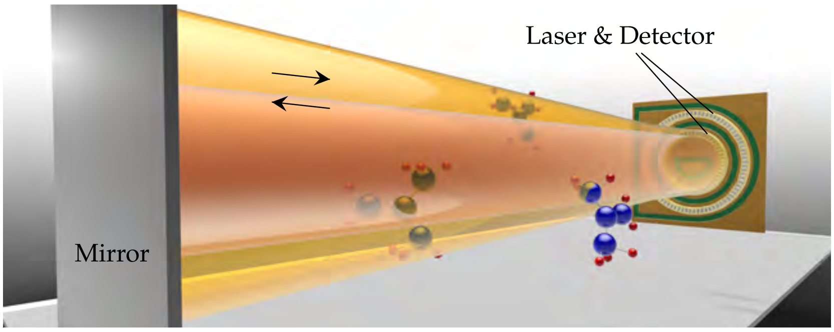

Figure A.5: Graphical TOC entry of the ACS Photonics Publication.
Reprinted with permission from [231]

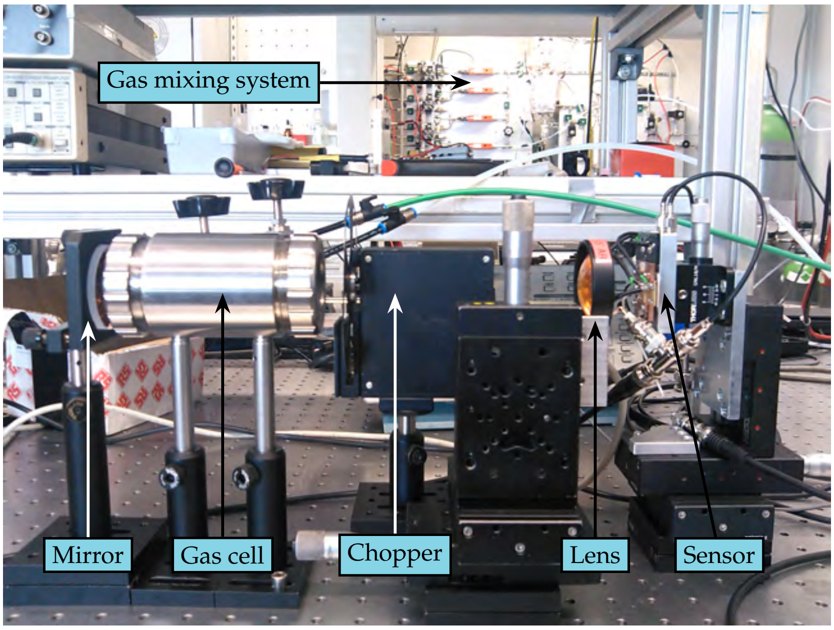

Figure A.6: Photograph of the remote sensing setup.

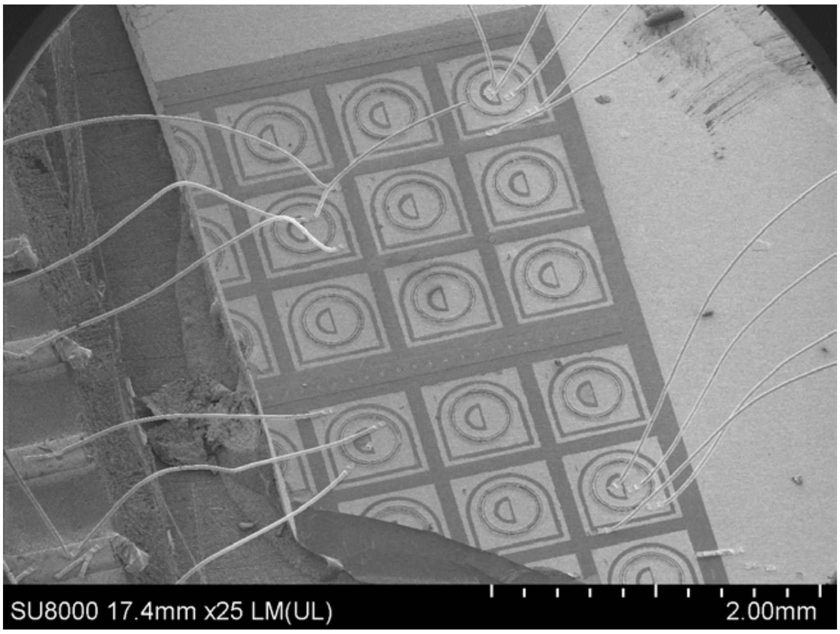

Figure A.7: SEM image of an array with several commutable on-chip sensors.

BIBLIOGRAPHY

[1] A. Einstein. *Über einen die Erzeugung und Verwandlung des Lichtes betreffenden heuristischen Gesichtspunkt*. Annalen der Physik, 322:132–148 (1905). doi: 10.1002/andp.19053220607. Cited on page 1.

[2] B. L. Milman. *Chemical Identification and its Quality Assurance*. Springer-Verlag (2011). Cited on page 1.

[3] W. Haynes. *CRC Handbook of Chemistry and Physics, 93rd Edition*. CRC Handbook of Chemistry and Physics. Taylor & Francis (2012). Cited on page 1.

[4] C. N. Banwell. *Fundamentals of Molecular Spectroscopy*. McGraw-Hill Book Company Europe (1983). Cited on page 2.

[5] W. Schmidt. *Optische Spektroskopie*. VCH Verlagsgesellschaft mbH (1994). Cited on page 2.

[6] P. W. Atkins. *Physical Chemistry*. Oxford University Press (1994). Cited on pages 2 and 3.

[7] P. M. Morse. *Diatomic Molecules According to the Wave Mechanics. II. Vibrational Levels*. Physical Review, 34:57–64 (1929). doi: 10.1103/PhysRev.34.57. Cited on page 2.

[8] W. Demtröder. *Molekülphysik: Theoretische Grundlagen und experimentelle Methoden*. Oldenbourg Wissenschaftsverlag GmbH (2013). Cited on pages 3 and 5.

[9] L. S. Rothman, I. E. Gordon, Y. Babikov, A. Barbe, D. C. Benner, P. F. Bernath, *et al.* *The HITRAN2012 molecular spectroscopic database*. Journal of Quantitative Spectroscopy and Radiative Transfer, 130:4–50 (2013). doi: 10.1016/j.jqsrt.2013.07.002. Cited on page 3.

[10] M. Planck. *Über das Gesetz der Energieverteilung im Normalspectrum*. Annalen der Physik, 309(3):553–563 (1901). doi: 10.1002/andp.19013090310. Cited on page 4.

[11] P. R. Griffiths and J. A. de Haseth. *Fourier Transform Infrared Spectrometry*. John Wiley & Sons, Inc. (2007). Cited on pages 4 and 5.

[12] A. A. Michelson and E. W. Morley. *On the relative motion of the Earth and the luminiferous ether*. American Journal of Science, 34(203):333–345 (1887). doi: 10.2475/ajs.s3-34.203.333. Cited on page 4.

[13] A. Einstein. *Zur Quantentheorie der Strahlung*. Physikalische Zeitschrift, 18:121–128 (1917). Cited on page 5.

[14] A. L. Schawlow and C. H. Townes. *Infrared and Optical Masers*. Physical Review, 112:1940–1949 (1958). doi: 10.1103/PhysRev.112.1940. Cited on page 5.

[15] T. H. Maiman. *Stimulated Optical Radiation in Ruby*. Nature, 187:493–494 (1960). doi: 10.1038/187493a0. Cited on page 5.

[16] D. L. Andrews. *Lasers in Chemistry*. Springer-Verlag (1990). Cited on page 5.

[17] C. K. N. Patel. *Continuous-Wave Laser Action on Vibrational-Rotational Transitions of* CO_2. Physical Review, 136:A1187–A1193 (1964). doi: 10.1103/PhysRev.136.A1187. Cited on page 5.

[18] K. M. Abramski and E. F. Plinski. *Principles of Gas Lasers*. In M. Endo and R. F. Walter (Editors), *Gas Lasers*, 2–38. CRC Press (2006). Cited on page 5.

[19] K. C. Byron and G. J. Pert. *A high-output-power near-infrared tunable dye laser*. Journal of Physics E: Scientific Instruments, 12(4):289–293 (1979). doi: 10.1088/0022-3735/12/4/016. Cited on page 5.

[20] L. Goldman. *Dye Lasers in Medicine*. In F. J. Duarte and L. W. Hillman (Editors), *Dye Laser Principles*, 419–432. Academic Press (1990). doi: 10.1016/B978-0-12-222700-4.50015-2. Cited on page 5.

[21] P. Moulton. *Ti-doped sapphire: tunable solid-state laser*. Optics News, 8(6):9–9 (1982). doi: 10.1364/ON.8.6.000009. Cited on page 5.

[22] J. E. Geusic, H. M. Marcos, and L. G. Van Uitert. *Laser Oscillations in Nd-doped Yttrium Aluminum, Yttrium Gallium and Gadolinium Garnets*. Applied Physics Letters, 4(10):182–184 (1964). doi: 10.1063/1.1753928. Cited on page 5.

[23] G. J. Wagner, T. J. Carrig, R. H. Page, K. I. Schaffers, J.-O. Ndap, X. Ma, and A. Burger. *Continuous-wave broadly tunable* Cr^{2+}*:ZnSe laser*. Optics Letters, 24(1):19–21 (1999). doi: 10.1364/OL.24.000019. Cited on page 5.

[24] J. F. Pinto, G. H. Rosenblatt, and L. Esterowitz. Tm^{3+}*:YLF laser continuously tunable between 2.20 and 2.46* μm. Optics Letters, 19(12):883–885 (1994). doi: 10.1364/OL.19.000883. Cited on page 5.

[25] S. R. Bowman, L. B. Shaw, B. J. Feldman, and J. Ganem. *A 7-*μm *praseodymium-based solid-state laser*. IEEE Journal of Quantum Electronics, 32(4):646–649 (1996). doi: 10.1109/3.488838. Cited on page 5.

[26] T. M. Shay and F. J. Duarte. *Tunable Fiber Lasers*. In F. J. Duarte (Editor), *Tunable Laser Applications*, 179–196. CRC Press (2009). Cited on page 6.

[27] R. N. Hall, G. E. Fenner, J. D. Kingsley, T. J. Soltys, and R. O. Carlson. *Coherent Light Emission From GaAs Junctions*. Physical Review Letters, 9:366–368 (1962). doi: 10.1103/PhysRevLett.9.366. Cited on page 6.

[28] M. I. Nathan, W. P. Dumke, G. Burns, F. H. Dill, and G. Lasher. *Stimulated Emission of Radiation from GaAs p-n Junctions*. Applied Physics Letters, 1(3):62–64 (1962). doi: 10.1063/1.1777371. Cited on page 6.

[29] T. M. Quist, R. H. Rediker, R. J. Keyes, W. E. Krag, B. Lax, A. L. McWhorter, and H. J. Zeigler. *Semiconductor Maser of GaAs*. Applied Physics Letters, 1(4):91–92 (1962). doi: 10.1063/1.1753710. Cited on page 6.

[30] N. Holonyak and S. F. Bevacqua. *Coherent (Visible) Light Emission from* $Ga(As_{1-x}P_x)$ *Junctions*. Applied Physics Letters, 1(4):82–83 (1962). doi: 10.1063/1.1753706. Cited on page 6.

[31] P. W. Milonni and J. H. Eberly. *Lasers*. John Wiley and Sons, Inc. (1988). Cited on pages 6, 14, and 33.

[32] H. Kroemer. *A proposed class of hetero-junction injection lasers*. Proceedings of the IEEE, 51(12):1782–1783 (1963). doi: 10.1109/PROC.1963.2706. Cited on page 6.

[33] H. Kressel and H. Nelson. *Close-confinement gallium arsenide pn junction lasers with reduced optical loss at room temperature*. RCA review, 30:106–113 (1969). doi: 10.1109/JQE.1970.1076457. Cited on page 6.

[34] Z. I. Alferov, V. Andreev, D. Garbuzov, Y. Zhilyaev, E. Morozov, E. Portnoy, and V. Trofim. *Effect of AlAs–GaAs heterostructure parameters on threshold current of lasers and the achievement of cw generation at room temperature*. Fizika i tekhnika poluprovodnikov, 4:1826–1829 (1970). Cited on page 6.

[35] J. Buus. *Semiconductor lasers*. In J. P. Dakin and R. G. W. Brown (Editors), *Handbook of Optoelectronics*, 385–412. CRC Press (2006). Cited on page 6.

[36] A. Nogee. *The Worldwide Market for Lasers*. Strategies Unlimited (2014). Cited on page 6.

[37] P. Crump, G. Erbert, H. Wenzel, C. Frevert, C. M. Schultz, K. H. Hasler, R. Staske, B. Sumpf, A. Maaßdorf, F. Bugge, S. Knigge, and G. Tränkle. *Efficient High-Power Laser Diodes*. IEEE Journal of Selected Topics in Quantum Electronics, 19(4):1501211–1501221 (2013). doi: 10.1109/JSTQE.2013.2239961. Cited on page 6.

[38] K. Thyagarajan. *Lasers - Theory and applications*. Plenum Publishing Corporation (1981). Cited on pages 6 and 14.

[39] S. Adachi. *Handbook on Physical Properties of Semiconductors*. Kluwer Academic Publishers (2004). Cited on page 6.

[40] H. Kressel, M. Ettenberg, J. P. Wittke, and I. Ladany. *Laser diodes and LEDs for fiber optical communication*. In H. Kressel (Editor), *Semiconductor Devices for Optical Communication*, 9–62. Springer-Verlag (1982). doi: 10.1007/3-540-11348-7_24. Cited on page 6.

[41] A. Joullié and P. Christol. *GaSb-based mid-infrared 2-5 μm laser diodes*. Comptes Rendus Physique, 4(6):621–637 (2003). doi: 10.1016/S1631-0705(03)00098-7. Cited on page 6.

[42] A. Baranov and E. Tournié. *Semiconductors lasers - Fundamentals and applications*. Woodhead Publishing Limited (2013). Cited on page 6.

[43] Y. Horikoshi. *Semiconductor Lasers with Wavelengths Exceeding 2 μm*. In W. T. Tsang (Editor), *Semiconductors and Semimetals*, 93–152. Academic Press, Inc. (1985). Cited on page 6.

[44] E. Hecht. *Optics*. Addison-Wesley Publishing Company, Inc. (1987). Cited on pages 6, 33, and 65.

[45] M. Tacke. *Lead Salt Lasers*. In M. Helm (Editor), *Long Wavelength Infrared Emitters based on Quantum Wells and Superlattices*, 347–396. Gordon and Breach Science Publishers (2000). Cited on page 6.

[46] M. Helm. *Introduction: Infrared Semiconductor Sources*. In M. Helm (Editor), *Long Wavelength Infrared Emitters based on Quantum Wells and Superlattices*, 1–12. Gordon and Breach Science Publishers (2000). Cited on pages 6 and 16.

[47] *Mid-infrared lasers*. Nature Photonics, 4(8):576–577 (2010). doi: 10.1038/nphoton.2010.173. Cited on page 6.

[48] J. Faist, F. Capasso, D. L. Sivco, C. Sirtori, A. L. Hutchinson, and A. Y. Cho. *Quantum Cascade Laser*. Science, 264(5158):553–556 (1994). doi: 10.1126/science.264.5158.553. Cited on pages 7, 16, and 97.

[49] P. A. Franken, A. E. Hill, C. W. Peters, and G. Weinreich. *Generation of Optical Harmonics*. Physical Review Letters, 7:118–119 (1961). doi: 10.1103/PhysRevLett.7.118. Cited on page 7.

[50] L. R. Elias, W. M. Fairbank, J. M. J. Madey, H. A. Schwettman, and T. I. Smith. *Observation of Stimulated Emission of Radiation by Relativistic Electrons in a Spatially Periodic Transverse Magnetic Field*. Physical Review Letters, 36:717–720 (1976). doi: 10.1103/PhysRevLett.36.717. Cited on page 7.

[51] T. J. Seebeck. *Ueber die magnetische Polarisation der Metalle und Erze durch Temperatur-Differenz*. Annalen der Physik, 82(2):133–160 (1826). doi: 10.1002/andp.18260820202. Cited on page 7.

[52] S. P. Langley. *The Bolometer and Radiant Energy*. Proceedings of the American Academy of Arts and Sciences, 16:342–358 (1880). doi: 10.2307/25138616. Cited on page 7.

[53] S. P. Langley. *The bolometer*. Nature, 25:14–16 (1881). doi: 10.1038/025014a0. Cited on page 7.

[54] M. J. E. Golay. *Theoretical Consideration in Heat and Infra-Red Detection, with Particular Reference to the Pneumatic Detector*. Review of Scientific Instruments, 18(5):347–356 (1947). doi: 10.1063/1.1740948. Cited on page 7.

[55] W. Lawson, S. Nielsen, E. Putley, and A. Young. *Preparation and properties of HgTe and mixed crystals of HgTe-CdTe*. Journal of Physics and Chemistry of Solids, 9(3):325–329 (1959). doi: 10.1016/0022-3697(59)90110-6. Cited on page 7.

[56] W. Schottky. *Zur Halbleitertheorie der Sperrschicht- und Spitzengleichrichter*. Zeitschrift für Physik, 113(5):367–414 (1939). doi: 10.1007/BF01340116. Cited on page 7.

[57] B. F. Levine, K. K. Choi, C. G. Bethea, J. Walker, and R. J. Malik. *New 10 μm infrared detector using intersubband absorption in resonant tunneling GaAlAs superlattices*. Applied Physics Letters, 50(16):1092–1094 (1987). doi: 10.1063/1.97928. Cited on pages 7 and 105.

[58] B. F. Levine. *Quantum-well infrared photodetectors*. Journal of Applied Physics, 74(8):R1–R81 (1993). doi: 10.1063/1.354252. Cited on page 7.

[59] F. R. Giorgetta, E. Baumann, M. Graf, Q. Yang, C. Manz, K. Kohler, H. E. Beere, D. A. Ritchie, E. Linfield, A. G. Davies, Y. Fedoryshyn, H. Jackel, M. Fischer, J. Faist, and D. Hofstetter. *Quantum Cascade Detectors*. IEEE Journal of Quantum Electronics, 45(8):1039–1052 (2009). doi: 10.1109/JQE.2009.2017929. Cited on pages 7 and 105.

[60] D. Hofstetter, F. R. Giorgetta, E. Baumann, Q. Yang, C. Manz, and K. Köhler. *Mid-infrared quantum cascade detectors for applications in spectroscopy and pyrometry*. Applied Physics B, 100(2):313–320 (2010). doi: 10.1007/s00340-010-3965-2. Cited on pages 7 and 105.

[61] M. A. Kinch. *Fundamentals of Infrared Detector Materials*. The Society for Photo-optical Instrumentation Engineers (2007). Cited on pages 7 and 106.

[62] A. Rogalski. *Infrared Detectors*. CRC Press (2011). Cited on pages 7 and 106.

[63] H. Ibach and H. Lüth. *Festkörperphysik - Einführung in die Grundlagen*. Springer-Verlag (1990). Cited on pages 11 and 13.

[64] N. W. Ashcroft and N. D. Mermin. *Solid State Physics*. Saunders College Publishing (1976). Cited on page 13.

[65] J. Faist. *Quantum Cascade Lasers*. Oxford University Press (2013). Cited on pages 14, 19, 21, 25, 30, 33, and 34.

[66] G. A. Reider. *Photonik: Eine Einführung in die Grundlagen*. Springer-Verlag (2005). Cited on pages 14 and 15.

[67] H. Fouckhardt. *Photonik: Eine Einführung in die integrierte Optoelektronik und technische Optik*. Teubner (1994). Cited on pages 15 and 50.

[68] M. G. A. Bernard and G. Duraffourg. *Laser Conditions in Semiconductors*. Physica Status Solidi (b), 1(7):699–703 (1961). doi: 10.1002/pssb.19610010703. Cited on page 15.

[69] P. Y. Yu and M. Cardona. *Fundamentals of Semiconductors*. Springer-Verlag (2005). Cited on page 15.

[70] E. Gornik and A. A. Andronov. *Far-infrared semiconductor lasers*. Optical and Quantum Electronics, 23(2) (1991). doi: 10.1007/BF00619760. Cited on page 16.

[71] M. Helm. *The Basic Physics of Intersubband Transitions*. In H. C. Liu and F. Capasso (Editors), *Intersubband Transitions in Quantum Wells: Physics and Device Applications*, 1–100. Academic Press (2000). Cited on pages 16 and 21.

[72] R. F. Kazarinov and R. A. Suris. *Possibility of the Amplification of Electromagnetic Waves in a Semiconductor with a Superlattice.* Soviet Physics: Semiconductors, 5(4):797–802 (1971). Cited on pages 16 and 22.

[73] J. Faist, F. Capasso, C. Sirtori, D. L. Sivco, A. L. Hutchinson, S. N. G. Chu, and A. Y. Cho. *Quantum-well intersub-band electroluminescent diode at lambda =5 μm.* Electronics Letters, 29(25):2230–2231 (1993). doi: 10.1049/el:19931497. Cited on page 16.

[74] J. Faist, F. Capasso, C. Sirtori, D. Sivco, A. L. Hutchinson, S.-N. G. Chu, and A. Y. Cho. *Mid-infrared field-tunable intersubband electroluminescence at room temperature by photon-assisted tunneling in coupled-quantum wells.* Applied Physics Letters, 64(9):1144–1146 (1994). doi: 10.1063/1.110833. Cited on page 16.

[75] G. Strasser, P. Kruck, M. Helm, J. N. Heyman, L. Hvozdara, and E. Gornik. *Mid-infrared electroluminescence in GaAs/AlGaAs structures.* Applied Physics Letters, 71(20):2892–2894 (1997). doi: 10.1063/1.119329. Cited on page 16.

[76] C. Sirtori, P. Kruck, S. Barbieri, P. Collot, J. Nagle, M. Beck, J. Faist, and U. Oesterle. *$GaAs/Al_xGa_{1-x}As$ quantum cascade lasers.* Applied Physics Letters, 73(24):3486–3488 (1998). doi: 10.1063/1.122812. Cited on page 16.

[77] R. Q. Yang. *Novel Concepts and Structures for Infrared Lasers.* In M. Helm (Editor), *Long Wavelength Infrared Emitters based on Quantum Wells and Superlattices*, 13–64. Gordon and Breach Science Publishers (2000). Cited on page 17.

[78] G. Bastard. *Wave mechanics applied to semiconductor heterostructures.* Les Éditions de Physique (1988). Cited on page 21.

[79] C. Sirtori and R. Teissier. *Quantum Cascade Lasers: Overview of Basic Principles of Operation and State of the Art.* In R. Paiella (Editor), *Intersubband Transitions in Quantum Structures*, 1–44. The McGraw-Hill Companies, Inc. (2006). Cited on page 21.

[80] R. F. Kazarinov and R. A. Suris. *Electric and electromagnetic properties of semiconductors with a superlattice.* Soviet Physics: Semiconductors, 6(1):120–131 (1972). Cited on page 22.

[81] F. Capasso, K. Mohammed, and A. Cho. *Resonant tunneling through double barriers, perpendicular quantum transport phenomena in superlattices, and their device applications.* IEEE Journal of Quantum Electronics, 22(9):1853–1869 (1986). doi: 10.1109/JQE.1986.1073171. Cited on page 23.

[82] F. Capasso. *Band-structure engineering of new photonic materials: high performance mid-infrared quantum cascade lasers.* In A. Miller, M. Ebrahimzadeh, and D. M. Finlayson (Editors), *Semiconductor Quantum Optoelectronics - From Quantum Physics to Smart Devices*, 391–432. Proceedings of the Fiftieth Scottish Universities Summer School in Physics (1999). Cited on page 23.

[83] C. Sirtori, F. Capasso, J. Faist, A. L. Hutchinson, D. L. Sivco, and A. Y. Cho. *Resonant tunneling in quantum cascade lasers.* IEEE Journal of Quantum Electronics, 34(9):1722–1729 (1998). doi: 10.1109/3.709589. Cited on page 23.

[84] J. Faist, F. Capasso, C. Sirtori, D. L. Sivco, J. N. Baillargeon, A. L. Hutchinson, S.-N. G. Chu, and A. Y. Cho. *High power mid-infrared ($\lambda \sim 5\,\mu m$) quantum cascade lasers operating above room temperature.* Applied Physics Letters, 68(26):3680–3682 (1996). doi: 10.1063/1.115741. Cited on page 23.

[85] C. Gmachl, F. Capasso, D. L. Sivco, and A. Y. Cho. *Recent progress in quantum cascade lasers and applications.* Reports on Progress in Physics, 64(11):1533–1601 (2001). doi: 10.1088/0034-4885/64/11/204. Cited on pages 25 and 34.

[86] J. Cockburn. *Mid-infrared Quantum Cascade Lasers.* In A. Krier (Editor), *Mid-infrared Semiconductor Optoelectronics*, 323–358. Springer-Verlag (2006). Cited on page 25.

[87] P. Blood, E. D. Fletcher, and K. Woodbridge. *Dependence of threshold current on the number of wells in AlGaAs-GaAs quantum well lasers.* Applied Physics Letters, 47(3):193–195 (1985). doi: 10.1063/1.96213. Cited on page 25.

[88] E. Mujagić. *Ring Cavity Surface Emitting Semiconductor Lasers.* TU Wien (Dissertation) (2010). Cited on pages 29, 31, and 66.

[89] N. Finger, W. Schrenk, and E. Gornik. *Analysis of TM-polarized DFB laser structures with metal surface gratings.* IEEE Journal of Quantum Electronics, 36(7):780–786 (2000). doi: 10.1109/3.848348. Cited on pages 29, 41, 54, and 115.

[90] H. Zappe. *Introduction to Semiconductor Integrated Optics.* Artech House, Inc. (1995). Cited on page 30.

[91] P. L. Chebyshev. *Théorie des mécanismes connus sous le nom de parallélogrammes.* Mémoires des Savants étrangers présentés à l'Académie de Saint-Pétersbourg, 7:539–586 (1854). Cited on page 36.

[92] J. Hong, W. Huang, and T. Makino. *On the transfer matrix method for distributed-feedback waveguide devices.* Journal of Lightwave Technology, 10(12):1860–1868 (1992). doi: 10.1109/50.202840. Cited on page 36.

[93] T. Makino. *Transfer Matrix Method with Applications to Distributed Feedback Optical Devices.* Progress in Electromagnetic Research, 10:271–319 (1995). Cited on page 36.

[94] H. Kogelnik. *Coupled Wave Theory for Thick Hologram Gratings.* The Bell System Technical Journal, 48:2909–2947 (1969). doi: 10.1002/j.1538-7305.1969.tb01198.x. Cited on pages 36 and 41.

[95] G. Morthier and P. Vankwikelberge. *Handbook of Distributed Feedback Laser Diodes.* Artech House, Inc. (1997). Cited on page 36.

[96] H. Kogelnik and C. V. Shank. *Coupled-Wave Theory of Distributed Feedback Lasers.* Journal of Applied Physics, 43(5):2327–2335 (1972). doi: 10.1063/1.1661499. Cited on page 41.

[97] J. Faist, C. Gmachl, F. Capasso, C. Sirtori, D. L. Sivco, J. N. Baillargeon, and A. Y. Cho. *Distributed feedback quantum cascade lasers.* Applied Physics Letters, 70(20):2670 (1997). doi: 10.1063/1.119208. Cited on pages 41 and 43.

[98] M. Troccoli, C. Gmachl, F. Capasso, D. L. Sivco, and A. Y. Cho. *Mid-infrared ($\lambda \approx 7.4\,\mu m$) quantum cascade laser amplifier for high power single-mode emission and improved beam quality.* Applied Physics Letters, 80(22):4103–4105 (2002). doi: 10.1063/1.1479453. Cited on page 43.

[99] S. Menzel, L. Diehl, C. Pflügl, A. Goyal, C. Wang, A. Sanchez, G. Turner, and F. Capasso. *Quantum cascade laser master-oscillator power-amplifier with 1.5 W output power at 300 K.* Optics Express, 19(17):16229–16235 (2011). doi: 10.1364/OE.19.016229. Cited on page 43.

[100] B. Hinkov, M. Beck, E. Gini, and J. Faist. *Quantum cascade laser in a master oscillator power amplifier configuration with Watt-level optical output power.* Optics Express, 21(16):19180–19186 (2013). doi: 10.1364/OE.21.019180. Cited on page 43.

[101] S. Ahn, C. Schwarzer, T. Zederbauer, D. C. MacFarland, H. Detz, A. M. Andrews, W. Schrenk, and G. Strasser. *High-power, low-lateral divergence broad area quantum cascade lasers with a tilted front facet.* Applied Physics Letters, 104(5):051101 (2014). doi: 10.1063/1.4863504. Cited on page 43.

[102] S. Ahn, C. Schwarzer, T. Zederbauer, H. Detz, A. M. Andrews, W. Schrenk, and G. Strasser. *Enhanced light output power of quantum cascade lasers from a tilted front facet.* Optics Express, 21(13):15869–15877 (2013). doi: 10.1364/OE.21.015869. Cited on pages 43 and 44.

[103] N. Yu, R. Blanchard, J. Fan, Q. J. Wang, C. Pflügl, L. Diehl, T. Edamura, M. Yamanishi, H. Kan, and F. Capasso. *Quantum cascade lasers with integrated plasmonic antenna-array collimators.* Optics Express, 16(24):19447–19461 (2008). doi: 10.1364/OE.16.019447. Cited on page 43.

[104] N. Yu and F. Capasso. *Wavefront engineering for mid-infrared and terahertz quantum cascade lasers.* Journal of the Optical Society of America B, 27(11):B18–B35 (2010). doi: 10.1364/JOSAB.27.000B18. Cited on page 43.

[105] J. Faist, C. Gmachl, M. Striccoli, C. Sirtori, F. Capasso, D. L. Sivco, and A. Y. Cho. *Quantum cascade disk lasers.* Applied Physics Letters, 69(17):2456–2458 (1996). doi: 10.1063/1.117496. Cited on pages 43 and 44.

[106] W. Schrenk, N. Finger, S. Gianordoli, L. Hvozdara, G. Strasser, and E. Gornik. *Surface-emitting distributed feedback quantum-cascade lasers.* Applied Physics Letters, 77(14):2086–2088 (2000). doi: 10.1063/1.1313807. Cited on pages 43, 44, and 54.

[107] C. Pflügl, M. Austerer, W. Schrenk, S. Golka, G. Strasser, R. P. Green, L. R. Wilson, J. W. Cockburn, A. B. Krysa, and J. S. Roberts. *Single-mode surface-emitting quantum-cascade lasers.* Applied Physics Letters, 86(21):211102 (2005). doi: 10.1063/1.1929070. Cited on pages 43 and 54.

[108] D. Hofstetter, J. Faist, M. Beck, and U. Oesterle. *Surface-emitting* $10.1\,\mu m$ *quantum-cascade distributed feedback lasers.* Applied Physics Letters, 75(24):3769–3771 (1999). doi: 10.1063/1.125450. Cited on page 43.

[109] R. F. Kazarinov and R. A. Suris. *Injection heterojunction laser with a diffraction grating on its contact surface*. Soviet Physics Semiconductors-USSR, 6(7):1184–1189 (1973). Cited on page 44.

[110] P. Jouy, C. Bonzon, J. Wolf, E. Gini, M. Beck, and J. Faist. *Surface emitting multi-wavelength array of single frequency quantum cascade lasers*. Applied Physics Letters, 106(7):071104 (2015). doi: 10.1063/1.4913203. Cited on page 44.

[111] R. Colombelli, K. Srinivasan, M. Troccoli, O. Painter, C. F. Gmachl, D. M. Tennant, A. M. Sergent, D. L. Sivco, A. Y. Cho, and F. Capasso. *Quantum Cascade Surface-Emitting Photonic Crystal Laser*. Science, 302(5649):1374–1377 (2003). doi: 10.1126/science.1090561. Cited on page 44.

[112] C. Sirtori, S. Barbieri, and R. Colombelli. *Wave engineering with THz quantum cascade lasers*. Nature Photonics, 7(9):691–701 (2013). doi: 10.1038/nphoton.2013.208. Cited on page 44.

[113] M. S. Vitiello, M. Nobile, A. Ronzani, A. Tredicucci, F. Castellano, V. Talora, L. Li, E. H. Linfield, and A. G. Davies. *Photonic quasi-crystal terahertz lasers*. Nature Communications, 5:5884–5891 (2014). doi: 10.1038/ncomms6884. Cited on page 44.

[114] R. Degl'Innocenti, Y. D. Shah, L. Masini, A. Ronzani, A. Pitanti, Y. Ren, D. S. Jessop, A. Tredicucci, H. E. Beere, and D. A. Ritchie. *Hyperuniform disordered terahertz quantum cascade laser*. Scientific Reports, 6:19325–19331 (2016). doi: 10.1038/srep19325. Cited on page 44.

[115] S. Schönhuber, M. Brandstetter, T. Hisch, C. Deutsch, M. Krall, H. Detz, A. M. Andrews, G. Strasser, S. Rotter, and K. Unterrainer. *Random lasers for broadband directional emission*. Optica, 3(10):1035–1038 (2016). doi: 10.1364/OPTICA.3.001035. Cited on pages 44 and 94.

[116] G. Liang, H. Liang, Y. Zhang, S. P. Khanna, L. Li, A. G. Davies, E. Linfield, D. F. Lim, C. S. Tan, S. F. Yu, H. C. Liu, and Q. J. Wang. *Single-mode surface-emitting concentric-circular-grating terahertz quantum cascade lasers*. Applied Physics Letters, 102(3):031119 (2013). doi: 10.1063/1.4789535. Cited on page 44.

[117] G. Xu, R. Colombelli, S. P. Khanna, A. Belarouci, X. Letartre, L. Li, E. H. Linfield, A. G. Davies, H. E. Beere, and D. A. Ritchie. *Efficient power extraction in surface-emitting semiconductor lasers using graded photonic heterostructures*. Nature Communications, 3:952–958 (2012). doi: 10.1038/ncomms1958. Cited on pages 44 and 47.

[118] N. Yu and F. Capasso. *Flat optics with designer metasurfaces*. Nature Materials, 13(2):139–150 (2014). doi: 10.1038/nmat3839. Cited on pages 44 and 85.

[119] E. Mujagić, S. Schartner, L. K. Hoffmann, W. Schrenk, M. P. Semtsiv, M. Wienold, W. T. Masselink, and G. Strasser. *Grating-coupled surface emitting quantum cascade ring lasers*. Applied Physics Letters, 93(1):011108 (2008). doi: 10.1063/1.2958910. Cited on pages 45 and 47.

[120] E. Mujagić, L. K. Hoffmann, S. Schartner, M. Nobile, W. Schrenk, M. P. Semtsiv, M. Wienold, W. T. Masselink, and G. Strasser. *Low divergence single-mode surface*

emitting quantum cascade ring lasers. Applied Physics Letters, 93(16):161101 (2008). doi: 10.1063/1.3000630. Cited on page 45.

[121] E. Mujagić, C. Deutsch, H. Detz, P. Klang, M. Nobile, A. M. Andrews, W. Schrenk, K. Unterrainer, and G. Strasser. *Vertically emitting terahertz quantum cascade ring lasers.* Applied Physics Letters, 95(1):011120 (2009). doi: 10.1063/1.3176966. Cited on page 45.

[122] L. Mahler, M. I. Amanti, C. Walther, A. Tredicucci, F. Beltram, J. Faist, H. E. Beere, and D. A. Ritchie. *Distributed feedback ring resonators for vertically emitting terahertz quantum cascade lasers.* Optics Express, 17(15):13031–13039 (2009). doi: 10.1364/OE.17.013031. Cited on pages 45, 57, and 59.

[123] L. Mahler, A. Tredicucci, F. Beltram, C. Walther, J. Faist, B. Witzigmann, H. E. Beere, and D. A. Ritchie. *Vertically emitting microdisk lasers.* Nature Photonics, 3(1):46–49 (2009). doi: 10.1038/nphoton.2008.248. Cited on pages 45 and 47.

[124] E. Mujagić, M. Nobile, H. Detz, W. Schrenk, J. Chen, C. Gmachl, and G. Strasser. *Ring cavity induced threshold reduction in single-mode surface emitting quantum cascade lasers.* Applied Physics Letters, 96(3):031111 (2010). doi: 10.1063/1.3292021. Cited on page 45.

[125] Y. Bai, S. Tsao, N. Bandyopadhyay, S. Slivken, Q. Y. Lu, D. Caffey, M. Pushkarsky, T. Day, and M. Razeghi. *High power, continuous wave, quantum cascade ring laser.* Applied Physics Letters, 99(26):261104 (2011). doi: 10.1063/1.3672049. Cited on pages 45 and 52.

[126] C. Schwarzer, E. Mujagić, Y. Yao, W. Schrenk, J. Chen, C. Gmachl, and G. Strasser. *Coherent coupling of ring cavity surface emitting quantum cascade lasers.* Applied Physics Letters, 97(7):071103 (2010). doi: 10.1063/1.3479913. Cited on page 45.

[127] E. Mujagić, C. Schwarzer, Y. Yao, J. Chen, C. Gmachl, and G. Strasser. *Two-dimensional broadband distributed-feedback quantum cascade laser arrays.* Applied Physics Letters, 98(14):141101 (2011). doi: 10.1063/1.3574555. Cited on pages 45 and 61.

[128] R. Szedlak. *Beam Modifications of Ring Quantum Cascade Lasers.* University of Konstanz (Master's thesis) (2013). Cited on page 46.

[129] R. J. Noll and S. H. Macomber. *Analysis of grating surface emitting lasers.* IEEE Journal of Quantum Electronics, 26(3):456–466 (1990). doi: 10.1109/3.52121. Cited on pages 46 and 47.

[130] S. H. Macomber. *Nonlinear analysis of surface-emitting distributed feedback lasers.* IEEE Journal of Quantum Electronics, 26(12):2065–2074 (1990). doi: 10.1109/3.64341. Cited on pages 46, 57, and 70.

[131] M. Schubert and F. Rana. *Analysis of terahertz surface emitting quantum-cascade lasers.* IEEE Journal of Quantum Electronics, 42(3):257–265 (2006). doi: 10.1109/JQE.2005.863138. Cited on pages 47 and 54.

[132] S. Kumar, B. S. Williams, Q. Qin, A. M. Lee, Q. Hu, and J. L. Reno. *Surface-emitting distributed feedback terahertz quantum-cascade lasers in metal-metal waveguides*. Optics Express, 15(1):113–128 (2007). doi: 10.1364/OE.15.000113. Cited on pages 47 and 54.

[133] G. Witjaksono and D. Botez. *Surface-emitting, single-lobe operation from second-order distributed-reflector lasers with central grating phaseshift*. Applied Physics Letters, 78(26):4088–4090 (2001). doi: 10.1063/1.1382633. Cited on pages 47 and 54.

[134] S. Li, G. Witjaksono, S. Macomber, and D. Botez. *Analysis of surface-emitting second-order distributed feedback lasers with central grating phaseshift*. IEEE Journal of Selected Topics in Quantum Electronics, 9(5):1153–1165 (2003). doi: 10.1109/JSTQE.2003.819467. Cited on pages 47 and 54.

[135] G. Witjaksono, S. Li, J. J. Lee, D. Botez, and W. K. Chan. *Single-lobe, surface-normal beam surface emission from second-order distributed feedback lasers with half-wave grating phase shift*. Applied Physics Letters, 83(26):5365–5367 (2003). doi: 10.1063/1.1636248. Cited on pages 47 and 54.

[136] L. Mahler, A. Tredicucci, F. Beltram, C. Walther, J. Faist, H. E. Beere, and D. A. Ritchie. *High-power surface emission from terahertz distributed feedback lasers with a dual-slit unit cell*. Applied Physics Letters, 96(19):191109 (2010). doi: 10.1063/1.3430522. Cited on page 47.

[137] C. Sigler, J. D. Kirch, T. Earles, L. J. Mawst, Z. Yu, and D. Botez. *Design for high-power, single-lobe, grating-surface-emitting quantum cascade lasers enabled by plasmon-enhanced absorption of antisymmetric modes*. Applied Physics Letters, 104(13):131108 (2014). doi: 10.1063/1.4869561. Cited on page 47.

[138] C. Boyle, C. Sigler, J. D. Kirch, D. F. L. III, T. Earles, D. Botez, and L. J. Mawst. *High-power, surface-emitting quantum cascade laser operating in a symmetric grating mode*. Applied Physics Letters, 108(12):121107 (2016). doi: 10.1063/1.4944846. Cited on page 47.

[139] Y. Liu, J. Zhang, F. Yan, Z. Jia, F. Liu, P. Liang, N. Zhuo, S. Zhai, L. Wang, J. Liu, S. Liu, and Z. Wang. *High efficiency, single-lobe surface-emitting DFB/DBR quantum cascade lasers*. Optics Express, 24(17):19545–19551 (2016). doi: 10.1364/OE.24.019545. Cited on page 47.

[140] D. H. Wu and M. Razeghi. *High power, low divergent, substrate emitting quantum cascade ring laser in continuous wave operation*. APL Materials, 5(3):035505 (2017). doi: 10.1063/1.4978810. Cited on page 47.

[141] A. Lyakh, P. Zory, M. D'Souza, D. Botez, and D. Bour. *Substrate-emitting, distributed feedback quantum cascade lasers*. Applied Physics Letters, 91(18):181116 (2007). doi: 10.1063/1.2803851. Cited on page 48.

[142] Y. Bai, S. Tsao, N. Bandyopadhyay, S. Slivken, Q. Y. Lu, and M. Razeghi. *Substrate emission quantum cascade ring lasers with room temperature continuous wave operation*. Proceedings of SPIE, 8268:82680N—82680N–6 (2012). doi: 10.1117/12.913655. Cited on page 48.

[143] C. Schwarzer, E. Mujagić, S. I. Ahn, A. M. Andrews, W. Schrenk, W. Charles, C. Gmachl, and G. Strasser. *Grating duty-cycle induced enhancement of substrate emission from ring cavity quantum cascade lasers*. Applied Physics Letters, 100(19):191103 (2012). doi: 10.1063/1.4712127. Cited on pages 48 and 49.

[144] J. Fourier. *Théorie analytique de la chaleur*. Chez Firmin Didot, père et fils (1822). Cited on page 49.

[145] J. W. Goodman. *Introduction to Fourier optics*. Roberts Englewood, Colo. (2005). Cited on page 50.

[146] M. Totzeck. *Optics for High Tech Industry*. University of Konstanz/Carl Zeiss AG (2012). Cited on page 50.

[147] R. Szedlak, C. Schwarzer, T. Zederbauer, H. Detz, A. M. Andrews, W. Schrenk, and G. Strasser. *Grating-based far field modifications of ring quantum cascade lasers*. Optics Express, 22(13):15829–15836 (2014). doi: 10.1364/OE.22.015829. Cited on pages 53, 54, 58, 59, and 60.

[148] M. J. Süss, P. Jouy, C. Bonzon, J. M. Wolf, E. Gini, M. Beck, and J. Faist. *Single-Mode Quantum Cascade Laser Array Emitting From a Single Facet*. IEEE Photonics Technology Letters, 28(11):1197–1200 (2016). doi: 10.1109/LPT.2016.2533443. Cited on pages 54 and 61.

[149] C. Schwarzer, R. Szedlak, S. I. Ahn, T. Zederbauer, H. Detz, A. M. Andrews, W. Schrenk, and G. Strasser. *Linearly polarized light from substrate emitting ring cavity quantum cascade lasers*. Applied Physics Letters, 103(8):081101 (2013). doi: 10.1063/1.4819034. Cited on pages 55, 56, 57, 76, and 77.

[150] R. Szedlak, M. Holzbauer, P. Reininger, D. MacFarland, T. Zederbauer, H. Detz, A. M. Andrews, W. Schrenk, and G. Strasser. *Ring quantum cascade lasers with grating phase shifts and a light collimating dielectric metamaterial for enhanced infrared spectroscopy*. Vibrational Spectroscopy, 84:101–105 (2016). doi: 10.1016/j.vibspec.2016.03.009. Cited on pages 55, 78, 79, 82, 83, 85, and 90.

[151] S. H. Macomber, J. S. Mott, B. D. Schwartz, R. S. Setzko, J. J. Powers, P. A. Lee, D. P. Kwo, R. M. Dixon, and J. E. Logue. *Curved-grating surface-emitting DFB lasers and arrays*. Proceedings of SPIE, 3001:42–54 (1997). doi: 10.1117/12.273813. Cited on page 57.

[152] P. Rauter and F. Capasso. *Multi-wavelength quantum cascade laser arrays*. Laser & Photonics Reviews, 9(5):452–477 (2015). doi: 10.1002/lpor.201500095. Cited on page 60.

[153] J. Faist, M. Beck, T. Aellen, and E. Gini. *Quantum-cascade lasers based on a bound-to-continuum transition*. Applied Physics Letters, 78(2):147–149 (2001). doi: 10.1063/1.1339843. Cited on page 60.

[154] C. Gmachl, D. L. Sivco, R. Colombelli, F. Capasso, and A. Y. Cho. *Ultra-broadband semiconductor laser*. Nature, 415(6874):883–887 (2002). doi: 10.1038/415883a. Cited on page 60.

[155] G. P. Luo, C. Peng, H. Q. Le, S. S. Pei, W.-Y. Hwang, B. Ishaug, J. Um, J. N. Baillargeon, and C.-H. Lin. *Grating-tuned external-cavity quantum-cascade semiconductor lasers*. Applied Physics Letters, 78(19):2834–2836 (2001). doi: 10.1063/1.1371524. Cited on page 60.

[156] R. Maulini, M. Beck, J. Faist, and E. Gini. *Broadband tuning of external cavity bound-to-continuum quantum-cascade lasers*. Applied Physics Letters, 84(10):1659–1661 (2004). doi: 10.1063/1.1667609. Cited on page 60.

[157] B. G. Lee, M. A. Belkin, R. Audet, J. MacArthur, L. Diehl, C. Pflügl, F. Capasso, D. C. Oakley, D. Chapman, A. Napoleone, D. Bour, S. Corzine, G. Höfler, and J. Faist. *Widely tunable single-mode quantum cascade laser source for mid-infrared spectroscopy*. Applied Physics Letters, 91(23):231101 (2007). doi: 10.1063/1.2816909. Cited on page 61.

[158] B. G. Lee, J. Kansky, A. K. Goyal, C. Pflügl, L. Diehl, M. A. Belkin, A. Sanchez, and F. Capasso. *Beam combining of quantum cascade laser arrays*. Optics Express, 17(18):16216–16224 (2009). doi: 10.1364/OE.17.016216. Cited on page 61.

[159] S. Hugger, R. Aidam, W. Bronner, F. Fuchs, R. Lösch, Q. Yang, J. Wagner, E. Romasew, M. Raab, H. D. Tholl, B. Höfer, and A. L. Matthes. *Power scaling of quantum cascade lasers via multiemitter beam combining*. Optical Engineering, 49(11):111111–111115 (2010). doi: 10.1117/1.3498766. Cited on page 61.

[160] G. Bloom, C. Larat, E. Lallier, G. Lehoucq, S. Bansropun, M.-S. L. Lee-Bouhours, B. Loiseaux, M. Carras, X. Marcadet, G. Lucas-Leclin, and P. Georges. *Passive coherent beam combining of quantum-cascade lasers with a Dammann grating*. Optics Letters, 36(19):3810–3812 (2011). doi: 10.1364/OL.36.003810. Cited on page 61.

[161] W. Zhou, N. Bandyopadhyay, D. Wu, R. McClintock, and M. Razeghi. *Monolithically, widely tunable quantum cascade lasers based on a heterogeneous active region design*. Scientific Reports, 6:25213–25219 (2016). doi: 10.1038/srep25213. Cited on page 61.

[162] G. Sevin, G. Xu, N. Isac, R. Colombelli, H. E. Beere, and D. A. Ritchie. *Monolithically integrated two-dimensional arrays of surface-emitting photonic-crystal terahertz lasers*. Journal of Infrared, Millimeter, and Terahertz Waves, 34(5):386–392 (2013). doi: 10.1007/s10762-013-9989-z. Cited on page 61.

[163] J. Rayleigh. *The Theory of Sound*. Macmillan (1894). Cited on page 63.

[164] G. Mie. *Beiträge zur Optik trüber Medien, speziell kolloidaler Metallösungen*. Annalen der Physik, 330(3):377–445 (1908). doi: 10.1002/andp.19083300302. Cited on page 63.

[165] P. Debye. *Der Lichtdruck auf Kugeln von beliebigem Material*. Annalen der Physik, 335(11):57–136 (1909). doi: 10.1002/andp.19093351103. Cited on page 63.

[166] K. J. Vahala. *Optical microcavities*. Nature, 424(6950):839–846 (2003). doi: 10.1038/nature01939. Cited on page 63.

[167] *COMSOL Multiphysics® v. 5.2*. www.comsol.com. COMSOL AB, Stockholm, Sweden. Cited on pages 64 and 115.

[168] J. S. Gu, P. A. Besse, and H. Melchior. *Novel method for analysis of curved optical rib-waveguides.* Electronics Letters, 25(4):278–280 (1989). doi: 10.1049/el:19890193. Cited on page 65.

[169] K. R. Hiremath, M. Hammer, R. Stoffer, L. Prkna, and J. Čtyroký. *Analytic approach to dielectric optical bent slab waveguides.* Optical and Quantum Electronics, 37(1):37–61 (2005). doi: 10.1007/s11082-005-1118-3. Cited on page 65.

[170] M. Heiblum and J. Harris. *Analysis of curved optical waveguides by conformal transformation.* IEEE Journal of Quantum Electronics, 11(2):75–83 (1975). doi: 10.1109/JQE.1975.1068563. Cited on page 65.

[171] M. K. Chin, D. Y. Chu, and S.-T. Ho. *Estimation of the spontaneous emission factor for microdisk lasers via the approximation of whispering gallery modes.* Journal of Applied Physics, 75(7):3302–3307 (1994). doi: 10.1063/1.356137. Cited on page 65.

[172] W. Berglund and A. Gopinath. *WKB analysis of bend losses in optical waveguides.* Journal of Lightwave Technology, 18(8):1161–1166 (2000). doi: 10.1109/50.857763. Cited on page 65.

[173] A. Ghatak, K. Thyagarajan, and M. Shenoy. *Numerical analysis of planar optical waveguides using matrix approach.* Journal of Lightwave Technology, 5(5):660–667 (1987). doi: 10.1109/JLT.1987.1075553. Cited on page 65.

[174] I. C. Goyal, R. L. Gallawa, and A. K. Ghatak. *Bent planar waveguides and whispering gallery modes: a new method of analysis.* Journal of Lightwave Technology, 8(5):768–774 (1990). doi: 10.1109/50.54485. Cited on page 65.

[175] M. K. Chin and S. T. Ho. *Design and modeling of waveguide-coupled single-mode microring resonators.* Journal of Lightwave Technology, 16(8):1433–1446 (1998). doi: 10.1109/50.704609. Cited on page 65.

[176] R. Szedlak, M. Holzbauer, D. MacFarland, T. Zederbauer, H. Detz, A. M. Andrews, C. Schwarzer, W. Schrenk, and G. Strasser. *The influence of whispering gallery modes on the far field of ring lasers.* Scientific Reports, 5:16668–16675 (2015). doi: 10.1038/srep16668. Cited on pages 67, 68, 69, 71, 73, 74, and 75.

[177] R. Szedlak, C. Schwarzer, T. Zederbauer, H. Detz, A. M. Andrews, W. Schrenk, and G. Strasser. *On-chip focusing in the mid-infrared: Demonstrated with ring quantum cascade lasers.* Applied Physics Letters, 104(15):151105 (2014). doi: 10.1063/1.4871520. Cited on pages 78, 80, 81, 82, 84, and 85.

[178] G. D. Pettit and W. J. Turner. *Refractive Index of InP.* Journal of Applied Physics, 36(6):2081–2081 (1965). doi: 10.1063/1.1714410. Cited on pages 79 and 91.

[179] R. D. Grober, R. J. Schoelkopf, and D. E. Prober. *Optical antenna: Towards a unity efficiency near-field optical probe.* Applied Physics Letters, 70(11):1354–1356 (1997). doi: 10.1063/1.118577. Cited on page 85.

[180] N. Yu, P. Genevet, M. A. Kats, F. Aieta, J.-P. Tetienne, F. Capasso, and Z. Gaburro. *Light Propagation with Phase Discontinuities: Generalized Laws of Reflection and Refraction.* Science, 334(6054):333–337 (2011). doi: 10.1126/science.1210713. Cited on page 85.

[181] P. Genevet, N. Yu, F. Aieta, J. Lin, M. A. Kats, R. Blanchard, M. O. Scully, Z. Gaburro, and F. Capasso. *Ultra-thin plasmonic optical vortex plate based on phase discontinuities.* Applied Physics Letters, 100(1):013101 (2012). doi: 10.1063/1.3673334. Cited on page 85.

[182] N. Yu, P. Genevet, F. Aieta, M. A. Kats, R. Blanchard, G. Aoust, J. P. Tetienne, Z. Gaburro, and F. Capasso. *Flat Optics: Controlling Wavefronts With Optical Antenna Metasurfaces.* IEEE Journal of Selected Topics in Quantum Electronics, 19(3):4700423–4700445 (2013). doi: 10.1109/JSTQE.2013.2241399. Cited on page 85.

[183] J.-C. Zhang, D.-Y. Yao, N. Zhuo, F.-L. Yan, F.-Q. Liu, L.-J. Wang, J.-Q. Liu, and Z.-G. Wang. *Directional collimation of substrate emitting quantum cascade laser by nanopores arrays.* Applied Physics Letters, 104(5):052109 (2014). doi: 10.1063/1.4864633. Cited on page 85.

[184] R. A. Beth. *Mechanical Detection and Measurement of the Angular Momentum of Light.* Physical Review, 50:115–125 (1936). doi: 10.1103/PhysRev.50.115. Cited on page 86.

[185] A. T. O'Neil, I. MacVicar, L. Allen, and M. J. Padgett. *Intrinsic and Extrinsic Nature of the Orbital Angular Momentum of a Light Beam.* Physical Review Letters, 88:053601–053604 (2002). doi: 10.1103/PhysRevLett.88.053601. Cited on page 86.

[186] J. Wang, J.-Y. Yang, I. M. Fazal, N. Ahmed, Y. Yan, H. Huang, Y. Ren, Y. Yue, S. Dolinar, M. Tur, and A. E. Willner. *Terabit free-space data transmission employing orbital angular momentum multiplexing.* Nature Photonics, 6(7):488–496 (2012). doi: 10.1038/nphoton.2012.138. Cited on page 86.

[187] W. Brullot, M. K. Vanbel, T. Swusten, and T. Verbiest. *Resolving enantiomers using the optical angular momentum of twisted light.* Science Advances, 2(3):e1501349 (2016). doi: 10.1126/sciadv.1501349. Cited on page 86.

[188] S. M. Barnett. *Optical angular-momentum flux.* Journal of Optics B: Quantum and Semiclassical Optics, 4(2):7–16 (2002). Cited on pages 86, 88, and 89.

[189] S. M. Barnett and L. Allen. *Orbital angular momentum and nonparaxial light beams.* Optics Communications, 110(5):670–678 (1994). doi: 10.1016/0030-4018(94)90269-0. Cited on pages 87 and 89.

[190] L. Allen, M. W. Beijersbergen, R. J. C. Spreeuw, and J. P. Woerdman. *Orbital angular momentum of light and the transformation of Laguerre-Gaussian laser modes.* Physical Review A, 45:8185–8189 (1992). doi: 10.1103/PhysRevA.45.8185. Cited on page 88.

[191] J. B. Götte and S. M. Barnett. *Light beams carrying orbital angular momentum.* In D. L. Andrews and M. Babiker (Editors), *The angular momentum of light*, 1–30. Cambridge University Press (2013). Cited on pages 88, 89, and 91.

[192] M. Padgett and L. Allen. *Light with a twist in its tail.* Contemporary Physics, 41(5):275–285 (2000). doi: 10.1080/001075100750012777. Cited on page 89.

[193] J. Durnin, J. J. Miceli, and J. H. Eberly. *Diffraction-free beams*. Physical Review Letters, 58:1499–1501 (1987). doi: 10.1103/PhysRevLett.58.1499. Cited on page 89.

[194] H. He, M. E. J. Friese, N. R. Heckenberg, and H. Rubinsztein-Dunlop. *Direct Observation of Transfer of Angular Momentum to Absorptive Particles from a Laser Beam with a Phase Singularity*. Physical Review Letters, 75:826–829 (1995). doi: 10.1103/PhysRevLett.75.826. Cited on page 90.

[195] M. Padgett, J. Arlt, N. Simpson, and L. Allen. *An experiment to observe the intensity and phase structure of Laguerre-Gaussian laser modes*. American Journal of Physics, 64(1):77–82 (1996). doi: 10.1119/1.18283. Cited on page 90.

[196] M. P. J. Lavery, J. Courtial, and M. J. Padgett. *Measurement of light's orbital angular momentum*. In D. L. Andrews and M. Babiker (Editors), *The angular momentum of light*, 330–351. Cambridge University Press (2013). Cited on page 90.

[197] M. Beijersbergen, R. Coerwinkel, M. Kristensen, and J. Woerdman. *Helical-wavefront laser beams produced with a spiral phaseplate*. Optics Communications, 112(5):321–327 (1994). doi: 10.1016/0030-4018(94)90638-6. Cited on page 90.

[198] V. I. Bazhenov, M. V. Vasnetsov, and M. S. Soskin. *Laser beams with wave front screw dislocations*. Pisma v Zhurnal Eksperimentalnoi i Teoreticheskoi Fiziki, 52:1037–1039 (1990). Cited on page 90.

[199] E. Karimi, S. A. Schulz, I. De Leon, H. Qassim, J. Upham, and R. W. Boyd. *Generating optical orbital angular momentum at visible wavelengths using a plasmonic metasurface*. Light Science & Applications, 3:167–170 (2014). Cited on page 90.

[200] H. Li, D. B. Phillips, X. Wang, Y.-L. D. Ho, L. Chen, X. Zhou, J. Zhu, S. Yu, and X. Cai. *Orbital angular momentum vertical-cavity surface-emitting lasers*. Optica, 2(6):547–552 (2015). doi: 10.1364/OPTICA.2.000547. Cited on pages 90 and 91.

[201] X. Cai, J. Wang, M. J. Strain, B. Johnson-Morris, J. Zhu, M. Sorel, J. L. O'Brien, M. G. Thompson, and S. Yu. *Integrated Compact Optical Vortex Beam Emitters*. Science, 338(6105):363–366 (2012). doi: 10.1126/science.1226528. Cited on page 90.

[202] B. Andreas, G. Mana, and C. Palmisano. *Vectorial ray-based diffraction integral*. Journal of the Optical Society of America A, 32(8):1403–1424 (2015). doi: 10.1364/JOSAA.32.001403. Cited on page 94.

[203] M. Tacke. *Lead–salt lasers*. Philosophical Transactions of the Royal Society of London A: Mathematical, Physical and Engineering Sciences, 359(1780):547–566 (2001). doi: 10.1098/rsta.2000.0742. Cited on page 97.

[204] M. Beck, D. Hofstetter, T. Aellen, J. Faist, U. Oesterle, M. Ilegems, E. Gini, and H. Melchior. *Continuous Wave Operation of a Mid-Infrared Semiconductor Laser at Room Temperature*. Science, 295(5553):301–305 (2002). doi: 10.1126/science.1066408. Cited on page 97.

[205] L. Hvozdara, N. Pennington, M. Kraft, M. Karlowatz, and B. Mizaikoff. *Quantum cascade lasers for mid-infrared spectroscopy*. Vibrational Spectroscopy, 30(1):53–58 (2002). doi: 10.1016/S0924-2031(02)00038-3. Cited on page 97.

[206] G. Plant, A. Hangauer, T. Wang, and G. Wysocki. *Fiber dispersion measurement using chirped laser dispersion spectroscopy technique*. Applied Optics, 54(33):9844–9847 (2015). doi: 10.1364/AO.54.009844. Cited on page 97.

[207] J. Wojtas, J. Mikolajczyk, and Z. Bielecki. *Aspects of the Application of Cavity Enhanced Spectroscopy to Nitrogen Oxides Detection*. Sensors, 13(6):7570–7598 (2013). doi: 10.3390/s130607570. Cited on page 97.

[208] P. Patimisco, G. Scamarcio, F. Tittel, and V. Spagnolo. *Quartz-Enhanced Photoacoustic Spectroscopy: A Review*. Sensors, 14(4):6165–6206 (2014). doi: 10.3390/s140406165. Cited on page 97.

[209] M. A. Pleitez, O. Hertzberg, A. Bauer, M. Seeger, T. Lieblein, H. v. Lilienfeld-Toal, and W. Mantele. *Photothermal deflectometry enhanced by total internal reflection enables non-invasive glucose monitoring in human epidermis*. Analyst, 140:483–488 (2015). doi: 10.1039/C4AN01185F. Cited on pages 97 and 98.

[210] G. Villares, A. Hugi, S. Blaser, and J. Faist. *Dual-comb spectroscopy based on quantum-cascade-laser frequency combs*. Nature Communications, 5:5192–5201 (2014). doi: 10.1038/ncomms6192. Cited on pages 97 and 98.

[211] G. Wysocki and D. Weidmann. *Molecular dispersion spectroscopy for chemical sensing using chirped mid-infrared quantum cascade laser*. Optics Express, 18(25):26123–26140 (2010). doi: 10.1364/OE.18.026123. Cited on pages 97 and 123.

[212] A. Wilk, J. C. Carter, M. Chrisp, A. M. Manuel, P. Mirkarimi, J. B. Alameda, and B. Mizaikoff. *Substrate-Integrated Hollow Waveguides: A New Level of Integration in Mid-Infrared Gas Sensing*. Analytical Chemistry, 85(23):11205–11210 (2013). doi: 10.1021/ac402391m. Cited on page 98.

[213] J. F. da Silveira Petruci, P. R. Fortes, V. Kokoric, A. Wilk, I. M. Raimundo, A. A. Cardoso, and B. Mizaikoff. *Real-time monitoring of ozone in air using substrate-integrated hollow waveguide mid-infrared sensors*. Scientific Reports, 3:3174 (2013). doi: 10.1038/srep03174. Cited on page 98.

[214] E. Tütüncü, M. Nägele, P. Fuchs, M. Fischer, and B. Mizaikoff. *iHWG-ICL: Methane Sensing with Substrate-Integrated Hollow Waveguides Directly Coupled to Interband Cascade Lasers*. ACS Sensors, 1(7):847–851 (2016). doi: 10.1021/acssensors.6b00238. Cited on page 98.

[215] R. L. Ribessi, T. d. A. Neves, J. J. R. Rohwedder, C. Pasquini, I. M. Raimundo, A. Wilk, V. Kokoric, and B. Mizaikoff. *iHEART: a miniaturized near-infrared in-line gas sensor using heart-shaped substrate-integrated hollow waveguides*. Analyst, 141:5298–5303 (2016). doi: 10.1039/C6AN01027J. Cited on page 98.

[216] V. Kokoric, D. Widmann, M. Wittmann, R. J. Behm, and B. Mizaikoff. *Infrared spectroscopy via substrate-integrated hollow waveguides: a powerful tool in catalysis research*. Analyst, 141:5990–5995 (2016). doi: 10.1039/C6AN01534D. Cited on page 98.

[217] A. Wilk, F. Seichter, S.-S. Kim, E. Tütüncü, B. Mizaikoff, J. A. Vogt, U. Wachter, and P. Radermacher. *Toward the quantification of the 13CO2/12CO2 ratio in*

exhaled mouse breath with mid-infrared hollow waveguide gas sensors. Analytical and Bioanalytical Chemistry, 402(1):397–404 (2012). doi: 10.1007/s00216-011-5524-z. Cited on page 98.

[218] D. Perez-Guaita, V. Kokoric, A. Wilk, S. Garrigues, and B. Mizaikoff. *Towards the determination of isoprene in human breath using substrate-integrated hollow waveguide mid-infrared sensors.* Journal of Breath Research, 8(2):026003–026010 (2014). Cited on page 98.

[219] E. Tütüncü, V. Kokoric, R. Szedlak, D. MacFarland, T. Zederbauer, H. Detz, A. M. Andrews, W. Schrenk, G. Strasser, and B. Mizaikoff. *Advanced gas sensors based on substrate-integrated hollow waveguides and dual-color ring quantum cascade lasers.* Analyst, 141:6202–6207 (2016). doi: 10.1039/C6AN01130F. Cited on pages 99, 100, 101, and 132.

[220] C. Y. L. Cheung, P. S. Spencer, and K. A. Shore. *Modulation bandwidth optimisation for unipolar intersubband semiconductor lasers.* IEE Proceedings - Optoelectronics, 144(1):44–47 (1997). doi: 10.1049/ip-opt:19971068. Cited on page 101.

[221] R. de L. Kronig. *On the Theory of Dispersion of X-Rays.* Journal of the Optical Society of America, 12(6):547–557 (1926). doi: 10.1364/JOSA.12.000547. Cited on page 102.

[222] P. Martín-Mateos and P. Acedo. *Heterodyne phase-sensitive detection for calibration-free molecular dispersion spectroscopy.* Optics Express, 22(12):15143–15153 (2014). doi: 10.1364/OE.22.015143. Cited on pages 102 and 103.

[223] P. Bouguer. *Essai d'optique sur la gradation de la lumière.* Claude Jombert (1729). Cited on page 102.

[224] J. H. Lambert. *Photometry, or, On the measure and gradations of light, colors, and shade.* Eberhardt Klett (1760). Cited on page 102.

[225] A. Beer. *Bestimmung der Absorption des rothen Lichts in farbigen Flüssigkeiten.* Annalen der Physik, 162(5):78–88 (1852). doi: 10.1002/andp.18521620505. Cited on page 102.

[226] A. Hangauer, G. Spinner, M. Nikodem, and G. Wysocki. *High frequency modulation capabilities and quasi single-sideband emission from a quantum cascade laser.* Optics Express, 22(19):23439–23455 (2014). doi: 10.1364/OE.22.023439. Cited on pages 102 and 103.

[227] B. Schwarz, P. Reininger, H. Detz, T. Zederbauer, A. Andrews, W. Schrenk, and G. Strasser. *Monolithically Integrated Mid-Infrared Quantum Cascade Laser and Detector.* Sensors, 13(2):2196–2205 (2013). doi: 10.3390/s130202196. Cited on pages 104 and 106.

[228] P. Jouy, M. Mangold, B. Tuzson, L. Emmenegger, Y.-C. Chang, L. Hvozdara, H. P. Herzig, P. Wagli, A. Homsy, N. F. de Rooij, A. Wirthmueller, D. Hofstetter, H. Looser, and J. Faist. *Mid-infrared spectroscopy for gases and liquids based on quantum cascade technologies.* Analyst, 139:2039–2046 (2014). doi: 10.1039/C3AN01462B. Cited on pages 104 and 105.

[229] B. Schwarz, P. Reininger, D. Ristanić, H. Detz, A. M. Andrews, W. Schrenk, and G. Strasser. *Monolithically integrated mid-infrared lab-on-a-chip using plasmonics and quantum cascade structures*. Nature Communications, 5:4085–4091 (2014). doi: 10.1038/ncomms5085. Cited on pages 104 and 107.

[230] A. Harrer, R. Szedlak, B. Schwarz, H. Moser, T. Zederbauer, D. MacFarland, H. Detz, A. M. Andrews, W. Schrenk, B. Lendl, and G. Strasser. *Mid-infrared surface transmitting and detecting quantum cascade device for gas-sensing*. Scientific Reports, 6:21795–21800 (2016). doi: 10.1038/srep21795. Cited on pages 104, 109, 110, 111, and 112.

[231] R. Szedlak, A. Harrer, M. Holzbauer, B. Schwarz, J. P. Waclawek, D. MacFarland, T. Zederbauer, H. Detz, A. M. Andrews, W. Schrenk, B. Lendl, and G. Strasser. *Remote Sensing with Commutable Monolithic Laser and Detector*. ACS Photonics, 3(10):1794–1798 (2016). doi: 10.1021/acsphotonics.6b00603. Cited on pages 104, 113, 114, 115, 116, 117, 118, 119, 120, and 133.

[232] A. Harrer, B. Schwarz, S. Schuler, P. Reininger, A. Wirthmüller, H. Detz, D. MacFarland, T. Zederbauer, A. M. Andrews, M. Rothermund, H. Oppermann, W. Schrenk, and G. Strasser. *4.3 μm quantum cascade detector in pixel configuration*. Optics Express, 24(15):17041–17049 (2016). doi: 10.1364/OE.24.017041. Cited on page 105.

[233] S. D. Gunapala, S. V. Bandara, J. K. Liu, J. M. Mumolo, S. B. Rafol, D. Z. Ting, A. Soibel, and C. Hill. *Quantum Well Infrared Photodetector Technology and Applications*. IEEE Journal of Selected Topics in Quantum Electronics, 20(6):154–165 (2014). doi: 10.1109/JSTQE.2014.2324538. Cited on page 105.

[234] H. Schneider. *Optimized performance of quantum well intersubband infrared detectors: Photovoltaic versus photoconductive operation*. Journal of Applied Physics, 74(7):4789–4791 (1993). doi: 10.1063/1.354352. Cited on page 105.

[235] H. Schneider, C. Schönbein, M. Walther, K. Schwarz, J. Fleissner, and P. Koidl. *Photovoltaic quantum well infrared photodetectors: The four-zone scheme*. Applied Physics Letters, 71(2):246–248 (1997). doi: 10.1063/1.119510. Cited on page 105.

[236] D. Hofstetter, M. Beck, and J. Faist. *Quantum-cascade-laser structures as photodetectors*. Applied Physics Letters, 81(15):2683–2685 (2002). doi: 10.1063/1.1512954. Cited on page 105.

[237] L. Gendron, M. Carras, A. Huynh, V. Ortiz, C. Koeniguer, and V. Berger. *Quantum cascade photodetector*. Applied Physics Letters, 85(14):2824–2826 (2004). doi: 10.1063/1.1781731. Cited on page 105.

[238] D. Hofstetter, S.-S. Schad, H. Wu, W. J. Schaff, and L. F. Eastman. *GaN/AlN-based quantum-well infrared photodetector for 1.55 μm*. Applied Physics Letters, 83(3):572–574 (2003). doi: 10.1063/1.1594265. Cited on page 105.

[239] M. Graf, G. Scalari, D. Hofstetter, J. Faist, H. Beere, E. Linfield, D. Ritchie, and G. Davies. *Terahertz range quantum well infrared photodetector*. Applied Physics Letters, 84(4):475–477 (2004). doi: 10.1063/1.1641165. Cited on page 105.

[240] H. C. Liu, M. Buchanan, and Z. R. Wasilewski. *How good is the polarization selection rule for intersubband transitions?* Applied Physics Letters, 72(14):1682–1684 (1998). doi: 10.1063/1.121151. Cited on page 106.

[241] H. Schneider and H. C. Liu. *Quantum Well Infrared Photodetectors*. Springer-Verlag (2007). Cited on page 106.

[242] L. Lundqvist, J. Y. Andersson, Z. F. Paska, J. Borglind, and D. Haga. *Efficiency of grating coupled AlGaAs/GaAs quantum well infrared detectors*. Applied Physics Letters, 63(24):3361–3363 (1993). doi: 10.1063/1.110145. Cited on page 106.

[243] P. Reininger, B. Schwarz, A. Harrer, T. Zederbauer, H. Detz, A. M. Andrews, R. Gansch, W. Schrenk, and G. Strasser. *Photonic crystal slab quantum cascade detector*. Applied Physics Letters, 103(24):241103 (2013). doi: 10.1063/1.4846035. Cited on page 106.

[244] A. Benz, M. Krall, S. Schwarz, D. Dietze, H. Detz, A. M. Andrews, W. Schrenk, G. Strasser, and K. Unterrainer. *Resonant metamaterial detectors based on THz quantum-cascade structures*. Scientific Reports, 4:4269–4278 (2014). doi: 10.1038/srep04269. Cited on page 106.

[245] A. Harrer, B. Schwarz, R. Gansch, P. Reininger, H. Detz, T. Zederbauer, A. M. Andrews, W. Schrenk, and G. Strasser. *Plasmonic lens enhanced mid-infrared quantum cascade detector*. Applied Physics Letters, 105(17):171112 (2014). doi: 10.1063/1.4901043. Cited on page 106.

[246] A. P. Ravikumar, D. Sivco, and C. F. Gmachl. *Wavelength independent normal incident quantum cascade detectors*. Optics Express, 24(22):25269–25276 (2016). doi: 10.1364/OE.24.025269. Cited on page 106.

[247] H. C. Liu. *The Basic Physics of Photoconductive Quantum Well Infrared Detectors*. In M. Razeghi (Editor), *Long Wavelength Infrared Detectors*, 1–60. Gordon and Breach Science Publishers (1996). Cited on page 106.

[248] A. W. Fang, R. Jones, H. Park, O. Cohen, O. Raday, M. J. Paniccia, and J. E. Bowers. *Integrated AlGaInAs-silicon evanescent racetrack laser and photodetector*. Optics Express, 15(5):2315–2322 (2007). doi: 10.1364/OE.15.002315. Cited on page 106.

[249] A. Spott, J. Peters, M. L. Davenport, E. J. Stanton, C. D. Merritt, W. W. Bewley, I. Vurgaftman, C. S. Kim, J. R. Meyer, J. Kirch, L. J. Mawst, D. Botez, and J. E. Bowers. *Quantum cascade laser on silicon*. Optica, 3(5):545–551 (2016). doi: 10.1364/OPTICA.3.000545. Cited on page 106.

[250] D. Hofstetter, H. P. Zappe, J. E. Epler, and P. Riel. *Monolithically integrated DBR laser, detector, and transparent waveguide fabricated in a single growth step*. IEEE Photonics Technology Letters, 7(9):1022–1024 (1995). doi: 10.1109/68.414689. Cited on page 106.

[251] B. Schwarz, P. Reininger, H. Detz, T. Zederbauer, A. M. Andrews, S. Kalchmair, W. Schrenk, O. Baumgartner, H. Kosina, and G. Strasser. *A bi-functional quantum cascade device for same-frequency lasing and detection*. Applied Physics Letters, 101(19):191109 (2012). doi: 10.1063/1.4767128. Cited on page 107.

[252] D. Ristanić, B. Schwarz, P. Reininger, H. Detz, T. Zederbauer, A. M. Andrews, W. Schrenk, and G. Strasser. *Monolithically integrated mid-infrared sensor using narrow mode operation and temperature feedback*. Applied Physics Letters, 106(4):041101 (2015). doi: 10.1063/1.4906802. Cited on page 107.

[253] E. J. Zhang, L. Tombez, J. Orcutt, S. Kamlapurkar, G. Wysocki, and W. M. Green. *Silicon Photonic On-chip Trace-gas Spectroscopy of Methane*. In *Conference on Lasers and Electro-Optics*, SF2H.1. Optical Society of America (2016). doi: 10.1364/CLEO_SI.2016.SF2H.1. Cited on page 107.

[254] T. J. Johnson, R. L. Sams, and S. W. Sharpe. *The PNNL quantitative infrared database for gas-phase sensing: a spectral library for environmental, hazmat, and public safety standoff detection*. Proceedings of SPIE, 5269:159–167 (2004). doi: 10.1117/12.515604. Cited on pages 110 and 118.

[255] D. W. Allan. *Statistics of atomic frequency standards*. Proceedings of the IEEE, 54(2):221–230 (1966). doi: 10.1109/PROC.1966.4634. Cited on page 120.

[256] P. Dean, Y. L. Lim, A. Valavanis, R. Kliese, M. Nikolić, S. P. Khanna, M. Lachab, D. Indjin, Z. Ikonić, P. Harrison, A. D. Rakić, E. H. Linfield, and A. G. Davies. *Terahertz imaging through self-mixing in a quantum cascade laser*. Optics Letters, 36(13):2587–2589 (2011). doi: 10.1364/OL.36.002587. Cited on page 123.

NOMENCLATURE

α	Spatial coordinate along the ring
α_c	Critical angle of metasubstrate
α_i	Incidence angle of incoming wave
α_m	Mirror losses
α_o	Incidence angle of outgoing wave
α_t	Grating slit tilt
α_w	Waveguide losses
α_{tot}	Total losses
β	Propagation constant
Δf	Frequency amplitude
Δf_{QCD}	Bandwidth
ΔI	Current modulation amplitude
ΔN	Population inversion
ΔP	Modulation power amplitude
δ	Normalized frequency parameter
ϵ	Permittivity
ϵ_0	Vacuum permittivity
ϵ_r	Relative permittivity
η	Absorption efficiency
η_{ee}	Extraction efficiency
η_{iqe}	Internal quantum efficiency
γ	Complex propagation constant
$\hbar$	Reduced Planck's constant
κ	Coupling constant
Λ	Grating period
λ	Wavelength
λ_B	Bragg wavelength
$\mathbf{A}$	Vector potential
$\mathbf{E}$	Electric field vector
$\mathbf{G}$	Reciprocal lattice vector
$\mathbf{H}$	Magnetic field
$\mathbf{J}$	Angular momentum
$\mathbf{K}$	Grating vector
$\mathbf{k}$	Wavevector
$\mathbf{L}$	Orbital angular momentum
$\mathbf{p}$	Momentum

$\mathbf{q}$	Photon wavevector
$\mathbf{S}$	Spin angular momentum
$\mathfrak{F}_{2D}$	Two dimensional Fourier transform
μ	Permeability
μ_0	Vacuum permeability
μ_r	Relative permeability
Ω	Tunneling rate
ω	Angular frequency
ω_c	Center frequency
Φ	Phase shift
Ψ	Wavefunction
ρ	Propagation constant of right traveling wave
ρ_k	Density
Σ	Confinement factor
σ	Conductivity
τ_{ij}	Relaxation time
Θ	Phase shift
θ	Incidence angle
θ_c	Critical angle for total internal reflection
φ	Spatial coordinate along the ring
φ_n	Atomic wavefunction
ϱ	Propagation constant of left traveling wave
ζ	Gain-coupling ratio
A_{ij}	Einstein coefficient for spontaneous transitions
A_{NF}	Near field amplitude
B_{ij}	Einstein coefficient for induced transitions
c	Speed of light
D^*	Detectivity
d_h	Hole diameter
d_{met}	Thickness of metasubstrate
d_{sub}	Substrate thickness
D_{ij}	Transfer matrix at interface
E	Energy
e	Elementary charge
E_n^M	Morse energy levels
E_B	Binding energy
E_n	Quantized energy levels
E_{NF}	Electric near field amplitude
E_{qF}	Quasi-Fermi level
$f(E)$	Fermi function
$f(x,y)$	Field distribution
f_0	Center frequency
F_j	Transfer matrix in uniform region
f_L	Modulated laser frequency
$f_l^{A,B}$	Envelope function
f_M	Modulation frequency
F_{ph}	Photon flux
g	Gain
g_p	Detector gain
G_w	Grating width

g_{th}	Threshold gain
H	Hamiltonian
h	Planck's constant
I	Intensity
I_0	DC current
I_L	Modulated laser current
I_n	Noise current
I_{FF}	Far field intensity
j	Current density
j_{ik}	Flux density
j_{th}	Threshold current density
k_B	Boltzmann constant
L	Cavity length
m	Topological charge
m_{DFB}	Grating order number
m_{diff}	Diffraction order
M_{zz}	Total angular momentum flux
N	Number of atoms
n	Refractive index
N_i	Population density
n_I	Imaginary part of refractive index
N_p	Number of active region periods
n_R	Real part of refractive index
n_{eff}	Effective refractive index
N_{inj}	Injector sheet density
$o(x', y')$	Object function
P_0	Average power
p_c	Capture efficiency
p_e	Extraction efficiency
p_h	Hole period
P_L	Modulated laser power
P_{int}	Internal laser power
P_{out}	Optical output power
q_k	Source density
R	Responsivity
r	Distance
r_0	Equilibrium distance
R_i	Reflectivity
R_{cont}	Grating ratio
R_{inj}	Electron injection rate
R_{ij}^{ab}	Absorption rate
R_{ij}^{in}	Induced transition rate
R_{ij}^{sp}	Spontaneous transition rate
s_t	Slit with of tilted grating
T	Temperature
t	Time
T_i	Total transfer matrix
$u(\nu)$	Spectral energy density
$u_k(r)$	Bloch wavefunction
U_m	Chebyshev polynomial

V	Potential
$V^{M(r)}$	Morse potential
W_i	Inner waveguide radius
W_o	Outer waveguide radius
$W_{i \to f}$	Transition probability
w_{qw}	Quantum well width
ARDE	Aspect ratio dependent etching
BC	Bottom contact
COM	Center of mass
CW	Continuous wave
DFB	Distributed feedback
DTGS	Deuterated triglycine sulfate
EBL	Electron beam lithography
FM	Frequency modulation
FSR	Free spectral range
FTIR	Fourier Transform Infrared
FWHM	Full width at half maximum
HMDS	Hexamethyldisilazane
HPSD	Heterodyne phase-sensitive detection
iHWG	Substrate-integrated hollow waveguide
IM	Intensity modulation
LCAO	Linear combination of atomic orbitals
LI	Light-current
LOD	Limit of detection
MBE	Molecular beam epitaxy
MCT	Mercury-cadmium-telluride
MIR	Mid-infrared
MOCVD	Metalorganic chemical vapor deposition
NIR	Near-infrared
OAM	Orbital angular momentum
PECVD	Plasma-enhanced chemical vapor deposition
PMMA	Polymethylmethacrylate
PNNL	Pacific Northwest National Laboratory
ppm	Parts-per-million
QCD	Quantum cascade detector
QCL	Quantum cascade laser
QWIP	Quantum well infrared photodetector
RIE	Reactive ion etching
SAM	Spin angular momentum
SEM	Scanning electron microscope
SiN	Silicon nitride
TC	Top contact
THz	Terahertz
TM	Transverse-magnetic
WGM	Whispering gallery mode
WKB	Wentzel-Kramers-Brillouin

LIST OF FIGURES

LIST OF TABLES

ACKNOWLEDGMENTS

Reminiscing about my time as a PhD student, leaves me with a great many of amazing memories. It goes without saying that completing a PhD requires the help from others. Besides acknowledging the people who enabled my graduation and contributed to these memorable experiences, the following lines shall serve the purpose of raising a smile while reading them in the future and thinking back to the good old times. I am deeply grateful to

Gottfried Strasser for his ceaseless support, foresighted guidance and for giving me the freedom to pursue and realize my own ideas. His wide-ranging expertise often helped me to identify important matters and get the most out of my research.

Thanks to Sangil Ahn, Alexander Alexewicz, Max Andrews, Mattia Capriotti, Hermann Detz, Christian Doiber, Clement Fleury, Roman Gansch, Andreas Harrer, Borislav Hinkov, Martin Holzbauer, Martin Kriz, Suzanne Lancaster, Donald MacFarland, Jürgen Maier, Peter Reininger, Matteo Rigato, Daniela Ristanić, Werner Schrenk, Benedikt Schwarz, Clemens Schwarzer and Tobias Zederbauer.

The mutual support in the cleanroom and the lab as well as fruitful discussions created a pleasant atmosphere in which scientific research could blossom. Furthermore, this facilitated deeper connections on a personal level and created friendships which will hopefully persist after graduation. Together we experienced plenty of exciting, funny and unforgettable moments. Thanks for the amusing nights at the Downstairs with Schwermatrosen and Justin Biebers, for risky hiking adventures in the presence of imaginary Californian black bears, for exciting road trips in the torrid summer heat of Texas, for keeping the gloating joy about the “best” haircut ever to a minimum, for numerous enjoyable party nights and the relaxing and mostly informative lunch breaks.

I would like to thank all persons who cooperated with me in the course of my PhD which allowed me to gain a broader expertise. Thanks to Andreas Genner, Jakob Hayden, Pedro Martin-Mateos, Harald Moser, Paul Waclawek and Bernhard Lendl for being permanent contact partners in all spectroscopic topics. I am thankful to Thomas Hisch and Stefan Rotter for constructive discussions. Thanks to Vjekoslav Kokoric, Erhan Tütüntü and Boris Mizaikoff for the joyful and extremely productive week in Ulm.

Furthermore, I would like to express my gratitude to every single member of the Institute of Solid State Electronics and all users of the cleanroom for the supportive and friendly climate which made everyday working life enjoyable. In this context I would like to thank Carlo Requiao for entertaining lunch breaks, Florian Aigner for his imaginative press release “The quantum sniffer dog”, the soccer guys and girls for fun and sometimes dangerous Monday evenings and all my students I supervised within the scope of the semiconductor physics lecture for giving me the opportunity to cope with new challenges.

Schließlich möchte ich mich bei meinen Eltern Maria und Georg sowie bei meiner Schwester Agnes für die grenzenlose Unterstützung bedanken, die ich zu jedem Zeitpunkt meines Lebens genießen durfte. Dieser ständige Rückhalt hat einen erheblichen Teil zur erfolgreichen Absolvierung meines Doktorats beigetragen.

Special thanks go to Svenja Wiemer for her constant support and for making my life so wonderful.

“It is a very interesting number.
It is the smallest number expressible as the sum of two cubes in two different ways.”
Srinivasa Ramanujan

“The past, like the future, is indefinite and exists only as a spectrum of possibilities.”
Stephen Hawking

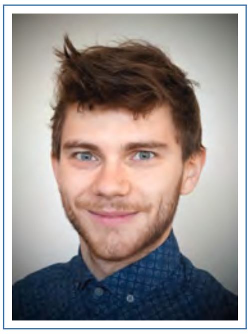

Rolf Szedlak

M.Sc.

Personal information

Address	Mariannengasse 12/2, 1090 Vienna, Austria
Phone	00-43-1-58801-36229
Mobile	00-43-699-18027930
E-mail	rolf.szedlak@tuwien.ac.at
Nationality	German
Date of Birth	27.05.1989 in Viseu de Sus, Romania

Career

since 10/2014	**Ph.D. student (University assistant)**, Technical science at the Institute of Solid State Electronics at TU Wien, Austria.
10/2013 – 09/2014	**Ph.D. student (FWF project assistant)**, Technical science at the Institute of Solid State Electronics at TU Wien, Austria.
04/2012 – 07/2012	**Scientific assistant**, AG Dekorsy at the University of Konstanz, Germany.

Education

10/2012 – 09/2013	**Master's thesis**, Institute of Solid State Electronics at TU Wien, Austria, Mark: 1.0.
10/2011 – 09/2013	**Postgraduate studies**, Physics at the University of Konstanz, Germany, ○ Degree: Master of Science (M.Sc.), Mark: 1.0.
04/2011 – 08/2011	**Bachelor's thesis**, Quantum Materials Laboratory at the University of British Columbia in Vancouver, Canada, Mark: 1.0.
10/2008 – 09/2011	**Undergraduate studies**, Physics at the University of Konstanz, Germany, ○ Degree: Bachelor of Science (B.Sc.), Mark: 1.1.
09/1999 – 06/2008	**Secondary school**, Hohenzollern-Gymnasium in Sigmaringen, Germany, ○ Degree: Abitur (General qualification for university entrance), Mark: 1.7 ○ Awarded with a book price of the German physics association (DPG) as appreciation for outstanding achievements in physics.

Honors & awards

09/2016	**Förderungen für Konferenzteilnahmen von Dissertantinnen und Dissertanten**, *TU Wien*, Stipend for the conference contributions at the IQCLSW in Cambridge, United Kingdom.
06/2016	**Research sponsorship program "International Communication"**, *Austrian Research Association (ÖFG)*, Stipend for the conference contributions at the CLEO in San Jose (CA), United States.
06/2014	**Förderungsstipendium**, *TU Wien*, Stipend for the conference contributions at the ICPS in Austin (TX), United States..
09/2013	**Master's degree with distinction**, *University of Konstanz*.
09/2011	**Bachelor's degree with distinction**, *University of Konstanz*.
06/2008	**DPG book prize**, *German Physical Society (DPG)*, Book prize of the German Physical Society as appreciation for outstanding achievements in physics.

Personal skills & competences

Languages

German	**Native proficiency**.
English	**Full professional proficiency**, 9 years of education and 5 months stay abroad in Canada.
French	**Elementary proficiency**, 5 years of education.
Romanian	**Elementary proficiency**.

Computer skills

MATLAB, LaTeX, Origin, AutoCAD/Autodesk.

Research activity

Peer-review publications: 9 (First author: 5)

Citations: 77; h-index: 5; i10-index: 4 (Google Scholar, May 2017)

Conference talks: 37 (Invited: 7, Presenting author: 17)

Conference presentations: 14 (Presenting author: 4)

ORCID ID: 0000-0002-2997-6715

Interests

Slack-Lining, Hiking, Bicycling, Soccer, Floorball, Jogging, Longboarding, Cooking, Science-Fiction

Publications

Peer-reviewed journals

- R. Szedlak, A. Harrer, M. Holzbauer, B. Schwarz, J. P. Waclawek, D. MacFarland, T. Zederbauer, H. Detz, A. M. Andrews, W. Schrenk, B. Lendl, and G. Strasser. *Remote Sensing with Commutable Monolithic Laser and Detector.* ACS Photonics **3**, 1794 (2016)
- R. Szedlak, M. Holzbauer, P. Reininger, D. MacFarland, T. Zederbauer, H. Detz, A. M. Andrews, W. Schrenk, and G. Strasser. *Ring quantum cascade lasers with grating phase shifts and a light collimating dielectric metamaterial for enhanced infrared spectroscopy.* Vibrational Spectroscopy **84**, 101 (2016)
- R. Szedlak, M. Holzbauer, D. MacFarland, T. Zederbauer, H. Detz, A. M. Andrews, C. Schwarzer, W. Schrenk, and G. Strasser. *The influence of whispering gallery modes on the far field of ring lasers.* Sci. Rep. **5**, 16668 (2015)
- R. Szedlak, C. Schwarzer, T. Zederbauer, H. Detz, A. M. Andrews, W. Schrenk, and G. Strasser. *Grating-based far field modifications of ring quantum cascade lasers.* Opt. Express **22**, 15829 (2014)
- R. Szedlak, C. Schwarzer, T. Zederbauer, H. Detz, A. M. Andrews, W. Schrenk, and G. Strasser. *On-chip focusing in the mid-infrared: Demonstrated with ring quantum cascade lasers.* Appl. Phys. Lett. **104**, 151105 (2014)
- A. Harrer, R. Szedlak, B. Schwarz, H. Moser, T. Zederbauer, D. MacFarland, H. Detz, A. M. Andrews, W. Schrenk, B. Lendl, and G. Strasser. *Mid-infrared surface transmitting and detecting quantum cascade device for gas-sensing* Sci. Rep. **6**, 21795 (2016)
- E. Tütüncü, V. Kokoric, R. Szedlak, D. MacFarland, T. Zederbauer, H. Detz, A. M. Andrews, W. Schrenk, G. Strasser, and B. Mizaikoff. *Advanced gas sensors based on substrate-integrated hollow waveguides and dual-color ring quantum cascade lasers.* Analyst **141**, 6202 (2016)
- S. Chi, S. Johnston, G. Levy, S. Grothe, R. Szedlak, B. Ludbrook, R. Liang, P. Dosanjh, S. A. Burke, A. Damascelli, D. A. Bonn, W. N. Hardy, and Y. Pennec. *Sign inversion in the superconducting order parameter of LiFeAs inferred from Bogoliubov quasiparticle interference.* Phys. Rev. B **89**, 104522 (2014)
- C. Schwarzer, R. Szedlak, S. I. Ahn, T. Zederbauer, H. Detz, A. M. Andrews, W. Schrenk, and G. Strasser. *Linearly polarized light from substrate emitting ring cavity quantum cascade lasers.* Appl. Phys. Lett. **103**, 081101 (2013)

Press releases

- F. Aigner, R. Szedlak. *The quantum sniffer dog.* TU Wien, Press release 69/2016

Conference talks

- R. Szedlak, A. Harrer, B. Schwarz, M. Holzbauer, J. P. Waclawek, H. Moser, D. MacFarland, T. Zederbauer, H. Detz, A. M. Andrews, W. Schrenk, B. Lendl, and G. Strasser. *Photonic Gas Sensing with Commutable Laser and Detector on the same Chip.* ICAVS 9, 11-16 June 2017, Victoria (BC), Canada. (accepted)
- R. Szedlak. *Quantum Cascade Lasers: Fundamentals and Perspectives.* 3rd TROPSENSE Workshop & Winter School, 09-10 January 2017, Ulm, Germany. (invited)
- R. Szedlak, A. Harrer, M. Holzbauer, B. Schwarz, J. P. Waclawek, H. Moser, D. MacFarland, T. Zederbauer, H. Detz, A. M. Andrews, W. Schrenk, B. Lendl, and G. Strasser. *Compact mid-IR sensors based on bi-functional and commutable semiconductor lasers and detectors on the same chip.* 3rd International WORKshop on Infrared Technologies, 07-08 November 2016, Olching, Germany. (invited)
- R. Szedlak, A. Harrer, B. Schwarz, M. Holzbauer, J. P. Waclawek, D. MacFarland, T. Zederbauer, H. Detz, A. M. Andrews, W. Schrenk, B. Lendl, and G. Strasser. *Remote gas sensing with commutable quantum cascade laser and detector on the same chip.* IQCLSW, 04-09 September 2016, Cambridge, United Kingdom. (invited)
- R. Szedlak, A. Harrer, M. Holzbauer, B. Schwarz, D. MacFarland, T. Zederbauer, H. Detz, A. M. Andrews, W. Schrenk, and G. Strasser. *Mid-infrared ring lasers for sensing applications.* EUROPHOTON, 21-26 August 2016, Vienna, Austria.
- R. Szedlak, A. Harrer, B. Schwarz, M. Holzbauer, H. Moser, D. MacFarland, T. Zederbauer, H. Detz, A. M. Andrews, W. Schrenk, B. Lendl, and G. Strasser. *Highly Integrated Gas Sensors based on Bi-functional Quantum Cascade Structures.* CLEO, 05-10 June 2016, San Jose (CA), United States.
- R. Szedlak, T. Hisch, M. Holzbauer, D. MacFarland, T. Zederbauer, H. Detz, A. M. Andrews, W. Schrenk, S. Rotter, and G. Strasser. *On-chip Generation of Infrared Orbital Angular Momentum Beams using a Dielectric Metamaterial.* CLEO, 05-10 June 2016, San Jose (CA), United States.
- R. Szedlak, M. Holzbauer, D. MacFarland, T. Zederbauer, H. Detz, A. M. Andrews, W. Schrenk, and G. Strasser. *Using the far field of ring lasers to characterize their whispering gallery modes.* Joint Annual Meeting of ÖPG, SPG, ÖGAA und SGAA, 01-04 September 2015, Vienna, Austria.
- R. Szedlak, M. Holzbauer, D. MacFarland, T. Zederbauer, H. Detz, A. M. Andrews, W. Schrenk, and G. Strasser. *Ring quantum cascade lasers for infrared spectroscopy.* ICAVS 8, 12-17 July 2015, Vienna, Austria.
- R. Szedlak, M. Holzbauer, D. MacFarland, T. Zederbauer, H. Detz, A. M. Andrews, W. Schrenk, and G. Strasser. *Probing whispering gallery modes in ring lasers.* 1st Next-Lite Workshop, 18-19 June 2015, Hirschwang an der Rax, Austria.

- R. Szedlak, A. Harrer, M. Holzbauer, B. Schwarz, H. Moser, E. Mujagić, C. Deutsch, D. MacFarland, T. Zederbauer, H. Detz, A. M. Andrews, W. Schrenk, K. Unterrainer, B. Lendl, and G. Strasser. *Infrared and terahertz spectroscopy with ring quantum cascade lasers.* German THz Conference, 08-10 June 2015, Dresden, Germany.
- R. Szedlak, C. Schwarzer, T. Zederbauer, H. Detz, A. M. Andrews, W. Schrenk, and G. Strasser. *Focused Emission Beam from Ring Quantum Cascade Lasers.* ICPS, 10-15 August 2014, Austin (TX), United States.
- R. Szedlak, C. Schwarzer, T. Zederbauer, H. Detz, A. M. Andrews, W. Schrenk, and G. Strasser. *Ring Quantum Cascade Lasers with Grating Phase Shifts.* ICPS, 10-15 August 2014, Austin (TX), United States.
- R. Szedlak, C. Schwarzer, T. Zederbauer, H. Detz, A. M. Andrews, W. Schrenk, and G. Strasser. *Ring Cascade Lasers - Integrated Phase Shifts & On-Chip Focusing.* Joint Symposium SFB IR-ON & SFB Next-Lite, 13-14 March 2014, Vienna, Austria.
- R. Szedlak, C. Schwarzer, A. Genner, D. MacFarland, T. Zederbauer, H. Detz, A. M. Andrews, W. Schrenk, and G. Strasser. *Grating-Design based Far Field Modifications of Ring Cavity Quantum Cascade Lasers.* Joint Annual Meeting of ÖPG, SPG, ÖGAA und SGAA, 02-06 September 2013, Linz, Austria.
- R. Szedlak, C. Schwarzer, D. MacFarland, T. Zederbauer, H. Detz, A. M. Andrews, W. Schrenk, and G. Strasser. *Ring Cascade Lasers with Grating Modifications* 3rd International Nanophotonics Meeting, 01-03 September 2013, Salzburg, Austria.
- R. Szedlak, C. Schwarzer, A. Genner, L. Burgstaller, D. MacFarland, T. Zederbauer, H. Detz, A. M. Andrews, W. Schrenk, and G. Strasser. *Polarization Versatility of Ring Cavity Quantum Cascade Lasers.* CLEO/Europe, 12-16 May 2013, Munich, Germany.
- R. Szedlak, A. Harrer, B. Schwarz, M. Holzbauer, J. P. Waclawek, D. MacFarland, T. Zederbauer, H. Detz, A. M. Andrews, W. Schrenk, B. Lendl, and G. Strasser. *Remote Gas Sensing with Quantum Cascade Systems.* Nano and Photonics, 22-25 March 2017, Mauterndorf, Austria. (invited)
- R. Szedlak, C. Schwarzer, T. Zederbauer, H. Detz, A. M. Andrews, W. Schrenk, and G. Strasser. *Ring Cascade Lasers with Integrated Pi-Phase-Shifts.* Photonics West, 01-06 February 2014, San Francisco (CA), United States. (invited)
- M. Holzbauer, R. Szedlak, H. Detz, R. Weih, S. Höfling, W. Schrenk, J. Koeth, and G. Strasser. *Substrate-emitting ring interband cascade lasers.* CLEO/Europe, 25-29 June 2017, Munich, Germany. (accepted)
- A. Harrer, B. Schwarz, R. Szedlak, M. Holzbauer, D. Ristanic, H. Detz, D. MacFarland, T. Zederbauer, A. M. Andrews, W. Schrenk, and G. Strasser. *Quantum cascade structures for sensing applications.* Daylight Solutions Seminar, 10-02 February 2017, San Diego (CA), United States.

- M. Holzbauer, R. Szedlak, D. MacFarland, T. Zederbauer, H. Detz, A. M. Andrews, W. Schrenk, and G. Strasser. *Sub-threshold measurements of the whispering gallery modes in ring quantum cascade lasers.* Annual Meeting of the ÖPG, 27-29 September 2016, Vienna, Austria.
- A. Harrer, B. Schwarz, R. Szedlak, D. Ristanic, H. Detz, A. M. Andrews, T. Zederbauer, D. MacFarland, W. Schrenk, and G. Strasser. *Quantum Cascade devices: from discrete to integrated systems.* MIOMD-XIII, 18-22 September 2016, Beijing, China. (invited)
- G. Strasser, B. Schwarz, R. Szedlak, A. Harrer, H. Detz, A. M. Andrews, T. Zederbauer, D. MacFarland, and W. Schrenk. *Quantum cascade detectors and monolithically integrated sensing devices.* FLAIR, 12-16 September 2016, Aix-les-Bains, France. (invited)
- M. Holzbauer, R. Szedlak, D. MacFarland, T. Zederbauer, H. Detz, A. M. Andrews, W. Schrenk, and G. Strasser. *Ring quantum cascade lasers with metal-covered distributed feedback gratings.* ICPS, 31 July-05 August 2016, Beijing, China.
- A. Harrer, R. Szedlak, B. Schwarz, M. Holzbauer, T. Zederbauer, H. Detz, A. M. Andrews, D. MacFarland, W. Schrenk, H. Moser, J. P. Waclawek, B. Lendl, and G. Strasser. *Mid-infrared bi-functional quantum cascade sensor for long interaction regions.* nanoFIS, 27-29 June 2016, Graz, Austria.
- M. Holzbauer, R. Szedlak, D. MacFarland, T. Zederbauer, H. Detz, A. M. Andrews, W. Schrenk, M. P. Semtsiv, W. T. Masselink, and G. Strasser. *Ring quantum cascade lasers for chemical sensing and spectroscopic applications.* Vienna young Scientists Symposium, 09-10 June 2016, Vienna, Austria.
- A. Harrer, B. Schwarz, P. Reininger, R. Szedlak, D. Ristanic, H. Detz, A. M. Andrews, T. Zederbauer, D. MacFarland, W. Schrenk, and G. Strasser. *MIR lab-on-a-chip: from discrete devices to an integrated system.* WOCSDICE-EXMATEC, 04-10 June 2016, Aveiro, Portugal.
- A. Harrer, B. Schwarz, R. Szedlak, M. Holzbauer, T. Zederbauer, H. Detz, A. M. Andrews, D. MacFarland, W. Schrenk, H. Moser, J. P. Waclawek, B. Lendl, and G. Strasser. *Mid-infrared sensing based on quantum cascade structures.* NextLite Workshop, 03-04 May 2016, Vienna, Austria.
- A. Harrer, B. Schwarz, P. Reininger, R. Szedlak, T. Zederbauer, H. Detz, D. MacFarland, A. M. Andrews, W. Schrenk, and G. Strasser. *An optimized bi-functional material for integrated mid-infrared quantum cascade based sensors.* Photonics West, 13-18 February 2016, San Francisco (CA), United States.
- W. Schrenk, R. Szedlak, D. Ristanić, B. Schwarz, P. Reininger, A. Harrer, H. Detz, D. MacFarland, A. M. Andrews, and G. Strasser. *Integrated Ring Laser Systems for Spectroscopy based on Quantum Cascade Structures.* SCIX 2015, 27 September - 02 October 2015, Providence (RI), United States.

- A. Harrer, B. Schwarz, R. Szedlak, J. Waclawek, H. Moser, D. MacFarland, T. Zederbauer, H. Detz, A. M. Andrews, W. Schrenk, B. Lendl and G. Strasser. *A bi-functional surface emitting and detecting mid-infrared device for sensing applications.* Joint Annual Meeting of ÖPG, SPG, ÖGAA und SGAA, 01-04 September 2015, Vienna, Austria.
- M. Holzbauer, R. Szedlak, D. MacFarland, T. Zederbauer, H. Detz, A. M. Andrews, W. Schrenk, and G. Strasser. *Thermal optimization of ring quantum cascade lasers.* Joint Annual Meeting of ÖPG, SPG, ÖGAA und SGAA, 01-04 September 2015, Vienna, Austria.
- A. Harrer, R. Szedlak, M. Holzbauer, B. Schwarz, H. Moser, E. Mujagić, D. MacFarland, T. Zederbauer, H. Detz, A. M. Andrews, W. Schrenk, B. Lendl and G. Strasser. *Monolithic integrated on-chip sensing using plasmonics.* 1st Next-Lite Workshop, 18-19 June 2015, Hirschwang an der Rax, Austria.
- M. Holzbauer, R. Szedlak, D. MacFarland, T. Zederbauer, H. Detz, A. M. Andrews, W. Schrenk, and G. Strasser. *Light extraction from ring quantum cascade lasers* Nanoforum, 08-09 June 2015, Linz, Austria.
- M. Holzbauer, R. Szedlak, C. Schwarzer, D. MacFarland, T. Zederbauer, H. Detz, A. M. Andrews, W. Schrenk, and G. Strasser. *Mid-Infrared Ring Cavities* 4th International Nanophotonics Meeting, 23-25 October 2014, Innsbruck, Austria.
- C. Schwarzer, R. Szedlak, S. I. Ahn, T. Zederbauer, H. Detz, A. M. Andrews, W. Schrenk, and G. Strasser. *Linearly Polarized Emission Beams from Vertically Emitting Quantum Cascade Ring Lasers.* ITQW, 15-20 September 2013, Bolton Landing (NY), United States.

Conference presentations

- R. Szedlak, A. Harrer, M. Holzbauer, B. Schwarz, J. P. Waclawek, D. MacFarland, T. Zederbauer, H. Detz, A. M. Andrews, W. Schrenk, B. Lendl, and G. Strasser. *Gas sensing with bi-functional ring resonators as laser and detector.* MESS16, 28-29 April 2016, Vienna, Austria.
- R. Szedlak, M. Holzbauer, D. MacFarland, T. Zederbauer, H. Detz, A. M. Andrews, W. Schrenk, and G. Strasser. *How whispering gallery modes can influence the far field of ring lasers.* ITQW, 06-11 September 2015, Vienna, Austria.
- R. Szedlak, C. Schwarzer, M. Holzbauer, T. Zederbauer, H. Detz, A. M. Andrews, W. Schrenk, and G. Strasser. *Polarization and Far Field Modifications of Ring Lasers.* IRDG Meeting, 24-25 April 2014, Vienna, Austria.
- R. Szedlak, C. Schwarzer, T. Zederbauer, H. Detz, A. M. Andrews, W. Schrenk, and G. Strasser. *Polarization Features of Ring Cascade Lasers.* 18th International Winterschool on New Developments in Solid State Physics, 23-28 February 2014, Mauterndorf, Austria.

- R. Szedlak, T. Hisch, M. Holzbauer, D. MacFarland, T. Zederbauer, H. Detz, A. M. Andrews, W. Schrenk, S. Rotter, and G. Strasser. *Creation of Orbital Angular Momentum using an On-chip Dielectric Metamaterial for Beam Shaping.* ICPS, 31 July-05 August 2016, Beijing, China.
- R. Szedlak, A. Harrer, M. Holzbauer, B. Schwarz, J. P. Waclawek, D. MacFarland, T. Zederbauer, H. Detz, A. M. Andrews, W. Schrenk, B. Lendl, and G. Strasser. *Laser Surface Emission and Detection from the same Quantum Cascade Element.* ICPS, 31 July-05 August 2016, Beijing, China.
- M. Holzbauer, R. Szedlak, D. MacFarland, T. Zederbauer, H. Detz, A. M. Andrews, W. Schrenk, and G. Strasser. *Substrate-emitting ring quantum cascade laser array with distributed feedback metal gratings.* IQCLSW, 04-09 September 2016, Cambridge, United Kingdom.
- A. Harrer, B. Schwarz, R. Szedlak, S. Schuler, H. Detz, A. M. Andrews, T. Zederbauer, D. MacFarland, W. Schrenk, and G. Strasser. *High performance quantum cascade detector array for CO2 detection.* IQCLSW, 04-09 September 2016, Cambridge, United Kingdom.
- M. Holzbauer, R. Szedlak, B. Schwarz, D. MacFarland, T. Zederbauer, H. Detz, A. M. Andrews, W. Schrenk, M. P. Semtsiv, W. T. Masselink and G. Strasser. *Towards continuous wave operation of ring cavity quantum cascade lasers.* EUROPHOTON, 21-26 August 2016, Vienna, Austria.
- A. Harrer, R. Szedlak, B. Schwarz, H. Moser, T. Zederbauer, H. Detz, A. M. Andrews, W. Schrenk, B. Lendl, and G. Strasser. *A mid-infrared gas-sensing device based on bi-functional quantum cascade structures.* 19th International Winterschool on New Developments in Solid State Physics, 21-26 February 2016, Mauterndorf, Austria.
- A. Harrer, R. Szedlak, B. Schwarz, H. Moser, T. Zederbauer, D. MacFarland, H. Detz, A. M. Andrews, W. Schrenk, and G. Strasser. *Towards a monolithic integrated surface emitting and detecting mid-infrared gas sensor.* ITQW, 06-11 September 2015, Vienna, Austria.
- M. Holzbauer, R. Szedlak, D. MacFarland, T. Zederbauer, H. Detz, A. M. Andrews, W. Schrenk, and G. Strasser. *Thermal management in ring quantum cascade lasers.* ITQW, 06-11 September 2015, Vienna, Austria.
- M. Holzbauer, R. Szedlak, D. MacFarland, T. Zederbauer, H. Detz, A. M. Andrews, W. Schrenk, and G. Strasser. *High Performance Ring Quantum Cascade Laser for Sensing Applications.* ICAVS 8, 12-19 July 2015, Vienna, Austria.
- C. Schwarzer, R. Szedlak, S. I. Ahn, D. MacFarland, T. Zederbauer, H. Detz, A. M. Andrews, W. Schrenk, and G. Strasser. *DFB Grating Phase-Shifts for Quantum Cascade Ring Lasers.* 18th International Winterschool on New Developments in Solid State Physics, 23-28 February 2014, Mauterndorf, Austria.

Theses

- R. Szedlak. *Beam Modifications of Ring Quantum Cascade Lasers.* University of Konstanz & TU Wien, Master's thesis, September 2013, Vienna, Austria.
- R. Szedlak. *Study of High-temperature Superconductivity in FeAs-based Superconductors by Angle-resolved Photoemission Spectroscopy.* University of Konstanz & University of British Columbia, Bachelor's thesis, September 2011, Vancouver, Canada.

References

Master's thesis and doctoral studies	Univ.-Prof. Dr. Gottfried Strasser, TU Wien Phone: 00-43-1-58801-36230 E-Mail: gottfried.strasser@tuwien.ac.at
Bachelor's thesis	Prof. Dr. Andrea Damascelli, University of British Columbia Phone: 00-1-604-822-4551 E-Mail: damascelli@physics.ubc.ca
Undergraduate and postgraduate studies	Prof. Dr. Thomas Dekorsy, University of Konstanz Phone: 00-49-7531-88-3072 E-Mail: thomas.dekorsy@uni-konstanz.de

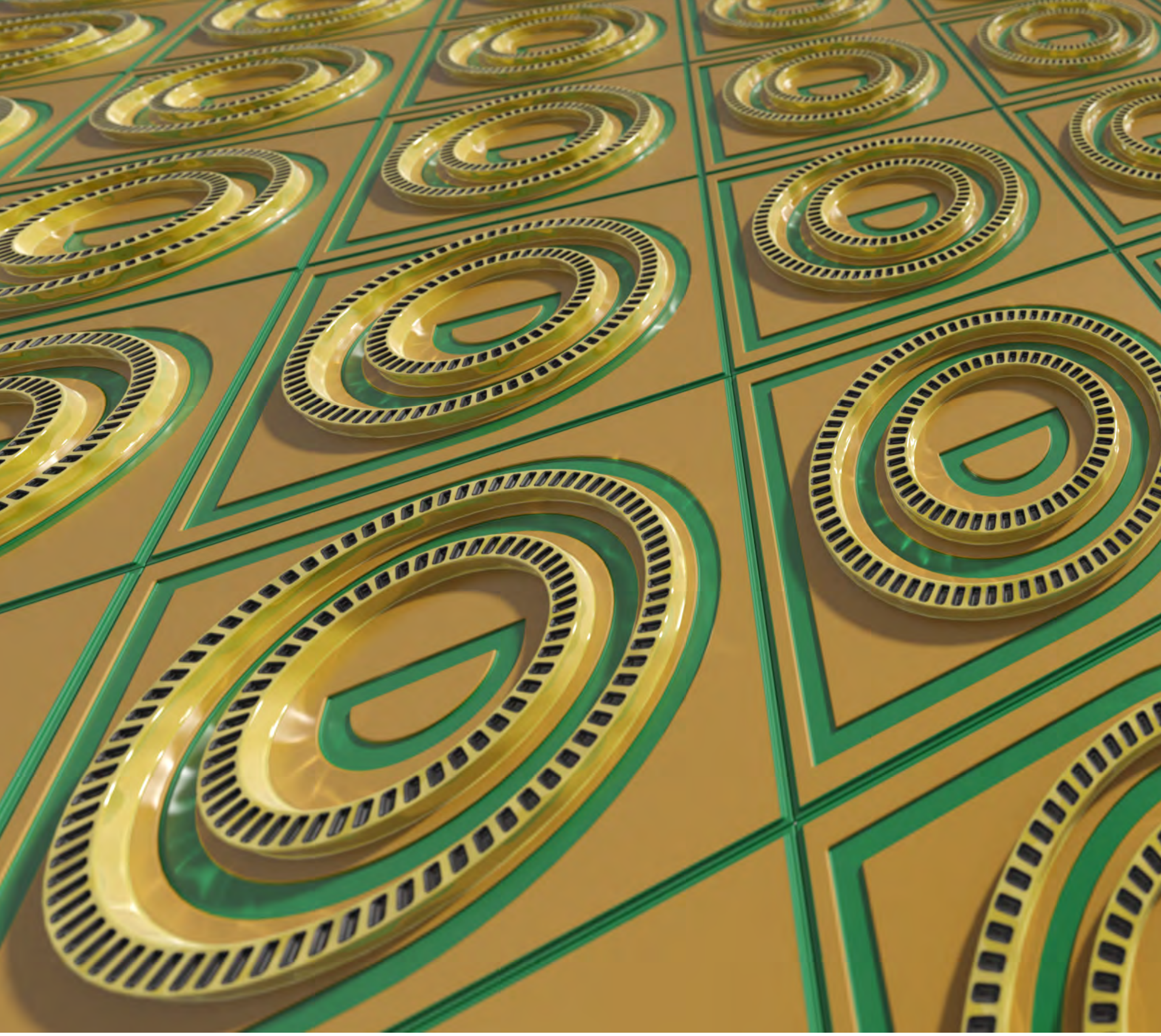

TECHNISCHE
UNIVERSITÄT
WIEN
Vienna | Austria